Quantum Magnets with Strong Spin-Orbit Interaction Probed via Neutron and X-ray Scattering



Alun Biffin
University College
University of Oxford

Thesis submitted for the Degree of
Doctor of Philosophy

Trinity 2014

Quantum Magnets with Strong Spin-Orbit Interaction Probed via Neutron and X-ray Scattering

Alun Biffin, University College

Thesis submitted for the Degree of Doctor of Philosophy, Trinity 2014

This thesis presents details of x-ray and neutron scattering experiments used to probe quantum magnets with strong spin-orbit interaction. The first of these systems are the three-dimensional iridate compounds, in which the three-fold co-ordination of IrO_6 octahedra has been theoretically hypothesized to stabilize anisotropic exchange between Ir^{4+} ions. This novel interaction between these spin-orbital entangled, J_{eff}=1/2 moments is described by a Hamiltonian first proposed by Kitaev, and would be the first physical realization of this Hamiltonian in a condensed matter system. This thesis details the determination of the structure of a new polytype within these compounds, the 'stripyhoneycomb' γ-Li_2IrO_3. Furthermore, through resonant magnetic x-ray diffraction experiments on single crystals of β-Li_2IrO_3 and γ-Li_2IrO_3, an incommensurate, non-coplanar structure with counter-rotating moments is found. The counter-rotating moment structure is a rather counter-intuitive result, as it is not stabilizied by Heisenberg exchange between magnetic sites, however, the Kitaev exchange naturally accounts for this feature. As such, these experiments reveal, for the first time, systems which exhibit dominant Kitaev interactions. The ordering wavevector of both β- and γ-Li_2IrO_3 polytypes are found to be identical, suggesting that the same magnetic interactions are responsible for stabilizing magnetic order in both materials, despite their different lattice topologies. Following this, the spinel $FeSc_2S_4$ is considered. Here, despite the presence of strong exchange between Fe^{2+}, and the fact that these ions sit in a Jahn-Teller active environment, the system does not order in the spin or orbital degrees of freedom. A 'spin-orbital singlet' has been theoretically proposed to describe the groundstate of this system, and here inelastic neutron scattering (INS) is used to probe the resulting triplon excitations. This allows determination of microscopic parameters in the single ion and exchange Hamiltonians, and moreover experiments in external magnetic field reveal the true spin-and-orbital nature of these triplon excitations. Finally, $Ba_3CoSb_2O_9$, a physical realization of the canonical triangular antiferromagnet model is explored with INS and the high energy excitations from the 120° magnetic structure are found to display significant differences from those calculated by linear spin wave theory, suggesting the presence of quantum dynamics not captured in the $1/S$ linear spin wave expansion.

Acknowledgements

I'd like to thank everyone who contributed to the work detailed in this thesis. Foremost among these is my supervisor, Radu Coldea, whose vast knowledge of neutron scattering, and moreover his intuitive understanding of condensed matter systems, have contributed immeasurably to the work I was able to do over these past four years. Throughout this time I've had many insightful and inspiring conversations with him which have been formative to my understanding of this field. Also I'd like to thank Roger Johnson, from whom I learned vast amounts about the resonant magnetic x-ray diffraction technique, and whose knowledge of this and the instrument I16 was invaluable to the iridate experiments described in this thesis. I'm also grateful to my collaborators at PSI, particularly Christian Rüegg and Oksana Zaharko, who were generous and patient in sharing their great knowledge of experimental techniques with me. Sungkyun Choi accompanied me on a number of experiments, and I thank him for his support and advice.

My time in the Clarendon Laboratory has been made orders of magnitude more enjoyable by the presence of my colleagues. In particular I thank my officemates Franz Lang, Jack Wright and Sungkyun Choi for providing me with insights into the German, Geordie and Korean ways of life, respectively. Thank you to Dave Keen for creating a calm and productive environment in 106. Thank you to Danielle Kaminski for disrupting this environment with her various and numerous tales of catastrophe. So many others within the lab have contributed to my happy time here – from Sam Blake's in-depth knowledge of South Coast football clubs, to Jordan Thompson's Canadian 'nonecdotes' – that it would take too long to mention them all.

I'm indebted to my family; Mum, Clifford and little Iwan for their love and support throughout my time in Oxford. Also thanks to my Nain, who persists in sending me baked goods even as I head deep into my twenties. Finally, I must thank Wesley Jarvis, whose encouragement and support has motivated me throughout this thesis. Moreover, his determined, inquisitive and uncompromising mindset lead me to believe that he could be one of the 21st century's finest physicists, were it not for the fact that he is a dog.

Contents

1 Introduction **1**

2 Introduction to the Magnetic Systems Explored **4**

2.1 Magnetic Moment 4

2.2 Spin-Orbit Interaction 8

2.3 Kitaev Physics in the Iridates 10

2.3.1 Introduction to Frustration and the Kitaev Interaction 12

2.3.2 Kitaev Physics in $\mathcal{A}_2IrO_3$ 13

2.3.3 Extension to three-dimensional Lattices 16

2.4 Spin Orbital Singlet State in $FeSc_2S_4$ 20

2.4.1 Conventional Spin Order on a Lattice 22

2.4.2 Spin Singlets on a Lattice 24

2.4.3 Spin Orbital Singlets on a Lattice 26

2.5 Triangular Lattice Antiferromagnet $Ba_3CoSb_2O_9$ 28

References 31

3 Experimental Techniques **37**

3.1 Principles of Neutron Scattering 37

3.1.1 Properties of the Neutron 37

3.1.2 Neutron Scattering Cross-section 38

3.1.3 Nuclear Scattering 42

3.1.4 Magnetic Scattering 48

3.1.5 Neutron Scattering Experiments 52

3.1.6 Sample Environments 55

3.2 Overview of x-ray experimental techniques on Single Crystals 56

3.2.1 Structure Determination through X-ray Diffraction 56

3.2.2 Resonant Magnetic X-ray Diffraction 61

3.2.3 The X-ray Diffractometer I16 67

References 68

4 Non-Coplanar and Counter-Rotating Incommensurate Magnetic Order Stabilized by Kitaev Interactions in γ-Li_2IrO_3 71

4.1 Discovering the Structure of γ-Li_2IrO_3 73
4.2 RMXD Experiment on γ-Li_2IrO_3 85
4.3 Structure Factor Analysis 88
4.4 Azimuthal Dependence of Intensities 92
4.5 Magnetic Structure of γ-Li_2IrO_3 96
4.6 Kitaev Physics in γ-Li_2IrO_3 Groundstate 99
4.7 Conclusions 103
References 104

5 Unconventional Magnetic Order on the Hyperhoneycomb Kitaev Lattice in β-Li_2IrO_3: Full Solution via Resonant Magnetic X-ray Diffraction 106

5.1 Structure of β-Li_2IrO_3 107
5.2 Neutron Powder Diffraction 109
5.3 Resonant Magnetic X-ray Diffraction on β-Li_2IrO_3 114
5.4 Structure Factor Analysis 117
5.5 Azimuthal Dependence of Intensities 122
5.5.1 Determination of Basis Vector Components 122
5.5.2 Peaks with Multiple Basis Vector Contributions 124
5.6 Magnetic Structure of β-Li_2IrO_3 127
5.7 Similarities between Magnetic Structures of β-Li_2IrO_3 and γ-Li_2IrO_3 . 133
5.8 Conclusions 136
References 137

6 Dynamics of a Spin-Orbital Singlet in $FeSc_2S_4$ Probed via Inelastic Neutron Scattering 139

6.1 Structure of, and Exchange Interactions within $FeSc_2S_4$ 140
6.2 Calculating Energy Levels and Excitations in $FeSc_2S_4$ 143
6.2.1 Single Ion Hamiltonian 143
6.2.2 Hopping of Spin-Orbital Triplons 148
6.3 Inelastic Neutron Scattering Experiments and Results 150
6.3.1 Zero Field Neutron Scattering 150
6.3.2 Background Subtraction 153

6.3.3 Neutron Scattering in Applied Magnetic Field 156
6.4 Analysis of Inelastic Neutron Scattering Data 159
6.4.1 Fitting Zero Field Data 160
6.4.2 Zero Field Data Results 163
6.4.3 Field Dependent Analysis 166
6.5 Conclusions 168
References 169

7 Crystal Field levels and Dynamics of $Ba_3CoSb_2O_9$ 171
7.1 Crystal Structure and single-ion energy levels of TAF $Ba_3CoSb_2O_9$ . . 171
7.1.1 Crystal Structure of $Ba_3CoSb_2O_9$ 172
7.1.2 Crystal Field Levels in $Ba_3CoSb_2O_9$ 173
7.2 Inelastic Neutron Scattering Experiments on $Ba_3CoSb_2O_9$ 177
7.2.1 Searching for Single Ion Levels 177
7.2.2 Excitations From the Ordered Phase 179
7.2.3 Inelastic Neutron Scattering from Spin Waves 183
7.2.4 Background Subtraction 185
7.2.5 2D TAF Spin Wave Model 187
7.3 Conclusions 191
References 192

8 Concluding Remarks 195
References 200

A Azimuth Dependence of the Magnetic Resonant X-ray Diffraction Intensity 202
A.1 Calculation for a General Azimuth 202
A.2 Calculation for a Specific Bragg Peak - *Fddd* 206
A.3 Calculation for a Specific Bragg Peak - *Cccm* 207
References 209

B Diagonalization of Pseudo Boson Hamiltonian 210
B.1 Pseudo Boson Technique 210
B.2 Dispersion of Triplons 212
References 218

C Linear Spin Wave Theory in a Helical Ordered Magnet **219**
C.1 Spin Waves in the Anisotropic TAF 219
C.2 Isotropic TAF 225
C.3 Sum Rules 225
References 227

List of Figures

2.1 The Kitaev interaction 13
2.2 Single ion Hamiltonian for Ir^{4+} 14
2.3 Comparison of α, β and γ structures 17
2.4 Comparison of AF Spin order, Spin Dimerization and the SOS state . 23
2.5 TAF $Ba_3CoSb_2O_9$ 28

3.1 Schematic of a neutron scattering event 39
3.2 Schematic of 3 TOF spectrometers 52
3.3 SuperNova diffractometer 59
3.4 Schematic of an RMXD event 63
3.5 I16 Diffractometer 67

4.1 Structural x-ray data for γ-Li_2IrO_3 72
4.2 Crystal structure of γ-Li_2IrO_3 76
4.3 Magnetic Bragg peak at $(0, 0, 16)+\boldsymbol{q}$ 83
4.4 Scanning reciprocal space for magnetic Bragg peaks 84
4.5 Azimuthal scans on γ-Li_2IrO_3 93
4.6 Magnetic Structure of γ-Li_2IrO_3 100

5.1 Crystal structure of β-Li_2IrO_3 and x-ray diffraction data 107
5.2 Neutron powder diffraction on β-Li_2IrO_3 110
5.3 Magnetic Bragg peaks in β-Li_2IrO_3 115
5.4 Integrated intensity as a function of azimuth for three magnetic Bragg peaks 123
5.5 Azimuth scans of "mixed" magnetic peaks 125
5.6 Magnetic Structure of β-Li_2IrO_3 128
5.7 Magnetic Structure of β-Li_2IrO_3 showing moment aligned along b-axis 130

6.1 Structure of, and exchange interactions within $FeSc_2S_4$ 140
6.2 Single ion energy levels for Fe^{2+} 144

6.3 INS data and simulation from MERLIN experiment 151
6.4 Temperature dependence of magnetic signal 153
6.5 Background subtraction procedure for MERLIN data 154
6.6 INS in magnetic field 157
6.7 Fitting procedure for zero field INS data 160

7.1 Crystal structure of $Ba_3CoSb_2O_9$ 172
7.2 Single ion energy levels in $Ba_3CoSb_2O_9$ 175
7.3 Low temperature 120° order in $Ba_3CoSb_2O_9$ 180
7.4 Spin wave spectrum from $S = 1/2$ isotropic TAF 182
7.5 Dynamical structure factor measured on OSIRIS 183
7.6 Background subtraction procedure 185
7.7 Paramagnetic signal 187
7.8 Comparisson with the 2D TAF spin wave model 188

A.1 Schematic diagram of the RMXD experiment at zero azimuth ($\Psi = 0$) 203
A.2 Schematic of azimuthal scan of $\boldsymbol{Q} = (0, 0, l) \pm \boldsymbol{q}$ peak 207

C.1 Mean field groundstate in a TAF 219

Chapter 1

Introduction

This thesis presents studies of quantum magnets with strong spin-orbit interaction probed via neutron and x-ray scattering. To begin, in Chapter 2 some general concepts relevant to all systems will be introduced – e.g. magnetic moments and the interactions between them, and the Hamiltonian which describes the spin-orbit interaction – before moving on to briefly describe the physics which define each system, namely; the Kitaev physics in the three-dimensional (3D) iridates β-Li_2IrO_3 and γ-Li_2IrO_3, the formation of a spin-orbital singlet in $FeSc_2S_4$ and the spin-1/2 triangular antiferromagnet (TAF) model appropriate to $Ba_3CoSb_2O_9$. Following this, in Chapter 3 the theoretical principles underlying, as well as the practical features facilitating neutron and x-ray scattering experiments are presented.

Chapters 4 and 5 describe resonant magnetic x-ray diffraction (RMXD) experiments on γ-Li_2IrO_3 and β-Li_2IrO_3 respectively. The three-fold geometry of edge-sharring IrO_6 octahedra in these systems is theoretically predicted to negate the usual isotropic, Heisenberg exchange, favouring instead the highly anisotropic Kitaev exchange where different components of the spin align preferentially along different bonds. The former of these iridates is a new structural polytype of Li_2IrO_3, and

contains a 'stripyhoneycomb' structure of Ir ions. Chapter 4 begins by explaining how this new structure was discovered for the first time, through analysis of single crystal x-ray diffraction measurements. Chapter 5 also begins with single crystal x-ray diffraction, and confirms a previously suggested 'hyperhoneycomb' system β-Li_2IrO_3. Then the RMXD experiments carried out on these crystals are described in some detail, where the experiments reveal magnetic Bragg peaks at positions incommensurate to the crystal structure. With the aid of azimuthal scans of particular magnetic peaks and use of group theory (especially the allowed basis vectors), the full low temperature magnetic structure of these 3D iridates is solved and is found to be a complex, non-coplanar, incommensurate structure with counter-rotating moments. The latter of these properties is somewhat counter-intuitive and is a result of the anisotropic exchange, which energetically favours such a structure. To close Chapter 5, a comparison is drawn between the magnetic structures of γ-Li_2IrO_3 and β-Li_2IrO_3, and it will be seen that in terms of basis vectors, the mapping between the two structures is entirely equivalent.

In Chapter 6 the spinel structure $FeSc_2S_4$ is introduced, and a large part will then be devoted to the description and analysis of inelastic neutron scattering experiments on a high quality powder sample of $FeSc_2S_4$. Despite the magnetic Fe^{2+} sites possesing spin and orbital moment, the system shows no sign of orbital or spin order down to the lowest temperatures, and a 'spin-orbital singlet' state has been proposed as its groundstate, where spin and orbital moments at each Fe site couple to form a zero moment state. Inelastic neutron scattering probes the excitations from this groundstate to the first excited triplet, and these excitations can be considered as

'spin-orbital triplons' in analogy with the conventional triplon excitations of a spin-singlet. These experiments, in the absence of field, show a dispersive mode which is interpreted as spin-orbital triplons hopping over the lattice, and parameters of a single ion Hamiltonian as well as the exchange interaction are extracted by fitting this data. In measurements in the presence of an external magnetic field the gap to spin-orbital triplon excitations is seen to increase with field, which is a clear departure from the behaviour of 'spin-only triplons' and signifies the presence of orbital physics in $FeSc_2S_4$ even at the lowest temperatures.

The TAF system $Ba_3CoSb_2O_9$ is the subject of Chapter 7, treatment of the single ion Hamiltonian – including cubic crystal fields, an axial distortion and spin orbit coupling – reveals that the Co^{2+} ions have a $J_{\text{eff}} = 1/2$ doublet as their groundstate, meaning that this system is a rare realisation of the canonical spin 1/2 TAF. Inelastic neutron scattering measurements are able to probe transitions from the groundstate to higher energy single ion levels, and through their observation the spin orbit coupling and axial distortion parameters can be deduced. The latter of these is found to be rather small, implying only weakly distorted CoO_6 octahedra. At low temperatures, weak exchange between the triangular layers lead to a 120° order, and the excitations are spin-waves. Again inelastic neutron scattering is used to measure these excitations, and the resulting data is compared to that expected from linear spinwave theory for a $S = 1/2$ moment on an isotropic triangular lattice.

To close, Chapter 8 makes some concluding remarks regarding the work outlined here, as well as suggestions for further work on these compounds, both theoretical and experimental.

Chapter 2

Introduction to the Magnetic Systems Explored

Here, the systems which will be explored throughout this thesis are introduced. The physics within them varies quite considerably; from incommensurate order with non-coplanar moments in β-Li_2IrO_3 and γ-Li_2IrO_3 stabilized by the anisotropic Kitaev interaction, to the more 'conventional' 120° ordering in the spin-half triangular antiferromagnet $Ba_3CoSb_2O_9$ and onto the complete absence of order in the spin-orbital singlet $FeSc_2S_4$. The role of this chapter is to give an outline of the various interactions and considerations appropriate to each of these systems, as well as place them in the wider context of experimental condensed matter physics.

2.1 Magnetic Moment

The object of interest in all the systems covered here are the magnetic moments within them. In the classical picture, an atom at site i within a crystal can produce a magnetic moment $\boldsymbol{\mu}_i$ through the motion of its electrons around the nucleus, e.g. in Cartesian co-ordinates the moment parallel to the z-axis is given by [1]

$$\mu_{i,z} = \frac{e}{2} \sum_j x_{i,j}\dot{y}_{i,j} - y_{ij}\dot{x}_{i,j}, \tag{2.1}$$

where the sum is taken over the j electrons (with charge e) 'orbiting' the atom's nucleus. Note that the quantities being summed are merely the angular momenta of the electrons, divided by their mass and multiplied by their charge.

Though this classical picture of electrons contributing to magnetic moments through their angular momentum seems to offer explanations of known magnetic phenomena – e.g. moments tend to line up with the application of a magnetic field H in paramagnetic materials, and the competition between this and thermal agitations results in a Curie $1/T$ behaviour of magnetic susceptibility, atoms with no net moment tend to resist an external field due to a law by Lenz and therefore show diamagnetic behaviour, etc – the picture is rather dull. This is because these moments only interact very weakly through the dipole-dipole interaction, and indeed through the use of more rigorous statistical mechanics it was found (e.g. van Leeuwen) that magnetism is in fact completely absent within pure classical statistics [2].

Magnetism must then be considered as an entirely quantum effect, where the magnitude of the angular momentum cannot vary continuously, but rather is split into quanta such that electrons sit in discretized orbitals. The magnetic moment has contributions from both spin $\boldsymbol{S}_i$ and orbital $\boldsymbol{L}_i$ components of the angular momentum, e.g. in an atom with only spin degrees of freedom one has

$$\boldsymbol{\mu}_i = -2\mu_B \boldsymbol{S}_i, \tag{2.2}$$

where μ_B is the Bohr magneton and the minus sign is due to the negative charge of

the electron. In fact, in general the single ion Hamiltonian for a given magnetic atom i will be solved and the effective total angular momentum, with both spin and orbital contributions, $\boldsymbol{J}_{\text{eff},i}$ in the groundstate found, which will then relate to the magnetic moment via

$$\boldsymbol{\mu}_i = -g\mu_B \boldsymbol{J}_{\text{eff},i}, \tag{2.3}$$

where g is the gyromagnetic ratio, which was simply = 2 in the case of a spin-only system (2.3). In all the systems encountered in this thesis it will be seen that the spin and orbital contributions to the angular momentum at an ion site i are coupled together (this spin-orbit coupling will be described in detail in the following section) resulting in a total angular momentum $\boldsymbol{J}_{\text{eff},i}$ at each site. Therefore it is this total angular momentum which is appropriate, and in fact it will be seen that the physics of these spin and orbital moments allows for qualitatively different physics compared to their spin-only parallels. Often the term 'spin' and symbol $\boldsymbol{S}$ will still be used to describe these generalized moments.

These quantum moments can then interact with each other via a multitude of interactions – direct exchange, superexchange, Dzyaloshinskii-Moriya interaction, etc – to produce an abundance of interesting groundstates and excitations for the system. For example the Heisenberg Hamiltonian is given by [3]:

$$\mathcal{H} = -\sum_{n,m} J(\boldsymbol{R}_m - \boldsymbol{R}_n)\boldsymbol{S}_m \cdot \boldsymbol{S}_n, \tag{2.4}$$

where spin $\boldsymbol{S}_m$ sits at lattice site m and interacts with spin $\boldsymbol{S}_n$ at lattice site n via the interaction term $J(\boldsymbol{R}_m - \boldsymbol{R}_n)$, which (as the form suggests) will be a function of the separation between the two sites. Such an interaction is termed an 'exchange'

interaction, due to the fact that it results from the minimization of a system's energy by allowing electrons to hop (or exchange) between sites m and n. Although the form of (2.4) implies that it is from a 'pure' spin-spin interaction (e.g. the interaction of two dipole moments) it results from the consideration of the symmetry of the total wavefunction (spatial + spin) of the electrons, and its expression here in terms of spins $\boldsymbol{S}_n$ is of great convenience, as all the dependence on the actual mechanism of exchange (i.e. hopping between specific orbitals) can be sequestered away in J.

When $J > 0$ moments will tend to align, and so this is termed a ferromagnetic (FM) interaction, however if $J < 0$ then the most energetically favourable thing for spins to do is anti-align and this is termed an antiferromagnetic (AF) ordering. The Hamiltonian (2.4) cannot be solved generally, but only in special cases, e.g. when one considers interactions between nearest neighbours on highly symmetric lattices, but this model Hamiltonian still proves to be a very useful thing when considering the groundstate and excitations in magnetic systems, as will be seen.

Regardless of the nature or origin of the magnetic state however, the object of interest remains the magnetic moment; determination of their equilibrium orientations (as in the experiments on γ-Li_2IrO_3 and β-Li_2IrO_3 described in Chapters 4 and 5, respectively) allow one to make deductions about the interactions leading to the ground state, while their dynamics (measured via inelastic neutron scattering in $FeSc_2S_4$ (Chapter 6) and $Ba_3CoSb_2O_9$ (Chapter 7)) reveal the nature of excitations within the system.

2.2 Spin-Orbit Interaction

As mentioned in the previous section, the magnetic moments of interest to this thesis arise due to the motion of electrons. A description of the magnetic system then will simply be the equation of motion of electrons, and this description should clearly be a relativistic one, and so the relevant equation is the *Dirac Equation* [4]. For an electron in an external electromagnetic field, the resulting Hamiltonian for the positive energy solutions has the form

$$\begin{aligned}\mathcal{H} &= \left[mc^2 + \tfrac{1}{2m}\left(\boldsymbol{p} - \tfrac{e}{c}\boldsymbol{A}\right)^2 - \tfrac{p^4}{8m^3c^2}\right] + e\phi - \tfrac{e\hbar}{2mc}\boldsymbol{\sigma}\cdot\boldsymbol{H} - i\tfrac{e\hbar^2}{8m^2c^2}\boldsymbol{\sigma}\cdot\boldsymbol{\nabla}\times\boldsymbol{E} \\ &\quad - \tfrac{e\hbar}{4m^2c^2}\boldsymbol{\sigma}\cdot\boldsymbol{E}\times\boldsymbol{p} - \tfrac{e\hbar^2}{8m^2c^2}\boldsymbol{\nabla}\cdot\boldsymbol{E},\end{aligned} \tag{2.5}$$

where the components σ_i of $\boldsymbol{\sigma}$ are the Pauli matrices

$$\sigma_x = \begin{bmatrix} 0 & 1 \\ 1 & 0 \end{bmatrix}, \quad \sigma_y = \begin{bmatrix} 0 & -i \\ i & 0 \end{bmatrix}, \quad \sigma_z = \begin{bmatrix} 1 & 0 \\ 0 & -1 \end{bmatrix}. \tag{2.6}$$

The 6^{th} and 7^{th} terms in (2.5) are spin-orbit terms. In a stationary vector potential and a spherically symmetric scalar potential $V(r)$ (appropriate for the Coulomb potential from the nucleus and filled inner electron shells) they reduce to

$$\mathcal{H}_{ls} = \frac{e\hbar^2}{4m^2c^2}\frac{1}{r}\frac{\partial V}{\partial r}\boldsymbol{\sigma}\cdot\boldsymbol{l}, \tag{2.7}$$

which is just as would be calculated for an electron spin interacting with the field produced by its orbital motion, but reduced by a factor of 1/2 because of the Thomas precession.

The Hamiltonian in (2.7) defines the interaction between a single electron's spin and its moment, however in the magnetic systems under consideration there will

typically be many electrons within an ion which contribute to the magnetic moment at a given lattice site. Therefore the full Hamiltonian to be considered is of the form

$$\mathcal{H}'_{\mathrm{SO}} = \sum_i \zeta(\boldsymbol{r}_i)\boldsymbol{l}_i \cdot \boldsymbol{s}_i, \tag{2.8}$$

where the sum is over all electrons in the outer (unfilled) shell, the conversion $\boldsymbol{s} = \hbar/2\boldsymbol{\sigma}$ has been made, and the prefactors of (2.7) have been absorbed into a term $\zeta(\boldsymbol{r}_i)$.

Typically, this Hamiltonian will be applied within some given LS term (where L and S denote the total spin and orbital angular moments, respectively), and so via the Wigner-Eckhart theorem [5], the matrix elements of (2.8) are proportional to those of $\boldsymbol{L} \cdot \boldsymbol{S}$. Therefore the *Spin-Orbit Hamiltonian* is:

$$\mathcal{H}_{\mathrm{SO}} = \lambda \boldsymbol{L} \cdot \boldsymbol{S} \tag{2.9}$$

where λ is an energy scale dependent on the configuration of the atom's outer electrons.

The Hamiltonian of (2.9) may seem rather innocuous; it causes degenerate states with well defined L and S values to become split into states defined by the value of J. However, this simple description of a total angular momentum $\boldsymbol{J} = \boldsymbol{L} + \boldsymbol{S}$ being the sum of spin and orbital moments obscures the very different nature of these contributions. $\boldsymbol{S}$ is the intrinsic spin of the electrons of a magnetic ion in a given state, it is not directly coupled to the lattice, though is typically able to interact with other spins through some interaction, e.g. equation (2.4), which will depend on the local connectivity of these spins within a given lattice. $\boldsymbol{L}$ is the orbital angular

momentum of the electrons of a magnetic ion, and as such describes the distribution of these electrons in space and so is affected by the Coulomb charges introduced by surrounding ions in the lattice, e.g. $\boldsymbol{L}$ can be entirely quenched due to local distortions (this is the Jahn-Teller effect and will be described later). The significance of (2.9) then is that it couples these two very different contributions together; the spin is now coupled to the lattice, orbitals are coupled to specific spin states, and so, subsequently rich physics is to be expected which is qualitatively different from that of 'spin only' quantum magnets.

The physics of the systems which make up this thesis all owe something to the spin orbit interaction of (2.9); from the anisotropic interactions of the Kitaev model in the lithium iridate compounds of Chapters 4 and 5 to the spin-orbital singlet state in $FeSc_2S_4$ which makes up Chapter 6 and finally the spin orbit entangled $J_{\text{eff}} = 1/2$ moments in $Ba_3CoSb_2O_9$ on the triangular lattice antiferromagnet of Chapter 7.

Having covered the basic principles of magnetic moments and spin-orbit interaction applicable to all the systems explored in this thesis, the defining physics of each system will now be introduced.

2.3 Kitaev Physics in the Iridates

Materials containing ions with a strong spin-orbit interaction are attracting much attention as candidates to display novel electronic states ranging from topological insulators with protected gapless surface states to quantum spin liquids with exotic excitations [6]. Complex magnetic behavior can arise when the strong spin-orbit coupling (as found for heavy transition metal $4d$ and $5d$ ions) and crystal field effects

stabilize spin-orbit entangled magnetic moments, which may interact via anisotropic exchange interactions where the anisotropy axis depends on the bond orientation. On certain lattices these anisotropic exchange interactions may be strongly frustrated, leading potentially to novel forms of cooperative magnetic order and/or excitations, not found for magnets of $3d$ ions, where the spin-orbit coupling is much weaker and the orbital moment is in general quenched (though we shall see in Chapter 6 that this is not always the case). The magnetic ground state of Ir^{4+} ions in a cubic IrO_6 octahedron is a doublet with a mixed spin-orbital character [7], $J_{\text{eff}} = 1/2$, and for edge-sharing IrO_6 octahedra it was proposed [8, 9] that the leading super-exchange is a ferromagnetic Ising coupling between the Ir magnetic moment components perpendicular to the Ir-O_2-Ir plane (see Fig 2.1(c)). For three-fold coordinated, edge-sharing octahedra (see Fig 2.1(b)) this leads to orthogonal Ir-O_2-Ir planes for the three Ir-Ir bonds and correspondingly orthogonal $\mathsf{x}, \mathsf{y}, \mathsf{z}$ components coupled along the three Ir-Ir bonds. For a honyecomb lattice this realizes the Kitaev model [10], where the strong frustration effects stabilize an (exactly solvable) quantum spin liquid state with novel excitations (Majorana fermions and fluxes) [11]. In search for realizations of such physics, α-Na_2IrO_3 [12, 13, 14, 15, 16] and α-Li_2IrO_3 [17, 18] have been actively explored experimentally, however no clear evidence of novel Kitaev phenomena has been observed.

In the following section a brief description of the Kitaev interaction and its application to the Iridates is given.

2.3.1 Introduction to Frustration and the Kitaev Interaction

Frustration, the inability of pairwise interactions to be simultaneously satisfied leads to a whole host of interesting phenomena in magnetic systems as, unlike in the case of 'simple' ordered systems (e.g. Ferromagnets) the groundstate is not uniquely defined [19]. The resulting ground states are often exotic (e.g. spin liquids [20], spin ices [21], spin glasses [22]) and the excitations from this state mirror its anomalous behaviour allowing for example modes with fractional quantum numbers [20].

The triangular lattice is the prototypical example of *geometrical* frustration, whereby interactions between sites are isotropic but the geometry of the lattice causes frustration. This is readily visualized by a single triangular plaquette with spins at the apexes interacting antiferromagnetically via an Ising Hamiltonian; all three interactions cannot be simultaneously satisfied and the groundstate is highly degenerate (see Fig 2.5). This triangular antiferromagnet (TAF) remains a system of intense study in condensed matter physics, and one example of such a system, $Ba_3CoSb_2O_9$, will be introduced in Section 2.5.

However, this need not be the only realization of frustration on a 2D lattice with 3-fold rotational symmetry. Kitaev [10] proposed a Hamiltonian for $S = \frac{1}{2}$ spins on the honeycomb lattice (which with only conventional AF nearest neighbour interactions would not exhibit frustration), whereby exchange between the three nearest neighbours (NN) couples only specific components of the moments. The interaction between two moments i and j is then given by:

$$\mathcal{H}_{ij} = -J_K S_i^{\eta} S_j^{\eta}, \tag{2.10}$$

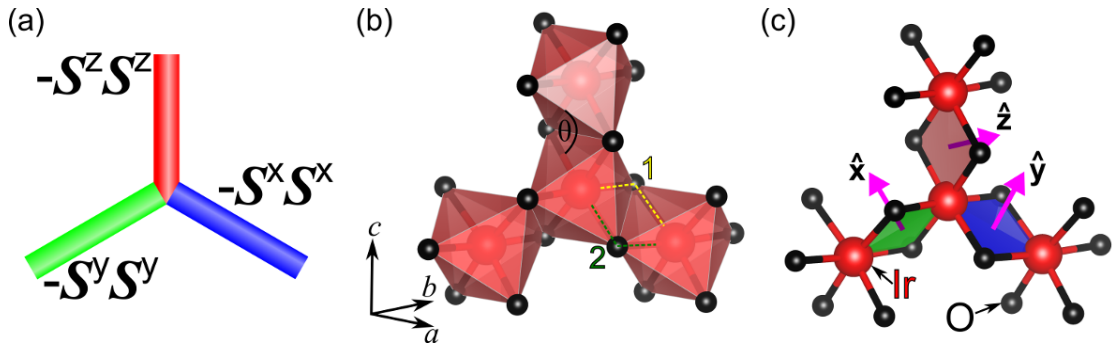


Figure 2.1: The Kitaev interaction (a) The Kitaev interaction describes an asymmetric exchange between ion sites on a honeycomb lattice, where each bond pairs a different component $\mathsf{x}, \mathsf{y}, \mathsf{z}$ of the spin. (b) In the $\mathcal{A}_2\mathrm{IrO}_3$ iridates, edge-sharing IrO_6 octahedra form a motif with 3-fold connectivity, the bond angle $\theta = 90°$ in the undistorted lattice and two exchange paths are shown 1 (yellow) and 2 (green). (c) The cancelation of isotropic exchange along these exchange paths causes Kitaev type exchange, where the component of the coupled moment is defined by the normal to the square plaquettes (coloured, with same convention as (a))

where η describes a given component of the spin $\mathsf{x}, \mathsf{y}, \mathsf{z}$ and J_K describes the strength of the exchange, note the anisotropic nature of this Hamiltonian compared to (2.4). This is shown schematically in Fig 2.1(a), the three bonds on the lattice couple different cartesian components of the spin, labelled $\mathsf{x}, \mathsf{y}, \mathsf{z}$, and the minus signs indicate a FM coupling. One can see that such a configuration leads to frustration, as each of the three bonds wish to co-align the spins along a different axis. Such a system is proposed to have a quantum spin liquid groundstate with Majorana fermion excitations [10].

2.3.2 Kitaev Physics in $\mathcal{A}_2\mathrm{IrO}_3$

A related model, the Kitaev-Heisenberg model, was proposed to occur in the iridate compounds $\mathcal{A}_2\mathrm{IrO}_3$ [9]. In these compounds the Iridium ion has a valence of 4+ and its outer electrons all reside in the $5d$ shell. They sit in the centre of IrO_6 octahedra where the usual d-orbital splitting into t_{2g} and e_g levels occur [23], where

$$e_g \begin{cases} |x^2-y^2\rangle &= \frac{1}{\sqrt{2}}\left(|2,2\rangle + |2,-2\rangle\right) \\ |z^2\rangle &= |2,0\rangle \end{cases}, \quad t_{2g} \begin{cases} |xy\rangle &= \frac{1}{i\sqrt{2}}\left(|2,2\rangle - |2,-2\rangle\right) \\ |yz\rangle &= \frac{1}{i\sqrt{2}}\left(-|2,1\rangle - |2,-1\rangle\right) \\ |zx\rangle &= \frac{1}{\sqrt{2}}\left(-|2,1\rangle + |2,-1\rangle\right) \end{cases}, \tag{2.11}$$

and on the rhs the notation $|l, m_l\rangle$ has been used. The t_{2g} group lies at a lower energy, due to its constituent orbitals being positioned between oxygen ions. This is illustrated in the central part of Fig 2.2 where the Ir and O ions are depicted as red and black spheres respectively. The large crystal field splitting, $\Delta_{\rm cf}$, results in the outer electrons arranging themselves in the low spin state.

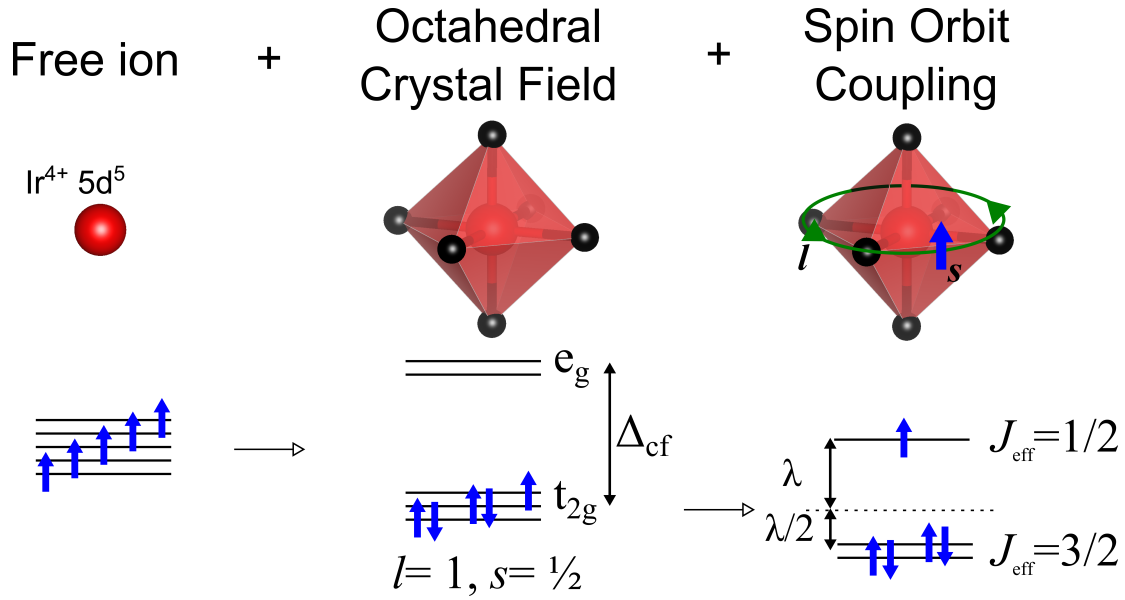


Figure 2.2: Single ion Hamiltonian for Ir^{4+}, Octahedral crystal field and spin orbit coupling terms split the $5d^5$ orbitals and the result is a $J_{\rm eff} = 1/2$ Kramer's doublet (see text).

This configuration has total $s = 1/2$ and $l = 1$ (the t_{2g} can be mapped onto an effective $l = 1$ triplet [24]), and due to the large atomic number of $5d$ transition metals a significant coupling between spin and orbital contributions to the angular

momentum on these sites would be expected. The spin s and orbital l components of the angular momentum at a lattice site couple through the 'Spin-Orbit Interaction' of (2.9) and the resulting splitting is shown in the right-most part of Fig 2.2. The outcome is an energy level scheme with a completely filled $J_{\text{eff}} = 3/2$ band[1] and so it follows that the single ion properties of the Ir^{4+} ions is governed by a $J_{\text{eff}} = 1/2$ Kramer's doublet [7].

The common building block in all $\mathcal{A}_2IrO_3$ compounds is the configuration of 4 IrO_6 octahedra shown in Fig 2.1(b); in the α-iridates, these blocks are co-planar and map out a honeycomb of[2] $S = 1/2$ Ir ions, whereas – as will be seen – in the β- and γ- polytypes they are arranged in a periodic, three dimensional manner, but in all cases the 3-fold connectivity remains.

The question now is whether these ions can support the Kitaev type exchange described (2.10). One might expect a large isotropic exchange interaction, of the type (2.4) between neighbouring Ir ions through Ir-O-Ir exchange paths, and two such paths are shown in Fig 2.1(b). However it can be shown [8] that for a perfect 90° Ir-O-Ir bond ($\theta = 90°$ in Fig 2.1(b)), the amplitudes for the isotropic exchange mediated by these pathways ('1' and '2') exactly cancel leaving a finite anisotropic exchange of the type (2.10). Moreover it is found that the component of the spin coupled along a particular Ir-Ir 'bond' is given by the vector normal to the square plaquette

[1] although this picture of levels being 'filled' by electrons is appealing, one should not be mislead; the free ion and crystal field Hamiltonians are independent of spin, and so the full state is found by filling the levels in such a way that the total system's energy is minimized (which due to the high Δ_{cf} results in all electrons being in the t_{2g} levels) as depicted in Fig 2.2 (left and center). The spin-orbit coupling term however explicitly contains the spin component, and the J_{eff} levels are complex admixtures of all l and s states, so the right side of Fig 2.2 is understood as a helpful schematic rather than a complete description of the groundstate wavefunction.

[2] again the notation 'S' is used, even though this moment has been shown to result form spin and orbital contributions

containing the bond. This is shown in Fig 2.1(c), where the square plaquettes are shaded and the corresponding normal drawn. It can be seen that these normals are mutually orthogonal, and these define the type 'η' of Kitaev exchange (2.10) between Ir ions (Fig 2.1(a)). The Kitaev axes $\mathsf{x}, \mathsf{y}, \mathsf{z}$ are naturally defined with respect to the axes of the IrO_6 octahedra, and comparison with the lattice vectors shown in Fig 2.1(b) reveals a mapping $\hat{\mathbf{x}} = (\hat{\boldsymbol{a}} + \hat{\boldsymbol{c}})/\sqrt{2}$, $\hat{\mathbf{y}} = (\hat{\boldsymbol{a}} - \hat{\boldsymbol{c}})/\sqrt{2}$ and $\hat{\mathbf{z}} = \hat{\boldsymbol{b}}$.

Search for realizations of such physics in the honeycomb iridates α-Na_2IrO_3 and α-Li_2IrO_3 have been intensely explored experimentally, however no clear evidence for novel Kitaev phenomena has been observed.

2.3.3 Extension to three-dimensional Lattices

Although the honeycomb iridates provide one possible realization of Kitaev physics, the search for anisotropic physics in these systems need not be confined to these α polytypes. One can consider systems of the same stochiometry, keeping the three-fold Ir connectivity depicted in Fig 2.1(b), but dropping the restriction that nearest neighbour Iridium ions must lie in the same plane. Such structures would maintain (in the case of undistorted lattices) the 90° Ir-O-Ir bond angles and anisotropic exchanges depicted in Fig 2.1(c) of the α phase, but now map out fully three-dimensional patterns of nearest-neighbour iridium ions.

The theoretical extension of the Kitaev model to these three-dimensional lattices have also been shown to have quantum spin liquid ground states ([25], [26]), and moreover non-trivial magnetic order has been predicted when additional interactions are present, suppressing the spin liquid phase and stabilizing magnetic order [27]. It is two of these 3-D systems that will be the focus of study in Chapters 4, and 5,

and so here this idea of a three-dimensional extension to the honeycomb, α polytype will be developed explicitly such that in the discussion of crystal structure in these following chapters the features common to all polytypes need not be repeated, and the reader is familiar with the similarities and differences between the two polytypes studied.

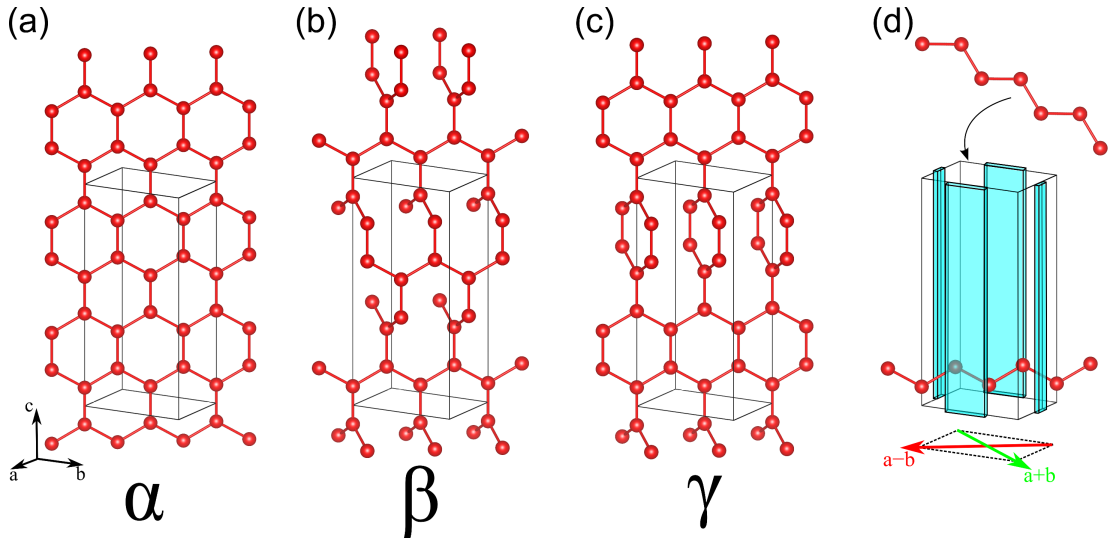


Figure 2.3: Comparison of α, β and γ structures. (a), (b) and (c) show a single 'plane' of the Ir lattice for α, β and γ polytypes, respectively. The orthorhombic unit cell common to the β and γ phases are shown for all polytypes (see text). (d) Constructing members of the series through stacking zig-zag chains parallel to $\boldsymbol{a}+\boldsymbol{b}$ or $\boldsymbol{a}-\boldsymbol{b}$.

In Fig 2.3(a), a single honeycomb plane of Ir ions is shown as red balls, with red cylinders connecting nearest neighbours. The three-fold connectivity of each ion (see Fig 2.1(c)) is apparent, and this structure is referred to as the α polytype, e.g. α-Na_2IrO_3, α-Li_2IrO_3, and Fig 2.3(a) could be said to represent either of these lattices, as the Li/Na and O ions have been removed for clarity. In Fig 2.3(b) and (c), the β and γ polytypes are shown respectively (again only the Ir sites, with links between nearest neighbours shown). Both these structures have the same stochiometry as the

α phase, but clearly the underlying network of Ir's is different between the three, even though inspection of Fig 2.3(b) and (c) show that the three-fold connectivity of Ir sites is maintained.

Comparison of Fig 2.3(a) and Fig 2.3(c) is most clear; here it is seen that both structures are built up of hexagonal plaquets formed in 'honeycomb rows', but whereas each row remains parallel in the α phase, in the γ phase, alternate rows line-up along alternating directions (the face diagonals of the orthorhombic unit cell $\boldsymbol{a} \pm \boldsymbol{b}$). This then gives an insight into how the β phase of Fig 2.3(b) fits into this scheme; here the zig-zag chains of Ir ions (two of which produce the honeycomb rows mentioned previously) alternate in orientation upon moving up the c-axis, again chains being parallel to the face diagonals of the ab-plane. The resulting structure contains none of the honeycomb rows of the α and γ phases, and is often referred to as a 'hyper-honeycomb' lattice.

It is clear then, that even though the honeycomb rows are the most immediate feature of the α structure, the true building blocks of this family are the zig-zag chains of Ir ions, which lie parallel to $\boldsymbol{a} + \boldsymbol{b}$ or $\boldsymbol{a} - \boldsymbol{b}$. One could imagine then 'constructing' a multitude of polytypes. A single unit cell can be considered (see Fig 2.3(d)), where some slats have been attached to the sides of this cell (blue rectangles), such that the zig-zag chains which will fill the cell can only go in one of two orientations; parallel to $\boldsymbol{a} + \boldsymbol{b}$ (green arrow) or $\boldsymbol{a} - \boldsymbol{b}$ (red arrow). Note that the slats are smaller than the dimensions of the cell, ensuring that chains are able to position themselves in such a way that the vertical Ir-Ir links are parallel to $\boldsymbol{c}$. The first chain is dropped into the cell, parallel to $\boldsymbol{a} - \boldsymbol{b}$, say. Now if the next chain is dropped in with the alternative

alignment (parallel to $\boldsymbol{a} + \boldsymbol{b}$), and this process is repeated, such that each chain is dropped in with a different orientation from the one which preceeded it, the resulting structure is as shown in Fig 2.3(b) i.e. the β phase.

Similarly, if two chains are dropped in with the same alignment, with the alignment changed for the next two, and so on, the resulting structure is that shown in Fig 2.3(c) i.e. the γ phase. One could imagine dropping three zig-zag chains in with the same alignment, then switching for the next three and so on, to produce a δ phase, or changing alignment every 4 chains and calling it an ϵ phase, and so on, and so forth. One might think the name α for the phase depicted in Fig 2.3(a) then is rather strange, as in terms of Fig 2.3(d), this structure results from sacking an *infinite* number of chains before deciding to change the alignment! However, the Greek alphabet has only a finite number of letters, and α-Li_2IrO_3 was here before its '3D' brothers, so calling it α, and shifting the rest of the series down one letter seems like a fair compromise.

N.B. the unit cells depicted in Fig 2.3 are those of the β and γ phase – it will be seen that they are very nearly exactly the same – and for consistency this unit cell has also been drawn for the α case, even though one can clearly see such a cell over-specifies the repeating unit, and in fact the structure of this phase is not so trivial, see [14]. Though they have almost identical unit cells, it will be seen that the β and γ phases are generated by different space groups (as one would expect, because the network of Ir ions is qualitatively different between the two, and therefore must be generated by different groups of symmetry operations), with the former belonging to the face-centred $Fddd$ space-group (no. 70) and the latter to the base centred $Cccm$ group (no. 66).

Although the generalization to three-dimensional lattices depicted in Fig 2.3 is an interesting concept, and such lattices present a further playground for theoretical calculations of Kitaev physics, the fact is that structures are not built in the manner shown in Fig 2.3(d). It is not the sample grower who carefully places each Ir, zig-zag chain into a box one after another, it is energetic considerations at the high-temperatures required for compound synthesis which decide whether the crystal that pops out is of α, β, γ, etc character. The remarkable thing, however is that single crystals of β-Li_2IrO_3 *and* γ-Li_2IrO_3 have recently become available. So not only is it possible to search for the existance of Kitaev physics on a 3-D lattice of Ir ions, but the physics of two such lattices can be directly compared. It turns out that Resonant Magnetic X-ray Diffraction (RMXD) is the best method to probe the magnetic groundstates of these systems, and this technique will be described in some detail in Section 3.2, before the main body of work on these compounds is presented in Chapters 4 and 5.

2.4 Spin Orbital Singlet State in $FeSc_2S_4$

In the previous section, the concept of frustration was discussed as applied to spins, and it was remarked how frustration on a lattice of spins can lead to highly non-trivial groundstates. One such exotic state is the spin liquid (SL) [20], in which local moments are strongly correlated between nearby sites but continue to fluctuate even at $T = 0$ without long range order. However, frustration need not be confined merely to the spin sector, transition metal ions in local high symmetry crystal environments can also have orbital degeneracies, leading to the absence of 'conventional' orbital

ordering (e.g. Jahn-Teller (J-T) type structural distortion [28]). When both the spin and orbital degrees of freedom are frustrated and continue to fluctuate down to the lowest measured temperatures, in analogy with the SL case, a state coined the Spin Orbital Liquid is believed to occur [29], [30].

Searches for a physical realization of this exotic state had centred on the triangular layered compound $LiNiO_3$ (e.g. [31]), however later arguments suggested that disorder effects were at the root of the anomalous behaviour of this system [32], and recent experiments have focussed on honeycomb magnetic insulators, with a dynamic spin-orbital state having been observed in $Ba_3CuSb_2O_9$ [33] for example. One way to realize such a coherent spin and orbital state is to start with a lattice covered with spin dimers - i.e. $S = 1/2$ spins coupled antiferromagnetically to produce a non-magnetic singlet (this is just a valence bond solid (VBS) state on the lattice [34]) and then associate with each dimer a particular orbital ordering (equivalent to a local distortion), the resulting ground state will have coupled spin and orbital degrees of freedom. A related state is the spin-orbital singlet (SOS), here, instead of spins at seperate lattice sites coupling, the spin and orbital moment at the *same* lattice site couple to form a zero moment groundstate which, unlike the 'simple' spin-only dimer case (e.g. $TlCuCl_3$ [35]) has both spin and orbital contributions. Such a state would have finite spin and orbital moments on each lattice site whilst lacking both spin and orbital order, moreover, the formation of the singlet would require strong coupling of the spin and orbital degrees of freedom. A system with spin and orbital frustration formed of magnetic ions with strong spin-orbit coupling then would be an ideal SOS candidate, and indeed such a state has been suggested for $FeSc_2S_4$ [36] which shows

no sign of spin or orbital order down to the lowest measured temperatures, despite the presence of strong exchange [37].

In the following section the Spin-Orbital Singlet state in $FeSc_2S_4$ will be described, experiments on which form the basis of Chapter 6. The strong spin-orbit coupling present makes such a groundstate, with its non-trivial spin and orbital contributions, preferable. However, it is interesting to draw a parallel between this complex spin-orbital groundstate with the analogous spin-only singlet state. To begin then, such spin-only groundstates are described, with the motive that doing so will elucidate the spin-orbital analogue in $FeSc_2S_4$.

2.4.1 Conventional Spin Order on a Lattice

Consider $S = 1/2$ spins on a square lattice, where exchange interactions are anisotropic and given by J_1 and J_2. The exchange interactions are such that $|J_2| > |J_1|$, both being antiferromagnetic and the Hamiltonian is the Heisenberg Hamiltonian, of the form (2.4). In the mean field case the groundstate is a Néel state, characterized by a bipartite lattice, i.e. the magnetic lattice can be split into two ferromagnetic lattices with spins in opposite orientations, in this case the atomic square lattice is split into two face-centred lattices. One such configuration is shown in Fig 2.4(a).

The excitations from such a groundstate are well known as spin waves [5], which can be thought of as a single spin flip propagating over the lattice. These excitations therefore have $S_z = 1$ (corresponding to the change of spin in the system $\Delta S_z = \pm 1$) and zero charge, and quantum mechanically they can be treated as bosons on the lattice, or 'magnons'. Such an excitation is shown on the right side of Fig 2.4(a);

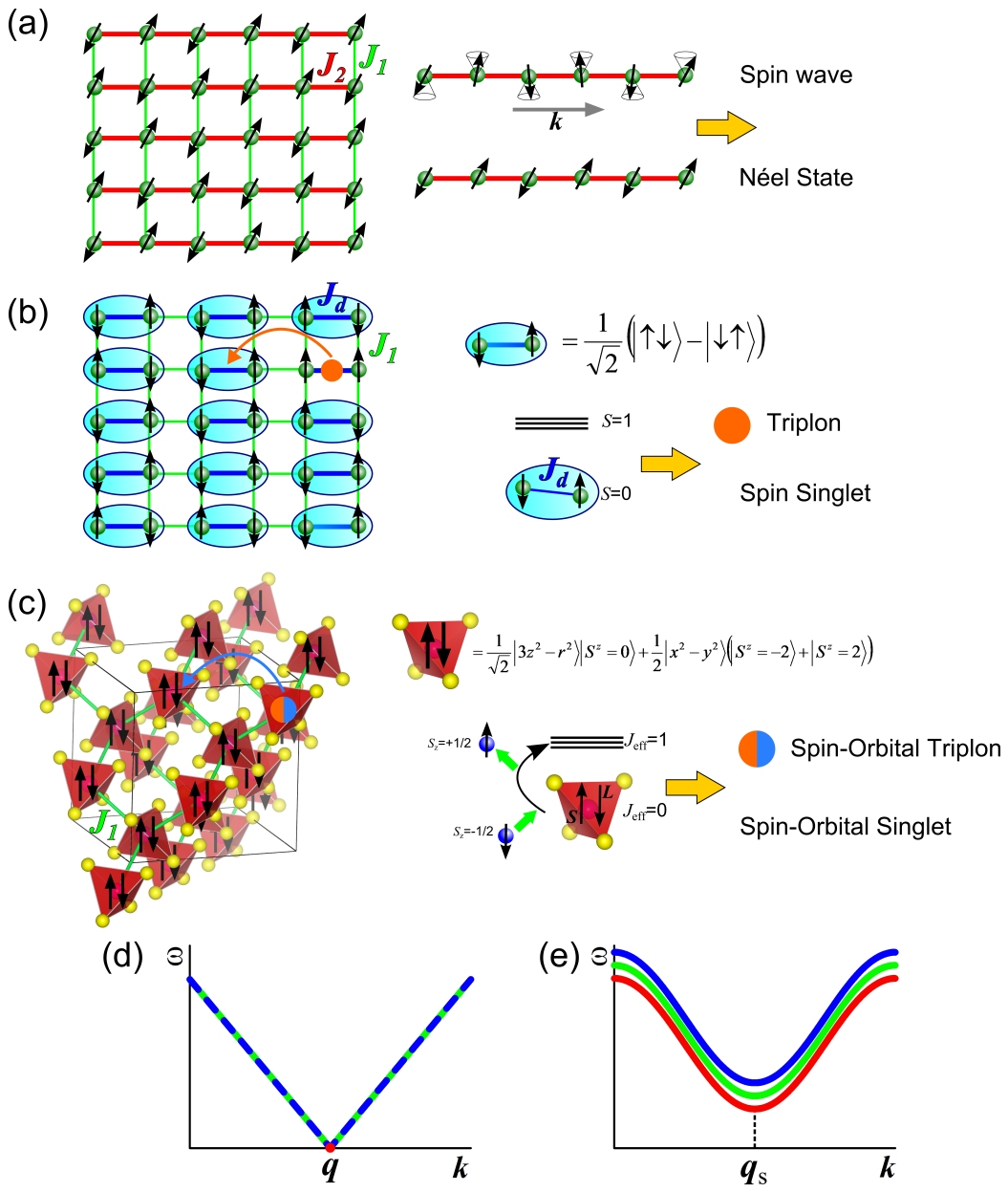


Figure 2.4: Comparison of AF spin order, spin dimerization and the SOS state (a) Spins form an ordered, antiferromagnetic (AF), Néel groundstate in the presence of exchanges J_1 and J_2. The excitations are spin waves. (b) Spins coupled via an exchange J_d pair up to form spin singlets and the excitations are triplons which hop over the lattice due to exchanges J_1. (c) Spin and orbital moments couple at the *same* lattice site to produce an SOS state (see text) the excitations are spin-orbital triplons. (d) Typical dispersion for a Goldstone mode of an ordered structure as in (a). (e) Schematic dispersion for triplon excitations of (b) and (c). $\boldsymbol{q}$ and $\boldsymbol{q}_s$ denote the ordering and mode softening wavevectors, respectively.

classically it may be considered as a canting of each spin away from its equilibrium position characterized by a wavevector $\boldsymbol{k}$, and quantum mechanically this is described as the creation of a magnon out of the vacuum $|0\rangle$ Néel state, where the excitation will be characterised by some disperssion relation $\omega(\boldsymbol{k})$ which is a function of J_1 and J_2.

These excitations are the *Goldstone modes* [38] of the antiferromagnetic order, which result from the spontaneous breaking of a continuous symmetry in the ground-state (in this case the $SU(2)$ symmetry of the spins). If the groundstate is described by a wavevector $\boldsymbol{q}$ – i.e. the ordering wavevector – then the energy of this Goldstone mode vanishes as $\boldsymbol{k} \rightarrow \boldsymbol{q}$. The dispersion of such excitations is shown schematically in Fig 2.4(d) where two modes (green solid and blue dashed lines) emanate from the ordering wavevector $\boldsymbol{q}$. Deviations are possible along both directions transverse to the ordered moment direction, hence the two modes in Fig 2.4(d), whereas longitudinal correlations generate magnetic Bragg peaks at $\boldsymbol{q}$ (red dot in Fig 2.4(d)).

2.4.2 Spin Singlets on a Lattice

However, this is not the only order possible for $S = 1/2$ spins, quantum effects allow for a ground state of interacting spins which are not associated with any broken symmetries [39]. Such an example is in the *dimerization* of spins, where neighbouring moments couple to form spin singlet states of the form [4]:

$$\text{Spin Singlet } = \frac{1}{\sqrt{2}}(|\uparrow\downarrow\rangle - |\downarrow\uparrow\rangle). \tag{2.12}$$

This is shown schematically in Fig 2.4(b), where an antiferromagnetic exchange J_d couples two spins and a weaker exchange J_1 also exists on the lattice. Blue and

green bonds represent the J_d and J_1 couplings respectively and cyan ellipses enclose spins which form a dimer pair. N.B. the black arrows are included to represent a moment at each lattice site, but do not represent their orientation within the dimer, as this of course is an admixture of both possible states, as given explicitly in (2.12). One physical realization of such a system is $TlCuCl_3$ [35], the only difference being that these Cu dimers sit in a full three-dimensional lattice.

Again, one may enquire as to the lowest excitation from this groundstate. The same reasoning as for the antiferromagnetic case considered above is a good starting point, namely; if the groundstate is the lowest energy configuration for a set of spins, then perhaps the next lowest configuration results from flipping a spin. In the case of a lattice of dimerized spins shown in Fig 2.4(b), flipping a single spin results in the destruction of a dimer bond by excitation to a spin-1 triplet state. Once again these excitations can be considered as bosons, this time created from the spin-singlet vacuum (see right side of Fig 2.4(b)), and these are often referred to as *triplons*. Although there is an energy cost J_d associated with such a flipping, once it has been created the boson is free to hop between dimer sites via exchanges J_1.

Such a hopping results in a dispersion as shown in Fig 2.4(e); the excitation has finite energy everywhere because no symmetries have been broken, and three modes are present, one for each of the $S = 1$ triplet states. Once again these modes are degenerate, but here shown split for clarity. Such a splitting would occur in a magnetic field, where spin flips parallel to the applied field are reduced in energy due to a Zeeman-type stabilization. Although in general such modes will be gapped (i.e. it costs energy to create them everywhere in reciprocal space) there will usually be

some point where the gap between the groundstate and the excitation is minimized. This point is referred to as the *mode-softening wavevector*, and is denoted by $\boldsymbol{q}_s$ in Fig 2.4. The location of $\boldsymbol{q}_s$ will depend on the form of the exchange – or more precisely the Fourier transform of the exchange – between dimers.

2.4.3 Spin Orbital Singlets on a Lattice

So far only spin degrees of freedom have been considered, but of course ions on a lattice may also posses orbital degrees of freedom. Consider then the case depicted in Fig 2.4(c), where each magnetic ion (denoted by red tetrahedra, for reasons which will become clear in Chapter 6) has both a spin and orbital degree of freedom (denoted by arrows which point in opposing directions) and spins at these sites interact via various nearest neighbour (J_1) and next-nearest neighbour (J_2, not shown), etc exchanges.

The spin, S, and orbital, L, components of the angular momentum at a lattice site couple through the spin-orbit interaction, whose Hamiltonian is given in (2.9). Inspection of (2.9) shows that for negative values of λ such a coupling results in $\boldsymbol{L}$ and $\boldsymbol{S}$ being anti-aligned. Therefore on each lattice site in Fig 2.4(c) it is possible to have a state with no net moment, composed of finite spin and angular momenta and is termed a *Spin Orbital Singlet* (SOS) state, in analogy with the 'conventional' spin singlet state of Fig 2.4(b). The difference here is that the singlet exists on a *single* lattice site, between the spin and orbital angular moments (hence the opposing arrows in Fig 2.4(c)), and now instead of being a simple combination of spins only, these singlets are in fact a complex admixture of spin and orbital components. Explicitly, it will be seen that under certain limits this (SOS) dimer state can be written as:

$$\frac{1}{\sqrt{2}}|L^z = 0\rangle|S^z = 0\rangle + \frac{1}{2\sqrt{2}}\left(|L^z = 2\rangle + |L^z = -2\rangle\right)\left(|S^z = \text{-}2\rangle + |S^z = 2\rangle\right). \quad (2.13)$$

From (2.13) it is clear that the expectation values of $S_{x,y,z}$ and $L_{x,y,z}$ are all zero within this groundstate.

Again, it will be found that the first excited state from the groundstate is a triplet, and excitations can once more be interpreted as a 'broken' singlet, or a boson excited from the vacuum sea of singlets. Once more, provided that the initial energy cost of producing such excitations has been paid, they are free to hop over the lattice thanks to the various exchange interactions present, and their dispersion relation will again look something like Fig 2.4(e). The key difference here is that these excitations inherit the spin and orbital nature of their parent groundstate and are spin-orbital triplons, in analogy with the spin-only triplons encountered earlier.

To have such a SOS groundstate be preferable would seem to be quite unlikely; as typically the orbital contribution to the angular moment is quenched by the crystal field produced by surrounding ligands, although if a high (e.g. cubic) symmetry is present, frustration might hinder such orbital ordering [40]. Moreover the exchange between sites will usually drive the system towards some kind of spin ordering, thus inhibiting a SOS state. However, in $FeSc_2S_4$ no such orbital quenching (which would result in structural distortions) or spin order (which would result in anomalies in the magnetic susceptibility) [37] was found, even in the presence of significant exchange interactions (as evident from Curie-Weiss behaviour [3] in susceptibility data of [37]). As a result a SOS state has been proposed for $FeSc_2S_4$, and many properties of its spin-orbital triplons predicted [36].

The goal of Chapter 6 will be to measure these excitations through inelastic neutron scattering (INS), and to reveal their spin-orbital nature by observing the predicted, somewhat counter-intuitive behaviour, in the presence of a magnetic field.

2.5 Triangular Lattice Antiferromagnet $Ba_3CoSb_2O_9$

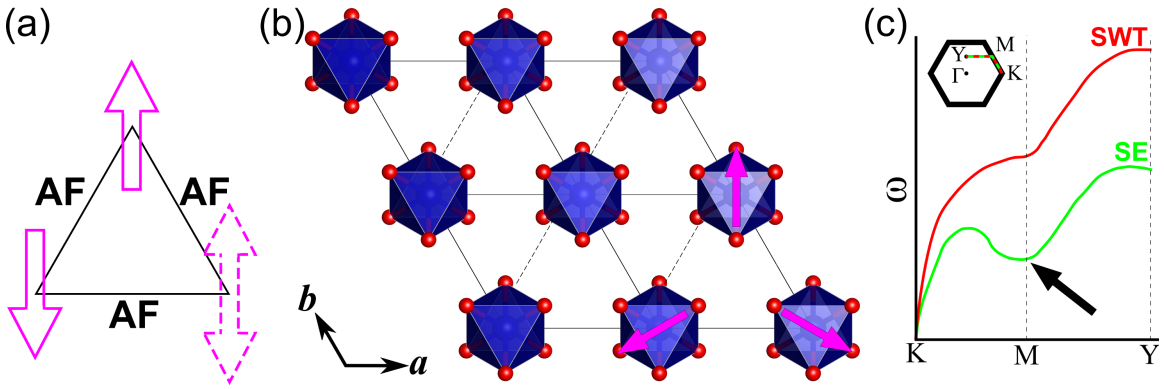


Figure 2.5: TAF $Ba_3CoSb_2O_9$ (a) The triangular antiferromagnet for Ising spins (after [19]). (b) Triangular lattice of Co^{2+} ions (blue spheres) in $Ba_3CoSb_2O_9$, O ions are also shown (red spheres) as well as the CoO_6 octahedra. The 120° magnetic order (magenta arrows) has been projected onto the *ab*-plane. (c) Schematic dispersion relation along a path in reciprocal space for a spin wave calculation and series expansion for an $S = 1/2$ lattice, showing the qualitative difference between the two (after [41]). Inset: first Brillouin zone with the path through reciprocal space plotted.

The triangular antiferromagnet is a prototypical model of geometric frustration. In the simplest case one can consider three Ising spins on the apexes of a triangle with antiferromagnetic exchange coupling between the spins. This is illustrated in Fig 2.5(a). It is possible to choose the orientation of two spins such that the antiferromagnetic coupling (denoted by 'AF') between them is satisfied, however the third spin cannot be oriented in such a way that its AF coupling with its neighbours is satisfied. This leads to frustration in the system, where interactions between moments can't be mutually satisfied, and no unique configuration of the spins can minimize

the system's energy.

Examining the groundstate of such a frustrated system of spins has been a long running goal of condensed matter physics (e.g. [42, 43]), and these states are typically characterised by the absence of conventional spin ordering and a large degeneracy [19]. As one considers spins of smaller and smaller magnitude on the lattice[3], quantum effects become ever more dominant, and several non-trivial groundstates are predicted for example, quantum spin liquids [20] or even nematic spin ordering [44].

The two-dimensional spin-1/2 triangular lattice Heisenberg antiferromagnet, where the exchange between spins is of the form given in (2.4), is an example of such a geometrically frustrated lattice. As well as being intensely studied theoretically it is advocated as a model which could be realised experimentally, for example in systems where the exchange in a triangular plane of ions is far greater than those between planes. Although anisotropic triangular lattice systems – where each triangular plaquet (Fig 2.5(a)) contains two distinct exchanges J and J' – have been explored in some detail, for example Cs_2CuCl_4 [45] and its sister compound Cs_2CuBr_4 (where $J'/J \approx 1/3$ and $1/2$ respectively), and, monoclinically distorted systems, for example α-$CaCr_2O_4$ [46] have been thoroughly studied through neutron scattering and other methods, experimental work on the isotropic triangular antiferromagnet remains sparse.

The synthesis of compounds $Ba_3MSb_2O_9$, where M is a magnetic ion, seem to have greatly improved the prospects of observing such novel physics. In these compounds, the magnetic ions sit on a triangular lattice, as shown in Fig 2.5(b), where the solid

[3]Spins $S \gg 1/2$ can be described as 'classical', as in the limit of $S \to \infty$ the discretization of S becomes irrelevant.

lines indicate the boundary of unit cells and the dashed lines are drawn to show the underlying triangular symmetry. Such systems appear to mantain the true three-fold symmetry down to the lowest temperatures, and the large Ba atoms act as spacers between the layers of magnetic ions in the *ab*-plane, thus creating an effective 2-dimensional antiferromagnetic triangular lattice.

Recent studies by Nakatsuji *et al* [47] on $Ba_3CuSb_2O_9$ have lead to the proposal of a spin liquid state in this system, a state also present in the sister compound $Ba_3NiSb_2O_9$ under pressure [48], however structural disorder effects between the Cu^{2+}/Ni^{2+} and Sb^{5+} on the same crystallographic site in these compounds raises concerns about the potential role of random disorder and/or spin freezing in stabilizing the groundstate. No such disorder is intrinsic to the compound $Ba_3CoSb_2O_9$ however, where the large energy difference between diamagnetic and magnetic sites allows well-characterised, stochiometric, disorder free samples to be synthasised with no site mixing.

In $Ba_3CoSb_2O_9$ it will be seen that the Co^{2+} ions sit on a triangular lattice as in Fig 2.5(b), moreover once crystal field and spin-orbit effects are taken into account it will be seen that the Co ions have an effective $S = 1/2$ moment. This then allows the measurement of the canonical model of Heisenberg exchange between $S = 1/2$ spins on the triangular antiferromagnet and these experiments will be described in Chapter 7.

This model is believed to have a three-sublattice 120° spiral order perpendicular to the *ab*-plane (magenta spins in Fig 2.5(b)) stabilized at low temperatures by weak inter-layer exchanges [49]. Therefore one would expect to observe the usual spin

waves, or Goldstone modes emanating from magnetic Bragg peaks located at the magnetic ordering wavevectors. However, theoretical calculations predict that the ordered spin moment is reduced due to zero-point quantum fluctuations, and moreover the dispersion relation of the spin dynamics is predicted to show anomalous features at high energies such as soft-modes and roton like minima [41]. The latter of these effects is shown schematically in Fig 2.5(c); in moving around the Brillouin zone (hexagonal inset) the spin excitations plot out dispersion relations dependent on the Fourier transform of the exchange distribution, and becoming gapless at ordering wavevectors (e.g. 'Q' in Fig 2.5(c)). Such dispersion relations can be calculated from classical spin wave theory and this is shown schematically as the red line in Fig 2.5(c). Note the linear behaviour of the dispersion as it rises from the magnetic Bragg peak, as expected for AF spinwaves. When series expansions are performed for the $S = 1/2$ triangular antiferromagnet (green line in Fig 2.5(c)) [41], qualitatively different behaviour is evident, namely minima in the dispersion relation, for example the one labelled by a black arrow. Such excitations are referred to as 'rotons' in analogy with the minima in the dispersion relations of ^{4}He.

The goal of Chapter 7 will be to observe the spin-excitations from a powder sample $Ba_3CoSb_2O_9$ and ascertain whether such quantum embelishments to the dispersion are present.

References

[1] J. Van Vleck, *The Theory of Electric and Magnetic Susceptibilities*, 1^{st} ed. (OUP, 1932).

[2] J. van Leeuwen, Le Journal de Physique **2**, 361 (1921).

[3] K. Yosida, *Theory of Magnetism*, 1^{st} ed. (Springer, 1996).

[4] R. Shankar, *Principles of Quantum Mechanics*, 2^{nd} ed. (Kluwer, 1994).

[5] R. White, *Quantum Theory of Magnetism*, 2^{nd} ed. (Springer, 1982).

[6] W. Witczak-Krempa, G. Chen, Y. B. Kim, and L. Balents, Annual Review of Condensed Matter Physics **5**, 57 (2014).

[7] B. Kim, H. Ohsumi, T. Komesu, and S. Sakai, Science **323**, 1329 (2009).

[8] G. Jackeli and G. Khaliullin, Physical Review Letters **102**, 017205 (2009).

[9] J. Chaloupka, G. Jackeli, and G. Khaliullin, Physical Review Letters **105**, 027204 (2010).

[10] A. Kitaev, Annals of Physics **321**, 2 (2006).

[11] J. Knolle, D. Kovrizhin, J. Chalker, and R. Moessner, Physical Review Letters **112**, 207203 (2014).

[12] Y. Singh and P. Gegenwart, Physical Review B **82**, 064412 (2010).

[13] X. Liu, T. Berlijn, W.-G. Yin, W. Ku, a. Tsvelik, Y.-J. Kim, H. Gretarsson, Y. Singh, P. Gegenwart, and J. P. Hill, Physical Review B **83**, 220403 (2011).

[14] S. K. Choi, R. Coldea, A. N. Kolmogorov, T. Lancaster, I. I. Mazin, S. J. Blundell, P. G. Radaelli, Y. Singh, P. Gegenwart, K. R. Choi, S.-W. Cheong, P. J. Baker, C. Stock, and J. Taylor, Physical Review Letters **108**, 127204 (2012).

[15] F. Ye, S. Chi, H. Cao, B. C. Chakoumakos, J. Fernandez-Baca, R. Custelcean, T. F. Qi, O. B. Korneta, and G. Cao, Physical Review B **85**, 180403 (2012).

[16] H. Gretarsson, J. P. Clancy, Y. Singh, P. Gegenwart, J. P. Hill, J. Kim, M. H. Upton, H. Said, D. Casa, T. Gog, and Y.-J. Kim, Physical Review B **87**, 220407 (2013).

[17] M. J. O'Malley, H. Verweij, and P. M. Woodward, Journal of Solid State Chemistry **181**, 1803 (2008).

[18] Y. Singh, S. Manni, J. Reuther, T. Berlijn, R. Thomale, W. Ku, S. Trebst, and P. Gegenwart, Physical Review Letters **108**, 127203 (2012).

[19] A. P. Ramirez, Annual Review of Materials Science **24**, 453 (1994).

[20] L. Balents, Nature **464**, 199 (2010).

[21] S. T. Bramwell and M. J. Gingras, Science (New York, N.Y.) **294**, 1495 (2001).

[22] K. Binder and A. P. Young, Reviews of Modern Physics **58**, 801 (1986).

[23] S. Blundell, *Magnetism in Condensed Matter*, 1^{st} ed. (OUP, 2001).

[24] A. Abragam and B. Bleaney, *Electron Paramagnetic Resonance of Transition Ions*, 1^{st} ed. (Dover, 1970).

[25] E. K.-H. Lee, R. Schaffer, S. Bhattacharjee, and Y. B. Kim, Physical Review B **89**, 045117 (2014).

[26] I. Kimchi, J. Analytis, and A. Vishwanath, arXiv:1309.1171v2 (2013).

[27] E. Lee and Y. Kim, arXiv (2014), arXiv:1407.4125v2.

[28] H. A. Jahn and E. Teller, Proceedings of the Royal Society A: Mathematical, Physical and Engineering Sciences **161**, 220 (1937).

[29] L. Feiner, Journal of Physics C: Solid State Physics **1515** (1982).

[30] Y. Li, M. Ma, D. Shi, and F. Zhang, Physical Review Letters **81**, 3527 (1998).

[31] F. Reynaud, D. Mertz, F. Celestini, J.-M. Debierre, A. Ghorayeb, P. Simon, A. Stepanov, J. Voiron, and C. Delmas, Physical Review Letters **86**, 3638 (2001).

[32] M. Mostovoy and D. Khomskii, Physical Review Letters **89**, 227203 (2002).

[33] Y. Ishiguro, K. Kimura, S. Nakatsuji, S. Tsutsui, A. Q. R. Baron, T. Kimura, and Y. Wakabayashi, Nature communications **4**, 2022 (2013).

[34] P. W. Anderson, *Basic Notions of Condensed Matter Physics*, 1^{st} ed. (Westview, 1984).

[35] C. Rüegg, B. Normand, M. Matsumoto, A. Furrer, D. McMorrow, K. Krämer, H. Güdel, S. Gvasaliya, H. Mutka, and M. Boehm, Physical Review Letters **100**, 205701 (2008).

[36] G. Chen, A. P. Schnyder, and L. Balents, Physical Review B **80**, 224409 (2009).

[37] V. Fritsch, J. Hemberger, N. Büttgen, E.-W. Scheidt, H. Krug von Nidda, A. Loidl, and V. Tsurkan, Physical Review Letters **92**, 116401 (2004).

[38] A. Auerbach, *Interacting Electrons and Quantum Magnetism*, 1^{st} ed. (Springer, 1994).

[39] S. Sachdev, (2008), Rapporteur talk at the 24th Solvay Conference on Physics, "Quantum Theory of Condensed Matter", Brussels.

[40] D. Khomskii and M. Mostovoy, Journal of Physics A: Mathematical and General **36**, 9197 (2003).

[41] W. Zheng, J. Fjæ restad, R. Singh, R. McKenzie, and R. Coldea, Physical Review B **74**, 224420 (2006).

[42] P. Anderson, Materials Research Bulletin **8**, 153 (1973).

[43] V. Kalmeyer and R. Laughlin, Physical review letters **59**, 2095 (1987).

[44] D. Podolsky and E. Demler, New Journal of Physics **7**, 59 (2005).

[45] R. Coldea, D. Tennant, M. Tsvelik, and Z. Tylczynski, Physical Review Letters **86**, 1335 (2001).

[46] S. Toth, B. Lake, K. Hradil, T. Guidi, K. C. Rule, M. B. Stone, and T. M. N. Islam, Physical Review Letters **109**, 127203 (2012).

[47] S. Nakatsuji, K. Kuga, K. Kimura, R. Satake, N. Katayama, E. Nishibori, H. Sawa, R. Ishii, M. Hagiwara, F. Bridges, T. U. Ito, W. Higemoto, Y. Karaki, M. Halim, a. a. Nugroho, J. a. Rodriguez-Rivera, M. a. Green, and C. Broholm, Science (New York, N.Y.) **336**, 559 (2012).

[48] J. G. Cheng, G. Li, L. Balicas, J. S. Zhou, J. B. Goodenough, C. Xu, and H. D. Zhou, Physical Review Letters **107**, 197204 (2011).

[49] Y. Doi, Y. Hinatsu, and K. Ohoyama, Journal of Physics: Condensed Matter **16**, 8923 (2004).

Chapter 3

Experimental Techniques

In the present chapter, the main techniques used in the experiments presented in this thesis will be discussed. Two probes have been used to study magnetic systems; neutrons and x-rays, and both the physical principles underlying these measurements as well as the technical details in conducting them will be presented.

3.1 Principles of Neutron Scattering

The experimental technique of neutron scatteing is now well established and its principles are described thoroughly and extensively elsewhere (e.g. [1]). Moreover the technicalities of a neutron scattering experiment are described, for example, in [2]. This section's goal then is not to give a complete and detailed account of every aspect of neutron scattering, but to explain some of the basic principles which underlie the technique and to offer a brief exposition of the quantities of interest in condensed matter systems, which can be measured this way.

3.1.1 Properties of the Neutron

The neutron is a charge neutral, spin half particle which interacts with matter through the nuclear strong and electromagnetic forces, the latter being due to its

finite magnetic dipole moment (reflecting the fact that even though the neutron is in a state that has particles with compensating electrical charges, these do not have compensating magnetic moments [3]), μ_n, given by:

$$\boldsymbol{\mu}_n = -\gamma \mu_N \boldsymbol{\sigma}, \tag{3.1}$$

where,

$$\mu_N = \frac{e\hbar}{2m_p}, \tag{3.2}$$

and $\hbar$ is the reduced Planck constant $h/2\pi$, $\gamma \approx 1.913$ is a positive constant, m_p is the mass of the proton, and e its charge. $\boldsymbol{\sigma}$ is the Pauli spin operator [3], the eigenvalues of its components being ± 1. The momentum $\boldsymbol{p}$ and energy E of the neutron are given by

$$\boldsymbol{p} = \hbar \boldsymbol{k}, \tag{3.3}$$

$$E = \frac{\hbar^2 k^2}{2m}, \tag{3.4}$$

where $\boldsymbol{k}$ is the wavevector of the neutron. From (3.4) and (3.3), it is found that thermal neutrons (i.e. neutrons with an energy $k_{\mathrm{B}}T$ with $T \approx 300\mathrm{K}$) have a wavelength of around 1.7 Å, and herein lies one of the useful aspects of neutron scattering in condensed matter physics; the energies and wavelengths are comparable to the energy and length scales found in solids.

3.1.2 Neutron Scattering Cross-section

A typical neutron scattering event is shown schematically in Fig 3.1; a single neutron, of wavevector $\boldsymbol{k}$ and energy E, is sent into a sample of interest. The neutron will be scattered by some potential within the sample and deflected into a solid angle $d\Omega$, with resulting wavevector and energy $\boldsymbol{k'}$ and E' respectively. In the ideal neutron

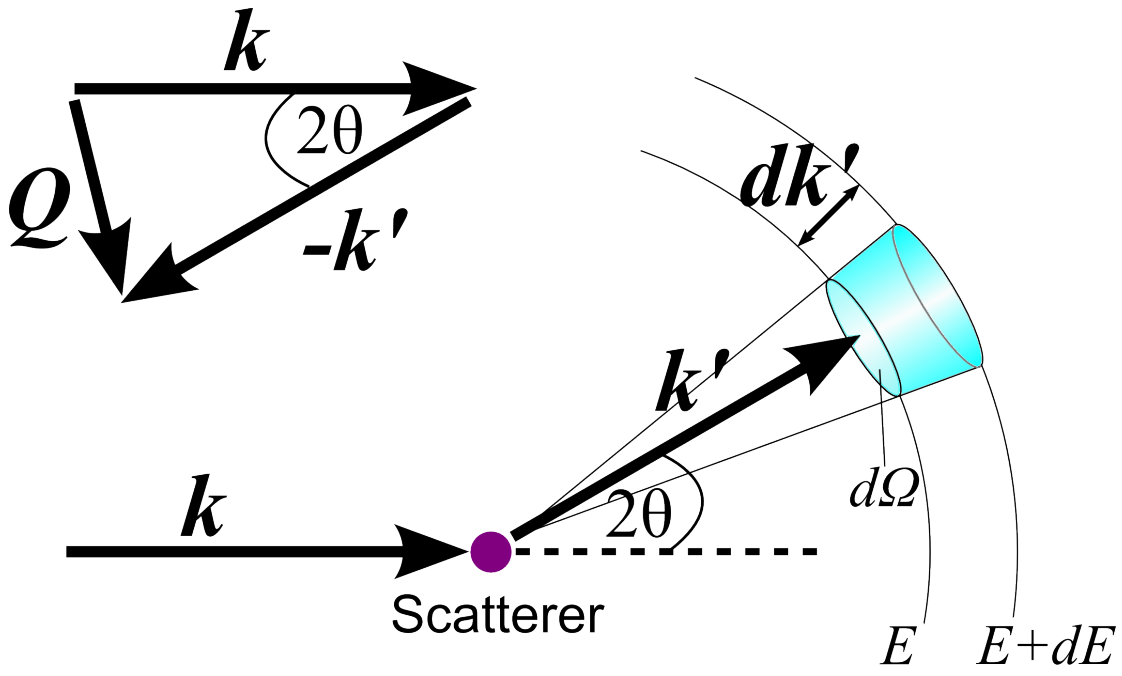


Figure 3.1: Schematic of a neutron scattering event: a neutron with wavevector $\boldsymbol{k}$ is scattered via some potential within the 'scatterer' into an element of volume $k'^2 dk' d\Omega$. Inset: Completed triangle to show the definition of the scattering vector $\boldsymbol{Q} = \boldsymbol{k} - \boldsymbol{k'}$, the scattering angle 2θ is also included.

scattering experiment, the sample will be surrounded by detectors such that each scattered neutron is detected in a given element $d\Omega$ of solid angle within the complete 4π of the area of a sphere. Moreover, these detectors will not only detect a scattered neutron's presence but also be sensitive to its energy in increments of dE'. Therefore the quantity that will be measured is the number of scattered neutrons per unit solid angle per unit scattered energy (or, in relation to Fig 3.1, the number of neutrons within a volume $k'^2 dk' d\Omega$), where typically the word 'intensity' is used in place of 'number'. However, it is not desirable for the scattering intensity to be dependent on the specifications of the incoming beam (e.g. if the sample is bombarded with more neutrons then the result will be a greater number of scattering events, however this is not due to any change in the sample of interest), therefore it will be divided by the incoming flux (number per unit area per second), thus arriving at the intensity of scattered neutrons per unit solid angle, per unit scattered energy, per unit incident flux, which is defined as the *differential scattering cross section.*

If ($\boldsymbol{k}$,E) and ($\boldsymbol{k'}$,E') are the initial and final wavevectors and energies of the neutron (the spin state of the neutron is ignored for the time being), and the scattering event takes the scattering system from state λ with energy E_λ into state λ' with energy $E_{\lambda'}$, through use of Fermi's Golden Rule (i.e. treating the interaction Hamiltonian as a perturbation to first order), this cross-section is given by [1],

$$\left(\frac{d\sigma}{d\Omega dE'}\right)_{\lambda\to\lambda'} = \frac{k'}{k}\left(\frac{m}{2\pi\hbar^2}\right)^2 |\langle \boldsymbol{k'}\lambda'|V|\boldsymbol{k}\lambda\rangle|^2 \delta(E_\lambda - E_{\lambda'} + E - E'), \tag{3.5}$$

where V is the potential which interacts with the neutron, and m is the mass of the neutron. However, in a neutron scattering experiment, the intensity of transitions

from a specific state λ to a state λ' will not be measured, but rather the differential cross-section defined earlier. To get this from (3.5) a sum over all final states λ' and average over initial states λ is required, i.e. [1]:

$$\frac{d\sigma}{d\Omega dE'} = \sum_{\lambda,\lambda'} P_\lambda \frac{k'}{k} \left(\frac{m}{2\pi\hbar^2}\right)^2 |\langle \boldsymbol{k'}\lambda'|V|\boldsymbol{k}\lambda\rangle|^2 \delta(E_\lambda - E_{\lambda'} + E - E'), \tag{3.6}$$

where P_λ is the probability that the system is initially initially in the state λ. This will typically be a function of temperature. The expression (3.6) is then a quantity measurable via a neutron scattering, expressing the probability with which a neutron with initial wavevector and energy ($\boldsymbol{k}$,E) will be scattered into an element of solid angle $d\Omega$ with final wavevector and energy ($\boldsymbol{k'}$,E'). However, it is yet to be seen whether this quantity can be related to something meaningful about the system under consideration.

To this end, it is useful to re-write the matrix element in (3.6). The potential V is considered as being due to the scattering centres within the sample. These scattering centres are at position $\boldsymbol{R}_j$ and contribute potential V_j such that the potential acting on a neutron at position $\boldsymbol{r}$ is

$$V = \sum_j V_j(\boldsymbol{r} - \boldsymbol{R}_j). \tag{3.7}$$

Subsequently it is found that

$$\langle \boldsymbol{k'}\lambda'|V|\boldsymbol{k}\lambda\rangle = \sum_j V_j(\boldsymbol{Q})|\langle\lambda'|e^{i\boldsymbol{Q}\cdot\boldsymbol{R}_j}|\lambda\rangle|, \tag{3.8}$$

where

$$V_j(\boldsymbol{Q}) = \int V_j(\boldsymbol{r} - \boldsymbol{R}_j) e^{i\boldsymbol{Q}\cdot(\boldsymbol{r}-\boldsymbol{R}_j)} d(\boldsymbol{r} - \boldsymbol{R}_j), \tag{3.9}$$

and $\boldsymbol{Q} = \boldsymbol{k} - \boldsymbol{k'}$ is the aforementioned scattering vector. Looking at (3.6), (3.8) and (3.9) one can see that the differential scattering cross section is sensitive to the Fourier transform of the interaction potential.

3.1.3 Nuclear Scattering

Now a specific form of the potential V is considered, namely the potential appropriate for scattering of neutrons by atomic nuclei. The strong force is responsible for this scattering and the functional form for this short range interaction can be approximated by the *Fermi pseudopotential*,

$$V(\boldsymbol{r}) = \frac{2\pi\hbar^2}{m} b\ \delta(\boldsymbol{r}), \tag{3.10}$$

where b is the *scattering length* and is a measure of the strength of the neutron-nucleus interaction. It is defined as positive/negative for repulsive/attractive interactions.

Using (3.9), $V_j(\boldsymbol{Q})$ can be calculated as

$$V_j(\boldsymbol{Q}) = \frac{2\pi\hbar^2}{m} b_j, \tag{3.11}$$

where the subscript j has been reintroduced to demonstrate the fact that in the sample a variety of nuclei, each with a different value of scattering length, will be present. Note that this potential is $\boldsymbol{Q}$-independent, which is merely a consequence of the model potential (3.10) being a single sharp mode in real space, therefore Fourier transforming to a homogeneous signal over all Q-space. Substituting (3.11) into (3.8) and the resulting expression into (3.6) yields [1]:

$$\left(\frac{d\sigma}{d\Omega dE'}\right)_{\text{nuc}} = \frac{k'}{k}\frac{1}{2\pi\hbar}\sum_{\text{J,J}'} b_j b_{j'} \int_{-\infty}^{\infty} \left\langle e^{-i\boldsymbol{Q}\cdot\boldsymbol{R}_{j'}(0)} e^{-i\boldsymbol{Q}\cdot\boldsymbol{R}_j(t)} \right\rangle e^{-i\omega t} dt, \tag{3.12}$$

where the neutron energy transfer, $\hbar\omega = E - E'$ has been used and the position vectors have been converted into time-dependent operators via a method of Heisenberg [3]. The angled brackets in (3.12) now refer to an average value over all λ, e.g. for some operator A, $\langle A \rangle = \sum_\lambda P_\lambda \langle \lambda | A | \lambda \rangle$.

Expression (3.12) then represents a quantity measurable via neutron scattering, however it is not immediately apparent what the physical significance of the rhs of (3.12) is. The Fourier transforms first introduced by van Hove [4] (appropriate to scattering from elements only, as b_j and $b_{j'}$ are not included):

$$G(\boldsymbol{r}, t) = \frac{1}{(2\pi)^3} \int \frac{1}{N} \sum_{\text{J,J}'} \left\langle e^{-i\boldsymbol{Q}\cdot\boldsymbol{R}_{j'}(0)} e^{-i\boldsymbol{Q}\cdot\boldsymbol{R}_j(t)} \right\rangle e^{-i\boldsymbol{Q}\cdot\boldsymbol{r}} d\boldsymbol{Q}, \tag{3.13}$$

and

$$S(\boldsymbol{Q}, \omega) = \frac{1}{(2\pi\hbar)} \int \frac{1}{N} \sum_{\text{J,J}'} \left\langle e^{-i\boldsymbol{Q}\cdot\boldsymbol{R}_{j'}(0)} e^{-i\boldsymbol{Q}\cdot\boldsymbol{R}_j(t)} \right\rangle e^{-i\omega t} dt, \tag{3.14}$$

are referred to as the space-time pair correlation function and dynamical structure factor respectively. Comparison with (3.12) shows that the **differential cross section is directly related to** $S(\boldsymbol{Q}, \omega)$ and is proportional to the space and time Fourier transform of $G(\boldsymbol{r}, t)$. Due to the close link between the cross-section and $S(\boldsymbol{Q}, \omega)$, in neutron scattering experiments the dynamical structure factor will typically be presented and plotted as a function of $\boldsymbol{Q}$ and ω when discussing results. Examples of such plots are shown in Fig 6.3 and Fig 7.2.

For this reason, there are many properties of the dynamical structure factor which are of great importance to neutron scattering experiments. Among these is the *Principle of Detailed Balance* in inelastic neutron scattering, which can be written, assuming states of the system obey Boltzmann statistics, as:

$$S(-\boldsymbol{Q}, -\omega) = e^{-\frac{\hbar\omega}{k_{\mathrm{B}}T}} S(\boldsymbol{Q}, \omega). \tag{3.15}$$

Formally, this is an expression of the effect of time-reversal on the dynamical structure factor, whereas physically it expresses the fact that the intensity for a given process which transfers energy $\hbar\omega$ to the neutron is exactly the same as for the reverse process (i.e. neutron transfers energy $\hbar\omega$ to the system) multiplied by a Boltzmann factor. It is seen that in the limit of $T \to \infty$ both processes are equally likely and contribute symmetrically to the intensity profile. This principle applies regardless of the potential responsible for the scattering, and will be important for the background subtraction process detailed in Section 6.3.2.

Returning to the case of nuclear scattering, using some properties of the Dirac delta function, $G(\boldsymbol{r}, t)$ can be re-written as:

$$G(\boldsymbol{r}, t) = \frac{1}{N} \sum_{\mathrm{J,J'}} \int \langle \delta\left(\boldsymbol{r'} - \boldsymbol{R}_{j'}(0)\right) \delta\left(\boldsymbol{r'} + \boldsymbol{r} - \boldsymbol{R}_{j}(t)\right) \rangle d\boldsymbol{r'}. \tag{3.16}$$

The meaning of $G(\boldsymbol{r}, t)$ is then elucidated by (3.16); it describes the correlation between site j' at time $t = 0$ and position $\boldsymbol{r'}$ and site j at a later time t at another position $\boldsymbol{r'} + \boldsymbol{r}$, i.e. the probablilty (as again $\langle ... \rangle$ corresponds to an average as defined following equation (3.12)) for two scattering sites to be spatially and temporally correlated. Neutron scattering from nuclei then allows this most general of properties of

the statics and dynamics of the solid to be probed; static responses (i.e. in the limit $t \to \infty$ in (3.16)) appear as features on the elastic ($E = E'$) part of the intensity spectrum whereas dynamic correlations will be seen as signal at finite values of ω.

Returning to (3.12), the case that b varies from site to site (e.g. due to nuclear spin or the presence of isotopes) can now be considered. The scattering length b_i occurs with frequency f_i within the sample ($\sum_i f_i = 1$) and the average values of b and b^2 for the system are

$$\bar{b} = \sum_i f_i b_i, \qquad (3.17) \qquad\qquad \bar{b^2} = \sum_i f_i b_i^2, \qquad (3.18)$$

respectively. It can be shown [1] that (3.12) can be split into a coherent (coh) and incoherent (inc) term:

$$\left(\frac{d\sigma}{d\Omega dE'}\right)_{\text{nuc}} = \left(\frac{d\sigma}{d\Omega dE'}\right)_{\text{coh}} + \left(\frac{d\sigma}{d\Omega dE'}\right)_{\text{inc}}, \qquad (3.19)$$

where,

$$\left(\frac{d\sigma}{d\Omega dE'}\right)_{\text{coh}} = \frac{\sigma_{\text{coh}}}{4\pi}\frac{k'}{k}\frac{1}{2\pi\hbar}\sum_{\text{J,J}'}\int_{-\infty}^{\infty}\left\langle e^{-i\boldsymbol{Q}\cdot\boldsymbol{R}_{j'}(0)}e^{-i\boldsymbol{Q}\cdot\boldsymbol{R}_j(t)}\right\rangle e^{-i\omega t}dt, \qquad (3.20)$$

is the coherent term and its incoherent counterpart is,

$$\left(\frac{d\sigma}{d\Omega dE'}\right)_{\text{inc}} = \frac{\sigma_{\text{inc}}}{4\pi}\frac{k'}{k}\frac{1}{2\pi\hbar}\sum_{\text{J}}\int_{-\infty}^{\infty}\left\langle e^{-i\boldsymbol{Q}\cdot\boldsymbol{R}_j(0)}e^{-i\boldsymbol{Q}\cdot\boldsymbol{R}_j(t)}\right\rangle e^{-i\omega t}dt, \qquad (3.21)$$

where $\sigma_{\text{coh}} = 4\pi(\bar{b^2})$, and $\sigma_{\text{inc}} = 4\pi(\bar{b^2} - (\bar{b})^2)$.

It can be seen from (3.20) that the coherent part contains terms where different nuclei interact at different times, which can therefore produce interference effects. The incoherent part (3.20) however, contains only the self correlation of nuclei at different times and cannot give interference effects. The prefactors in (3.20) and (3.21) also hint to their significance; σ_{inc} is related to differences between scattering lengths and

so describes the incoherent self correlation of nuclei with different b_i, whereas σ_{coh} contains only the mean scattering length, i.e. neutrons 'see' an average b for the sample and scatter coherently from it.

In the case of scattering from a static Bravais lattice, the above equations reduce to

$$\left(\frac{d\sigma}{d\Omega}\right)_{\text{coh}} = N_0 \frac{(2\pi)^3}{v_0} (\bar{b})^2 \sum_{\boldsymbol{\tau}} \delta(\boldsymbol{Q} - \boldsymbol{\tau}), \tag{3.22}$$

and,

$$\left(\frac{d\sigma}{d\Omega}\right)_{\text{inc}} = N(\bar{b^2} - (\bar{b})^2), \tag{3.23}$$

where N is the total number of nuclei within the sample, N_0 is the number of unit cells (v_0 being the volume of those cells) and $\boldsymbol{\tau}$ is a reciprocal lattice vector. From (3.22) it is seen that the coherent scattering of neutrons produces sharp features at reciprocal lattice vectors; these are the structural Bragg peaks. The incoherent scattering on the other hand (3.23) contributes a featureless background to the scattering intensity. N.B. the above expressions can easily be applied to a non-Bravais lattice through use of a structure factor.

Note that the energy dependence has been integrated out in (3.22) and (3.23); strictly they should be multiplied by a factor $\delta(\hbar\omega)$, i.e. they result from elastic processes where no energy is transferred from the neutron to the system or vice versa. They are static processes relating to scattering from the equilibrium positions of nuclei, and one might ask how motion or vibration of these scattering sites will contribute to the differential cross-section. In the discussion following (3.16), it is explained that such dynamic correlations will manifest themselves as features with

finite energies and physically one can think of this as a neutron coming in and exciting a vibrational mode of the system. These modes are referred to as 'phonons' and are the Goldstone bosons [5] emanating from the broken translational symmetry of the lattice.

The details of the differential scattering cross section for phonons will not be discussed in detail here as they are not relevant for this thesis (indeed, most of the time phonon excitations are quite an inconvenience in neutron experiments as their contribution obscures the magnetic signal of interest, e.g. the Al cans used in experiments cause strong phonon lines in the scattering spectrum), however a few general points regarding them should be noted

- In elastic phonon scattering processes (i.e. those where the net amount of phonons created is zero) the spectrum is unaltered except now the scattering terms in (3.22) and (3.23) are multiplied by an additional term e^{-2W}, where W is called the Debye-Waller factor.

- In one-phonon scattering events there are inelastic processes (i.e. energy is transferred to or from the scattered neutron) which can be: coherent, resulting in sharp phonon modes emanating linearly from structural Bragg peaks[1], or incoherent, generating a diffuse background.

- The phonon scattering is heavily temperature dependent, with the number of phonons within the system being given by Bose-Einstein statistics.

[1]Phonon modes result from nuclei's coherent deviations from equilibrium positions, therefore it is to be expected that these modes will have vanishing energy upon approaching a Bragg peak which corresponds to scattering from equilibrium positions. The linear behaviour is reminiscent of other Goldstone bosons without a conservation law, e.g. photons.

So, by considering only one kind of potential, the Fermi pseudopotential to model the interaction between the nucleus and neutron, it is seen that there are a number of contributions to the neutron scattering pattern. Along the elastic line there will be a background of incoherent scattering from nuclei in different states within the sample and sharp Bragg peaks relating to the crystal structure. Phonon modes will emanate from these Bragg peaks and will be superimposed over a diffuse incoherent phonon spectrum, and these contributions will be temperature dependent, having greater and greater intensity as the sample is heated. In the following section the second interaction of interest to the neutron scattering experiments described in this thesis is introduced.

3.1.4 Magnetic Scattering

Next, the interaction between the neutron and the electrons within the system will be considered. In doing so, the spin state of the neutron first touched upon in (3.1) and (3.2) must be considered explicitly, therefore the expression (3.6) is modified to [1]:

$$\frac{d\sigma}{d\Omega dE'} = \sum_{\sigma,\sigma'} \sum_{\lambda,\lambda'} P_\sigma P_\lambda \frac{k'}{k} \left(\frac{m}{2\pi\hbar^2}\right)^2 |\langle \boldsymbol{k'}\sigma'\lambda'|V_m|\boldsymbol{k}\sigma\lambda\rangle|^2 \delta(E_\lambda - E_{\lambda'} + E - E'), \quad (3.24)$$

where the initial and final spin state of the neutron are denoted by σ and σ' respectively and P_σ denotes the probability of the neutron being initially in state σ. V_m denotes the magnetic potential, and explicitly it can be shown that:

$$V_m = -\boldsymbol{\mu}_n \cdot \boldsymbol{B} = \sum_j -2\frac{\mu_0}{4\pi}\gamma\mu_N\mu_B \, \boldsymbol{\sigma} \cdot \left[\nabla \times \left(\frac{\boldsymbol{s}_j \times \hat{\boldsymbol{R}}_j}{R_j^2}\right) - \frac{1}{\hbar}\frac{\boldsymbol{p_j} \times \hat{\boldsymbol{R}}_j}{R_j^2}\right], \quad (3.25)$$

where the sum is over all j electrons, which have spin $\boldsymbol{s}_j$ and momentum $\boldsymbol{p}_j$. In the approximation of dipole scattering or spin-only scattering, (3.24) becomes

$$\frac{d\sigma}{d\Omega dE'} = (\gamma r_0)^2 \frac{k'}{k} N \left[\frac{1}{2} g F(\boldsymbol{Q})\right]^2 e^{-2W} \sum_{\alpha,\beta} \left(\delta_{\alpha\beta} - \frac{Q_\alpha Q_\beta}{Q^2}\right) S^{\alpha\beta}(\boldsymbol{Q},\omega), \qquad (3.26)$$

where r_0 is the classical radius of the electron and g is the Landé splitting factor included to take account of the gyromagnetic ratio of a system with spin and orbital angular momentum. $F(\boldsymbol{Q})$ is the magnetic form factor, and is the Fourier transform of the charge density surrounding a magnetic ion. The indices α and β are summed over the spatial co-ordinates x, y, z and the term in rounded brackets results from the fact that neutron scattering is sensitive only to components of the moment perpendicular to the scattering vector $\boldsymbol{Q}$. $S^{\alpha\beta}(\boldsymbol{Q},\omega)$ is the magnetic scattering function given by

$$S^{\alpha\beta}(\boldsymbol{Q},\omega) = \frac{1}{2\pi\hbar} \sum_{j,j'} \int_{-\infty}^{\infty} e^{i\boldsymbol{Q}\cdot(\boldsymbol{R}_j - \boldsymbol{R}_{j'})} \left\langle S_j^\alpha(0) S_{j'}^\beta(t) \right\rangle e^{-i\omega t} dt. \qquad (3.27)$$

The term $\left\langle S_j^\alpha(0) S_{j'}^\beta(t) \right\rangle$ looks similar to the pair correlation function encountered earlier (3.16), only now the correlation of moments, S, are being dealt with as opposed to the positions of the nuclei themselves. Specifically, this term in (3.27) describes how correlated a given component α of a moment at postion j is with a component β of a moment at position j' at a later time t. *This really is the quantity of interest when trying to gain understanding of a magnetic system*, and substituting (3.27) into (3.26) shows that neutron scattering *directly measures the space and time Fourier transform of this quantity.*

Consider as an example a paramagnet in zero applied magnetic field i.e. a system whose spins are randomly oriented, the spins are uncorrelated in both space and time, and thus

$$\sum_{j,j'} \left\langle S_j^{\alpha}(0) S_{j'}^{\beta}(t) \right\rangle_{\text{para}} = \sum_{j} \frac{1}{3} \delta_{\alpha\beta} S_j(S_j+1), \tag{3.28}$$

and substituting (3.28) into (3.27) and the resulting in (3.26) leads to the result that scattering from a paramagnet produces a featureless, diffuse scattering along the elastic line.

For ordered systems, spins are statically correlated (i.e. there is correlation in the limit $t \to \infty$) and the scattering intensity is formed of sharp peaks on the elastic line; these are 'magnetic Bragg peaks'. In the case of collinear order of the moments (e.g. Ferromagnetism, Antiferromagnetism) the $\boldsymbol{Q}$-dependence of the differential cross section is similar to that for nuclear Bragg peaks in (3.22), only now the Dirac delta peaks occur at reciprocal lattice vectors of the *magnetic unit cell* i.e. the smallest unit which when translated accross the lattice, reproduces the magnetic system (N.B. both crystal and magnetic unit cells are equivalent in the case of ferromagnetic order).

If the system exhibits helical spin order i.e. a state in which moments are confined to rotate within a plane and the angle between spins at sites j and j' is given by a relation $\boldsymbol{q} \cdot (\boldsymbol{R}_j - \boldsymbol{R}_{j'})$ where $\boldsymbol{q}$ is the *magnetic ordering wavevector* of the system, the scattering cross section is slightly modified again. E.g. for the case of moments $\boldsymbol{S}$ confined to the xy-plane, it is found that the scattering cross section is given by

$$\begin{aligned} \frac{d\sigma}{d\Omega} = \frac{N}{4} \frac{(2\pi)^3}{v_0} (\gamma r_0)^2 e^{-2W} F^2(\boldsymbol{Q}) \langle S \rangle \left(1 + \left(\frac{Q_z}{Q} \right)^2 \right)^2 \\ \times \sum_{\tau} \left(\delta(\boldsymbol{Q} + \boldsymbol{q} - \boldsymbol{\tau}) + \delta(\boldsymbol{Q} - \boldsymbol{q} - \boldsymbol{\tau}) \right). \end{aligned} \tag{3.29}$$

Inspection of (3.29) shows that magnetic Bragg peaks occur at $\boldsymbol{Q} = \boldsymbol{\tau} \pm \boldsymbol{q}$, i.e. each structural Bragg peak is flanked symmetrically by two magnetic Bragg peaks.

Just as in the case of phonon scattering from nuclei, neutrons may also scatter from deviations or 'canting' of moments away from their equilibrium positions. Classically these are treated as spin waves, where moments collectively deviate from their equilibrium positions, and these features are observed in neutron scattering as sharp modes with a well-defined dispersion relation, emanating from magnetic Bragg peaks. Equivalently these modes can be thought of as magnons; they are the Goldstone bosons resulting from the broken spin symmetry on ordering. Spin waves will be considered in Chapter 7 in the context of the dynamics in $Ba_3CoSb_2O_9$, and a more detailed theoretical discussion is contained in Appendix C.

The magnetic scattering function need not, however, be confined to correlations within the ground state and deviations from it. Let the transitions between two states be considered, where specifically, the transition is from state Γ_n to Γ_m, with energies E_n and E_m respectively, in the magnetic system of interest. Then (3.27) can be written as

$$S^{\alpha\beta}(\boldsymbol{Q},\omega) = NP_n\langle\Gamma_n|S^{\alpha}|\Gamma_m\rangle\langle\Gamma_m|S^{\beta}|\Gamma_n\rangle\delta(\hbar\omega + E_n - E_m), \tag{3.30}$$

where P_n is the probability of the system initially being in state Γ_n. So, even though the interpretation of $S^{\alpha\beta}$ as the Fourier transform of the spin correlations was useful in the discussion of magnetic structures and coherent spin-wave excitations, its implications are are actually far more general, and (3.30) shows that neutron scattering can observe (as long as the matrix element is non-zero) transitions between the eigenstates of the system, whether they be, for example, the single ion levels in $Ba_3CoSb_2O_9$ (Chapter 7) or magnetic excitations from the spin-orbital singlet state

in $FeSc_2S_4$ (Chapter 6).

3.1.5 Neutron Scattering Experiments

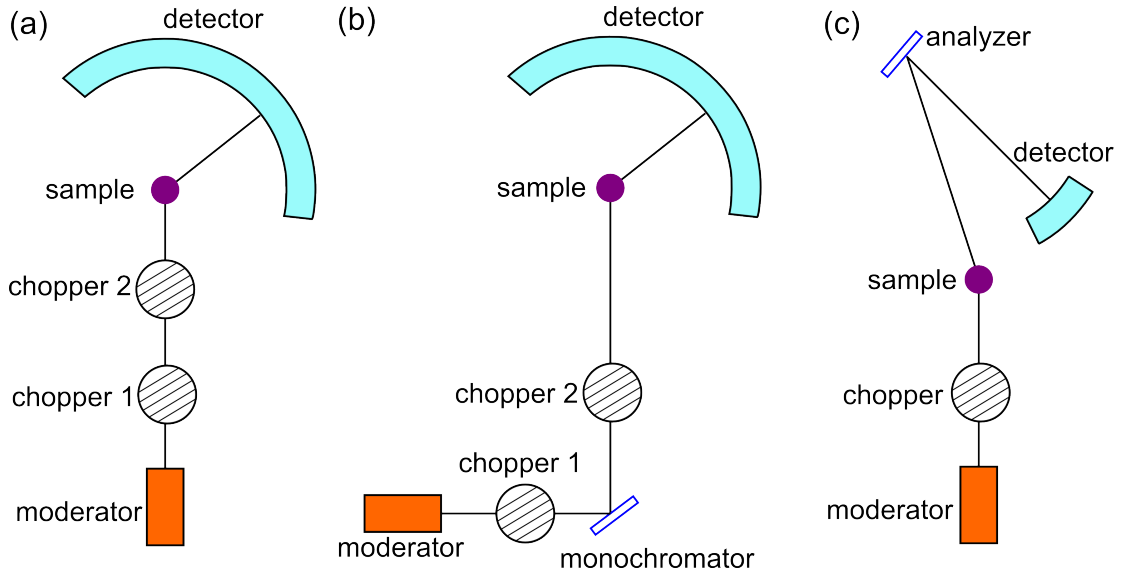


Figure 3.2: Schematic of 3 TOF spectrometers: (a) MERLIN and (b) FOCUS are both direct geometry instruments whereas (c) OSIRIS is in the indirect geometry.

Having discussed the theory behind a neutron scattering experiment, the next section will briefly touch on how this technique is put into practice for condensed matter experiments.

There are two main methods of producing neutrons for research: in a fission source the self-sufficient chain reaction of neutron capture in and subsequent fission of large nuclei (e.g. ^{235}U) creates a continuous stream of neutrons; in a spallation source, high energy protons are impingent upon a heavy metal (e.g. W) and the result is excited nuclei which expel high energy neutrons. All the experiments which contributed to this thesis occured on instruments using the latter type. Due to the short timescale of the spallation process, the time distribution of neutrons produced is determined from the driving proton pulse. At ISIS the proton source produces particles in bunches

such that the neutrons also arrive in bunches. At PSI however, the proton beam is continuous and so a continuous neutron beam is possible. On leaving the spallation source the neutrons have high energies, around 1 MeV, however neutrons of the order of 1-100 meV are required for condensed matter experiments, therefore these neutrons are passed through a moderator (composed of light molecules, e.g. water, methane, ...) before going on to the instrument beamline.

It was seen that the functional form of the scattering intensity is encoded in the scattering function ((3.30), (3.27), (3.14)), and so any neutron scattering instrument must be able to record the energy ($\hbar\omega$) and scattering vector ($\boldsymbol{Q}$) of each scattered neutron. All the neutron instruments discussed in this thesis are *Time of Flight* (TOF) instruments, called such because the energy of the scattered neutron is measured by recording how long it takes to travel from the sample to the detector. In order to determine the scattering vector $\boldsymbol{Q}$, one of $\boldsymbol{k}$ or $\boldsymbol{k'}$ is known whilst the other is measured. These differences categorize TOF instruments as 'direct' or 'indirect'.

The MERLIN spectrometer at ISIS [6] is an example of a direct TOF flight instrument, where $\boldsymbol{k}$ is known and $\boldsymbol{k'}$ is measured. A schematic of the instrument is shown in Fig 3.2(a), following the moderator two choppers (rotating mechanical devices designed to block the neutron beam for some fraction of each revolution of the chopper) are in place before the sample. The first is a so called T_0 chopper, whose role is to block the prompt pulse (instantaneous flow of high energy neutrons from the spallation source) by only allowing neutrons through with a desired range of energies. For the TOF method to work effectively, the time at which neutrons enter the instrument must be known very precisely. The point during the T_0 chopper's rotation at which

neutrons are able to pass through then acts as the 'starting gun' for the neutrons' race towards the detector. The second chopper, the so called Fermi chopper selects a desired energy for the incoming neutrons, and so defines $\boldsymbol{k}$ (via (3.4)).

Monochromatic neutrons are then scattered by the sample into a bank of detectors which measure the position of the scattered neutrons within and out of the scattering plane. In the case of MERLIN the detectors are in the form of tubes, up to 3m in length, containing ^{3}He. This instrument was used to measure the spin-orbital dispersion in $FeSc_2S_4$ shown in Fig 6.3 and the single ion levels in $Ba_3CoSb_2O_9$ shown in Fig 7.2.

FOCUS at PSI [7] is another example of a direct TOF instrument, and is shown schematically in Fig 3.2(b). The first disk chopper cuts the beam into pulses, then the beam is impingent upon a crystalline monochromator, which monochromates through Bragg reflection. This component is composed of an array of crystals, arranged such that the beam is also focussed vertically and horizontally as it is monochromated. Scattering by this crystal array allows selection of a given wavelength λ, but also allows through multiples $2\lambda, 3\lambda, ...$ A second Fermi chopper, placed afterwards, guarantees a monochromatic beam impingent upon the sample. Once again, these neutrons are then scattered into ^{3}He position sensitive detector tubes. The field-dependent data from $FeSc_2S_4$ shown in Fig 6.6 were collected at the FOCUS spectrometer.

The OSIRIS spectrometer at ISIS [8] is an indirect TOF instrument, i.e. the final wavevector $\boldsymbol{k'}$ is known, and $\boldsymbol{k}$ is measured. The instrument is shown schematically in Fig 3.2(c). A disk chopper is again used to give a precise starting time for the neutron pulse, however this time a white beam (i.e. containing many different wavelengths)

of neutrons is impingent upon the sample. Having been scattered, the neutrons then travel towards an analyzer crystal - on OSIRIS this is pyrolytic graphite (PG) - and are scattered into a bank of ^{3}He detectors. The scattering from the analyzer crystal fixes $\boldsymbol{k'}$, and typically the analyzer scattering angle will be close to back-scattering (i.e. scattered back towards the direction of the incoming beam) to avoid contamination from direct neutrons which travel almost undeflected through the sample. The high resolution data on $Ba_3CoSb_2O_9$ spin waves was captured using this instrument.

3.1.6 Sample Environments

In order to probe condensed matter systems of interest, often non-ambient conditions are required. For example, to study its ground state and excitations, it is desirable to perform scattering experiments on systems cooled to low temperature, such that that the ground state's population overwhelms that of excited states. In this thesis such cooling was performed using 2 techniques. In the case of MERLIN and FOCUS experiments, a ^{4}He cryostat was used. In such a device, the sample is immersed in He exchange gas, and temperatures of down to 1.8K can be achieved. Closed Cycle Refrigerators (CCR) on the other hand, as used on OSIRIS do not require exchange gas; instead the slow compression and fast decompression of He gas cycling in a closed system is used to cool to around 4K.

To achieve fields of up to 8.5 Tesla at FOCUS, a Cryomagnet was used; here two superconducting coils are split by a spacer to allow the passage of incident and scattered neutrons in a given plane. In all of the above cases Aluminium, with its minimal absorption and almost negligible incoherent cross-section, is used to maximise the flux into and out of the sample environment, whilst not compromising its

structural stability.

3.2 Overview of x-ray experimental techniques on Single Crystals

Though neutrons historically are the scattering probe *par excellence* for magnetic systems, in some cases it can prove quite difficult to glean any meaningful data from a neutron experiment when, for example, the system of interest contains a strongly absorbing nucleus (e.g. Iridium), or, due to technical constraints, only small sample volumes are available. X-ray scattering provides an alternative experimental probe of magnetic systems, and careful analysis of data collected at highly-engineered instruments can yield a glut of information on the magnetic groundstate and excitations of a system of interest. This aspect of x-ray scattering will be described momentarily, however first the more 'conventional' use of x-rays in determining the structure of crystalline materials is described.

3.2.1 Structure Determination through X-ray Diffraction

As with neutron scattering, this topic is now well established, with x-ray diffraction patterns having been collected for over 100 years [9], so this section will merely summarize the key results in order to make sense of the data which will be presented in following chapters.

In x-ray diffraction, the x-ray photons are scattered from the sample in such a way that the energy of out going and incoming photons is the same (termed 'elastic scattering'). Unlike the technique which will be described in Section 3.2.2, this scattering is non-resonant. Within systems of interest to this thesis, in a diffraction experiment

x-rays interact with the atoms in a sample by (Thomson) scattering from the electrons within it [10]. Just as was discussed for the case of neutron scattering in Section 3.1.3, the ordering of atoms into a lattice causes coherent scattering to occur at well defined points in k-space corresponding to reciprocal lattice vectors of the sample, the only difference now being that the probe observes the periodic arrangement of electron density as opposed to nucleon density.

As before, the object which will be measured is the differential cross section, $\left(\frac{d\sigma}{d\Omega}\right)$, where the energy dependence is omitted as a diffraction experiment integrates over an energy range, thus is sensitive only to the quasi-elastic reponse of the system. However, in x-ray language it is the scattering amplitude, f, which is spoken of, the square of which is directly proportional to the cross section. For the current purpose, any polarization dependence related to this scattering is neglected (this will be included explicitly in the following section) and it is found that [11]

$$f_{\mathrm{coh}}(\boldsymbol{\tau}) = N_0 r_e \sum_j e^{-i\boldsymbol{\tau}\cdot\boldsymbol{R}_j} \left[\int n_j(\boldsymbol{r}-\boldsymbol{R}_j) e^{-i\boldsymbol{\tau}\cdot(\boldsymbol{r}-\boldsymbol{R}_j)}\, d\boldsymbol{r} \right], \tag{3.31}$$

where, as before, N_0 is the number of unit cells within the system, $\boldsymbol{\tau}$ is a reciprocal lattice vector, $\boldsymbol{R}_j$ is the position vector of atom j, where the index j covers all atoms within a single unit cell. n_j describes the electron concentration at $\boldsymbol{r}$ due to the atom j and r_e is the classical radius of the electron ($\approx 0.3 \times 10^{-12}$cm). The scattering amplitude as written above (3.31) is split into two parts, the term in square brackets is the Fourier transform of the electron density due to atom j in the unit cell; this is often referred to as the atomic form factor, as it relates to the specific atom. The term outside the bracket is a pure phase, and corresponds to the phase of the scattered

wave from atom j. This is just the *Structure Factor* mentioned previously in the case of nuclear scattering of neutrons. In a non-bravais lattice (i.e. more than one atom per unit cell) this term leads to differences in scattering intensity for different Bragg peaks $\boldsymbol{\tau}$, and indeed can cause the complete absence of some peaks due to perfect cancellation.

In an x-ray diffraction experiment then, the observation of a set of Bragg peaks allows one to work out the reciprocal lattice, and hence deduce the real-space lattice (unit cell) of the system. The variation in intensity of these peaks caused by the phase term in (3.31) allows the determination (given reasonable starting parameters, e.g. chemical composition) of the species and positions of atoms within the unit cell. With this in mind then, perhaps a more 'suitable' form for (3.31) for diffraction experiments might be:

$$f_{\mathrm{coh}}(\boldsymbol{\tau}) = N_0 r_e \sum_j f_j e^{-i\boldsymbol{\tau}\cdot\boldsymbol{R}_j}, \tag{3.32}$$

where f_j is the atomic form factor for atom j, which in a simple diffraction experiment is not typically of interest except for the fact that;

- f_j will increase as the size of the scattering atom is increased (magnitude of n_j is larger)
- f_j will decrease with increasing $\boldsymbol{\tau}$ (because n_j is spread over a finite volume in real-space), with the practical result that Bragg peaks become weaker at larger values of $\boldsymbol{\tau}$

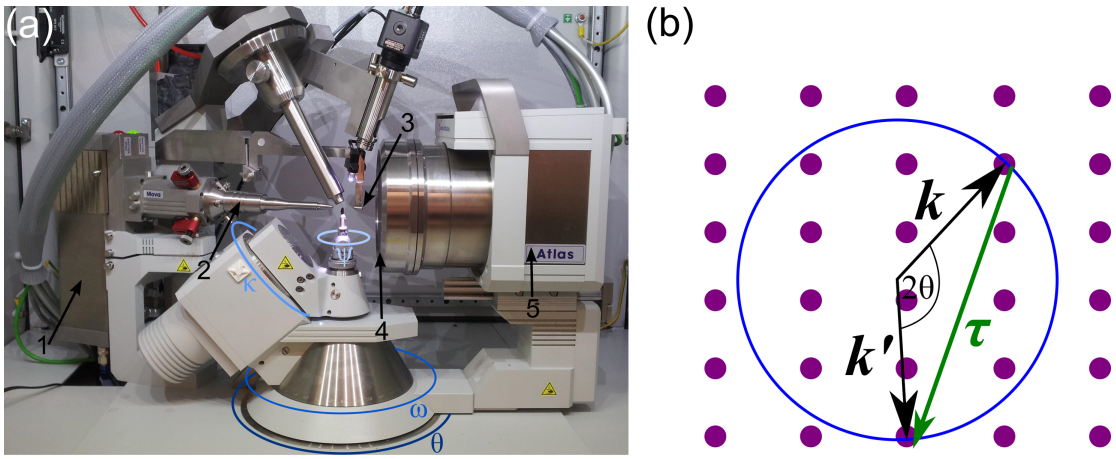


Figure 3.3: X-ray diffraction experiment. (a) The SuperNova x-ray diffractometer with the 1. x-ray tube, 2. collimator, 3. beam stop, 4. Be window, 5. CCD area detector labelled. The 4 rotational angles $\psi, \kappa, \omega, \theta$ of the 4-circle kappa-diffractometer are also shown. (b) Ewald construction for the rotating-crystal method implemented in such a device (after [11]).

The diffraction experiments outlined in this thesis were performed on a SuperNova diffractometer, and this is shown in Fig 3.3(a). X-rays are generated by a Molybdenum x-ray tube ($\lambda = 0.707$ Å), before being collimated towards the sample position. The scattered beams then travel towards the CCD area detector. The detector consists of a scintillation screen to convert the x-ray photons into visible photons, which are then processed and digitised by the CCD chip and sent to a computer for analysis. To avoid background scattering, the detector is placed in vaccum, and a Beryllium window (Beryllium has only 4 electrons per atom, and so is a very weak scatterer of x-rays) is used to allow scattered x-rays passage through. A beam stop is also used to avoid damage to the detector caused by the high intensity of the direct (un-scattered) beam.

This kind of diffractometer is referred to as a '4-circle kappa-diffractometer' due to the 4 axes of rotation of the sample possible (these are labelled in Fig 3.3(a) as

$\psi, \kappa, \omega, \theta$), and the principle underlying its operation is schematically drawn in Fig 3.3(b). This depiction is down to a concept of the 'Ewald sphere' [12], which is briefly summarised here. The incoming and outgoing x-rays, $\boldsymbol{k}$ and $\boldsymbol{k'}$ respectively, have the same magnitude, because coherent, elastic scattering from the crystal is being considered. Drawn from the same origin then, $\boldsymbol{k}$ and $\boldsymbol{k'}$ define a sphere, and whenever 2 reciprocal lattice points lie on the surface of the sphere – the so called 'Ewald sphere' – then the scattering vector[2] $\boldsymbol{Q} = \boldsymbol{k'} - \boldsymbol{k}$ is equal to a reciprocal lattice vector, and coherent Bragg scattering occurs.

This is shown for a special case in Fig 3.3(b), where the incoming and outgoing beams are parallel to a reciprocal lattice plane. As discussed, $\boldsymbol{k}$ and $\boldsymbol{k'}$ define a sphere (the cross-section of which is circular), and this locus so happens to cross two reciprocal lattice points seperated by a reciprocal lattice vector $\boldsymbol{\tau}$, equivalently it can be said that $\boldsymbol{\tau}$ is in 'the scattering condition'. One may now ask how other reciprocal lattice vectors (corresponding to other Bragg peaks) are brought into the scattering condition? One can imagine rotating the reciprocal lattice in Fig 3.3(b) in the plane of the paper, while keeping the Ewald circle fixed, and envisage many more pairs of points simultaneously crossing the circle, and so many more Bragg peaks being observed. Indeed, if one could rotate the lattice about all three axes, being sure to move in very fine steps, then it is clear that all reciprocal lattice vectors within the limit $\tau \leq 2k$ (i.e. bounded by the size of the Ewald sphere) can be recorded.

This is exactly the principle used on the SuperNova machine of Fig 3.3(a); $\boldsymbol{k}$

[2]N.B. although the same notation, $\boldsymbol{Q}$, is being used for the scattering vector when discussing neutron and x-ray scattering, the definition actually varies between the two methods by a minus sign such that $\boldsymbol{Q}_{\text{x-ray}} = \boldsymbol{k'} - \boldsymbol{k}$ but $\boldsymbol{Q}_{\text{neutron}} = \boldsymbol{k} - \boldsymbol{k'}$. This difference is historical and does not change the fundamental physics of a scattering event, so subscripts $\boldsymbol{Q}_{\text{x-ray}}$ or $\boldsymbol{Q}_{\text{neutron}}$, will not be used, with the understanding that $\boldsymbol{Q}$ means slightly different things in these two contexts.

is fixed (the position of the collimator does not move throughout the experiment), while the 4-cycle kappa-diffractometer rotates the crystal (ψ, κ, ω) and detector (θ), and correspondongly the reciprocal lattice, through space.

3.2.2 Resonant Magnetic X-ray Diffraction

Now the attention is turned to resonant magnetic x-ray diffraction (RMXD), again, the theoretical framework underlying these experiments has been covered extensively elsewhere (e.g. S.W. Lovesey [10]) and has also been formulated in a language of matrices (Hill & McMorrow [13]) which is very appropriate for the x-ray experiments described in this thesis. So included here is the bare minimum required for an understanding of the results which will follow, and this discussion will not deviate greatly from the expositions put forth in the two aforementioned references.

Unlike x-ray diffraction mentioned previously, this scattering involves the excitation of a core electron to an intermediate state and then detection of the photon emitted as the electron returns to its original state. Hence no net energy is exchanged to the atom, and this is still a diffraction experiment, but by probing the outer shells of the atom one can learn about the local moments in the system of interest.

The scattering amplitude for an RMXD event for a 2^L-pole resonance is given by [14]

$$f^e_{\mathrm{EL}}(\omega) = \frac{4\pi}{|k|} f_D \sum_{M=-L}^{L} \left[\hat{\boldsymbol{\epsilon}}'^{*} \cdot \boldsymbol{Y}^{(e)}_{LM}(\hat{\boldsymbol{k}}') \boldsymbol{Y}^{(e)*}_{LM}(\hat{\boldsymbol{k}}) \cdot \hat{\boldsymbol{\epsilon}} \right] F^{(e)}_{LM}(\omega), \tag{3.33}$$

where $\boldsymbol{\epsilon}$ and $\boldsymbol{\epsilon}'$ are the incident and scattered polarization vectors respectively, $\boldsymbol{k}$ and $\boldsymbol{k}'$ are their respective wavevectors and f_D is the Debye-Waller factor mentioned previously in the context of neutron scattering, and again results from the thermal motion

of atoms. $\boldsymbol{Y}_{LM}^{(e)}(\hat{\boldsymbol{k}})$ are vector spherical harmonics. The strength of the resonance is contained in the factor $F_{LM}^{(e)}(\omega)$ (where $-L \leq M \leq L$) determined by properties of the atom:

$$F_{LM}^{(e)}(\omega) = \sum_{\mu,\eta} \frac{P_\mu P_\mu(\eta)\Gamma_x(\mu M\eta; EL)/\Gamma(\eta)}{x(\mu,\eta) - i}. \tag{3.34}$$

Here, η and μ are the excited and initial states of the ion respectively, P_μ is the probability that the ion is initally in state μ whereas $P_\mu(\eta)$ is the probability of a transition from μ to η. Γ_x/Γ is the ratio of the partial line width of the excited state due to a pure electric dipole radiative decay (EL) to that due to all processes, radiative and non-radiative. Lastly, $x = (E_\eta - E_\mu - \hbar\omega)/(\Gamma/2)$ is the deviation from the resonance condition in units of total half-width.

The situation is drawn schematically in Fig 3.4(a), where initially an x-ray photon is impingent upon an ion (in state μ following previous notation), this is then absorbed by the ion resulting in the promotion of a core electron to the outer shells (navy circle), thus leaving a hole in the core (white circle). The atom is now in intermediate state η. The excited electron then returns to the core emiting an x-ray photon. An electron excited in this manner performs a transition from μ to all possible states η and so interference is possible between these multiple channels (depicted as multiple waves in Fig 3.4(a)).

Next, the specific case of dipole transitions (i.e. $L = 1$, or an '$E1$' transition) is considered, as this order of transition typically dominates the resonant cross-section, and is the only transition probed in this thesis. In this case, the coherent scattering amplitude on resonance for the n$^{\text{th}}$ ion is given by:

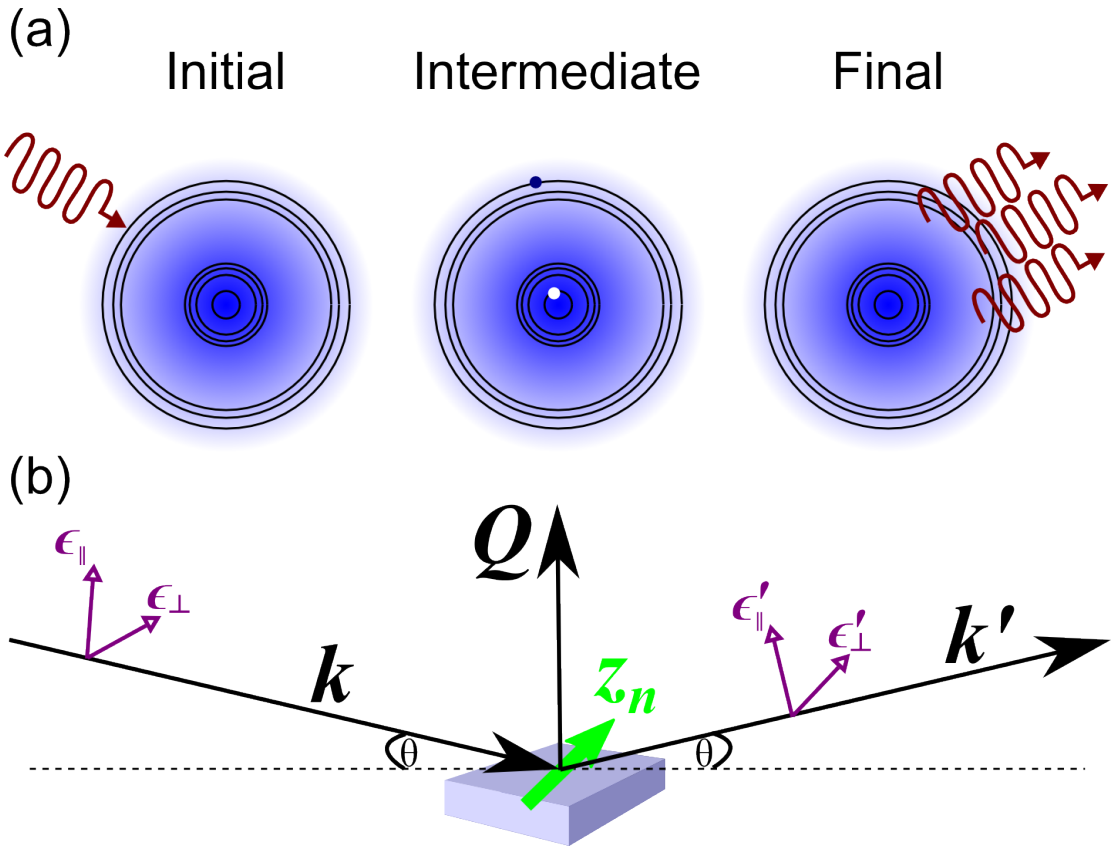


Figure 3.4: RMXD process. (a) An x-ray photon is absorbed by an ion (gradiated blue circle) thus forming an intermediate, excited state in the ion with a hole in the core electron shell (white circle) which then decays by emitting an x-ray. The electron undergoes all possible transitions from its initial to final state and so interference between these pathways can be seen (after [15]). (b) Schematic of an RMXD experiment, the initial x-ray wavevector $\boldsymbol{k}$ is scattered into $\boldsymbol{k'}$ following an interaction with a magnetic moment $\boldsymbol{z}_n$.

$$f_{n\mathrm{E1}} = (\hat{\boldsymbol{\epsilon}}' \cdot \hat{\boldsymbol{\epsilon}})F^{(0)} - i(\hat{\boldsymbol{\epsilon}}' \times \hat{\boldsymbol{\epsilon}}) \cdot \hat{\boldsymbol{z}}_n F^{(1)} + (\hat{\boldsymbol{\epsilon}}' \cdot \hat{\boldsymbol{z}}_n)(\hat{\boldsymbol{\epsilon}} \cdot \hat{\boldsymbol{z}}_n)F^{(2)}, \tag{3.35}$$

where $\hat{\boldsymbol{z}}_n$ is a unit vector in the direction of the moment of the n$^{\mathrm{th}}$ ion and:

$$F^{(0)} = (3/4k)[F_{11} + F_{1-1}], \tag{3.36}$$

$$F^{(1)} = (3/4k)[F_{11} - F_{1-1}], \tag{3.37}$$

$$F^{(2)} = (3/4k)[2F_{10} - F_{11} - F_{1-1}], \tag{3.38}$$

and the F_{LM} terms in (3.36), (3.37), (3.36) are just those written in (3.34).

The experimental setup shown schematically in Fig 3.4(b) is considered; an x-ray with initial wavevector and polarization $\boldsymbol{k}$, $\boldsymbol{\epsilon}$ is scattered into $\boldsymbol{k'}$, $\boldsymbol{\epsilon'}$, and the resulting scattering vector is $\boldsymbol{Q} = \boldsymbol{k'} - \boldsymbol{k}$. The setup suggests a natural basis for the polarization of the incoming and outgoing x-rays, in that it will either be parallel or perpendicular to the scattering plane defined by $\boldsymbol{k}$-$\boldsymbol{k'}$. The terminology usually adopted experimentally is that σ polarization is perpendicular to the scattering plane ($\boldsymbol{\epsilon}_\perp$ in Fig 3.4(b)) whereas π polarization is parallel to it ($\boldsymbol{\epsilon}_\parallel$ in Fig 3.4(b)), again primed and unprimed symbols will be used to denote incident and scattered beams, respectively.

This basis can be put to use by rewriting (3.35) in terms of 2×2 matrices [16] such that each term, T, has the representation

$$T(\boldsymbol{k}, \boldsymbol{\epsilon} \rightarrow \boldsymbol{k'}, \boldsymbol{\epsilon'}) = \begin{bmatrix} A_{\boldsymbol{\sigma}\rightarrow\boldsymbol{\sigma'}}(\boldsymbol{k}, \boldsymbol{k'}) & A_{\boldsymbol{\pi}\rightarrow\boldsymbol{\sigma'}}(\boldsymbol{k}, \boldsymbol{k'}) \\ A_{\boldsymbol{\sigma}\rightarrow\boldsymbol{\pi'}}(\boldsymbol{k}, \boldsymbol{k'}) & A_{\boldsymbol{\pi}\rightarrow\boldsymbol{\pi'}}(\boldsymbol{k}, \boldsymbol{k'}) \end{bmatrix}, \tag{3.39}$$

where the $A_{i\rightarrow f}$ terms are the amplitudes for scattering from an initial polarization state to a final polarization state, which will in general be dependent on $\boldsymbol{k}$ and $\boldsymbol{k'}$.

The first term in (3.35) is independent of the moment $\boldsymbol{z}_n$, and the $(\hat{\boldsymbol{\epsilon}}' \cdot \hat{\boldsymbol{\epsilon}})$ term is simply the polarization dependence of Thompson scattering of x-rays (and actually describes the polarization dependence of diffracted x-rays which was neglected from the discussion in the previous section). This term will be appropriate for the discussion of polarizers later, in the form of (3.39) it is expressed as:

$$\hat{\boldsymbol{\epsilon}} \cdot \hat{\boldsymbol{\epsilon}}' = \begin{pmatrix} 1 & 0 \\ 0 & \hat{\boldsymbol{k}} \cdot \hat{\boldsymbol{k}}' \end{pmatrix} = \begin{pmatrix} 1 & 0 \\ 0 & \cos 2\theta \end{pmatrix}, \tag{3.40}$$

where θ is the scattering angle as defined in Fig 3.4(b).

The second term in (3.35), is seen to be linear in $\boldsymbol{z}_n$, and it is found that;

$$(\hat{\boldsymbol{\epsilon}} \times \hat{\boldsymbol{\epsilon}}') \cdot \hat{\boldsymbol{z}}_n = \begin{pmatrix} 0 & \hat{\boldsymbol{k}} \\ -\hat{\boldsymbol{k}}' & \hat{\boldsymbol{k}} \times \hat{\boldsymbol{k}}' \end{pmatrix} \cdot \hat{\boldsymbol{z}}_n. \tag{3.41}$$

Unlike the case of conventional Thompson scattering calculated in (3.40), the second term in (3.35) allows processes of the kind $\boldsymbol{\sigma} \rightarrow \boldsymbol{\pi}'$ and $\boldsymbol{\pi} \rightarrow \boldsymbol{\sigma}'$, this immediately provides a method to measure the magnetic scattering on resonance in a sample of interest. If the initial x-ray beam is σ-polarized, say, by measuring only the π'-polarized component of the scattered beam, it is possible to filter out all the charge scattering and see only the contribution from magnetic scattering. Moreover, further inspection of (3.41) shows that RMXD is not only sensitive to the presence of magnetic moments, but to their direction. Specifically, the measurement in the $\boldsymbol{\sigma} \rightarrow \boldsymbol{\pi}'$ and $\boldsymbol{\pi} \rightarrow \boldsymbol{\sigma}'$ channels is sensitive only to components of the moment parallel to the scattered ray[3]. This allows the magnetic structures of systems to be solved unambiguously through this method.

[3] *c.f.* with neutron scattering where measurements are sensitive to moments perpendicular to the scattering vector (3.26)

Such an experiment will then require the polarization analysis of the outgoing beam. The typical method of such polarization analysis is to scatter this beam from another 'analyzer' material. This material could be an amorphous material producing incoherent scattering; e.g. amorphous Kapton foil, where the polarization can be determined through use of the result from classial optics known as *Brewster's angle* [17], or as is the case in the experiments outlined here, the analyzer can be a crystal producing coherent scattering.

The polarization dependence of coherent charge scattering is given by (3.40), it can be seen that when $\cos 2\theta = 0$ then only σ-polarized light is scattered. This is shown schematically in Fig 3.5(a); the beam scattered from the sample, $\boldsymbol{k'}$, will in general include both π and σ components of polarization, however, upon being coherently Bragg scattered by a scattering vector $\boldsymbol{Q}$ with $\theta = 45°$, only the component perpendicular to this scattering plane survives ($\boldsymbol{\sigma''}$). By rotating the analyzer crystal about the scattered beam $\boldsymbol{k'}$ (rotation shown as red arrow in Fig 3.5(a)) it is possible to isolate the $\boldsymbol{\sigma'}$ or $\boldsymbol{\pi'}$ components as required. The only remaining difficulty of this process is to find an appropriate Bragg reflection for the given wavelength (corresponding to the atomic resonance being probed), Bragg reflections from various crystals are used [18] e.g. the (3,3,3) reflection in Au has $2\theta = 90°$ for $E = 11.16$ keV and so is ideal for use with the L_3 edge[4] in Iridium, where the resonance occurs at 11.215 keV.

Coherent scattering resonant magnetic scattering from magnetic materials, as was the case with neutrons, result in extra Bragg peaks in the diffraction pattern. For

[4]In RMXD experiments the x-ray notation is typically used, such that resonances are described by the core electron which is excited, e.g. L_3 corresponds to excitations from the $nl_j = 2p_{(3/2)}$ orbital

commensurate ordering – e.g. colinear, constant moment antiferromagnetic order – this results in Bragg peaks which can be described by integer co-ordinates in the magnetic reciprocal latice. For incommensurate ordering however – e.g. helical, constant moment order, or spin density wave – magnetic Bragg peaks occur at satellite positions to structural Bragg peaks, governed by the ordering vector $\boldsymbol{P}$.

The third term in (3.35) goes as the square of the moment, and is scattering of second order. Such scattering events are not recorded in this thesis and so this term will not be examined in detail, but it is noted that their contribution to scattering from helical ordered systems is to produce a further, weaker set of satellites $2\boldsymbol{P}$ away from the original structural peak.

3.2.3 The X-ray Diffractometer I16

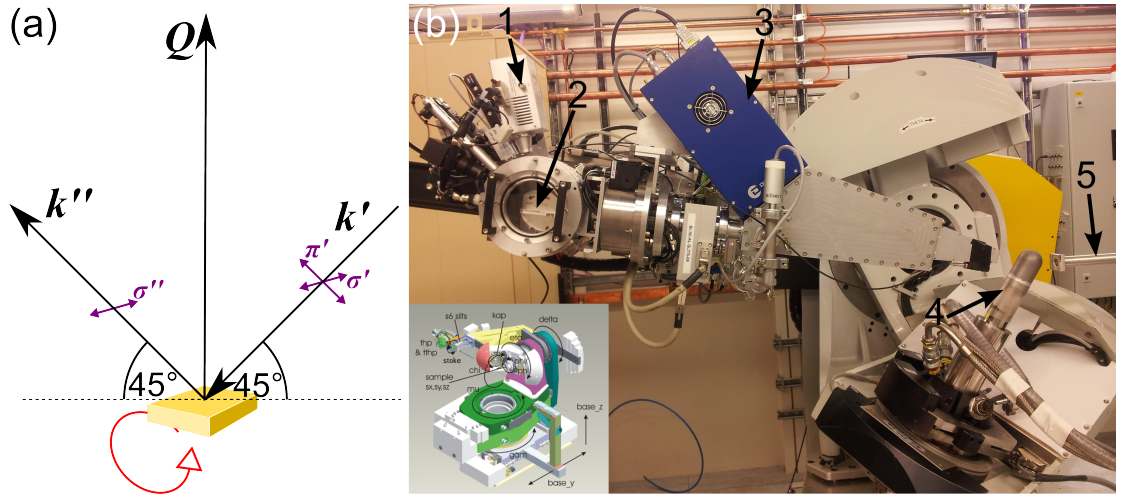


Figure 3.5: The I16 diffractometer. (a) Schematic of the polarization analyzer (PA) setup on I16, a PA crystal in the condition $2\theta = 90°$ will allow only the component $\boldsymbol{\sigma''}$ through to the detector, rotation (red arrow) around the scattered beam from the sample $\boldsymbol{k'}$ allows isolation of $\boldsymbol{\sigma'}$ or $\boldsymbol{\pi'}$ component as required. (b) Photograph of the I16 instrument at the Diamond Light Source showing, 1. x-ray camera, 2. PA crystal 3. 2D x-ray detector, 4. Be domes of CCR containing sample, 5. Incoming x-ray beam. Inset: Schematic of the I16 diffractometer from [19] showing the various angles on the 6-circle kappa diffractometer.

The I16 diffractometer at the Diamond Light Source is shown in Fig 3.5(b), with several components labelled. The fundamental sample setup is no different from that discussed in the context of the SuperNova diffractometer in Fig 3.3(a); x-rays with a fixed $\boldsymbol{k}$ (5 in Fig 3.5(b)) are collimated towards the sample (4 in Fig 3.5(b)) and then scattered into a detector. Again, rotation of the crystal allows mapping throughout k-space, and this is done via a 6-circle kappa-diffractometer (inset, Fig 3.5(b)). The difference here however is that intense, high energy x-rays generated by a synchrotron source are targeted on the sample. Energy selection is also possible via a pair of adjustable mirrors and an array of Al foils are used to attenuate the beam (neither component shown in Fig 3.5(b), they are 'upstream' from 5).

Another important difference between these two setups is the polarization analysis possible on I16. The monochromatic x-rays focussed on the sample are polarized in the σ direction and with a given alignment of the PA crystal (2 in Fig 3.5(b)) only the π' scattering is recorded in the detector (2 in Fig 3.5(b)), thus showing only the magnetic contribution to the scattering (3.41). An area detector (3 in Fig 3.5(b)) is also in place, this has no polarization analysis, but is useful for scanning k-space.

Low temperature sample environments are possible on I16 with use of a CCR. The underlying principles of the device are no different from that discussed for neutron scattering in Section 3.1.6, however here, two concentric Be domes are used at the head of the CCR to allow minimum attenuation of the x-ray beam.

References

[1] G. Squires, *Introduction to the Theory of Thermal Neutron Scattering*, 1^{st} ed. (Cambridge University Press, 1978).

[2] A. Furrer, J. Mesot, and T. Strässle, *Neutron Scattering in Condensed Matter Physics*, 1^{st} ed. (World Scientific, 2009).

[3] R. Shankar, *Principles of Quantum Mechanics*, 2^{nd} ed. (Kluwer, 1994).

[4] L. Van Hove, Physical Review **95**, 249 (1954).

[5] A. Auerbach, *Interacting Electrons and Quantum Magnetism*, 1^{st} ed. (Springer, 1994).

[6] R. Bewley, R. Eccleston, K. McEwen, S. Hayden, M. Dove, S. Bennington, J. Treadgold, and R. Coleman, Physica B: Condensed Matter **385-386**, 1029 (2006).

[7] J. Mesot, S. Janssen, L. Holitzner, and R. Hempelmann, Journal of Neutron Research **3**, 293 (1996).

[8] M. T. F. Telling and K. H. Andersen, Physical chemistry chemical physics : PCCP **7**, 1255 (2005).

[9] W. Friedrich, P. Knipping, and M. Laue, Annalen der Physik **346**, 971 (1913).

[10] S. Lovesey, *X-ray Scattering and Absorption by Magnetic Materials*, 1^{st} ed. (OUP, 1996).

[11] C. Kittel, *Introduction to Solid State Physics*, 8^{th} ed. (Wiley, 2005).

[12] N. Ashcroft and N. Mermin, *Solid State Physics*, 1^{st} ed. (Brooks/Cole, 1976).

[13] J. P. Hill and D. F. McMorrow, Acta Crystallographica Section A Foundations of Crystallography **52**, 236 (1996).

[14] J. Hannon, G. Trammell, M. Blume, and D. Gibbs, Physical Review Letters **61**, 1245 (1988).

[15] B. Kim, H. Ohsumi, T. Komesu, and S. Sakai, Science **323**, 1329 (2009).

[16] F. de Bergevin and M. Brunel, Acta Crystallographica Section A **37**, 314 (1981).

[17] D. Griffiths, *Introduction to Electrodynamics*, 3^{rd} ed. (Pearson, 2008).

[18] C. Detlefs, M. Sanchez del Rio, and C. Mazzoli, The European Physical Journal Special Topics **208**, 359 (2012).

[19] S. Collins, http://doc.diamond.ac.uk/i16manual/instructions.html, 2010.

Chapter 4

Non-Coplanar and Counter-Rotating Incommensurate Magnetic Order Stabilized by Kitaev Interactions in γ-Li_2IrO_3

Materials that realize Kitaev spin models with bond-dependent anisotropic interactions have long been searched for, as the resulting frustration effects are predicted to stabilize novel forms of magnetic order or quantum spin liquids. In this chapter the crystal structure of a new polytype of lithium iridate, the 'stripyhoneycomb' γ-Li_2IrO_3 is determined, and the magnetism within this structure – which has the topology of a 3D Kitaev lattice of inter-connected Ir honeycombs – is explored. Using resonant magnetic x-ray diffraction a complex, yet highly-symmetric incommensurate magnetic structure is found with non-coplanar and counter-rotating Ir moments. A minimal Kitaev-Heisenberg Hamiltonian is proposed that naturally accounts for all key features of the observed magnetic structure. These results provide strong evidence that γ-Li_2IrO_3 realizes a spin Hamiltonian with dominant Kitaev interactions.

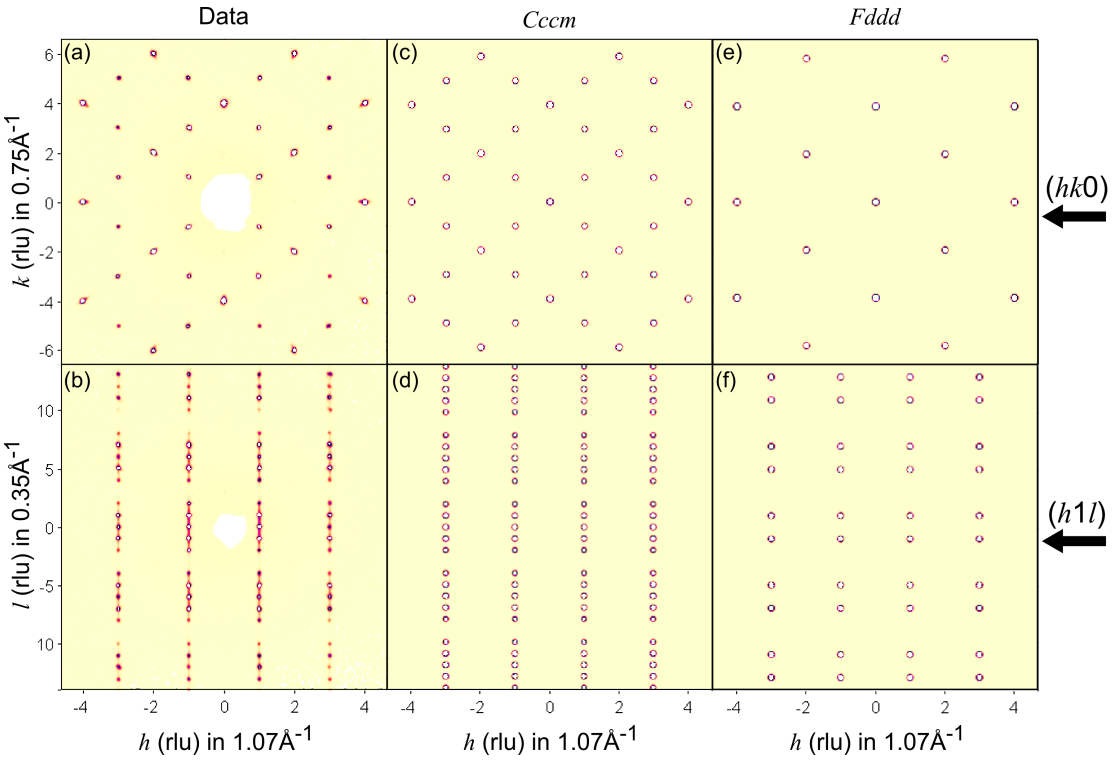


Figure 4.1: Structural x-ray data for γ-Li_2IrO_3 plotted in reciprocal lattice units, top and bottom rows show $(hk0)$ and $(h1l)$ planes respectively. The left most images (a) and (b) show data collected via x-ray diffraction on the single crystal of γ-Li_2IrO_3 shown in Fig 4.2(b). (c), (d) and (e), (f) show calculations for the ideal $Cccm$ and $Fddd$ structures respectively.

4.1 Discovering the Structure of γ-Li_2IrO_3

High-purity, flux-grown (see [1] for details of synthesis) single crystals of Li_2IrO_3 had been synthesised Dr J. Analytis *et al.* Bulk measurements performed on these samples (magnetic susceptibility (χ) and and torque magnetometry [1]) revealed an anomaly indicative of magnetic order at $T_N = 38$K. SQUID measurements performed with the field aligned along each of the orthorhombic axes showed the occurence of this anomaly to be consistent along the a, b and c directions. However, although these three components of the susceptibility (χ_a, χ_b, χ_c) showed similar behaviour in the temperature range 300 K to 100 K, below this range χ_b shows a marked increase, being approximately an order of magnitude greater than χ_a and a factor of five greater than χ_c. This disparity was attributed to the fact that the b-axis is perpendicular to a subset of the square Ir-O_2-Ir planes introduced in Section 2.3.1. Equivalently this is expressed by the fact that $\boldsymbol{b}$ is parallel to the Kitaev axis $\mathbf{z}$, which will be introduced explicitly later in this chapter. The room temperature limit of χ_a, χ_b, χ_c could not be fit to a consistent Curie-Weiss temperature. Specific heat measurements taken at Oxford [2] on these samples confirmed this ordering temperature.

This very different ordering temperature compared to previously measured, polycrystalline samples of α-Li_2IrO_3, $T_N = 15$K [3], suggested that the flux-grown samples may realize a polytype of Li_2IrO_3 with a different crystal structure. This was clearly revealed by x-ray diffraction measurements performed using an Mo-source Supernova diffractometer (see Section 3.2.1 for more information on this diffractometer). Several crystals were measured and the diffraction patterns were all consistent in terms of the unit cell and selection rules for the observed diffraction peaks. In this thesis the

data on an approximate rhombus-shaped, $\approx 35 \times 10^3 \mu m^3$ flux- grown crystal (shown in Fig4.2 (b)) will be reported.

The lattice parameters of the monoclinic layered honeycomb crystal structure [4] could not account for the positions of over 2000 Bragg peaks measured in the diffraction experiment, which instead could be indexed with an orthorhombic unit cell with parameters given in Table 4.1. Note that the errors included in this table, for lattice constants and fractional atomic co-ordinates, represent error bars on the fitting procedure's ability to fit a parameter to the collected data set, and does not take account of any intrinsic error in the measurement, e.g. a misalignment of the instrument, which would affect all collected peaks. This is also true of Table 5.1.

Representative diffraction patterns are illustrated in Fig 4.1(a,b), where (h, k, l) refer to wavevector components in reciprocal lattice units of the orthorhombic unit cell. The highest-symmetry orthorhombic space groups that can account for all of the observed peaks in the diffraction patterns are $Cccm$ (no. 66) and $Ccc2$ (no. 37). Both have the same selection rule for allowed reflections for a general atomic position, (hkl) : $h + k$ even, $(0kl)$: both k and l even, $(h0l)$: both h and l even. Both have a C-centered unit cell, corresponding to a translation of $(\frac{1}{2}, \frac{1}{2}, 0)$, and $Ccc2$ is obtained from $Cccm$ by removing a mirror plane normal to the c-axis. In the final refinements of the crystal structure reported below, no significant atomic displacements nor corresponding improvement in the goodness of fit was found when the crystal symmetry was lowered from $Cccm$ to $Ccc2$, so in the following only the higher symmetry case is discussed. The unit cell volume is approximately $4\times$ the unit cell volume of the layered honeycomb structure ($Z = 4$), which suggested that the

present polytype has the same mass density, but with $Z = 16$ formula units per unit cell. Since iridium is by far the dominant x-ray scatterer with 77 electrons (oxygen 8 and lithium 3 electrons), a preliminary fit to the x-ray data was first attempted assuming a simplified structural model composed solely of Ir ions located in general positions within the $Cccm$ space group symmetry. The iridium coordinates were set free to refine within the bounds of the orthorhombic unit cell. Remarkably, the refinement easily converged with Ir ions occupying two crystallographic sites with coordinates close to those listed in Table 4.1.

To test that this solution was reliable, and not an accidental local minimum in the least squares refinement, simulated annealing techniques were implemented by Dr R. Johnson using FullProf [5] to explore the full parameter space of the structural model against the full data set (treating each observed (h, k, l) reflection as an independent point without imposing any symmetry constraints). By constructing a lattice with the dimensions of the orthorhombic unit cell $a \times b \times c$ but with lowered symmetry $P\bar{1}$, and populating it with eight iridium ions with atomic fractional coordinates free to vary within the full unit cell according to the annealing process, an unconstrained (except for inversion symmetry) yet highly reproducible iridium lattice that corresponded to a global minimum in the parameter space was found. This structure was found to be in perfect agreement with the iridium framework of the initial refinement, confirming both the structural model and the space group, $Cccm$.

Using the measured Bragg peak intensities, space group symmetry, and the identified iridium positions, electron density maps in the unit cell were calculated (using Shelxl [6] and Wingx [7]). This revealed additional electron density pockets, which

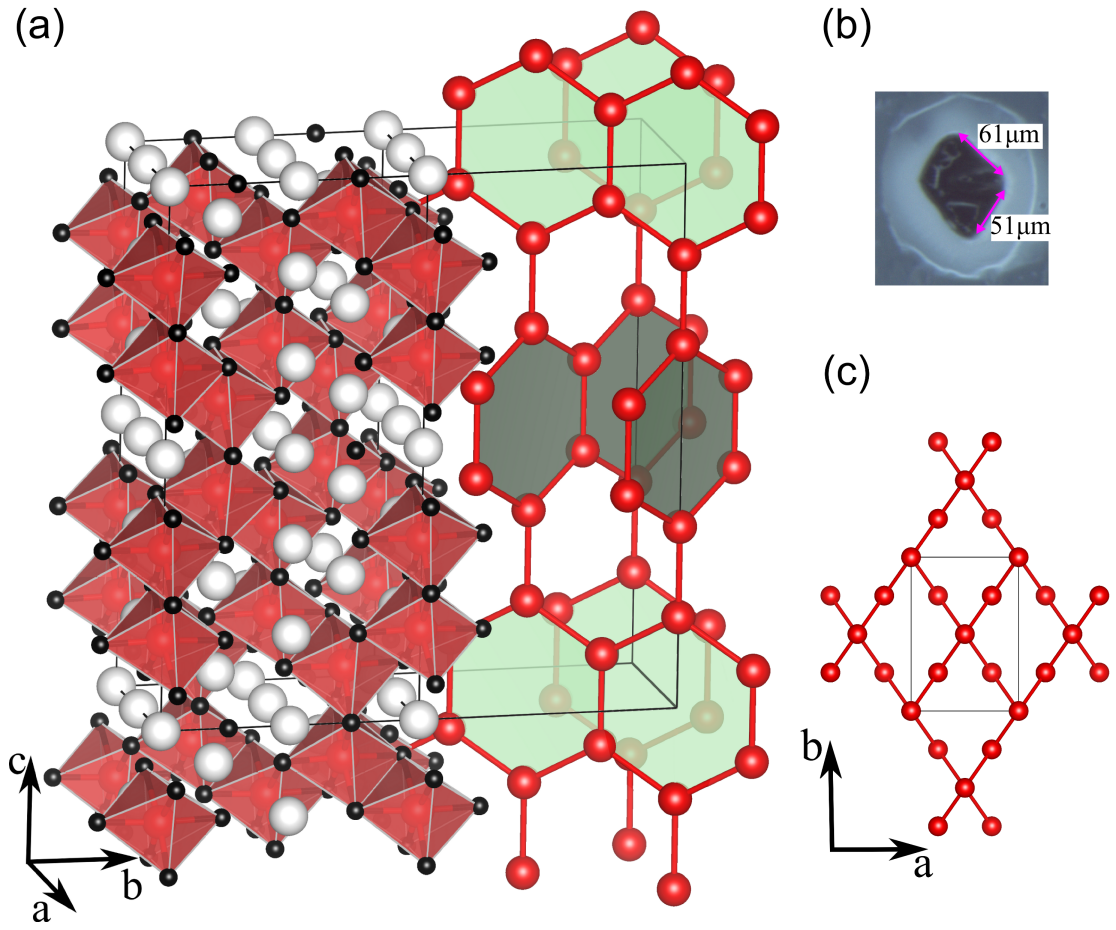


Figure 4.2: Crystal structure of γ-Li_2IrO_3. (a) Two unit cells, on the left Ir (red), O (black) and Li (white) ions are depicted as spheres, the IrO_6 octahedra are shown as light red polyhedra. In the neighbouring cell, only the Ir atoms have been included and the shading of the honeycomb rows demonstrates how they alternate in orientation – parallel to $\boldsymbol{a} + \boldsymbol{b}$ (light green) and $\boldsymbol{a} - \boldsymbol{b}$ (dark green) – upon moving up the c-axis. (b) Sample of γ-Li_2IrO_3 used for experiments, the rhombic geometry is a result of the lattice, best demonstrated by viewing along the c-axis (c).

Cell parameters

Space group: $Cccm$ (#66, origin choice 1)

Z = 16

a, b, c(Å):	5.9119(3)	8.4461(5)	17.8363(10)
α, β, γ(°):	90	90	90

Volume (Å^3): 890.61(9)

Fractional atomic coordinates and isotropic A.D.P.'s

Atom	Site	x	y	z	U_{iso}(Å^2)
Ir	8k	0.25	0.25	0.0836(2)	0.0124(4)
Ir$'$	8i	0.5	0.5	0.1670(3)	0.0206(6)
Li1	8j	0	0.5	0.3333	0.01
Li2	8k	0.75	0.25	0.25	0.01
Li3	8k	0.75	0.25	0.91667	0.01
Li4	4c	0.5	0.5	0.5	0.01
Li5	4d	0.5	0	0	0.01
O1	16m	0.77(1)	0.515(3)	0.087(4)	0.02(1)
O2	8g	0.72(2)	0.5	0.25	0.04(1)
O3	8l	0.00(1)	0.262(8)	0	0.006(9)
O4	16m	0.49(1)	0.262(6)	0.163(3)	0.006(9)

Table 4.1: Structural parameters of γ-Li_2IrO_3 at 300 K [1].

were identified as the location of oxygen ions. Lithium ions scatter x-rays very weakly (only 3 electrons) and their positions cannot be reliably identified using x-ray scattering techniques, especially in the presence of heavy elements such as iridium. However, assuming that the fundamental building blocks of the structure are edge-sharing IrO_6 and LiO_6 octahedra (as in the honeycomb polytype), one can readily determine idealized lithium positions (listed in Table 4.1 and shown in Fig 4.2(a)) required to

achieve this connectivity. Assuming lithium ions to be fixed at the ideal positions, a full structural model was refined against the data set using FullProf [5]. Iridium and oxygen ions were located in the initial positions determined above, and their atomic coordinates were set free to vary within the constraints of *Cccm* crystal symmetry. It became apparent that the structural model gave an excellent fit to most reflections, but over-estimated the diffraction intensity of a small subset. Specifically, the empirically-determined selection rules for observed (h, k, l) reflections give three families: (even, even, even) with $h + k + l = 4n$, $n \in \mathbb{Z}$, (odd, odd, odd) except l = 3+6n, $n \in \mathbb{Z}$, and (odd, odd, even). The intensities calculated for the *Cccm* structure were found to be in excellent agreement with the (even, even, even) and (odd, odd, odd) reflections measured. The model also explains the presence of the third family of reflections, the (odd, odd, even), but the observed intensity is weaker than predicted. In fact those reflections showed an asymmetry in the intensity not expected under orthorhombic symmetry, i.e. $I_{(\text{odd,odd,even})} \neq I_{(\text{-odd,odd,even})}$. The degrees of both the lowered average intensity and asymmetry were found to vary across a number of different samples measured, however, the excellent agreement to the (even, even, even) and (odd, odd, odd) reflections was robust and consistent across all samples tested. The discrepancies in (odd, odd, even) intensities are most likely due to sample-dependent structural stacking faults, as discussed later in this section. A final refinement was performed against the (even, even, even) and (odd, odd, odd) reflections with excellent reliability factors $R_{\text{F2}} = 3.83\%$, $wR_{\text{F2}} = 4.91\%$, and $R_{\text{F}} = 2.27\%$ [including also the (odd, odd, even) reflections in the refinement resulted only in very small changes in the oxygen positions, which are regarded to be below the

accuracy that can be reliably determined]. The obtained structural parameters from the final refinement are given in Table 4.1; essentially the same results are obtained in refinement done using Sir-92 [8] and Shelxl [6]. The above refinement assumed stoichiometric Li_2IrO_3 with all atomic positions fully occupied. However, the possibility that each of the seven cation sites (Ir1-2, Li1-5) could have a mixed Li/Ir occupancy has also been tested. In this test the total site occupancy is constrained to unity (i.e. no structural vacancies) with no constraint on the total Li:Ir atomic ratio (i.e. stoichiometry free to vary). Under these constraints a full refinement of Li/Ir occupancies on the cation sites lead to no significant improvement in the refinement parameters. Furthermore, the occupancies of the Li and Ir sublattices refined to their nominal values (Li only in Li1-5 sites and Ir only in Ir1-2 sites) within an error of less than 3%, further confirming the stoichiometric composition and the structural model in Table 4.1. The obtained crystal structure is illustrated in Fig 4.2(a). The full 3D x-ray diffraction pattern observed is well accounted for by this model and representative plots are shown in Fig 4.1(c,d). The refined structure has IrO_6 octahedra distorted from ideal cubic with non-equivalent Ir-O distances spanning a range of up to ≈ 7 % for each octahedron, comparable to the range of Ir-O distances reported for the IrO_6 octahedra in the layered honeycomb polytype [4].

The resulting Ir network shown in Fig 4.2(a) is a novel arrangement of near-ideal honeycombs in three dimensions not reported before (as far as known by the author) in other $3d$ or $5d$ oxides. In the left cell of Fig 4.2(a) Ir ions (red spheres) are seen to be in an octahedral environment of O ligands (black spheres), and these octahedra are depicted as light red polyhedra, the Li ions are also shown (white spheres), and

the three-fold connectivity of IrO_6 octahedra is apparent. In the neighbouring cell, the Oxygen and Lithium ions have been removed, leaving only the Iridium ions, and bonds have been drawn between neighbouring Ir ions (red cylinders) to demonstrate the 3D connectivity of this lattices, and the Ir hexagons have been coloured in two shades of green. Ir honeycombs form parallel rows – hence the 'stripyhoneycomb' nomenclature – that alternate along the two diagonals of the unit cell in the ab plane, namely along $\boldsymbol{a}+\boldsymbol{b}$ at $z = 0$ (light green) and along $\boldsymbol{a}-\boldsymbol{b}$ at $z = 1/2$ (light green). This alternation leads to a 3D network of inter-connected honeycomb rows stacked along the c-axis, where all nearest-neighbor Ir-Ir links are nearly the same length ($\approx c/6$) and all Ir-Ir-Ir bond angles are close to 120°. The Ir positions are indeed very close to such an ideal lattice realized for Ir1 at $8k$ (1/4, 1/4, 1/12), Ir2 at $8i$ (1/2, 1/2, 1/6) and $c = \sqrt{3(a^2 + b^2)}$, compare with Table 4.1 where the latter equation is satisfied to within 0.1%. This near-regularity of the Ir lattice is directly manifested in the observed x-ray diffraction pattern by a conspicuous absence of detectable scattering intensity along the c-axis for $l = 3 + 6n$, $n \in \mathbb{Z}$, as illustrated in Fig. 4.1(b), this is not due to a general symmetry-imposed selection rule of the space group, but is due to a near cancellation of intensity for a lattice built out of near-ideal honeycomb sections stacked along the c-axis. Note that viewing the γ-Li_2IrO_3 structure along the c-axis (Fig 4.2(c)) gives a clear indication of the morphology of the sample, as the Ir lattice maps out a rhombic shape when viewed in such a manner, and indeed through the previously discussed x-ray diffraction measurements it was ascertained that the c-axis is normal to the rhombic surface shown in Fig 4.2(b).

For completeness, it is noted that the stripyhonecomb, γ-Li_2IrO_3 described here

can easily be distinguished experimentally from other Li_2IrO_3 structures described in Section 2.3.3, as they have different symmetries and/or different unit cell sizes, and consequently distinct diffraction patterns. For illustration, the hyperhoneycomb, β-Li_2IrO_3 polytype shown in Fig 2.3(b) is considered. The periodic iridium atomic arrangement can be described by an orthorhombic unit cell of the same size $a \times b \times c$ and orientation of axes as for γ-Li_2IrO_3 but face-centered and with diamond glide planes. In the corresponding space group, $Fddd$ (no. 70), iridium ions occupy a single crystallographic site, 16g (0,0,z) (origin choice 1), with z =1/12 assuming the c-axis Ir-Ir bond length is $c/6$.

Fig 4.1(a,b) and (e,f) show the comparison between data and the calculated diffraction pattern for the hyperhoneycomb β-Li_2IrO_3. This structure will be described in greater detail in Chapter 5, but for now the ideal structure is used, with Li1 16g (0,0,1/4), Li2 16g (0,0,5/12), O1 32h(1/4, 0, 1/6), O2 16e (1/4, 0, 0). As illustrated in Fig 4.1(e,f) the $Fddd$ space group has a much more restrictive selection rule for allowed reflections compared to $Cccm$, for example in the (hk0) plane $h + k$ is required to be a multiple of 4 and both h and k to be even, as opposed to the less restrictive $h + k$ even for $Cccm$, and for (h1l) both h and l odd, as opposed to h odd and l unrestricted for $Cccm$. The $Cccm$ selection rules can account for all the experimentally observed reflections, whereas an $Fddd$ unit cell could not account for the presence of the (odd, odd, even) reflections, such as the relatively strong (110), see Fig 4.1(a,e). Furthermore, refinement of the $Fddd$ structure against the intensities of reflections allowed in this symmetry, namely (even, even, even) and (odd, odd, odd), gives a statistically rather poor fit with R_{F2} = 21.4%, wR_{F2}= 36.2%, and R_F =

13.3%. These results, coupled with the conclusions drawn from the simulated annealing tests, conclusively show that the hyper-honeycomb $Fddd$ structural model (and lower-symmetry structures obtained by small distortions of an $Fddd$ parent structure) can be ruled out for the single crystals reported in this study.

Finally, it is noted that in addition to sharp Bragg peaks the x-ray diffraction pattern also revealed the presence of weak, but clearly visible diffuse scattering in the form of 'rods' of scattering intensity in-between Bragg peaks along the l-direction, sharply defined in the h and k directions, as clearly seen in Fig 4.1(b) with the selection rule h odd and k odd. Whilst a quantitative refinement of the data including the diffuse scattering is beyond the scope of this present study, it is likely that this diffuse scattering originates from occasional structural faults in the nominal $Cccm$ atomic stacking sequence along the c-axis. The presence of diffuse scattering takes intensity away from the sharp Bragg peaks, and it is possible that some families of Bragg peaks are affected more than others; this might explain why the intensity of one particular family of reflections, namely the (odd, odd, even) peaks located on the diffuse scattering rods, appears weaker in experiment than predicted by a structurally-perfect $Cccm$ model considered in our refinement.

Having confidently ascertained that the sample under consideration is a new structural polytype – the stripyhoneycomb γ-Li_2IrO_3 – the next step is to ascertain the nature of the magnetic order below $T_N = 38K$, and RMXD allows such a determination, even on samples of the size considered here (Fig 4.2(b)).

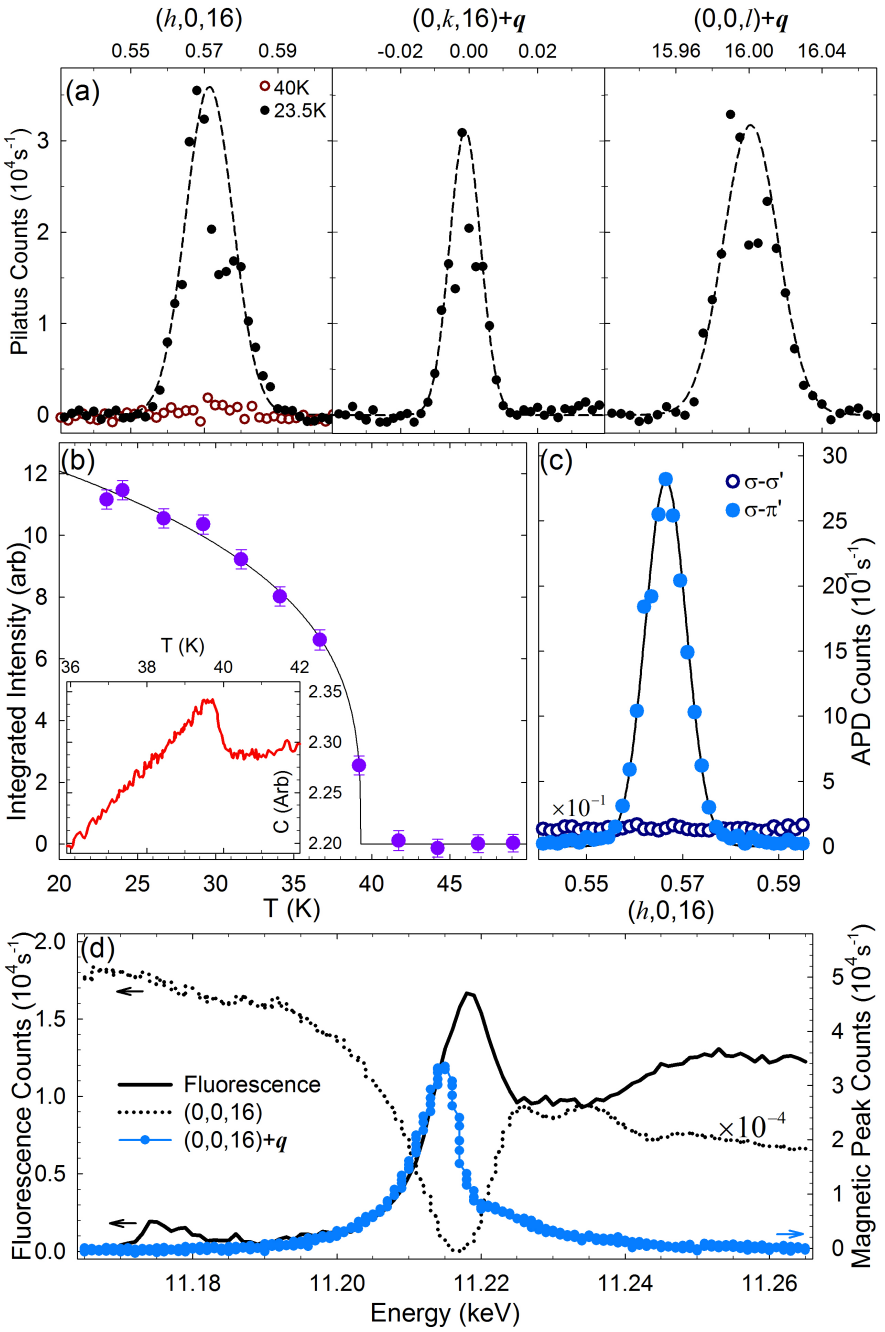


Figure 4.3: Magnetic Bragg peak at $(0, 0, 16)$+$\boldsymbol{q}$. (a) Scans along orthogonal directions in reciprocal space (filled/open symbols at base temperature/above T_N). Dashed lines are fits to a Gaussian shape. (b) Temperature-dependence of the integrated magnetic peak intensity (solid line is guide to the eye, temperature values are corrected for beam heating effects, see text). Inset: specific heat data showing an anomaly at the onset of magnetic order. (c) Scans with a polarizer in the scattered beam: the magnetic signal is present only in the σ-π' channel (filled circles) and disappears in the σ-σ' (open circles) dominated by charge scattering (intensity scaled by 1/10). (d) Energy scan through the magnetic peak (blue squares) and a structural Bragg peak $(0, 0, 16)$ (dotted line, scaled by $1/10^4$), as well as the fluorescence scan (solid line).

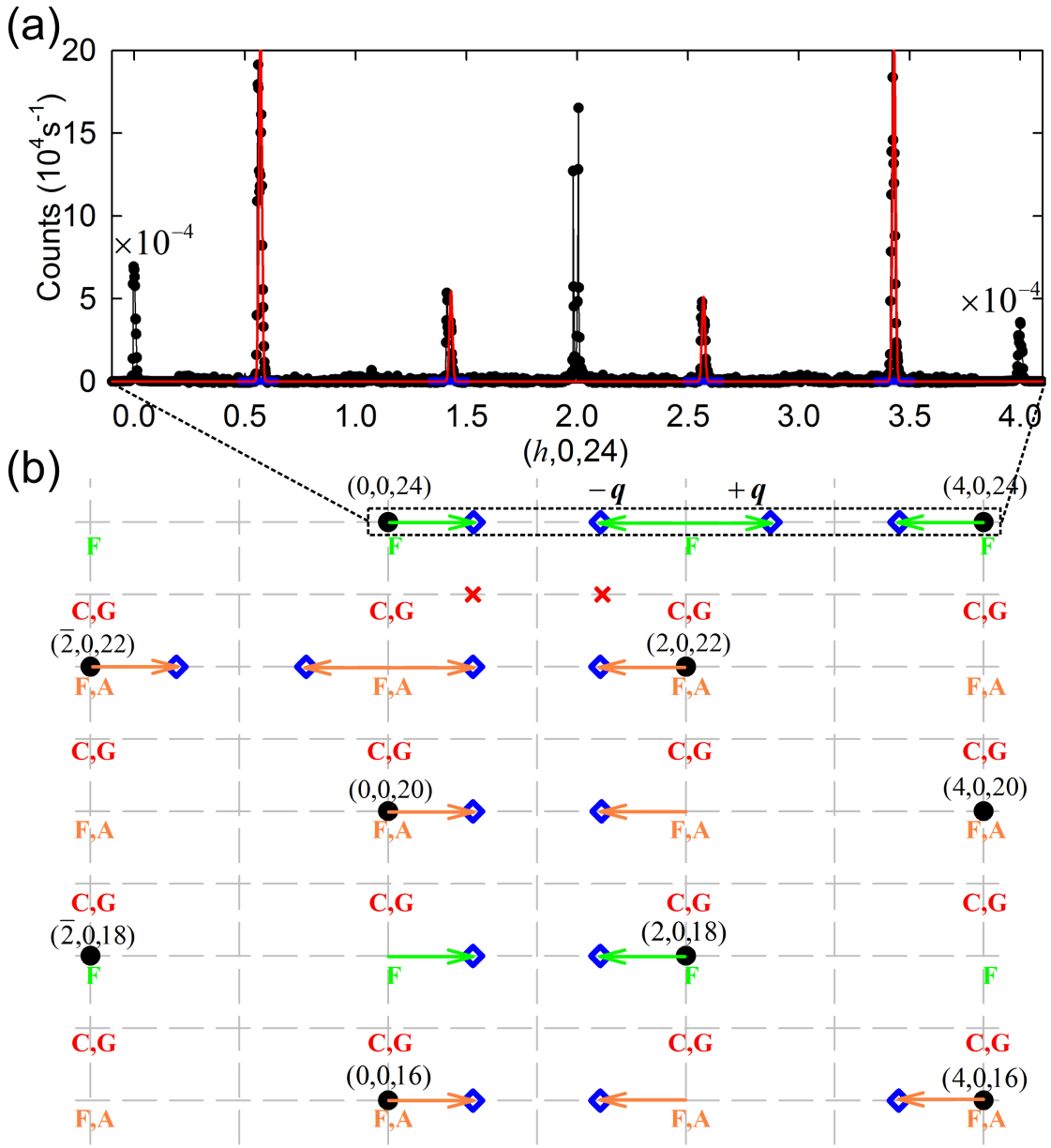


Figure 4.4: (a) Scan along the $(h, 0, 24)$ direction observing structural peaks at $h = 0, 4$ (intensity scaled by $1/10^4$ for clarity), a multiple-scattering signal centered at $h = 2$, and magnetic peaks at $h = 0 + q, 2 \pm q, 4 - q$. Solid red line is the calculated magnetic scattering intensity [9] for the magnetic structure model depicted in Fig. 4.6. (b) $(h0l)$ reciprocal plane with filled circles, diamonds and red crosses indicating positions of structural peaks, measured magnetic peaks and the absence of peaks, respectively. Lattice points are also labelled by the magnetic basis vectors that have finite structure factor for magnetic peaks at satellite $\pm\boldsymbol{q}$ positions.

4.2 RMXD Experiment on γ-Li_2IrO_3

The RMXD experiments were performed using the I16 beamline at Diamond (see Section 3.2.3 for details). The single crystal sample was placed onto a silicon disc ((1,1,1) plane) facing upwards just as shown in Fig 4.2(b), i.e. with its c-axis almost precisely surface normal (the grease used to secure the crystal to the disk lead to the c-axis being slightly off vertical), which was then attached to a copper mount which could be secured onto I16. The Si disc provides a clean background for the experiment, producing characteristic Bragg peaks at known positions, whereas the Cu mount allows good thermal conduction between the CCR and sample. Again for reasons of thermal conductivity, RS Silver Conductive Adhesive was used to secure the Si disk into place.

Having secured the sample and placed it within the Be domes of the CCR, the crystal was lowered to base temperature ($\approx$ 9K) and x-rays were focussed onto it. The beam size was defocussed to 200 μm $\times$ 200 μm to ensure the sample was fully illumniated at all orientations, and tuned in energy to the L_3 edge (i.e. electron excited from the $2p_{3/2}$ level) at 11.215 keV, where previous RMXD experiments on Ir^{4+} iridates had shown strong resonant effects [10, 11].

Systematic searches along high-symmetry directions in reciprocal space revealed that at low temperatures new magnetic Bragg peaks appeared at satellite positions of reciprocal lattice points with an incommensurate propagation vector $\boldsymbol{q} = (0.57(1), 0, 0)$ where the uncertainty in q is estimated from combining uncertainties in the crystal orientation (characterised by an imperfect UB-matrix, which provides a mapping from the physical crystal orientation to its direction reciprocal space) and

the I16 instrument's intrinsic sphere of uncertainty.

The satellite peaks were found to be of the same shape as structural Bragg peaks; the multi-featured nature of the peaks resulting from the mosaicity of the sample, which apparently consists of several crystallites, slightly mis-aligned relative to eachother[1]. Moreover, Gaussian fits were made to these peaks as illustrated for the $(0, 0, 16)+\boldsymbol{q}$ reflection in Fig. 4.3(a), and by using the full width, half-maximum (FWHM) of these fits one can obtain a crude estimate of the correlation length resulting in these features. The so obtained correlation lengths were over 20 unit cells in all three reciprocal lattice directions, which was found to be comparable with fits of structural Bragg peaks, indicating no anomalous broadening of the magnetic peaks compared to structural peaks, i.e. the magnetic order is well-developed and as long-range as the structural order. These fits have intrinsic errors associated with them; as can be seen in Fig. 4.3(a), an envelope is fitted over a mosaic of peaks, which again has inherent uncertainties.

The peaks disappeared upon heating [Fig. 4.3(a), open circles] and the temperature-dependence of the intensity had a typical order parameter behavior [see Fig. 4.3(b)]. It should be noted that the absolute temperature values recorded from I16 have been corrected for beam-heating effects through a calibration against specific heat measurements on the *same* sample, shown in Fig. 4.3(b) inset, which give $T_N = 39.5$ K (these specific heat measurements were conducted by R. Morris, and the data is reproduced from [2]). One would expect such effects here, as the sample is relatively cubic in its distribution of volume and so can not be expected to dissipate heat effectively, the

[1]It is interesting to note that such mosaicity was completely absent from the x-ray diffraction measurements of Fig 4.1 (a) and (b). This is testament to the high spatial resolution available on I16.

covering of grease probably further hinders this process.

The magnetic origin of the satellite reflections was further confirmed by analyzing the polarization of the scattered beam. The setup for such analysis is shown in Fig 3.4(b) and Fig 3.5(a), and the (3,3,3) reflection from an Au crystal was used as an analyzer. Fig. 4.3(c) shows that the peak at $(0, 0, 16)+\boldsymbol{q}$ appeared only in the σ-π' channel (filled circles), and is absent in the σ-σ' channel (open circles), as expected for resonant diffraction that is of pure magnetic origin (as discussed in Section 3.2.2). An energy scan performed whilst centered on the magnetic peak [Fig. 4.3(d)] showed a large resonant enhancement of the scattered intensity, again as expected for RMXD. The energy dependence is in stark contrast to that characteristic of a nearby structural peak (dotted line), whose intensity actually shows a dip at resonance, due to the absorption of x-rays here. Furthermore, the obtained resonance energy is similar to values found in other iridates [12, 11] and agrees well with the edge of the measured fluorescence signal from the sample (solid line in Fig. 4.3(d)).

In total, over 30 magnetic Bragg peaks were observed, and those measured in the $(h0l)$-plane are labelled in Fig. 4.4(b) as blue diamonds. A representative scan along the $(h, 0, 24)$ direction is plotted in Fig. 4.4(a), which shows strong structural Bragg peaks centered at $h = 0, 4$, and a multiple scattering signal centered at $h = 2$. The four other peaks visible in this scan are magnetic Bragg peaks symmetrically displaced away from the above reflections. The scan illustrates the highly symmetric nature of the magnetic peak intensities and that $\boldsymbol{q}$ is distinctly different from the commensurate wavevector $(\frac{1}{2}, 0, 0)$.

4.3 Structure Factor Analysis

The observation of magnetic Bragg peaks at specific points in reciprocal space can already say an awful lot about the underlying magnetic structure through using knowledge of the structure and some symmetry analysis. As discussed in the previous section, the magnetic iridium ions are located on two inequivalent sublattices in the orthorhombic unit cell, referred to as Ir and Ir$'$, respectively (light and dark balls in Fig. 4.6) and their fractional co-ordinates are given in Table 4.1. Each sublattice contains four sites in the primitive cell labelled 1 to 4 and $1'$ to $4'$, respectively (labels are shown in Fig. 4.6) with the additional 8 sites required to fill the unit cell being generated by the C-centering operation + $(\frac{1}{2}\ \frac{1}{2}\ 0)$.

Only satellite magnetic Bragg peaks corresponding to a wavevector $\boldsymbol{q} = (q, 0, 0)$ were observed, and so only the Fourier components associated with this wavevector need be considered. As such, the magnetic moment at position $\boldsymbol{r}$ belonging to site index $n = 1-4, 1'-4'$ can be written as

$$\boldsymbol{M}_n(\boldsymbol{r}) = \boldsymbol{M}_{\boldsymbol{q},n} e^{-i\boldsymbol{q}\cdot\boldsymbol{r}} + \boldsymbol{M}_{-\boldsymbol{q},n} e^{i\boldsymbol{q}\cdot\boldsymbol{r}}, \tag{4.1}$$

where the terms $\boldsymbol{M}_{\boldsymbol{q},n}$, $\boldsymbol{M}_{-\boldsymbol{q},n}$ on the right hand side of (4.1) are the Fourier components of the magnetic moment and $\boldsymbol{M}_{-\boldsymbol{q},n} = \boldsymbol{M}^*_{\boldsymbol{q},n}$ since the magnetic moment distribution must be a real quantity.

For a propagation vector $\boldsymbol{q} = (q, 0, 0)$ symmetry analysis [13] gives four types of magnetic basis vectors for *each* of the two sublattices: $++++(F)$, $++--(C)$, $+--+(A)$ and $+--+(G)$ where the $\pm$ signs denote a symmetry-imposed relation between the magnetic Fourier components at the sites 1-4 and $1'$-$4'$, e.g. for basis

vector A on the Ir sublattice the Fourier components on sites 1-4 are related by $\boldsymbol{M}_{\pm\boldsymbol{q},1}{=}{-}\boldsymbol{M}_{\pm\boldsymbol{q},2}{=}{-}\boldsymbol{M}_{\pm\boldsymbol{q},3}{=}\boldsymbol{M}_{\pm\boldsymbol{q},4}$. These basis vectors transform according to the irreducible representations listed in Table 4.2, where the subscripts x, y, z correspond to a given component of the Fourier magnetic moment.

Irreducible representation	Basis vectors
Γ_1	C_x, A_y, G_z
Γ_2	F_x, G_y, A_z
Γ_3	A_x, C_y, F_z
Γ_4	G_x, F_y, C_z

Table 4.2: Irreducible representations and basis vectors for a magnetic structure with propagation vector $\boldsymbol{q} = (q, 0, 0)$.

In direct analogy to the calculation of structure factors for nuclear Bragg peaks outlined in Section 3.2.1, the structure factor of *magnetic* Bragg peaks can also be calculated. Specifically, for a magnetic Bragg reflection at wavevector $\boldsymbol{Q} = (h, k, l){\pm}\boldsymbol{q}$ the structure factor is

$$\boldsymbol{\mathcal{F}}(\boldsymbol{Q}) = \boldsymbol{\mathcal{F}}((h, k, l){\pm}\boldsymbol{q}) = f_C \sum_n \boldsymbol{M}_{\pm\boldsymbol{q},n} e^{i\boldsymbol{Q}\cdot\boldsymbol{r}_n}, \tag{4.2}$$

where the pre-factor $f_C = 1 + e^{i\pi(h+k)}$ is due to the C-centering of the orthorhombic structural unit cell. The sum extends over all 8 iridium sites in the primitive cell (n =1−4, 1′−4′) and $\boldsymbol{M}_{\pm\boldsymbol{q},n}$ are the Fourier components of the magnetic moments at site n with position in the unit cell $\boldsymbol{r}_n$. Through inspection of (4.2) and the definitions of the basis vectors F, C, A, G above, one would anticipate that each of the four types of basis vectors has its own selection rules for a non-zero structure factor and

indeed direct calculation of the structure factors shows that the four types of basis vectors F, C, A and G produce finite intensity magnetic peaks only for satellites of certain integer (h, k, l) reciprocal lattice positions and not others. To make those selection rules transparent the structure factors have been calculated analytically for an "ideal" iridium lattice, which is very close to the one refined experimentally in Table 4.1, but with the Ir coordinate at $z = 1/12$ and Ir$'$ at $z' = 1/6$. In this case the structure factors are obtained as:

$$\boldsymbol{\mathcal{F}}_F(\boldsymbol{Q}) = 8e^{i\zeta_\pm}\boldsymbol{M}_{\pm\boldsymbol{q},1}\cos\frac{\pi l}{6}\left[\cos\frac{\pi(k+l)}{2} + e^{\pm i\alpha}e^{i\frac{\pi(h+l)}{2}}\cos\frac{\pi l}{2}\right]\delta_{h+k,2p}, \tag{4.3}$$

$$\boldsymbol{\mathcal{F}}_C(\boldsymbol{Q}) = 8e^{i\zeta_\pm}\boldsymbol{M}_{\pm\boldsymbol{q},1}\left[\sin\frac{\pi l}{6}\sin\frac{\pi(k+l)}{2} - ie^{\pm i\alpha}e^{i\frac{\pi(h+l)}{2}}\cos\frac{\pi l}{6}\sin\frac{\pi l}{2}\right]\delta_{h+k,2p}, \tag{4.4}$$

$$\boldsymbol{\mathcal{F}}_A(\boldsymbol{Q}) = 8ie^{i\zeta_\pm}\boldsymbol{M}_{\pm\boldsymbol{q},1}\sin\frac{\pi l}{6}\left[\cos\frac{\pi(k+l)}{2} - e^{\pm i\alpha}e^{i\frac{\pi(h+l)}{2}}\cos\frac{\pi l}{2}\right]\delta_{h+k,2p}, \tag{4.5}$$

$$\boldsymbol{\mathcal{F}}_G(\boldsymbol{Q}) = -8e^{i\zeta_\pm}\boldsymbol{M}_{\pm\boldsymbol{q},1}\left[i\cos\frac{\pi l}{6}\sin\frac{\pi(k+l)}{2} + e^{\pm i\alpha}e^{i\frac{\pi(h+l)}{2}}\sin\frac{\pi l}{6}\sin\frac{\pi l}{2}\right]\delta_{h+k,2p}, \tag{4.6}$$

where δ is the Kronecker symbol and $p \in \mathbb{Z}$, i.e.

$$\delta_{h+k,2p} = \begin{cases} 1, & h+k \text{ even} \\ 0, & h+k \text{ odd} \end{cases},$$

and this term arises in the structure factor due to the C-centering. Here $\zeta_\pm = \pi(h/2 \pm q/2 + k + l/3)$ and the 1$^{\text{st}}$ and 2$^{\text{nd}}$ terms in the square brackets come from the Ir and Ir$'$ sublattices, respectively, where it is assumed that their magnetic Fourier components are the same up to a complex phase offset α, i.e. $\boldsymbol{M}_{\boldsymbol{q},1'} = e^{i\alpha}\boldsymbol{M}_{\boldsymbol{q},1}$.

Using the above equations, one can calculate which of the four basis vectors contribute to given satellites in reciprocal space, and this is shown for a region of the $(h0l)$ plane in Fig 4.4(b), where (h, k, l) points are labelled with the basis vectors which produce satellite magnetic peaks around these positions. Motivated by the h-scan shown in Fig 4.4(a), from the above equations it is clear that in the $(h0l)$ plane for $l = 6n$ ($n \in \mathbb{Z}$) only F-basis vectors contribute, as the structure factor for all the other basis vectors cancels ($\mathcal{F}_C = \mathcal{F}_A = \mathcal{F}_G = 0$). In this case, further inspection of the structure factors shows that satellites can be separated into those corresponding to $\alpha = 0$ and those with $\alpha = \pi$, for example the magnetic satellites at $(0, 0, 24) \pm \boldsymbol{q}$ come from an (F, F) – where short-hand notation has been introduced for ease of notation, the first term in brackets corresponds to the basis vector of the Ir sublattice, and the second term the basis vector for the Ir$'$ sublattice – basis vector ($\alpha = 0$) and peaks at $(2, 0, 24) \pm \boldsymbol{q}$ come from an $(F, -F)$ basis vector ($\alpha = \pi$). For the $(h, 0, l)$ plane depicted in Fig. 4.4(b) magnetic satellite peaks occur only for h even with the further selection rule l odd for both C and G, and l even for both F, A with pure F (no A contribution) for $l = 6n$, $n \in \mathbb{Z}$. Systematic searches were made for peaks of C/G character in this plane, specifically searches were performed at the satellite positions $(q, 0, 23)$ and $(2-q, 0, 23)$ using four different azimuth angles and failed to detect any intensity above the background (shown as red crosses in Fig 4.4(b)). Therefore, within experimental error the presence of C and G basis vectors can be discounted from contributing to the magnetic groundstate of γ-Li_2IrO_3.

Inspection of Fig 4.4(b) shows that all peaks measured can be described by the F basis vector, and the presence or absence of A cannot be clarified by measuring

satellite peaks in this plane. Referring back to the structure factors of (4.3)-(4.6) however, it is seen that satellites of (odd, odd, $l = 3 + 6n$), $n \in \mathbb{Z}$, such as (1,1,21) are of A, G type (no F or C contribution) and so the detection of a magnetic Bragg peak at (1,1,21)+$\boldsymbol{q}$ allows the existence of an A-basis vector in the magnetic ground state to be proven.

By measuring a set of magnetic Bragg peaks and making sufficiently thorough searches to clarify that a certain set of such peaks are not present, a great deal about the magnetic ground state of γ-Li_2IrO_3 becomes known. Specifically, it is known that only two out of the four possible basis vectors (i.e. F and A) contribute to the low T state. However, this is far from a complete solution to the problem; each component of the magnetization will typically be associated with a different basis vector (e.g. see the irreducible representations of Table 4.2), and this cannot be determined from the presence/absence of Bragg peaks alone. Moreover, the phase α between sublattices Ir and Ir$'$ introduced earlier is also not completely constrained by the above treatment – although the presence of two sets of satellites along the h-scan of Fig 4.4(a) leads to the conclusion that both (F, F) $(\alpha = 0)$ and $(F, -F)$ $(\alpha = \pi)$ contributions are present. However, there is a subtlety of the RMXD technique which can assist in determining these phases, and ultimately the full magnetic structure, as will be introduced in the following section.

4.4 Azimuthal Dependence of Intensities

In the electric dipole approximation the magnetic resonant x-ray scattering intensity is proportional to

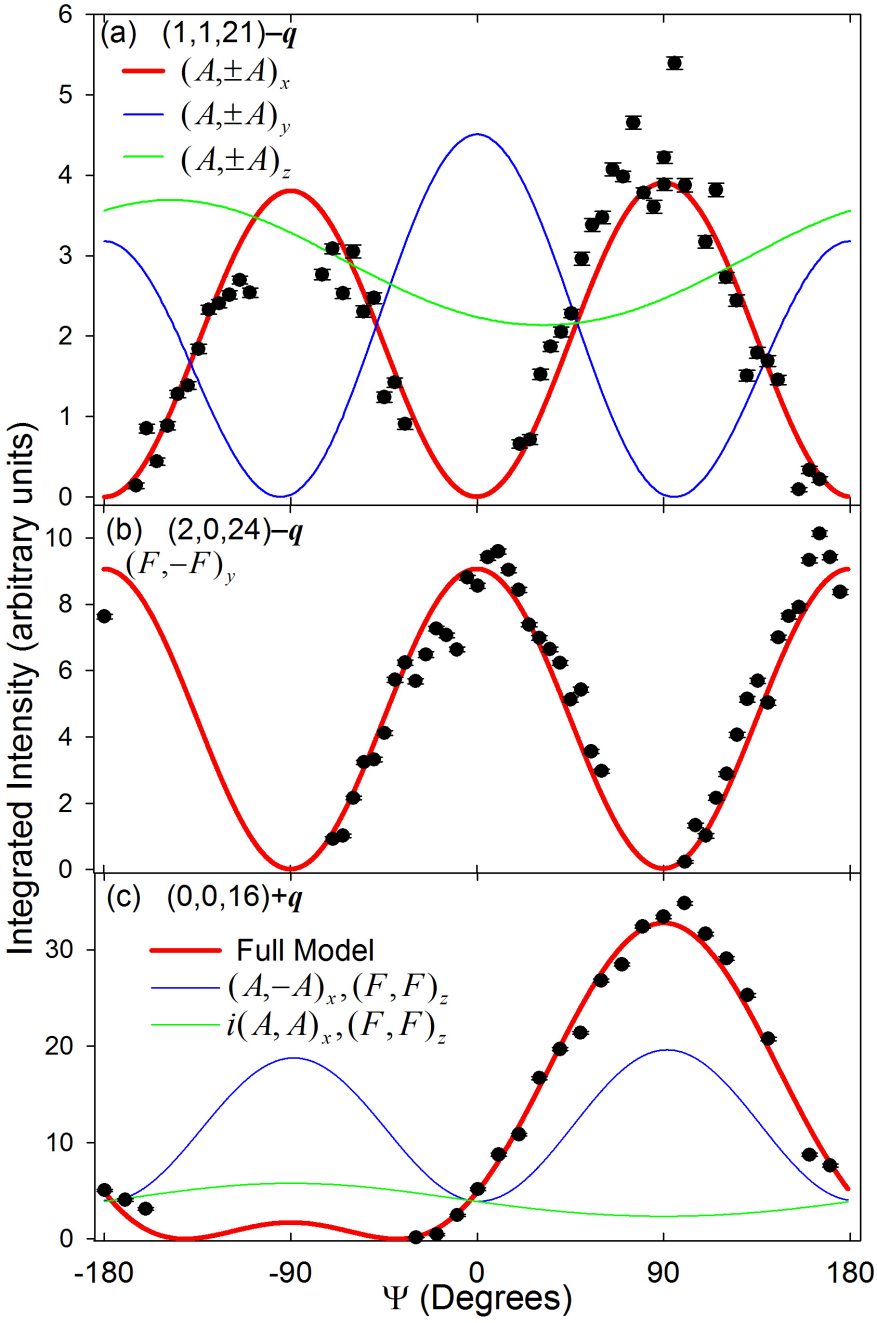


Figure 4.5: Integrated intensity as a function of azimuth for three magnetic Bragg peaks, (a) pure-A_x, (b) pure-F_y and (c) mixed-F_zA_x. Top diagram illustrates the scattering geometry. Data points (filled circles) are integrated peak intensities from rocking curve scans corrected for absorption and Lorentz factor. Thick (red) lines show fits that include all contributions to the RMXD structure factor [9, 14] from the magnetic structure model $i(A,-A)_x, -i(F,-F)_y, (F,F)_z$, depicted in Fig. 4.6. Blue/green curves in (a),(c) illustrate that other phase combinations of basis vectors are ruled out.

$$L(\theta)\mathcal{A}\left|(\hat{\boldsymbol{\epsilon}}' \times \hat{\boldsymbol{\epsilon}}) \cdot \boldsymbol{\mathcal{F}}(\boldsymbol{Q})\right|^2 \tag{4.7}$$

where $L(\theta)$ is the Lorentz factor at the scattering angle 2θ, $\mathcal{A}$ is an absorption correction dependent upon the experimental geometry, $\boldsymbol{\mathcal{F}}(\boldsymbol{Q})$ is the magnetic structure factor given in eq. (4.2), and $\hat{\boldsymbol{\epsilon}}'$ and $\hat{\boldsymbol{\epsilon}}$ are unit vectors along the polarization of the electric field component of the scattered and incident x-ray beams, respectively [14]. For a σ-polarized incident beam magnetic resonant scattering occurs only in the σ-π' channel (see diagram in Fig. 3.4(b)), meaning that the product of the electric field polarization vectors is along the scattered beam direction, i.e. $\hat{\boldsymbol{\epsilon}}' \times \hat{\boldsymbol{\epsilon}} = \hat{\boldsymbol{k}}'$.

The orientation of the magnetic moments can be experimentally determined by exploiting the polarization dependence of the scattering intensity as only the component of the structure factor vector along the scattered beam direction, $\mathcal{F}_{\parallel} = \boldsymbol{\mathcal{F}} \cdot \hat{\boldsymbol{k}}'$, contributes. By keeping the instrument in the scattering condition and rotating the sample around the scattering wavevector $\boldsymbol{Q} = \boldsymbol{k}' - \boldsymbol{k}$ the projection $\mathcal{F}_{\parallel}$ of the structure factor vector varies depending on the azimuth angle Ψ with maximum intensity when the moments that give rise to the scattering make the smallest angle with $\hat{\boldsymbol{k}}'$ and zero intensity when they are perpendicular.

The azimuth dependence for three magnetic peaks close to the sample surface normal were measured, such that the Ψ rotation is almost around (001). The origin, $\Psi = 0$, is defined as when the (010) direction is in the scattering plane and pointing away from the source. Fig. 4.5(a) shows the azimuth scan for a pure-A magnetic Bragg peak at (1,1,21)$-\boldsymbol{q}$. The intensity drops to zero at $\Psi = 0$ and 180° and has maxima at ±90°, uniquely identifying that scattering comes from magnetic moment components

along x (here x, y, z are along the orthorhombic a, b, c axes and scattering from y- and z-moment components, blue and green lines, respectively, have been calculated for comparison); hence identifying basis vector components in the combination $(A, \pm A)_x$, where the two sublattices are assumed to have equal magnitude moments.

Similarly, the azimuth of the pure-F peak (2,0,24)$-\boldsymbol{q}$ in Fig. 4.5(b) shows maxima at $\Psi = 0$ and 180°, thus determining the signal as originating from y-components. Following the discussion of the peaks in the h-scan of Fig 4.4(a), this intensity results from moments antiparallel on the two sublattices, identifying the basis vector $(F, -F)_y$.

Fig. 4.5(c) shows the azimuthal dependence for a mixed FA peak (0,0,16)$+\boldsymbol{q}$. From (4.3), it is seen that in fact only (F, F) and A contribute to this peak (i.e. no $(F, -F)$ contribution). The form of the azimuth uniquely identifies it as coming from basis vector components $\pi/2$ out-of-phase in the combination $i(A, -A)_x, (F, F)_z$. It should be noted that this combination of relative phases between the x and z components on all the iridium sites is unique, where other combinations can be qualitatively ruled out (see blue/green curves in the same figure). The observed phase combination describes counter-rotating moments between consecutive sites along c (curly arrows in Fig. 4.6), which form counter-rotating zig-zag chains along a.

The calculations to produce the red, green and blue lines in Fig. 4.5(c) were performed using the *Magnetix* [9] software, and show qualitatively different azimuth patterns for different phased combinations of x and z moments. One might wonder how such a measurement could provide such powerful results. For magnetic Bragg reflections where moments along two orthogonal directions contribute, such as the

$(0, 0, 16) + \boldsymbol{q}$ in Fig. 4.5(c) of mixed A_x, F_z character, the scattering intensity has a cross term that is sensitive to the complex phase between the structure factor vectors along the two directions, so it can distinguish between moments varying sinusoidally along a line in the xz plane (phase offset 0 or π) or rotating in the xz plane (phase offset $\pm\pi/2$). The explicit calculation is described in Appendix A, and the cross term is given for the $(0, 0, 16) + \boldsymbol{q}$ peak in Section A.3 of the same appendix.

To determine the relative magnitudes of the magnetic moment components a simultaneous fit was performed to the magnetic scattering intensities in the three azimuth scans in Fig. 4.5 with four free parameters: the magnitudes of the moment amplitudes M_x and M_y relative to M_z, an overall intensity scale factor for the $(1, 1, 21)-\boldsymbol{q}$ and $(2, 0, 24)-\boldsymbol{q}$ peaks and a separate intensity scale factor for the $(0, 0, 16)+\boldsymbol{q}$ peak (which was measured on the same sample, but in a different experiment). The fit is shown by red solid lines in Fig. 4.5(a-c), and gave values for the moment magnitude ratios $M_x : M_y : M_z = 0.65(4) : 0.58(1) : 1$. Note that this also quantitatively reproduces the observed ratio of the magnetic peak intensities in Fig. 4.4(a) (red line).

4.5 Magnetic Structure of γ-Li_2IrO_3

Symmetry operations of the full space group that map $\boldsymbol{q}$ into $-\boldsymbol{q}$ (in the present case a two-fold rotation axis along c at the iridium sites) impose further constraints onto the allowed values for the relative phases between basis vectors corresponding to the same irreducible representation. In particular, for the Γ_3 representation in Table 4.2, the only allowed basis vector combinations (obtained using the ISODISTORT

Site	Coordinates	v_x	v_y	v_z
1	$(0.25, 0.25, z)$	+	+	+
2	$(0.25, 0.75, 0.5 - z)$	−	+	+
3	$(0.25, 0.25, 1 - z)$	−	+	+
4	$(0.25, 0.75, 0.5 + z)$	+	+	+
$1'$	$(0.5, 0.5, z')$	−	−	+
$2'$	$(0.5, 0.5, 0.5 - z')$	+	−	+
$3'$	$(0.5, 0.5, 1 - z')$	+	−	+
$4'$	$(0.5, 0.5, 0.5 + z')$	−	−	+

Table 4.3: Fractional atomic coordinates of the iridium sites in the primitive cell and corresponding magnetic basis vector components in the determined magnetic structure.

[15] software) are $(\pm iA_x, \pm iC_y, F_z)$ for each of the two iridium sublattices separately. Moreover, the Fourier components on the two iridium sublattices are also constrained to be in-phase or anti-phase, i.e. the overall symmetry-allowed combination of basis vectors in the Γ_3 representation is $\pm i(A, \pm A)_x, \pm i(C, \pm C)_y, (F, \pm F)_z$, where all the $\pm$ signs are independent of one another. The above constraints on the relative phases between basis vectors along the different axes and between the two sublattices follow from the requirement that the magnetic structure should be invariant under the 2_z rotation applied at an iridium site where the magnetic moment is along the c-axis; this is only possible if the components along x and y are in-phase or anti-phase with one another, and $\pm\pi/2$ out of phase with respect to the z-components, and between the two sublattices the components are in-phase or anti-phase, no other relative phases are allowed.

This then constrains the value of α to be π or 0, giving the basis vector combination

for the magnetic groundstate as $i(A,-A)_x, i(-1)^m(F,-F)_y, (F,F)_z$, with $m = 1$ or 2. Both values of m give similar structures and in Fig. 4.6 the case $m = 1$ is plotted. The moments are confined to rotate in one of two planes, obtained from the (ac) plane by rotation around the c-axis by an angle $\pm\phi$, with $\phi = \tan^{-1}\frac{M_y}{M_x} = 42(2)^\circ$ (see Fig 4.6 (d) and (e)). The pattern is such that neighboring iridium zig-zag chains have alternate orientations of the spin rotation plane as indicated by the light and dark shaded envelopes in Fig. 4.6. The $m = 2$ case simply gives the opposite alternation of the rotation planes.

In terms of the irreducible representations presented in Table 4.2, the deduced groundstate configuration $i(A,-A)_x, i(-1)^m(F,-F)_y, (F,F)_z$ corresponds to a mixture of two irreducible representations Γ_3 (A_x and F_z) and $\Gamma_4(F_y)$. The magnetic moment at position $\boldsymbol{r}$ belonging to a site index $n = 1-4, 1'-4'$ can be written explicitly as

$$\boldsymbol{M}_n(\boldsymbol{r}) = [\hat{\boldsymbol{x}} M_x v_x(n) + (-1)^m \hat{\boldsymbol{y}} M_y v_y(n)] \sin \boldsymbol{q}\cdot\boldsymbol{r} + \hat{\boldsymbol{z}} M_z v_z(n) \cos \boldsymbol{q}\cdot\boldsymbol{r} \tag{4.8}$$

where $\hat{\boldsymbol{x}}$, $\hat{\boldsymbol{y}}$, $\hat{\boldsymbol{z}}$ are unit vectors along the orthorhombic $\boldsymbol{a}$, $\boldsymbol{b}$, $\boldsymbol{c}$ axes, respectively. $v_{x,y,z}$ are combined (8-site) basis vectors for the two sublattices expressed in shorthand vector notation as $v_x = (A,-A)$, $v_y = (F,-F)$, $v_z = (F,F)$ and with values listed explicitly for all sites in the primitive cell in Table 4.3. The Fourier components of the magnetic moments are

$$\boldsymbol{M}_{\boldsymbol{q},n} = i\left[\hat{\boldsymbol{x}}\frac{M_x}{2} v_x(n) + (-1)^m \hat{\boldsymbol{y}}\frac{M_y}{2} v_y(n)\right] + \hat{\boldsymbol{z}}\frac{M_z}{2} v_z(n) \tag{4.9}$$

and again, $\boldsymbol{M}_{-\boldsymbol{q},n} = \boldsymbol{M}^*_{\boldsymbol{q},n}$. Eqs. (4.8), (4.9) describe all iridium sites, including those related by the C-centering translation $(\frac{1}{2}\frac{1}{2}0)$, where $\boldsymbol{r}$ is the actual position of the ion and n is the site index at the equivalent position $(1-4, 1'-4')$ in the primitive unit cell.

4.6 Kitaev Physics in γ-Li_2IrO_3 Groundstate

The deduced magnetic structure of γ-Li_2IrO_3 is shown in Fig 4.6, and here the salient features will be discussed in some detail. The blue/cyan moments denote primed/unprimed Ir sites respectively, and if one tracks a given site (equivalent to sites at the same height on the c-axis) along the a-axis (Fig 4.6(a)) the rotation of moments goverened by the phase $\boldsymbol{q} \cdot \boldsymbol{r}$ can be seen. What is striking however is that the sense of rotation of this order alternates between neighbouring sites along the c-axis, this is illustrated by the curly arrows to the left of Fig 4.6(a), where the arrows denote the sense of rotation of the magnetic order as one moves along $\boldsymbol{a}$.

The second unit cell in Fig 4.6(a) includes the elliptical envelopes which confine the moments at given sites throughout the unit cell. The light/dark shading of these ellipses denote different planes of confinement for these moments, and this is made clearer in the ab-plane projections of Fig 4.6(b)-(e), where it is seen that alternate zig-zag chains have moments confined in different planes and vary by an angle $\pm\phi$ relative to the ac plane, where $\phi = \tan^{-1}\frac{M_y}{M_x} = 42(2)^\circ$, between consecutive chains. The magnetic groundstate is then characterised by a non-trivial pattern of counter-rotating, non-coplanar Ir moments.

In the third unit cell of Fig 4.6(a), the bonds between Iridium nearest neighbours

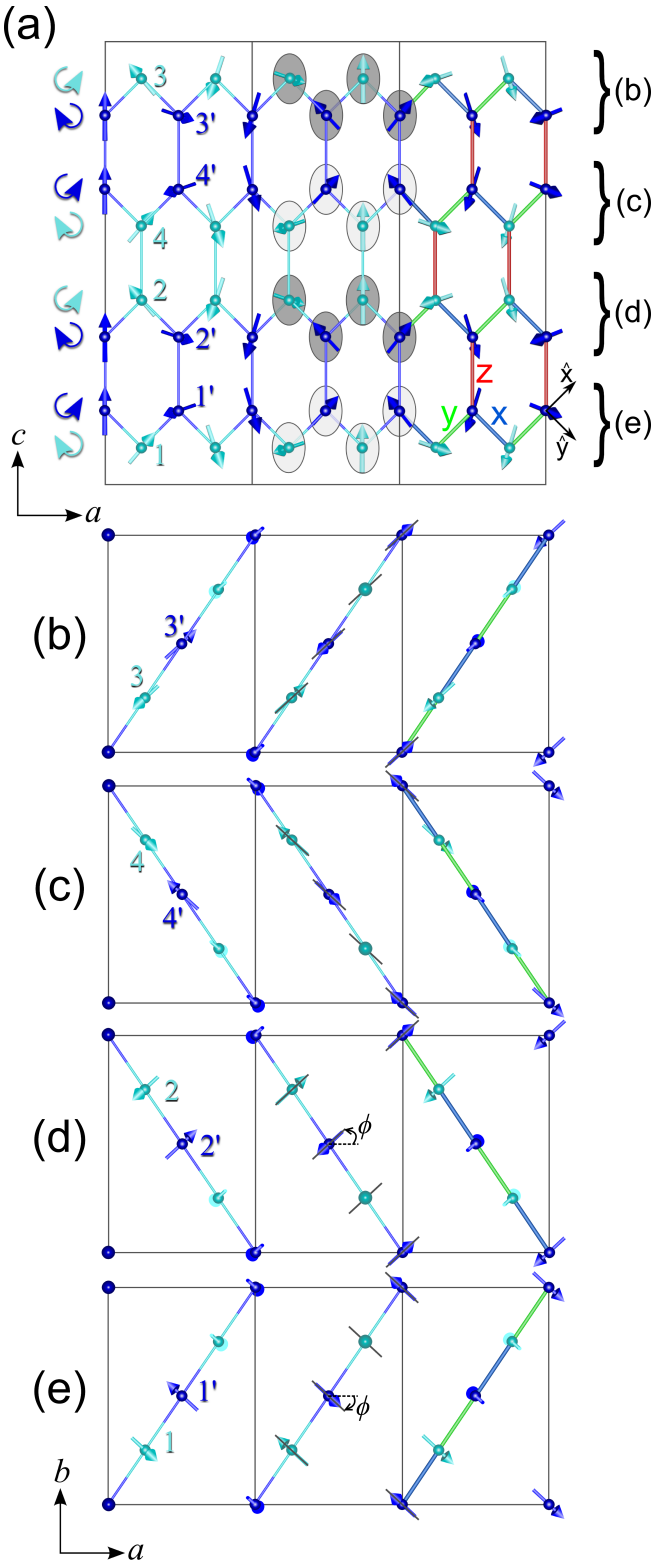


Figure 4.6: (a) Projection of the magnetic structure on the ac plane highlighting counter-rotation of moments between the different sites (1-4,1′-4′) of the primitive cell. Light/dark shading of the elliptical moment envelopes indicate an alternating tilt of the plane of moments' rotation away from the (ac) plane. In the rightmost unit cell the x, y and z Kitaev bonds are coloured blue, green and red respectively. Kitaev axes $\hat{\mathbf{x}}$ and $\hat{\mathbf{y}}$ are also shown. Right-hand labels (b)-(e) indicate where slices through the magnetic structure are taken at different heights in the unit cell and projected onto the (ab) plane to illustrate the direction of the zig-zag chains. Note the alternating tilt of the plane of rotation of the moments away from the ac plane by $\pm\phi$ between consecutive zig-zag chains stacked along c. Produced by Dr. R Johnson using the FPStudio software [5].

have been coloured to denote the nature of the anisotropic exchange between them, deduced from the orientation of the (in the case of ideal, undistorted IrO_6 octahedra) square Ir-O-Ir-O plaquets in which the bond lies (see Section 2.3). These $\mathsf{x}, \mathsf{y}, \mathsf{z}$ Kitaev axes can be related to the orthorhombic co-ordinate system via the transformation,

$$\hat{\mathbf{x}} = (\hat{\boldsymbol{a}} + \hat{\boldsymbol{c}})/\sqrt{2}, \quad \hat{\mathbf{y}} = (\hat{\boldsymbol{a}} - \hat{\boldsymbol{c}})/\sqrt{2}, \quad \text{and} \quad \hat{\mathbf{z}} = \hat{\boldsymbol{b}} \tag{4.10}$$

and axes $\hat{\mathbf{x}}$ and $\hat{\mathbf{y}}$ are shown in Fig 4.6(a).

A model with dominant Kitaev physics has been derived by our collaborators Kimchi *et al* ([2], sup. mat., [16]) to describe the observed groundstate, and this is reproduced here for completeness. In terms of spin components parallel to the unit cell's orthorhombic axes, (4.8) can be rewritten, such that the spin at site n is given by

$$\boldsymbol{S}_n(\boldsymbol{r}) = \pm \left[\nu_n \hat{\boldsymbol{a}} \langle S^a \rangle + (-1)^m \hat{\boldsymbol{b}} \langle S^b \rangle\right] \sin \boldsymbol{q}\cdot\boldsymbol{r} + \hat{\boldsymbol{c}} \langle S^c \rangle \cos \boldsymbol{q}\cdot\boldsymbol{r} \tag{4.11}$$

where, $\nu_n = \nu_{n'} = 1$ for $n = 1, 4$ and $\nu_n = \nu_{n'} = -1$ for $n = 2, 3$, and the $\pm$ differentiates between primed and unprimed sites respectively.

Correlations between Kitaev components of the spin can be computed by applying the transformations in (4.10) to (4.11). However, before performing this transformation explicitly, it is already apparent that spin components S^{z}=S^b are always ferromagnetically correlated over a z-type bond (linking sites of type $1'2'$, $3'4'$, 13 and 24, see Fig. 4.6(a)), because such bonds only link atoms from the same sublattice (therefore the $\pm$ sign in (4.11) multiplies to 1 when calculating correlations) and have the same phase factor $\boldsymbol{q} \cdot \boldsymbol{r}$.

The correlation between S^{x} and S^{y} components is less obvious from (4.11), however using (4.10), the correlations of components $S^{\mathsf{x}}/S^{\mathsf{y}}$ over x/y type bonds can be calculated as;

$$\langle S^{\mathsf{x}}_n S^{\mathsf{x}}_{n'} \rangle_{\mathsf{x}} = \langle S^{\mathsf{y}}_n S^{\mathsf{y}}_{n'} \rangle_{\mathsf{y}} = \langle S^a \rangle \langle S^c \rangle \frac{1}{2} \sin \frac{\pi q}{2} \tag{4.12}$$

where, the correlation between primed and unprimed sites is appropriate as it is seen from Fig 4.6(a) that x,y bonds always couple sublattices (blue linked with cyan).

It is seen in Fig 4.6(a) that along each x-type bond the spins are aligned when they point along x, and anti-aligned when they point along y, and similarly for y-type bonds. Thus, the Kitaev interactions can stabilize the counter-rotating moments with a propagation vector $\boldsymbol{q}$ along the orthorhombic $\boldsymbol{a}$ direction, as observed, as components of the moments preferentially align ferromagnetically along their corresponding Kitaev bonds.

The full Hamiltonian proposed is [16]:

$$\mathcal{H} = \sum_{c-\text{bonds}} \left[K_c S_i^{\eta_{ij}} S_j^{\eta_{ij}} + J_c \boldsymbol{S}_i \cdot \boldsymbol{S}_j + I_c^c S_i^c S_j^c \right] + \sum_{d-\text{bonds}} \left[K_d S_i^{\eta_{ij}} S_j^{\eta_{ij}} + J_d \boldsymbol{S}_i \cdot \boldsymbol{S}_j \right] + \sum_{2^{\text{nd}}\ \langle\langle ij \rangle\rangle} J_2 \boldsymbol{S}_i \cdot \boldsymbol{S}_j \tag{4.13}$$

where interactions along the vertical (along c) bonds are denoted by the subscript c and interactions along the zig-zag (diagonal) bonds are denoted by the subscript d. K_c and K_d are the Kitaev interactions along c-bonds (of type $\eta_{ij} = \mathsf{z}$) and d-bonds (of type $\eta_{ij} = \mathsf{x}$ or y), respectively. An Ising coupling I_c^c of the S^c spin components, and a Heisenberg coupling J_2 between second nearest neighbors is also included.

Analysis of this Hamiltonian in Fourier space gives a lowest-energy mode with the observed counter-rotating structure, and mixture of a further mode, with the next lowest energy available for this same wavevector, reproduces the non-coplanar pattern of moments, where the angle ϕ is tuneable by parameters in (4.13). Importantly, it is found that the non-coplanar tilt angle observed in γ-Li_2IrO_3 requires relatively large Kitaev exchanges within this minimal model. The values used to produce the magnetic structure observed in experiment are shown in Table 4.4.

K_c	-15
J_c	5
I_c^c	-4.5
K_d	-12
J_d	2.5
J_2	-0.9

Table 4.4: Parameters, in meV, for Hamiltonian (4.13) (from [2]).

4.7 Conclusions

To summarize, the structure of a new polytype of Li_2IrO_3 was discovered using x-ray diffraction. This structure, γ-Li_2IrO_3, contains a 'stripyhoneycomb' pattern of Ir ions not reported before in other $3d$ or $5d$ oxides. Following this, without prior experimental information (e.g. from neutron scattering at low temperatures), the incommensurate magnetic ordering vector in γ-Li_2IrO_3 was ascertained as $\boldsymbol{q} = (0.57(1), 0, 0)$ through RMXD measurements on a single crystal sample. Furthermore, RMXD experiments allowed – through the detection and absence of peaks at special positions in reciprocal space and measuring the azimuthal dependence of a subset

of these magnetic peaks – the unambiguous determination of the complete magnetic structure in γ-Li_2IrO_3. The resulting structure is incommensurate and non-coplanar with a pattern of counter-rotating moments which cannot be stabilized by isotropic Heisienberg interactions alone. A Kitaev-Heisenberg Hamiltonian however can fully explain the observed complex magnetic structure, providing strong evidence that γ-Li_2IrO_3 is an experimental realization of 3D Kitaev physics in the solid state.

References

[1] K. A. Modic, T. E. Smidt, I. Kimchi, N. P. Breznay, A. Biffin, S. Choi, R. D. Johnson, R. Coldea, P. Watkins-Curry, G. T. McCandless, J. Y. Chan, F. Gandara, Z. Islam, A. Vishwanath, A. Shekhter, R. D. McDonald, and J. G. Analytis, Nature communications **5**, 4203 (2014).

[2] A. Biffin, R. D. Johnson, I. Kimchi, R. Morris, A. Bombardi, J. G. Analytis, A. Vishwanath, and R. Coldea, arXiv:1407.3954v1 (2014).

[3] Y. Singh and P. Gegenwart, Physical Review B **82**, 064412 (2010).

[4] M. J. O'Malley, H. Verweij, and P. M. Woodward, Journal of Solid State Chemistry **181**, 1803 (2008).

[5] J. Rodríguez-Carvajal, Physica B: Condensed Matter **192**, 55 (1993).

[6] P. Muller, *Crystal structure refinement : a crystollographers guide : SHELXL* (Oxford ; New York : International Union of Crystallograpny : Oxford University Press, 2006), Formerly CIP.

[7] L. J. Farrugia, Journal of Applied Crystallography **45**, 849 (2012).

[8] A. Altomare, G. Cascarano, C. Giacovazzo, A. Guagliardi, M. C. Burla, G. Polidori, and M. Camalli, Journal of Applied Crystallography **27**, 435 (1994).

[9] L. Chapon, http://forge.ill.eu/svn/magnetix.

[10] B. Kim, H. Ohsumi, T. Komesu, and S. Sakai, Science **323**, 1329 (2009).

[11] S. Boseggia, R. Springell, H. Walker, H. Rø nnow, C. Rüegg, H. Okabe, M. Isobe, R. Perry, S. Collins, and D. McMorrow, Physical Review Letters **110**, 117207 (2013).

[12] X. Liu, T. Berlijn, W.-G. Yin, W. Ku, a. Tsvelik, Y.-J. Kim, H. Gretarsson, Y. Singh, P. Gegenwart, and J. P. Hill, Physical Review B **83**, 220403 (2011).

[13] J. Rodríguez-Carvajal, Physica B: Condensed Matter **192**, 55 (1993), Part of the *FullProf* software suite.

[14] J. P. Hill and D. F. McMorrow, Acta Crystallographica Section A Foundations of Crystallography **52**, 236 (1996).

[15] B. J. Campbell, H. T. Stokes, D. E. Tanner, and D. M. Hatch, Journal of Applied Crystallography **39**, 607 (2006).

[16] I. Kimchi, J. Analytis, and A. Vishwanath, arXiv:1309.1171v2 (2013).

Chapter 5

Unconventional Magnetic Order on the Hyperhoneycomb Kitaev Lattice in β-Li_2IrO_3: Full Solution via Resonant Magnetic X-ray Diffraction

The recently-synthesized iridate β-Li_2IrO_3 has been proposed as a candidate to display novel magnetic behavior stabilized by frustration effects from bond-dependent, anisotropic interactions (Kitaev model) on a three-dimensional "hyperhoneycomb" lattice. This chapter describes a resonant x-ray diffraction experiment on a single crystal of β-Li_2IrO_3 where, unlike for the case of γ-Li_2IrO_3, the results of previous neutron scattering on a powder sample are available and guide the search in reciprocal space for magnetic Bragg peaks, and eventually full determination of the magnetic structure. A complex, incommensurate magnetic order with non-coplanar and counter-rotating Ir moments is found, which surprisingly shares many of its features with the related structural polytype "stripyhoneycomb" γ-Li_2IrO_3 of the previous chapter, where dominant Kitaev interactions have been invoked to explain the stability of the observed magnetic structure.

5.1 Structure of β-Li_2IrO_3

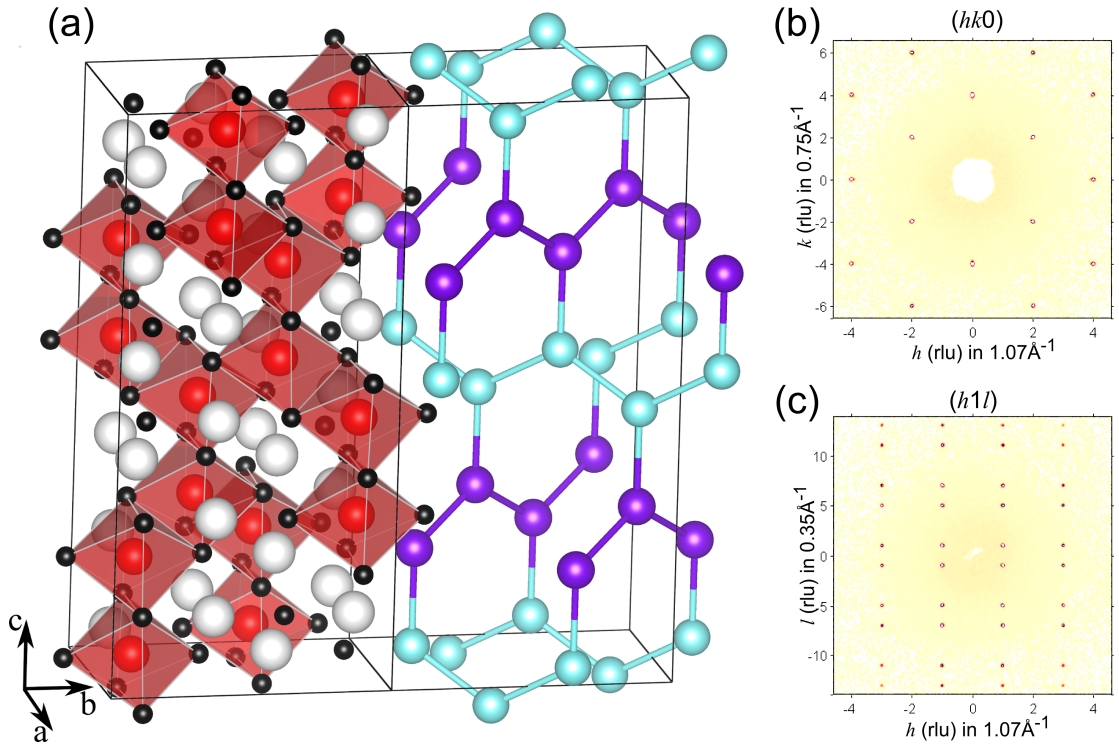


Figure 5.1: Crystal structure of β-Li_2IrO_3 and x-ray diffraction data. (a) Two unit cells are shown: (left) full structure with Li (white balls), O (black) and Ir (red) located inside IrO_6 octahedra (shaded polyhedra), (right) 3D iridium lattice connectivity. Light (cyan) and dark (purple) colours indicate zig-zag chains stacked along c and directed alternatingly along $\boldsymbol{a} \pm \boldsymbol{b}$. X-ray diffraction data from a single crystal of β-Li_2IrO_3 is shown for the (b) $(hk0)$ and (c) $(h1l)$ planes, respectively.

The structure of β-Li_2IrO_3 is shown in Fig 5.1(a) [1], on the left an orthorhombic unit cell with all atoms is shown, and it is clearly seen that the structure is built up of edge-sharing IrO_6 octahedra. The connectivity of the Ir ions (of which there are 16 in each cell) within the unit is illustrated in the right unit cell of Fig 5.1(a). Each Ir ion has the three-fold connectivity of a honeycomb lattice, however the honeycomb rows (and hexagonal plaquets) associated with such a lattice are absent; it is a 'hyperhoneycomb' lattice, with three-dimensional connectivity and no closed Ir hexagons. This is in contrast to the γ-Li_2IrO_3 structure of Fig 4.2, with its honeycomb stripes which

alternate along the $\mathbf{a}+\mathbf{b}$ and $\mathbf{a}-\mathbf{b}$ directions, and the relation to the honeycomb is clear.

However, following the discussion of Section 2.3.3, it is seen that the family of iridates Li_2IrO_3 can be thought of as built from zig-zag chains of Ir ions, and the β-Li_2IrO_3 lattice corresponds to the case where these zig-zag chains alternate in orientation – parallel to the $\mathbf{a}+\mathbf{b}$ and $\mathbf{a}-\mathbf{b}$ directions sequentially – upon moving up the c-axis. In Fig 5.1(a) this is illustrated by having cyan and purple sites denote chains along the $\mathbf{a}+\mathbf{b}$ and $\mathbf{a}-\mathbf{b}$ directions respectively.

The structural polytype β-Li_2IrO_3 was first synthesized by Takayama *et. al.* [1]. Susceptibility measurements on a powder sample showed a typical Curie-Weiss behaviour upon lowering temperature ($\theta_{\mathrm{CW}} = 40$ K), until an anomaly at $T_{\mathrm{N}} \approx 38$ K, after which the susceptibility is broadly constant. This ordering temperature was further confirmed by a corresponding anomaly in the specific heat data, which showed a sharp peak at 38 K before decreasing linearly as the temperature was reduced [1].

Once again, x-ray diffraction is the ideal tool for such structural determination (Section 3.2.1). A small single crystal (largest dimension less than 17μm) extracted from a powder batch of β-Li_2IrO_3 synthesized by Prof P. Gegenwart *et al* as described in [1] was measured at 100K (where such temperatures were achieved by positioning the sample in a jet of N_2). A complete x-ray diffraction data set was collected using a Mo source SuperNova diffractometer, and representative diffraction patterns in the $(hk0)$ and $(h1l)$ planes are shown in Fig. 5.1 (b) and (c). The observed empirical selection rules for diffraction peaks confirm the $Fddd$ space group. Moreover comparison with Fig 4.1 shows that these peaks are not the result of scattering from a

$Cccm$ structure, as in the $(hk0)$ plane for example all peaks h, k odd are missing.

Moreover, the diffuse scattering along the l-axis seems to be absent from this data set. If such scattering is the result of the stacking faults described in the context of Fig 2.3(d), then perhaps the absence (or at least reduction) of such an effect here is understandable as it is a simpler structure than the γ-Li_2IrO_3 polytype.

The result of the structural refinement of absorption-corrected data is given in Table. 5.1. The same convention for the origin of the unit cell as in [1] has been used. As in Table 4.1, atomic displacement parameters are assumed isotropic. The reliability factors of the Rietveld refinement were $R_{F2} = 4.50\%$, $wR_{F2} = 5.24\%$, $R_F = 2.42\%$ and $\chi^2 = 0.318$. The atomic positions listed are consistent with those previously reported for β-Li_2IrO_3 at room temperature [1].

5.2 Neutron Powder Diffraction

Neutron powder diffraction measurements to obtain information about the magnetic propagation vector were performed by Dr S. Choi [2] using the high-resolution time-of-flight diffractometer WISH at ISIS, and the results of this experiment are reproduced here for clarity. There, 0.71g of powder β-Li_2IrO_3 was placed in an aluminium can of annular geometry (to minimize the strong neutron absorption by the Ir nuclei) and was mounted on the cold finger of a closed cycle refrigerator. Diffraction patterns were collected at a range of temperatures from base (5.6 K) to paramagnetic (70 K), the latter being well above the magnetic ordering transition $T_N \approx 38$ K inferred from thermodynamic measurements [1]. It was found that even after a counting time of 7 hours per temperature the neutron diffraction data was not sufficiently

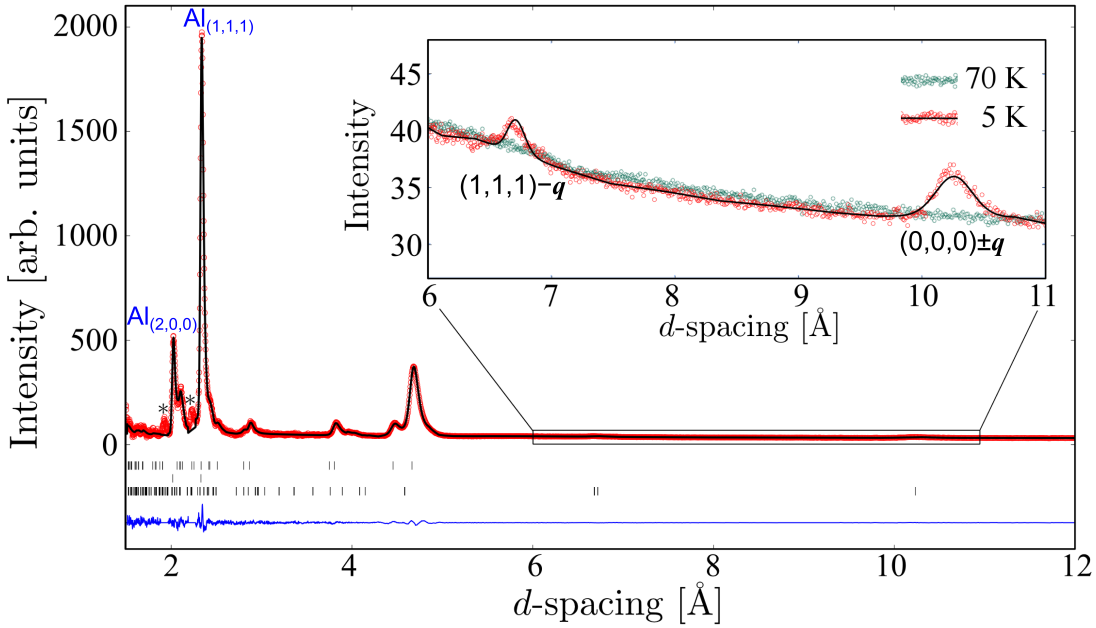


Figure 5.2: Neutron powder diffraction at base temperature 5.6 K, and in the paramagnetic regime, 70 K, in the lowest-angle detector bank, data (red and grey circles, respectively) and fit (black line). Positions of structural β-Li_2IrO_3 peaks, aluminium peaks and magnetic Bragg peaks are marked below the pattern in the upper, middle and lower rows, respectively and the blue line underneath represents the difference between data and fit. Labels "Al" indicate aluminium peaks and (*) denote two impurity peaks removed from the fit. Inset: zoom into the large d-spacing region showing two magnetic Bragg peaks, labels indicate the magnetic peaks index (symmetrically equivalent indexes are omitted).

Cell parameters

Space group: $Fddd$ (#70, origin choice 2)

Z = 16

a, b, c (Å):	5.8903(2)	8.4261(3)	17.7924(7)
α, β, γ:	90°	90°	90°

Volume: 883.08(6)

Atomic fractional coordinates and isotropic A.D.P.'s

Atom	x	y	z	U_{iso}(Å^2)
Ir	0.125	0.125	0.70845(7)	0.0025(3)
Li1	0.125	0.125	0.04167	0.00633
Li2	0.125	0.125	0.875	0.00633
O1	0.855(7)	0.125	0.125	0.002(5)
O2	0.621(8)	0.3669(19)	0.0384(7)	0.002(3)

Data collection

measured reflections: 3770

Data reduction R_{int}: 6.99%

(Criterion for observed reflections: $I > 2.0\sigma(I)$)

observed independent reflections: 298

fitted parameters: 9

Table 5.1: β-Li_2IrO_3 structural parameters at 100 K

accurate to be able to perform a full structural refinement (most likely due to neutron absorption effects), so the x-ray data described in the previous section performed on a small single crystal from the same batch was used to determine precise internal atomic positions in the unit cell, and the temperature of 100 K was considered to be cold enough to be representative of the crystal structure in the low-temperature

limit.

Fig. 5.2 shows the neutron powder diffraction pattern in the lowest angle bank of detectors. In the main panel the visible diffraction peaks are of structural origin, β-Li_2IrO_3 peak positions are denoted by the upper row of vertical marks and the two large peaks in the data at d-spacing near 2 Å (labelled "Al") are the lowest-order diffraction peaks from the Al can and were fitted as such. The pattern also showed two peaks labelled (*), attributed to an unidentified impurity phase, and those regions in the data were excluded from the analysis. A structural fit was performed (using FullProf [3]) on the neutron data (both paramagnetic and base temperature) with the internal atomic positions kept fixed, and only the lattice parameters fitted. The structural fit was consistent over all detector banks – corresponding to a range of scattering angles and resolutions – and it was also possible to consistently fit the instrument parameters (which provide the conversion from time-of-flight to d-spacing) over all the detector banks tested. Fig. 5.2 (solid line) illustrates the very good agreement in describing the structural diffraction pattern.

The inset in Fig. 5.2 highlights the region of large d-spacing, where upon cooling below T_N two new Bragg peaks appear, attributed to the onset of magnetic ordering. The peak widths are comparable to those of structural Bragg peaks, implying long-range magnetic order. With only two magnetic peaks the magnetic structure of β-Li_2IrO_3 cannot be solved uniquely (typically at least 5 or 6 magnetic peaks are required), however the data provides strong constraints on the magnetic propagation vector, $\boldsymbol{q}$. Typically $\boldsymbol{q}$ will lie on a point, line or plane of high symmetry in the Brillouin zone. Using the *isotropy* tool in FullProf [3] all such positions for the $Fddd$

space group were generated in order of decreasing symmetry and were tested to see whether such propagation vectors could reproduce the magnetic peak positions observed in the neutron data. All commensurate orderings with wavevectors at the Γ, Z, Y, T and L points (where the Miller-Love convention for labelling high-symmetry Brillouin zone points has been used [4]) were ruled out by this analysis. Such a result in itself is significant, as previously only commensurate magnetic structures had been considered on the hyperhoneycomb [5]. Therefore propagation vectors along lines of high symmetry were considered with general points denoted by Σ, Δ, Λ. Only the first two were compatible with the neutron data and the obtained solutions are listed in Table 5.2, along with possible solutions for other high symmetry directions. The ellipses denotes the fact that multiple solutions exist for a general propagation vector in the *ab*-plane. Although with only two magnetic Bragg peaks the neutron data cannot uniquely determine the propagation vector, it provides very important constraints to focus the search for magnetic Bragg peaks in single crystal samples.

Position	$\boldsymbol{q}_{\text{fit}}$
Σ	(0.57,0,0)
Δ	(0,0.81,0)
J	(0.27,0,$^1/_2$)
E	(0,0.39,$^1/_2$)
M	(0.43,0.53,0)
	$\vdots$

Table 5.2: Candidate propagation vectors along high symmetry directions in the Brillouin zone compatible with the magnetic peak positions observed in the neutron powder diffraction pattern.

5.3 Resonant Magnetic X-ray Diffraction on β-Li_2IrO_3

To determine which of the candidate magnetic propagation wavectors identified by the neutron data actually occurs, resonant magnetic x-ray diffraction (RMXD) was performed at the I16 beamline at Diamond in reflection geometry. The same single crystal of β-Li_2IrO_3 as used for the structural refinement was used, with an orthorhombic morphology and its maximum dimension less than 17μm. The sample was placed on a Si (1,1,1) disk with the reciprocal lattice vector (-6,5,7) being surface normal and it was cooled using a CCR with Be domes. The x-ray energy was tuned to the L_3 edge of Iridium (11.215 keV) and on cooling below T_N new Bragg peaks appeared at satellite positions of reciprocal lattice points at $(h,k,l) \pm \boldsymbol{q}$, with h,k,l integers and an incommensurate ordering wavevector $\boldsymbol{q} = (0.57(1), 0, 0)$, where the error in $\boldsymbol{q}$ is a combination of errors in the UB matrix and the intrinsic sphere of uncertainty of I16. The former of these contributions was reduced by centring on a nearby Bragg peak before scanning a satellite magnetic peak.

Scans through such a peak are shown in Fig. 5.3(a-c). The scans emphasize the incommensurate position along h and centering at integer k and l values. In the language of Table 5.2 this is then a propagation vector along the Σ line of symmetry, and the magnitude found from the x-ray data is consistent with the positions of peaks in the neutron data (first line in Table 5.2). Lorentzian squared fits to the peak shape profiles (dashed lines in Fig. 5.3 (a-c),(e)) gave widths comparable to those measured for the nearby structural Bragg peak (-6,6,12), indicating that the magnetic order is long-range in all three directions. The inverse of the observed peak half-widths gives a lower bound on the correlation length estimated as 100, 200 and 300 Å along the

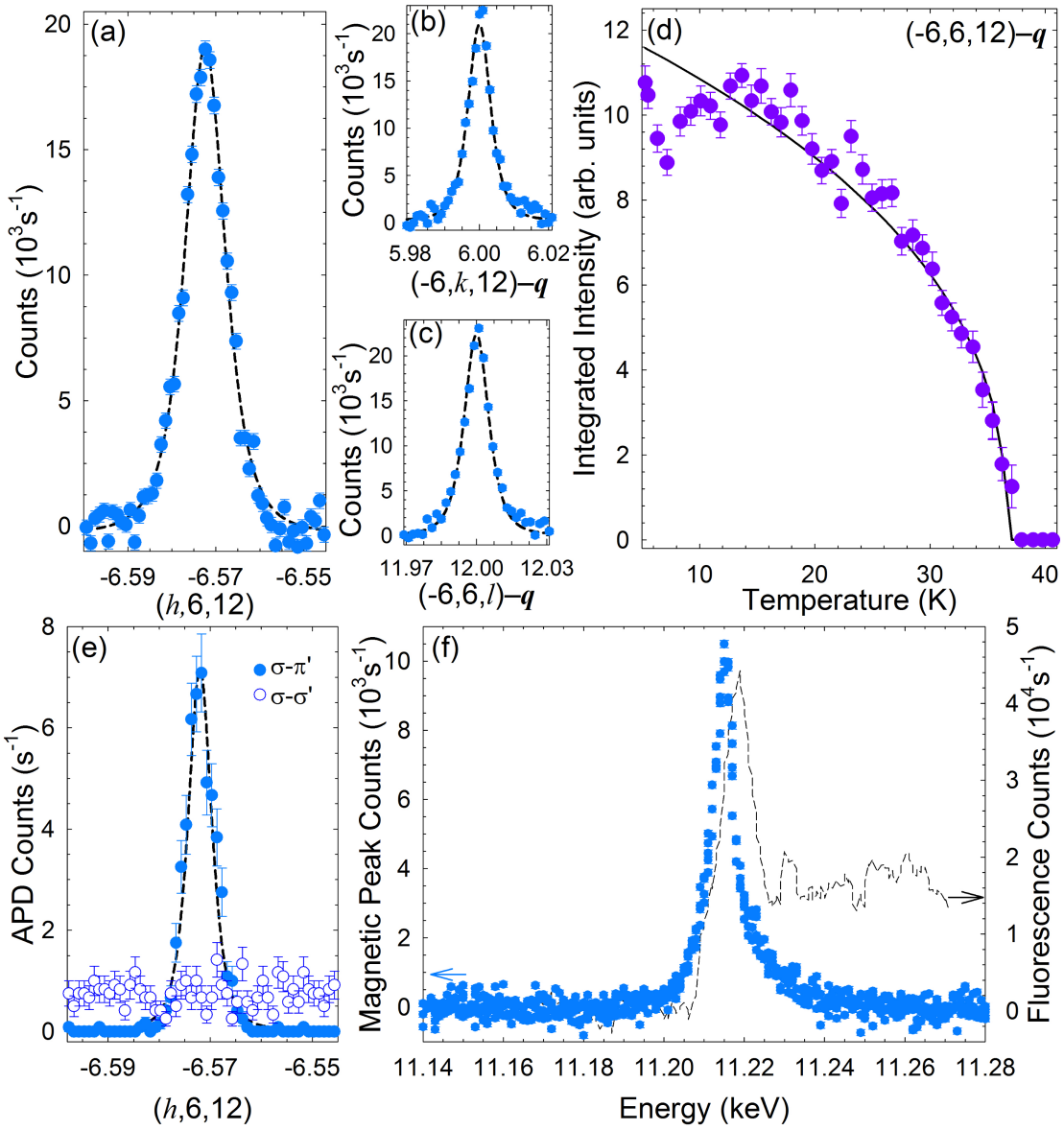


Figure 5.3: Magnetic Bragg peak at (-6,6,12)$-\boldsymbol{q}$; (a) Scan shows that the peak occurs at an incommensurate position along h, and is well-centered at integer (b) k, and (c) l. (d) Order parameter of the integrated magnetic peak intensity (solid line is a power-law fit to determine T_N). (e) The peak is only present in the σ-π' polarization channel (light blue, filled) as expected for magnetic scattering. (f) Energy scan (filled points) shows that the peak appears only at resonance, on the edge of the fluorescence signal onset (thin dashed line). Thick dashed lines in (a)-(c),(e) are fits to a Lorentzian-squared function.

a, b and c axes, respectively (more than ≈20 unit cells in each direction). Those are comparable to values obtained from analyzing scans through a nearby structural Bragg peak (-6,6,12), indicating no anomalous broadening of the magnetic peaks compared to structural peaks, i.e. the magnetic order is well-developed and as long-range as the structural order.

Several independent tests can be performed to confirm the magnetic origin of the observed diffraction peaks. Firstly, in Fig. 5.3(d) the integrated intensity of (-6,6,12)-$\boldsymbol{q}$ as a function of temperature (filled circles) shows a typical order-parameter behavior where a power-law fit (solid line) gives an onset temperature of $T_{\rm N} = 36.7$ K, which is very close to the value of the critical temperature deduced from specific heat measurements [1]. The small offset of $\Delta T \simeq 1.3$ K is most likely due to the fact that the temperature readout at the base of the sample mounting support in the x-ray experiments did not take into account the extra heating at the sample due to the intense synchrotron x-ray beam, as a result of which the actual sample temperature was slightly higher than that of the support. The magnitude of the small temperature offset deduced is very reasonable, and it is likely that the rather small crystal size in fact minimized this offset by enhancing the heat dissipation compared for example to the experiments conducted on γ-Li_2IrO_3 presented in Section 4.2 performed on a sample of larger volume.

Further evidence of the magnetic origin of the incommensurate diffraction peaks can be obtained via polarization analysis of the scattered beam. For a scattering experiment with incident beam polarization $\hat{\boldsymbol{\epsilon}}$ normal to the $(\boldsymbol{k}, \boldsymbol{k'})$ scattering plane (σ-polarized), magnetic scattering is expected to rotate the polarization by 90° com-

pared to the incident beam direction (scattering in the σ-π' channel, see Fig 3.4(b) and Fig 3.5(a)), whereas conventional (charge) scattering would leave the polarization direction unchanged (scattering in the σ-σ' channel), as explained in Section 3.2.2. In these experiments, polarization analysis was achieved via the 3rd order reflection from the (1,1,1) planes of an Au crystal, the d-spacing of 0.785 Å being ideally suited for polarization analysis at the L_3 edge of Ir (giving perfect filtering at 11.16 keV, see Ref. [6]). Fig. 5.3(e) shows an h-scan across the incommensurate peak performed with polarizer parallel (open symbols, σ-σ') and perpendicular (filled symbols, σ-π') to the original incident beam polarization. The signal appears only in the rotated polarization channel, as expected for magnetic scattering. Note that the higher background in the σ-σ' is due to the large incoherent x-rays scattering, which is largely filtered out by the polarization analysis in the σ-π' channel revealing a pure magnetic signal.

A third test is the dependence on the x-ray energy, as the magnetic scattering is expected to experience a substantial increase in intensity at resonance. Indeed, the incommensurate peak intensity has a characteristic resonant response as shown in Fig 5.3(f) (filled blue symbols) with a maximum at the resonance energy of 11.215 keV in agreement with previous resonant studies on other iridates [7, 8], and coincides with the edge of the fluorescence signal from the sample (black, dotted line).

5.4 Structure Factor Analysis

The observation of incommensurate magnetic Bragg peaks indicates a magnetic structure with rotating moments, or an amplitude modulated structure (e.g. spin-

density wave) which is incommensurate to the underlying crystal lattice periodicity. In order to distinguish between these two scenarios and to determine fully the orientations of the magnetic moments at all magnetic sites in the unit cell, the symmetry-allowed basis vectors for magnetic structures compatible with the observed propagation vector $\boldsymbol{q}$ are considered, as this provides a natural framework to directly link diffraction data with a magnetic structure model and allows one to develop a systematic strategy in experiments to determine the magnetic structure completely.

From Table 5.1 it is seen that the magnetic ions, Ir^{4+}, occupy a single crystallographic site with generating position $(1/8, 1/8, z)$ with $z = 0.70845(7) \simeq 5/8+1/12$. There are four unique sites in the primitive unit cell, they are labelled 1-4 in Fig. 5.6 and their positions are listed explicitly in Table. 5.3. The total 16 sites in the unit cell are generated by the F-centering translations; + $(\frac{1}{2}\frac{1}{2}0)$, + $(\frac{1}{2}0\frac{1}{2})$ and + $(0\frac{1}{2}\frac{1}{2})$.

Site	Coordinates	v_x	v_y	v_z
1	$(0.125, 0.125, z)$	+	+	+
2	$(0.125, 0.625, 3/4 - z)$	−	+	+
3	$(0.375, 0.375, 1 - z)$	−	−	+
4	$(0.375, 0.875, 1/4 + z)$	+	−	+

Table 5.3: Fractional atomic coordinates of the iridium sites in the primitive cell and corresponding magnetic basis vector components in the determined magnetic structure, $z = 0.70845(7) \simeq 5/8+1/12$.

Taking into account that at each site the magnetic moment could have components along the x, y and z-axes (along the orthorhombic a, b, c-axes), gives a 12-component representation of the magnetic structure. Its irreducible representations and associated magnetic basis vectors (obtained using the *BasIrreps* tool part of the FullProf

suite [3]) are listed in Table 5.4.

Irreducible Representation	Basis Vectors
Γ_1	F_x, G_y, A_z
Γ_2	C_x, A_y, G_z
Γ_3	G_x, F_y, C_z
Γ_4	A_x, C_y, F_z

Table 5.4: Irreducible representations and basis vectors for a magnetic structure with propagation vector $\boldsymbol{q} = (q, 0, 0)$.

As was the case in Section 4.3, all magnetic satellite peaks can be indexed by a single propogation vector, and as such the magnetic moments, $\mathbf{M}_n(\mathbf{r})$ can be expanded in terms of its Fourier components as given in (4.1). The basis vectors contain symmetry-imposed relations between these Fourier components of the magnetic structure between the four sites in the primitive cell, and the types of basis vectors that can occur are listed in (5.1) below

$$F = \begin{bmatrix} 1 \\ 1 \\ \delta \\ \delta \end{bmatrix}, \quad C = \begin{bmatrix} 1 \\ 1 \\ -\delta \\ -\delta \end{bmatrix}, \quad A = \begin{bmatrix} 1 \\ -1 \\ -\delta \\ \delta \end{bmatrix}, \quad G = \begin{bmatrix} 1 \\ -1 \\ \delta \\ -\delta \end{bmatrix}, \tag{5.1}$$

where for each vector the four values are relative phase factors between the Fourier components at the four sites. $\delta = e^{-i\boldsymbol{q}\cdot(\boldsymbol{r}_3 - \boldsymbol{r}_1)} = e^{-i\pi q/2}$ is a displacement phase factor which takes into account that sites 3 and 4 are displaced relative to sites 1 and 2 by $a/4$ in the direction of the propagation vector $\boldsymbol{q}$. In an F basis vector the Fourier components at the 4 sites are related by $\boldsymbol{M}_{\boldsymbol{q},1} = \boldsymbol{M}_{\boldsymbol{q},2} = \delta^{-1}\boldsymbol{M}_{\boldsymbol{q},3} = \delta^{-1}\boldsymbol{M}_{\boldsymbol{q},4}$, i.e. there are no additional phase factors between the four sites apart from the natural

displacement phase factor, and in the limit $q \to 0$ one recovers ferromagnetic order. For the basis vectors C, A and G two out of the four sites have a change in sign in addition to the normal displacement phase offset, and in the limit $q \to 0$ one finds an antiferromagnetic alignment between the 4 sites. In the following the strategy adopted in determining the magnetic structure is to first identify which types of magnetic basis vectors exist, determine their polarization (i.e. along x, y or z) and then find the relative phase between then.

For each magnetic basis vector, the magnetic moments at the various sites in the primitive cell are inter-related, therefore there are associated selection rules for magnetic scattering, i.e. each basis vector will only contribute to magnetic satellite reflections of certain reciprocal lattice points (h, k, l) and will have zero structure factor for others. Therefore simply the presence or absence of magnetic Bragg peaks at certain positions can already identify which basis vectors are present.

Explicitly, the structure factor for a magnetic superlattice reflection at $\boldsymbol{Q} = (h, k, l) \pm \boldsymbol{q}$ is

$$\boldsymbol{\mathcal{F}}(\boldsymbol{Q}) = \boldsymbol{\mathcal{F}}((h, k, l) \pm \boldsymbol{q}) = \sum_j \boldsymbol{M}_{\pm \boldsymbol{q}, j} e^{i\boldsymbol{Q}\cdot\boldsymbol{r}_j} \tag{5.2}$$

where the sum extends over all 16 sites in the orthorhombic unit cell (sites $1-4$ and their F-centering translations by $(1/2, 1/2, 0)$, $(0, 1/2, 1/2)$ and $(1/2, 0, 1/2)$). $\boldsymbol{M}_{\pm \boldsymbol{q}, j}$ are the Fourier components of the magnetic moments at site j with position in the unit cell $\boldsymbol{r}_j$ (sites related by F-centering translations have the same Fourier components).

The structure factors for the different basis vectors can be explicitly calculated as

$$\boldsymbol{\mathcal{F}}_F(\boldsymbol{Q}) = \begin{cases} 16\boldsymbol{M}_{\pm \boldsymbol{q}, 1} \cos\frac{\pi l}{6} e^{i\xi_\pm}, & h + k + l = 4n \ (h, k, l \text{ even}) \\ 16\boldsymbol{M}_{\pm \boldsymbol{q}, 1} \cos\frac{\pi l}{6} \cos\frac{\pi(h+l-k)}{4} e^{i\chi_\pm}, & h, k, l \text{ odd} \\ 0, & \text{otherwise} \end{cases} \tag{5.3}$$

$$\boldsymbol{\mathcal{F}}_C(\boldsymbol{Q}) = \begin{cases} 16\boldsymbol{M}_{\pm\boldsymbol{q},1}\cos\frac{\pi l}{6}e^{i\xi_\pm}, & h+k+l \neq 4n \ (h,k,l \text{ even}) \\ 16\boldsymbol{M}_{\pm\boldsymbol{q},1}\cos\frac{\pi l}{6}\sin\frac{\pi(h+l-k)}{4}e^{i(\chi_\pm+\pi/2)}, & h,k,l \text{ odd} \\ 0, \qquad \text{otherwise} \end{cases} \tag{5.4}$$

$$\boldsymbol{\mathcal{F}}_A(\boldsymbol{Q}) = \begin{cases} 16\boldsymbol{M}_{\pm\boldsymbol{q},1}\sin\frac{\pi l}{6}e^{i(\xi_\pm-\pi/2)}, & h+k+l = 4n \ (h,k,l \text{ even}) \\ 16\boldsymbol{M}_{\pm\boldsymbol{q},1}\sin\frac{\pi l}{6}\cos\frac{\pi(h+l-k)}{4}e^{i(\chi_\pm-\pi/2)}, & h,k,l \text{ odd} \\ 0, \qquad \text{otherwise} \end{cases} \tag{5.5}$$

$$\boldsymbol{\mathcal{F}}_G(\boldsymbol{Q}) = \begin{cases} 16\boldsymbol{M}_{\pm\boldsymbol{q},1}\sin\frac{\pi l}{6}e^{i(\xi_\pm+\pi/2)}, & h+k+l \neq 4n \ (h,k,l \text{ even}) \\ 16\boldsymbol{M}_{\pm\boldsymbol{q},1}\sin\frac{\pi l}{6}\sin\frac{\pi(h+l-k)}{4}e^{i(\chi_\pm+\pi)}, & h,k,l \text{ odd} \\ 0, \qquad \text{otherwise,} \end{cases} \tag{5.6}$$

where subscripts to $\mathcal{F}$ denote the basis vectors in (5.1), $\xi_\pm = \pi(h+k-3l \ \pm q)/4$ and $\chi_\pm = \pi(2h-2l \ \pm q)/4$ and to obtain a closed-form analytic form, the "ideal" Iridium position z=5/8+1/12 was used. From (5.3) it is seen that an F basis vector will contribute to the intensity of $\pm\boldsymbol{q}$ satellites of reciprocal lattice points (h,k,l) with the selection rule h,k,l all odd, or all even with $h+k+l = 4n$, $n \in \mathbb{Z}$. This is the same selection rule as for structural Bragg peaks at those (h,k,l) points, as expected since the F-type magnetic basis vectors are a generalization of ferromagnetic ($q = 0$) ordering. The resulting selection rule for an A basis vector is the same as for F, with the only difference that there is no contribution from A if $l = 6m$ and no contribution from F if $l = 3+6m$, $m \in \mathbb{Z}$ (for iridium at the "ideal" position $z = 5/8+1/12$). The selection rule for C and G is h,k,l all odd, or all even and $h+k+l = 4p+2$, $p \in \mathbb{Z}$, with no contribution from G if $l = 6m$ and no contribution from C if $l = 3+6m$, $m \in \mathbb{Z}$.

The rather arbitrary specular reflection of ≈(-6,5,7) meant that the search for magnetic Bragg peaks was confined to regions of reciprocal space in this vicinity,

and using (5.3)-(5.6) three positions of interest for studying the basis vectors contributing to the magnetic structure were ascertained, namely; (-6,6,12)$\pm\boldsymbol{q}$ (pure F), (-8,6,12)$\pm\boldsymbol{q}$ (pure C) and (-5,5,9)$\pm\boldsymbol{q}$ (mixed A and G) and magnetic peaks were found at all these positions. Therefore it is deduced that the structure contains F, C and one (or both) of A and G. To determine the direction of the magnetic moment components for each of those basis vectors the polarization dependence of the magnetic x-ray scattering can be used, as will be described in the following section.

5.5 Azimuthal Dependence of Intensities

5.5.1 Determination of Basis Vector Components

In the electric dipole approximation the magnetic x-ray scattering intensity at resonance is proportional to

$$L(\theta)\mathcal{A}\left|(\hat{\boldsymbol{\epsilon}}' \times \hat{\boldsymbol{\epsilon}}) \cdot \boldsymbol{\mathcal{F}}(\boldsymbol{Q})\right|^2 \tag{5.7}$$

where $L(\theta)$ is the Lorentz factor at the scattering angle 2θ, $\mathcal{A}$ is an absorption correction dependent upon the angle between the incoming ($\mathbf{k}$) and outgoing ($\mathbf{k}'$) beams and the normal to the crystal surface, $\boldsymbol{\mathcal{F}}(\boldsymbol{Q})$ is the magnetic structure factor vector given in (5.2), and $\hat{\boldsymbol{\epsilon}}'$ and $\hat{\boldsymbol{\epsilon}}$ are unit vectors along the polarization of the electric field component of the scattered and incident x-ray beams, respectively (see Section 3.2.1). For a σ-polarized incident beam magnetic resonant scattering occurs only in the σ-π' channel [see diagram in Fig 3.4(b)], meaning that the product of the electric field polarization vectors is along the scattered beam direction, i.e. $\hat{\boldsymbol{\epsilon}}' \times \hat{\boldsymbol{\epsilon}} = \hat{\boldsymbol{k}}'$, so only the component of the structure factor vector along the scattered beam direction, $\mathcal{F}_{\parallel} = \boldsymbol{\mathcal{F}} \cdot \hat{\boldsymbol{k}}'$, contributes to the magnetic intensity. By keeping the instrument in

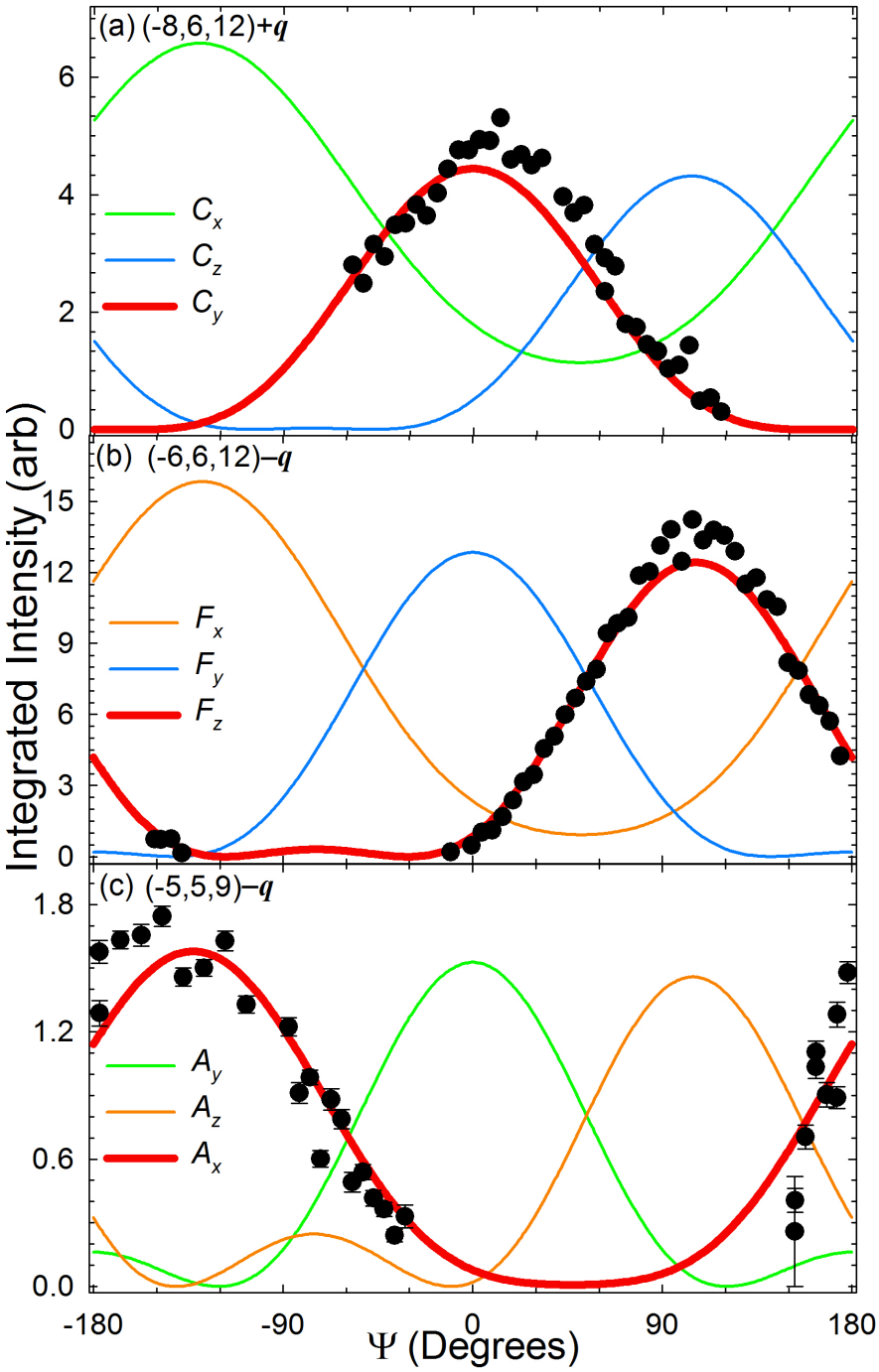


Figure 5.4: Integrated intensity as a function of azimuth for three magnetic Bragg peaks (a) C_y, (b) F_z and (c) A_x. Data points (filled circles) are integrated peak intensities (in sample rocking curve scans) corrected for absorption and Lorentz factor. Thick (red) lines show fits to the calculated magnetic scattering from the magnetic structure model Γ_4 depicted in Fig. 5.6. Orange, green and blue lines denote other models (Γ_1, Γ_2 and Γ_3, respectively) that can be easily ruled out. $\Psi = 0$ corresponds to the (010) axis in the scattering plane making the smallest angle with the incident beam direction $\boldsymbol{k}$.

the scattering condition and rotating the sample around the scattering wavevector $\boldsymbol{Q} = \boldsymbol{k'} - \boldsymbol{k}$ the projection $\mathcal{F}_{\parallel}$ of the structure factor vector onto the (fixed) direction $\hat{\boldsymbol{k'}}$ varies depending on the azimuth angle Ψ, with maximum magnetic intensity when the magnetic moments that give rise to the scattering make the smallest angle with $\hat{\boldsymbol{k'}}$ and zero intensity when they are perpendicular.

Azimuth scans are shown in Figs. 5.4(a-c) where the data points are obtained by integrating the magnetic peak intensity in rocking curve scans for each value of the azimuth Ψ. As discussed earlier, the selection rules identify the signal in panel (a) at (-8,6,12)+$\boldsymbol{q}$ to be of C-character and the observed maximum intensity at $\Psi = 0$ uniquely identifies the polarization to be along the y-axis (red thick line, calculated intensity including all contributions to the structure factor [9]). This is because, at $\Psi = 0$ the y-axis is in the scattering plane and makes the smallest angle with $\hat{\boldsymbol{k'}}$ direction and makes a larger angle with $\hat{\boldsymbol{k'}}$ for all azimuths away from 0. Other curves show the expected intensity dependence for other polarizations and those models can be clearly ruled out. Similarly, in panel (b) the peak at (-6,6,12)$-\boldsymbol{q}$ is identified as being of F character and polarized along z (thick red line). Panel (c) shows data at (-5,5,9)$-\boldsymbol{q}$, clearly of x-polarization (thick red line). The structure factor at (-5,5,9)$-\boldsymbol{q}$ is compatible with both an A or G character and it will be shown later that a pure A character can describe this and other azimuth scans quantitatively, so this peak is identified as coming from an A_x basis vector.

5.5.2 Peaks with Multiple Basis Vector Contributions

The next step in solving the structure is to determine the relative phase between the A_x, C_y and F_z basis vectors. A phase of 0 or π between basis vectors with

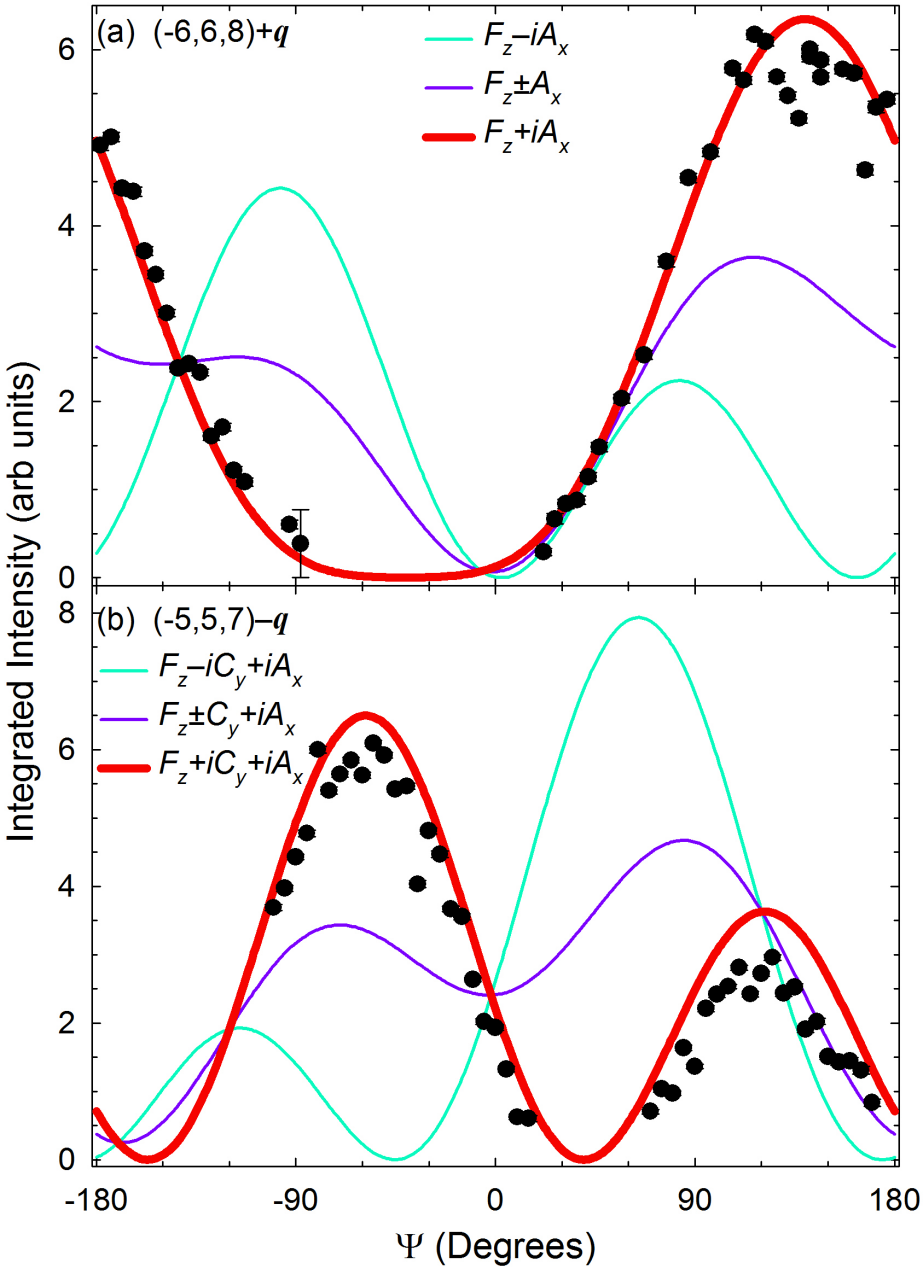


Figure 5.5: Azimuth scans of "mixed" magnetic peaks (black circles) corrected for absorption and Lorentz factor, compared to calculations (red thick line) for the magnetic structure model in Fig. 5.6, as well as calculations for other possible models (a) (-6,6,8)+$\boldsymbol{q}$ is a mixed $F:A$ peak with contributions in the ratio 1 : 3, (b) (-5,5,7)−$\boldsymbol{q}$ is a mixed $F:C:A$ peak with contributions in the ratio 3 : 3 : 1. Note that the data clearly distinguishes between different relative phases of basis vectors (cyan and purple).

orthogonal components, say along A_x and F_z, means that the moments vary sinusoidally along a direction in the xz plane, whereas a phase offset of $\pi/2$ means that the moments rotate in the xz plane. The relative phase between two basis vectors can be determined from an azimuth scan at a magnetic Bragg peak position where both basis vectors contribute, as the intensity is the sum of the intensities due to the two separate basis vectors plus an additional cross-term that is sensitive to the phase offset (this is discussed in Appendix A, and the phase factor is calculated explicitly for the $(-6, 6, 8) + \boldsymbol{q}$ peak in Section A.2).

Fig. 5.5(a) shows the azimuth at (-6,6,8)+$\boldsymbol{q}$ where structure factor calculations show that both F and A basis vectors contribute in the ratio 1:3. The intensity dependence uniquely identifies it as originating from the particular basis vector combination $F_z + iA_x$, i.e. the x components are $\pi/2$ out-of-phase with respect to the z-components, meaning that the magnetic moments rotate in the xz plane (in a particular sense on each site, note that the opposite sense of rotations encoded in the basis vector $F_z - iA_x$ is not consistent with the data - cyan line). The data clearly rules out the case when the moments are not rotating in the xz plane, but are varying sinusoidally along a line in the xz plane ($F_z \pm A_x$, purple line), a model with no A_x component is also ruled out (not shown). This analysis shows that an A_x basis vector must exist in the ground state and that it is $\pi/2$ out-of-phase with respect to F_z. Similarly, to determine the phase offset between the F_z and C_y basis vectors an azimuth scan at the magnetic reflection (-5,5,7)$-\boldsymbol{q}$ was measured and is shown in Fig. 5.5(b). This peak contains mixed F, C and A contributions in the ratio 3:3:1, and only a model with the basis vector contribution $F_z + iC_y$ (thick red line) matches

the data, with other combinations (cyan and purple curves) clearly ruled out (note that those calculations also include the iA_x contribution as already determined).

5.6 Magnetic Structure of β-Li_2IrO_3

Having established all the basis vectors that are present, their polarization and relative phases, the relative magnitudes are obtained by quantitatively fitting the azimuth intensity dependencies with the only free parameters the relative ratio M_x/M_z, M_y/M_z and a *single* overall intensity scale factor for all the data. The simultaneous fit of this magnetic structure model to the data in Figs. 5.4(a-c) and Fig. 5.5(a-b) (shown by the thick red solid lines) with only those three free parameters gave the moment amplitudes in the relative ratio $M_x : M_y : M_z = 0.45(1) : 0.65(1) : 1$. It is worth reiterating that no arbitrary intensity scale factors are used between different azimuthal scans, and so the agreement is striking given that these scans are performed at vastly different points in reciprocal space. Note that the basis vector combination (iA_x, iC_y, F_z) with the above moment amplitudes quantitatively explains the mixed F_z, A_x peak in Fig. 5.5, and the *same* magnitude A_x basis vector also quantitatively accounts for the azimuth dependence in Fig. 5.4(a), further confirming the identification of the signal in this magnetic Bragg peak as coming from a pure A_x basis vector. That is, if a G_x basis vector is also present, its magnitude is very small, beyond the accuracy of the present experiments. Given this, it is concluded that the magnetic structure is described by the basis vector combination (iA_x, iC_y, F_z), which corresponds to a single irreducible representation, Γ_4 in Table 5.4.

The determined magnetic structure can be written explicitly in terms of the mag-

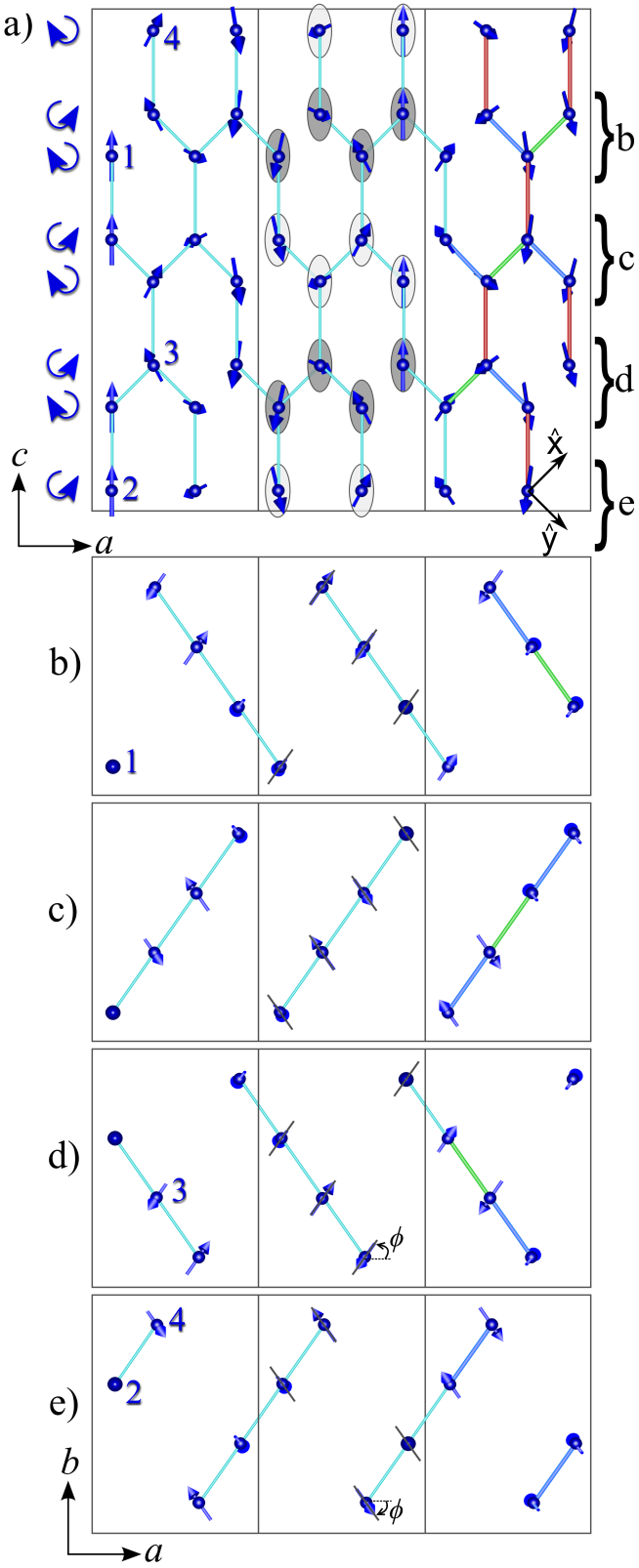


Figure 5.6: (a) Projection of the magnetic structure on the (ac) plane showing the sites 1-4 of the primitive cell. Left curly arrows indicate counter-rotation of moments between consecutive sites along c. In unit cell 2 light and dark shaded elliptical envelopes indicate an alternating tilt of the plane of moments' rotation away from the ac plane. In unit cell 3 the colour of bonds shows the anisotropy axis of the exchange in a Kitaev model ((for the $\langle ij \rangle$ bond the exchange $-KS_i^\eta S_j^\eta$, with $\eta = \mathsf{x}, \mathsf{y}, \mathsf{z}$ for blue/green/red bonds, with the cubic axes orientations $\hat{\mathbf{x}} = (\hat{\boldsymbol{a}} + \hat{\boldsymbol{c}})/\sqrt{2}$, $\hat{\mathbf{y}} = (\hat{\boldsymbol{a}} - \hat{\boldsymbol{c}})/\sqrt{2}$ and $\hat{\mathbf{z}} = \hat{\boldsymbol{b}}$). Right-hand labels (b)-(e) indicate where slices through the magnetic structure are taken at different heights in the unit cell and projected onto the (ab) plane to illustrate the direction of the zig-zag chains and the alternating tilt of the plane of rotation away from the ac plane by $\pm\phi$ between consecutive zig-zag chains stacked along c.

netic moment at position $\boldsymbol{r}$ belonging to site index $n = 1{-}4$ as

$$\boldsymbol{M}_n(\boldsymbol{r}) = \hat{\boldsymbol{x}} M_x v_x(n) \sin \boldsymbol{q}\cdot\boldsymbol{r} + \hat{\boldsymbol{y}} M_y v_y(n) \sin \boldsymbol{q}\cdot\boldsymbol{r} + \hat{\boldsymbol{z}} M_z v_z(n) \cos \boldsymbol{q}\cdot\boldsymbol{r}, \qquad (5.8)$$

where, as before, $\hat{\boldsymbol{x}}$, $\hat{\boldsymbol{y}}$, $\hat{\boldsymbol{z}}$ are unit vectors along the orthorhombic $\boldsymbol{a}$, $\boldsymbol{b}$, $\boldsymbol{c}$ axes, respectively. The pre-factors $v_{x,y,z}$ are obtained from the basis vectors along the corresponding axes, but without the displacement phase factors $\delta = e^{-i\boldsymbol{q}\cdot(\boldsymbol{r}_n - \boldsymbol{r}_1)}$, i.e. $v_x = [+ - -+]$ (from A_x), $v_y = [+ + --]$ (from C_y) and $v_z = [+ + ++]$ (from F_z), and these are tabulated in Table 5.3. Eq. (5.8) describes all iridium sites, including those related by F-centering translations, where $\boldsymbol{r}$ is the actual position of the ion and n is the site index at the equivalent position $(1{-}4)$ in the primitive unit cell.

The magnetic moments are expressed in terms of their Fourier components as $\boldsymbol{M}_n(\boldsymbol{r}) = \sum_{\boldsymbol{k}=\pm\boldsymbol{q}} \boldsymbol{M}_{\boldsymbol{k},n} e^{-i\boldsymbol{k}\cdot\boldsymbol{r}}$, where

$$\boldsymbol{M}_{\boldsymbol{q},n} = \left\{ i \left[\hat{\boldsymbol{x}} \frac{M_x}{2} v_x(n) + \hat{\boldsymbol{y}} \frac{M_y}{2} v_y(n) \right] + \hat{\boldsymbol{z}} \frac{M_z}{2} v_z(n) \right\} e^{-i\boldsymbol{q}\cdot(\boldsymbol{r}_n - \boldsymbol{r}_1)}, \qquad (5.9)$$

with $\boldsymbol{M}_{-\boldsymbol{q},n} = \boldsymbol{M}^*_{\boldsymbol{q},n}$ as the magnetic moment distribution is real.

The only remaining parameter still to be determined is the absolute magnitude of the magnetic moments. This cannot be extracted reliably from the magnetic resonant x-ray diffraction data as it requires careful absorption corrections and accurate determination of scale factors between the magnetic and structural peaks (the latter being of order $10^5 - 10^6$ more intense). However, in neutron scattering experiments the magnetic and structural peaks are of comparable magnitudes and one can obtain a reliable determination of the relative scale factor. To this aim the powder neutron

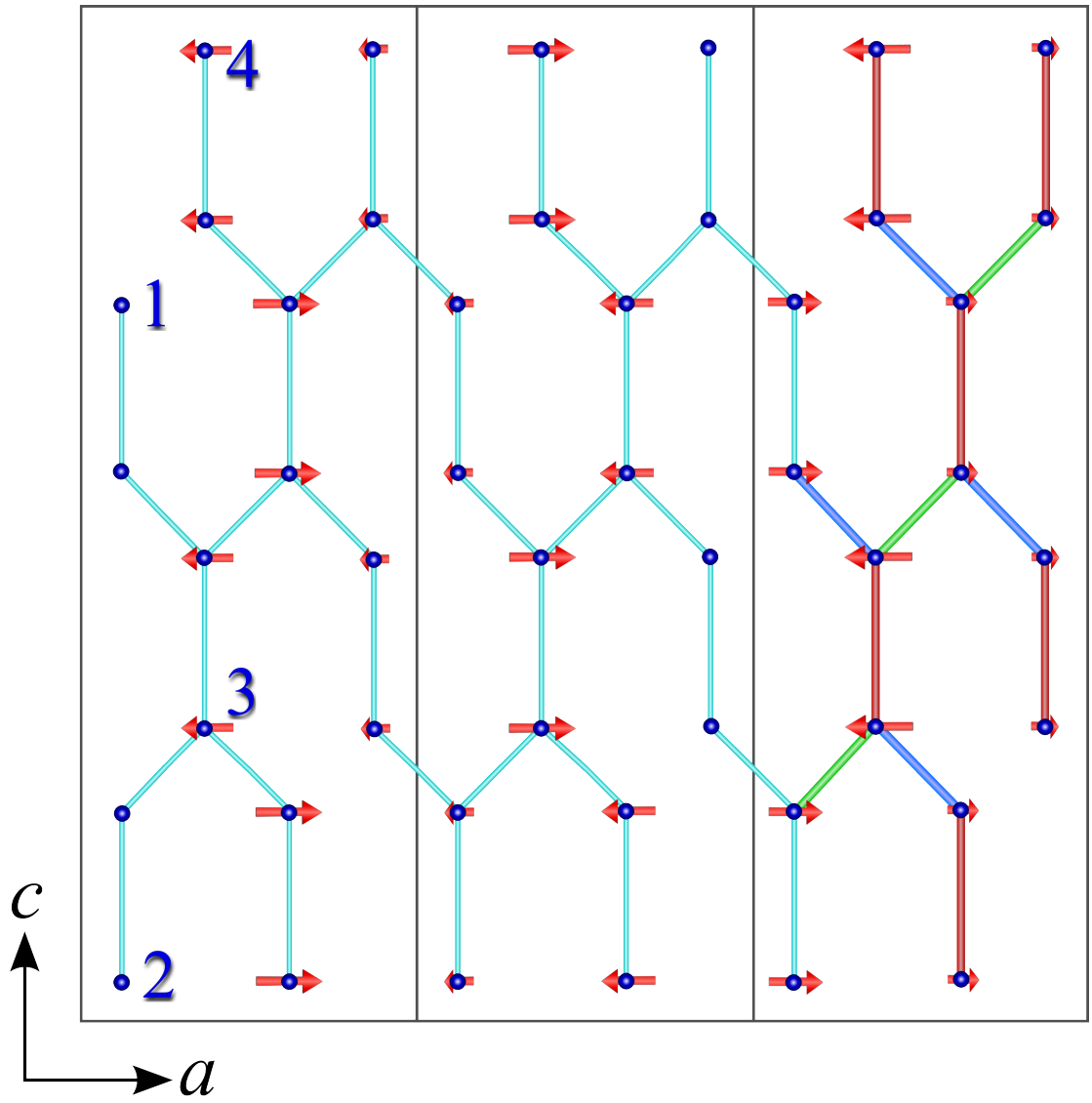


Figure 5.7: Projection of the iridium lattice on the ac plane showing the ordering of the magnetic moment components along the b-axis only. These are shown rotated (for ease of visualization) from the b to the a-axis and indicated by horizontal red arrows (length of arrow indicates magnitude of $M_y(\boldsymbol{r})$ at each site. Note the ferromagnetic alignment between the two sites of each vertical (c-axis) bond.

data in Fig. 5.2 is reconsidered, and three contributions are simultaneously fit to the data; structural peaks of the sample calculated using the crystal structure with fixed internal parameters (as deduced from single crystal x-ray diffraction), aluminium structural peaks (from the sample can), and magnetic peaks calculated using the full magnetic structure model deduced from the resonant x-ray experiments. The fit is plotted as a solid black line in Fig. 5.2 and shows excellent agreement with the data. The resulting magnetic moment is of magnitude $0.47(1)\mu_{\mathrm{B}}$ when aligned along the c-axis, and slightly reduced by $\sim$20% when in the ab-plane. The propagation vector was also fitted and it is found that $\boldsymbol{q} = (0.5768(3), 0, 0)$, consistent with the x-ray measurements.

The obtained magnetic structure projected onto the ac plane is shown in Fig. 5.6(a). The magnetic moments are counter-rotating between all nearest-neighbor sites and the plane of rotation alternates between the two sites of every vertical (c-axis) bond as illustrated by the pattern of light and dark shaded elliptical envelopes. The planes of rotation are obtained from the ac plane by rotation around the c-axis by an angle $\pm\phi$, with $\phi = \tan^{-1}\frac{M_y}{M_x} = 55(1)^\circ$. Each zig-zag chain has the top and bottom sites counter-rotating in one and the same plane, which then alternates between consecutive zig-zag chains vertically-linked along the c-axis (see Fig. 5.6(b-e)). The zig-zag chains are directed alternatingly along the $\boldsymbol{a} \pm \boldsymbol{b}$ directions and are made up of iridium sites of type (2,4) and (1,3), respectively, with vertical (c-axis) bonds coupling sites of types 1-2 and 3-4. The magnetic order pattern is such that for every vertical bond the spin components along the y-axis are ferromagnetically-aligned (see Fig. 5.7), in accordance with the basis vector C_y, which has equal Fourier

components at sites 1-2 and 3-4, respectively [see eq. (5.1)].

It is noted that the magnetic moment rotation at each site defines an elliptical envelope, distorted from circular with the moment slightly smaller when in the *ab* plane compared to when along the *c*-axis, $\sqrt{M_x^2 + M_y^2}/M_z = 0.80(1)$. This effect may be due to a larger *g*-factor along the *c*-axis compared to the $\hat{\boldsymbol{a}}\cos\phi \pm \hat{\boldsymbol{b}}\sin\phi$ directions in the *ab* plane. Single-crystal susceptibility data [10] in the related polytype γ-Li_2IrO_3 do provide evidence for the presence of *g*-tensor anisotropy for the iridium moments (in the high-temperature limit the susceptibility, χ, is expected to be proportional to the squared *g*-factor along the applied field direction, and experiments observe χ_c larger than both χ_a and χ_b, implying an anisotropic *g*-tensor). The very similar local environment around the iridium sites in β-Li_2IrO_3 suggests that an anisotropic *g*-tensor is also likely here. Another possibility is that zero-point quantum fluctuations may prefer a non-fixed length ordered moment between sites, with a larger ordered moment along the *c*-axis, which is the only direction that is common to all planes of rotation. Evidence for the presence of zero-point quantum fluctuations in the ground state is provided by the fact that the absolute magnitude of the ordered moment (0.47(1) μ_B) is significantly reduced from what is believed to be the available full-moment value (estimated at $g\mu_B J_{\text{eff}} \simeq 1\mu_B$ assuming $g \simeq 2$ [11]), so a structure with small modulations on an already significantly reduced ordered moment could be compatible with the experimental results.

5.7 Similarities between Magnetic Structures of β-Li_2IrO_3 and γ-Li_2IrO_3

It is interesting to note that the obtained magnetic structure has striking similarities with the magnetic structure in the related polytype γ-Li_2IrO_3 of Chapter 4, with which β-Li_2IrO_3 shares the same size orthorhombic unit cell ($a \times b \times c$) and also many key structural features. In both polytypes the iridium lattice is locally three-fold coordinated and is made up of vertically-linked zig-zag chains that alternate in orientation between the $\boldsymbol{a} \pm \boldsymbol{b}$ direction. The only difference between them is that in the hyperhoneycomb β-polytype this alternation occurs between consecutive zig-zag chains, whereas in the stripyhoneycomb γ-polytype the alternation occurs between pairs of parallel zig-zag chains which form a honeycomb row (see Fig 2.3). The magnetic structures in both polytypes are incommensurate with the same propagation vectors within experimental error, $\boldsymbol{q}$=$(0.57(1), 0, 0)$. The moments are counter-rotating between the sites of every nearest-neighbour bond, and the plane of rotation alternates between two orientations tilted away (by an angle ϕ) from the ac plane between consecutive zig-zag iridium chains vertically-linked along the c-axis. The ϕ angle was found to be somewhat smaller in γ-Li_2IrO_3, but apart from this difference the magnetic structure in γ-Li_2IrO_3 can be regarded as "equivalent" to that in β-Li_2IrO_3 but in a different lattice setting.

When both structures are viewed in projection onto the ac plane [as shown in Fig. 5.6(a) and Fig. 4.6] the two iridium lattice arrangements then look identical. This suggests that a formal mapping can be constructed between the notations used to describe the sites of the primitive cells of the two materials, and also between

Site $Cccm$	Site $Fddd$	Translation
1	4	-(0,0,1)
2	3	(0,0,0)
3	3	(0,1/2,1/2)
4	4	-(0,1/2,1/2)
$1'$	2	(1/2,1/2,0)
$2'$	1	(1/2,0,-1/2)
$3'$	1	(1/2,1/2,0)
$4'$	2	(1/2,1,1/2)

Table 5.5: Equivalence between the Iridium sites in γ-Li_2IrO_3 ($Cccm$ space group) with those in β-Li_2IrO_3($Fddd$ space group) (when both are projected onto the ac plane). Last column shows additional translations to be applied to primitive lattice sites in the $Fddd$ structure (column 2) in addition to a common translation by (-1/8,0,1/8) to get the positions in the $Cccm$ structure (column 1). For each structure the "ideal" iridium positions have been used.

the magnetic basis vectors, such that one can then describe a magnetic structure equivalently in the notation of one or the other space group. Of course the magnetic structures would only be "equivalent" up to the projection of the sites onto the b-axis. Table 5.5 lists the equivalence between the sites in the primitive cell of the two structures (up to the y-coordinate of sites), where for the γ-polytype the notation in Chapter 4 is followed (two iridium sublattices with sites 1-4 and $1'$-$4'$). Using this site equivalence one can construct a mapping of the magnetic basis vectors as listed in Table 5.6. The magnetic structure described by the basis vector combination (iA_x, iC_y, F_z) in the $Fddd$ setting then corresponds, in the notation of the $Cccm$ setting, to $i(A, -A)_x, i(-1)^m(F, -F)_y, (F, F)_z$ with $m = 1$.

These similarities are strongly suggestive that the defining features of the magnetic

Basis vector	Basis vector
$Fddd$ (4-site [1-4])	$Cccm$ (8-site,[1-4,1′-4′])
A $[+--+]$	$(A,-A)$ $[+--+-++-]$
C $[++--]$	$(-F,F)$ $[----++++]$
F $[++++]$	(F,F) $[++++++++]$

Table 5.6: Mapping of magnetic basis vectors between the $Fddd$ and $Cccm$ notations.

structure, namely non-coplanarity, the counter-rotation on every nearest-neighbor bond, and the direction and even the magnitude of the incommensurate ordering wavevector, are determined by the same type of short-range magnetic interactions in both polytypes. Moreover, those features appear to be robust against changes in the global lattice connectivity (i.e. how zig-zag chains are vertically-linked in a long-range pattern) which leave the local connectivity of the zig-zag chains unchanged. In the γ-polytype it was shown in Chapter 4 that the key features of the magnetic order can be stabilized by a spin Hamiltonian with dominant Kitaev couplings with some additional interactions. The observation of similar magnetic structures in the β- and γ-polytypes suggests the same underlying magnetic interactions occur in both cases. The relevant parent Kitaev model for the β-polytype has been considered in Refs. [5, 12] and is illustrated in Fig. 5.6(a) (unit cell 3) where the colour of the bonds indicates the anisotropy axis of the exchange, i.e. a ferromagnetic Ising coupling between the components normal to the Ir-O_2-Ir plane of each Ir-Ir bond, whose directions define the cubic axes x, y and z related to the crystallographic axes by $\hat{\mathbf{x}} = (\hat{\boldsymbol{a}} + \hat{\boldsymbol{c}})/\sqrt{2}$, $\hat{\mathbf{y}} = (\hat{\boldsymbol{a}} - \hat{\boldsymbol{c}})/\sqrt{2}$ and $\hat{\mathbf{z}} = \hat{\boldsymbol{b}}$ (where the "idealized" lattice with cubic IrO_6 octahedra and a:b:c=1:$\sqrt{2}$:3 has been assumed). It could also be suggested that the magnetic interactions are very similar in magnitude between the β

and γ-polytypes, as both materials show very similar values for the magnetic ordering temperature.

Indeed, recently Kimchi *et al* [13] have proposed a model Hamiltonian including only nearest neighbour Kitaev and Heisenberg couplings (K and J, respectively) as well as an Ising coupling between Ir sites linked along bonds parallel to c (I_c). Values of $(K, J, I_c) = (-12, 0.6, -4.5)$ meV yield a counter rotating groundstate appropriate to both β and γ polytypes, and the level of non-coplanarity (which is found to vary between the two polytypes; $\phi_\gamma = 42(2)^\circ$, $\phi_\beta = 55(1)^\circ$) can be set by varying the anisotropy of the Kitaev term (see K_d and K_c in (4.13)).

5.8 Conclusions

To conclude, single-crystal resonant magnetic x-ray diffraction experiments at the L_3 edge of Ir have been conducted on a 17 μm wide sample of β-Li_2IrO_3, which is a unique realization of a hyperhoneycomb iridium lattice, a candidate to display 3D Kitaev physics of strongly-frustrated, bond-anisotropic interactions. Previous neutron powder diffraction data motivated and guided the search in reciprocal space for magnetic Bragg peaks, and using the RMXD experimental technique not only were these peaks measured, with an incommensurate ordering vector $\boldsymbol{q}$=$(0.57(1), 0, 0)$, but the full magnetic structure of β-Li_2IrO_3 was solved unambiguously. An incommensurate, non-coplanar magnetic structure with moments counter-rotating on every nearest-neighbor bond was found, and through fitting this model to the aformentioned neutron data, the magnitude of the Ir magnetic moment was deduced as 0.47(1) μ_B. Note that this moment is significantly reduced from what is believed to be the available

full-moment value (estimated at $g\mu_B J_{\text{eff}} \simeq 1\mu_B$ assuming $g \simeq 2$) and can be taken as evidence for zero-point quantum fluctuations in the groundstate. The magnetic structure shows striking similarities to the magnetic structure of the related structural polytype γ-Li_2IrO_3, suggesting that the same underlying Hamiltonian (with dominant Kitaev interactions) stabilizes the defining features of the magnetic structure in both structural polytypes.

References

[1] T. Takayama, A. Kato, R. Dinnebier, J. Nuss, and H. Takagi, arXiv:1403.3296 (2014).

[2] A. Biffin, R. D. Johnson, S. Choi, F. Freund, S. Manni, A. Bombardi, P. Manuel, P. Gegenwart, and R. Coldea, arXiv:1408.0246v1 (2014).

[3] J. Rodríguez-Carvajal, Physica B: Condensed Matter **192**, 55 (1993).

[4] S. Miller and W. Love, *Tables of Irreducible Representations of Space Groups and Co-Representations of Magnetic Space Groups*, 1^{st} ed. (Pruett Boulder, 1967).

[5] E. K.-H. Lee, R. Schaffer, S. Bhattacharjee, and Y. B. Kim, Physical Review B **89**, 045117 (2014).

[6] C. Detlefs, M. Sanchez del Rio, and C. Mazzoli, The European Physical Journal Special Topics **208**, 359 (2012).

[7] X. Liu, T. Berlijn, W.-G. Yin, W. Ku, a. Tsvelik, Y.-J. Kim, H. Gretarsson, Y. Singh, P. Gegenwart, and J. P. Hill, Physical Review B **83**, 220403 (2011).

[8] S. Boseggia, R. Springell, H. Walker, H. Rø nnow, C. Rüegg, H. Okabe, M. Isobe, R. Perry, S. Collins, and D. McMorrow, Physical Review Letters **110**, 117207 (2013).

[9] L. Chapon, http://forge.ill.eu/svn/magnetix.

[10] K. A. Modic, T. E. Smidt, I. Kimchi, N. P. Breznay, A. Biffin, S. Choi, R. D. Johnson, R. Coldea, P. Watkins-Curry, G. T. McCandless, J. Y. Chan, F. Gandara, Z. Islam, A. Vishwanath, A. Shekhter, R. D. McDonald, and J. G. Analytis, Nature communications **5**, 4203 (2014).

[11] Y. Singh and P. Gegenwart, Physical Review B **82**, 064412 (2010).

[12] I. Kimchi, J. Analytis, and A. Vishwanath, arXiv:1309.1171v2 (2013).

[13] I. Kimchi, R. Coldea, and A. Vishwanath, arXiv:1408.3640v1 (2014).

Chapter 6

Dynamics of a Spin-Orbital Singlet in $FeSc_2S_4$ Probed via Inelastic Neutron Scattering

The A-site spinel $FeSc_2S_4$ is believed to form a novel, spin-orbital singlet (SOS) state, where entangled spin and orbital moments remain disordered down to the lowest measurable temperatures, even in the presence of strong exchange interactions between magnetic Fe^{2+} ions. Here the results of inelastic neutron scattering experiments on a powder sample of $FeSc_2S_4$ is presented and a model of spin-orbiton triplet excitations is proposed to explain the dispersive excitations observed, in both zero-field and in-field measurements. With the application of field, the spin and orbital nature of the excitations is truly apparent, leading to an increase in the gap between the singlet groundstate and triplet of excited states, which is contrary to that observed in the spin-only analogue.

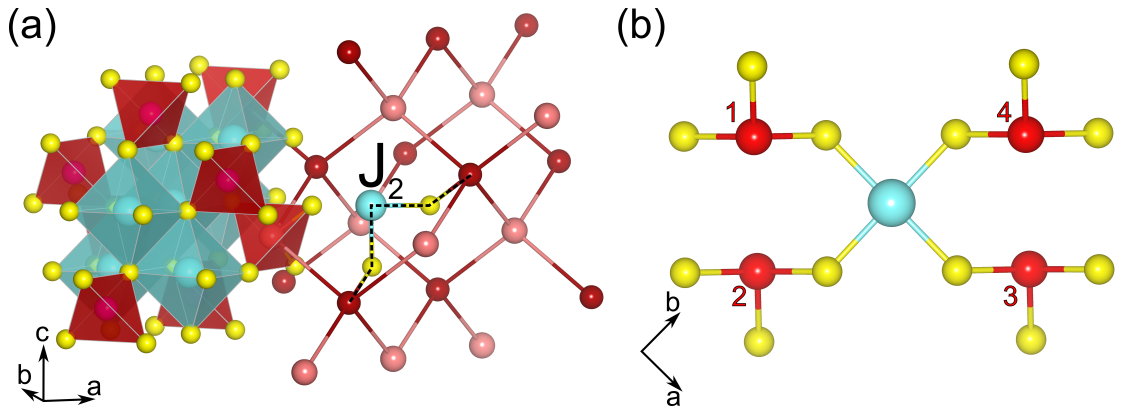


Figure 6.1: Structure of, and exchange interactions within $FeSc_2S_4$ (a) Two unit cells are shown, in the left cell Fe, Sc and S ions are shown as red, cyan and yellow spheres respectively. Fe and Sc ions are in tetrahedral and octahedral environments of S ligands, and these are shown as partially opaque polyhedra. In the right cell Fe ions are shown as light and dark red spheres to demonstrate the decoupling of this diamond lattice into its constituent FCC lattices, an example of a J_2 exchange path is shown. (b) Projection of section of the lattice from (a) onto the *ab*-plane to demonstrate the different exchange paths between NN, NNN, and NNNN (see text).

6.1 Structure of, and Exchange Interactions within $FeSc_2S_4$

In Fig 6.1(a) two unit cells of a spinel structure are shown, such structures have the general formula AB_2X_4 and belong to the space group $Fd\bar{3}m$ (no. 227). The A-site ions (red spheres in left unit cell of Fig 6.1(a)) sit in a tetrahedral environment of ligands X (yellow spheres), whereas the B-site ions (cyan spheres) are in an octahedral envionment of these ligands. These corresponding environments are plotted as red and cyan polyhedra respectively in the left cell of Fig 6.1(a). The B-sites map out a network of corner-sharing tetrahedra, a structure familiar from pyrochlore systems, however of interest here will be the A-sites within this structure. These are shown isolated in the second cell of Fig 6.1(a) as two different shades of red spheres (the shading will be explained shortly), one can see that they map out a diamond lattice

i.e. two FCC lattices displaced by $(\frac{1}{4},\frac{1}{4},\frac{1}{4})$

$FeSc_2S_4$ crystallizes in such a structure, with the magnetic Fe^{2+} ions sat in a tetrahedral environment in a $3d^6$, high-spin configuration $L = 2$, $S = 2$. Scandium is in a 3+ oxidation state, and so has the electron configuration of an Argon atom, and therefore plays no part in the magnetism of the system.

The distance between A-sites in the structure is inhibitive of direct exchange, therefore – as discussed previously [1] – the dominant interactions occur via superexchange along A-X-B-X-A paths, favouring antiferromagnetic order. One might expect such effects to be weak, as the exchange path involves 3 intermediate ions (one such path is shown in Fig 6.1(a)), however the multiplicity of such paths leads to a sizeable coupling between Fe-sites. Specifically, each Fe^{2+} ion is connected to its 4 nearest neighbours (NN) via 6 possible paths, and to its 12 next nearest neighbours (NNN) through 2 possible paths. Thus it might be anticipated that the NN interaction, J_1 and NNN interaction J_2 to contribute on an equal footing to the physics of such systems.

Fig 6.1(b) shows a section of the structure projected onto the *ab*-plane. The colour coding is the same as in Fig 6.1(a), and the four Fe sites present have been labelled 1-4. Let us consider Fe #1; its nearest neighbour (NN) is Fe #2, its next nearest neighbour (NNN) is Fe #4 and its NNNN is Fe #3. NNNN interactions will not be considered here, the large separation between NNNNs as well as the reduced multiplicity (= 12) compared with NN and NNN exchange paths contribute to its weakness in this system. However as discussed above, both NN and NNN exchange paths should be of comparable strength.

The complex nature of the 5-site superexchange along A-X-B-X-A paths makes it difficult to calculate such exchanges directly, or even develop some schematic understanding of why one exchange should be greater in magnitude than another. However density-functional calculations have been performed [2] which predict a large difference in magnitude between the two interactions. The origin of such a difference is in the variation of Fe-Sc-Fe, Fe-S-Fe and S-Sc-S bonds between NN and NNN exchange paths. From Fig 6.1(b) it can be seen that these bond angles are approximately 60°, 80°and 90° for NN hopping and for NNN the equivalent angles are 120°, 130°and 90°, respectively. Such differences in angle are argued to prioritize direct Fe-Sc hybridization and anion mediated exchange Fe-S, respectively for NN and NNN hopping, and the spherical charge distribution of Sc^{3+} makes hybridization a very weak effect and so the next nearest neighbour exchange, J_2 dominates, s.t. $J_2/J_1 \approx 40$ [2]. This discrepancy is also suggested by neutron scattering experiments performed by Krimmel *et al* [3], where an excitation with a softening wavevector at approximately $2\pi/a(1,0,0)$ was observed, which corresponds to an ordering vector of Néel antiferromagnetic ordering on an FCC lattice.

In terms of the diamond lattice of Fe ions discussed earlier (Fig 6.1(a), right), the result of a dominant J_2, or next nearest neighbour interaction is to effectively split the diamond lattice into its constituent FCC lattices, which in the limit of $J_2/J_1 \to \infty$ are completely decoupled. This is demonstrated by the light and dark red sites in the right-hand cell of Fig 6.1(a), which upon inspection can be seen to map out FCC lattices. With $J_2 < 0$, this intra-sublattice exchange leads to frustration - this is most easily visualised by viewing the FCC lattice down the [1,1,1] direction, where

the triangular network of magnetic ions is revealed (triangles being the prototypical building blocks of frustration in magnetism).

Previous measurements of magnetic susceptibility on $FeSc_2S_4$ showed a Curie-Weiss behaviour with $\theta_{CW} = -45(1)$ K [4] with no sign of magnetic order measured to 1.7 K. Moreover the deduced paramagnetic moment of $\mu_{eff} = 5.1(1)\ \mu_B$ is higher than the spin-only value of 4.90 μ_B, signalling that orbital degrees of freedom are still present. Specific heat data on this sample shows no anomalies indicative of structural or magnetic ordering down to 50mK [4], but displays a broad peak close to 6K, a feature often observed in geometrically frustrated magnets [5]. These results suggest that the spin frustration in $FeSc_2S_4$ remains at the lowest measurable temperatures.

6.2 Calculating Energy Levels and Excitations in $FeSc_2S_4$

Having described the crystal structure and dominant exchanges, now the model used to calculate excitations within $FeSc_2S_4$ will be laid out in detail. Before calculating the dispersion of the spin-orbital triplons presented in Section 2.4.3 however, a careful study of the single ion physics of Fe^{2+} in $FeSc_2S_4$ will need to be made, and so that is where the next section shall begin.

6.2.1 Single Ion Hamiltonian

As discussed above, the Fe^{2+} ions in $FeSc_2S_4$ sit in an tetrahedral environment in a $3d^6$, high-spin configuration $L = 2$, $S = 2$. The effect of the crystal field is to split the d-orbitals in the conventional manner into a lower doublet of on-axis orbitals, e, (denoted by $|x^2 - y^2\rangle$, $|z^2\rangle$ in (2.11)) and a higher triplet of off-axis t_2 (denoted

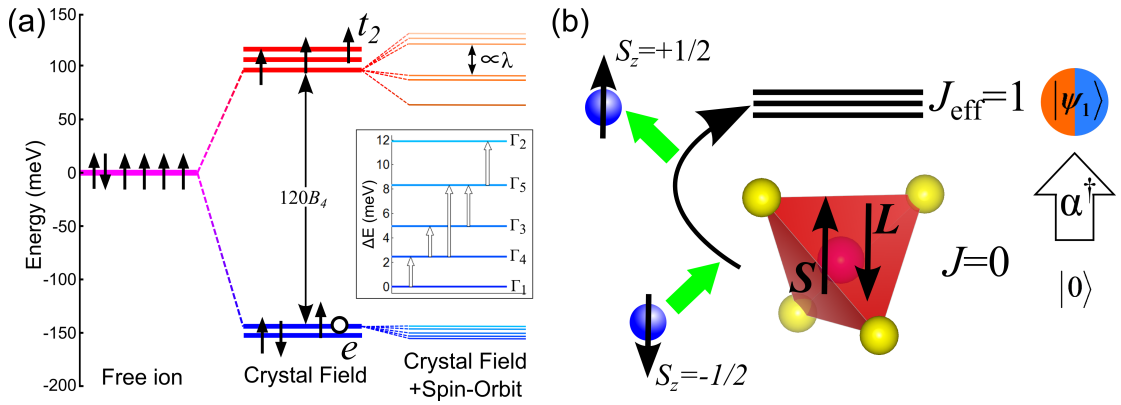


Figure 6.2: Single ion energy levels for Fe^{2+} (a) Successive reduction in degeneracy of states as extra terms are considered in the Hamiltonian, black arrows/ white circles denote electrons/holes. Note that the crystal field produces a doubly degenerate configuration, as the hole can lie in either of the e doublets. Inset: Allowed transitions via INS between levels derived from the e-doublet, as calculated from (6.5). (b) Schematic showing how a neutron can interact with the SOS groundstate to produce a triply degenerate excitation, this is interpreted as the spin-orbital triplon introduced in Section 2.4.3, one such mode $|\psi_1\rangle$ is created from the vacuum ($|0\rangle$) by the creation operator $\alpha^\dagger$.

by $|xy\rangle$, $|yz\rangle$, $|zx\rangle$ in (2.11))[1] orbitals, and this is shown in Fig 6.2(a). It can be seen that in the high-spin state the 6 electrons (depicted as black arrows) are shared between e and t_2, however this leads to a hole in the e yielding a doubly degenerate orbital groundstate. That this degeneracy persists to low temperature is evident from previous neutron diffraction measurements [4], where no structural distortion – the calling card of Jahn Teller orbital ordering [6] – is evident. Therefore not only is $FeSc_2S_4$ a system with disordered spins, but also a system of disordered orbitals down to the lowest measureable temperatures.

With its unquenched orbital moment, a significant spin-orbit coupling term of the usual form (2.9), is to be expected. Therefore to a good approximation the single ion

[1]N.B. on comparison with (2.11) it can be seen that the 'g' substcript has been dropped from the notation. The subscript signifies a point of inversion symmetry in the system, 'g' standing for *gerade*. In the IrO_6 octahedra discussed in Section 2.3.1, such a point existed, however the tetrahedra of FeS_4 have no such inversion symmetry, hence the subscript is dropped.

Hamiltonian of the Fe^{2+} ions may be characterised as having two key contributions; the crystal field resulting from the tetrahedral environment of Sulfur ligands, $\mathcal{H}_{cf}$ and the spin-orbit coupling (as explained above, the orbital moment is not quenched via the Jahn-Teller mechanism), $\mathcal{H}_{SO}$, such that the full single ion Hamiltonian may be written as,

$$\mathcal{H}_{\mathrm{Fe}} = \mathcal{H}_{cf} + \mathcal{H}_{SO}. \tag{6.1}$$

The former contribution is readily expressed in terms of angular momentum operators (the crystal field not acting on spin components) via a method of Wigner and Eckhart [7], and for a tetrahedral ligand environment is given by $-B_4(O_4^0 + 5O_4^4)$, where O_4^0 and O_4^4 denote orbital operators, and B_4 contains information about the strength of the ion-ligand interaction. These equivalent operators are tabulated [8], and explicitly $\mathcal{H}_{cf}$ can be expanded as

$$\mathcal{H}_{cf} = -B_4([35L_z^4 - 30L(L+1)L_z^2 + 25L_z^2 - 6L(L+1) + 3L^2(L+1)^2] + \frac{5}{2}[L_+^4 + L_-^4]), \tag{6.2}$$

where L is the orbital angular momentum quantum number and the $\pm$ ladder operators are the standard ones, $J_\pm|j,m\rangle = [(j \mp m)(j \pm m + 1)]^{1/2}|j, m \pm 1\rangle$ [9]. This leads to the t_2-e splitting shown in Fig 6.2(a). The latter contribution to (6.1) is just the 'standard' spin orbit coupling, $\mathcal{H}_{SO} = \lambda \boldsymbol{L} \cdot \boldsymbol{S}$, described in Section 2.2. The $\boldsymbol{L} \cdot \boldsymbol{S}$ part can be expanded in terms of ladder operators:

$$\boldsymbol{L} \cdot \boldsymbol{S} = L_z S_z + \frac{1}{2}(L_+ S_- + L_- S_+) \tag{6.3}$$

It is seen then that the single ion Hamiltonian is a function of these spin-orbit and crystal field coupling constants, i.e. $\mathcal{H}_{\mathrm{Fe}}(\lambda, B_4)$.

The Fe^{2+} ions are in an $S = 2$, $L = 2$ configuration, therefore their state can be described in terms of the 25-element representation $|M_L, M_S\rangle$ (where M_L and M_S take the values -2,-1, ..., 2). In this representation the spin and orbital angular momentum operators $(S, L, S_x, L_x, ...)$ can also be written as 25×25 matrices, and therefore the entire single ion Hamiltonian $\mathcal{H}_{\mathrm{Fe}}(\lambda, B_4)$ can be expressed as such a matrix.

To find the eigenstates of the single ion system, all that is required is to diagonalise this matrix, which was done numerically, and from this the full spectrum of states for a single Fe^{2+} ion in $FeSc_2S_4$ have been derived. For typical values (e.g. single ion measurements on Fe^{2+} in CdTe [10]), the groundstate is found to be a singlet with a complex admixture of spin and orbital contributions, which is identified as the 'Spin Orbital Singlet' (SOS). In the limit of $\lambda \ll B_4$ this singlet state is given by:

$$|0\rangle = \frac{1}{\sqrt{2}}|L^z = 0\rangle|S^z = 0\rangle + \frac{1}{2\sqrt{2}}\left(|L^z = 2\rangle + |L^z = -2\rangle\right)\left(|S^z = \text{-}2\rangle + |S^z = 2\rangle\right). \tag{6.4}$$

Although the exact groundstate contains added terms due to the mixing with states in the t_2 level, this form is adequate to describe the qualitative properties of the SOS; i.e. it is a non-magnetic, singlet state which has a mixture of orbital and spin components. Later on once the values of λ and B_4 have been deduced for $FeSc_2S_4$ this groundstate will be calculated explicitly and the effect of this mixing will be discussed further.

The spectrum of states is shown in Fig 6.2(a), the degeneracy of the e doublet and

t_2 triplet is lifted, with the splitting of these levels being proportional to λ, though there remain degeneracies within the level scheme due to the high symmetry of the $\boldsymbol{L} \cdot \boldsymbol{S}$ term. N.B. the layout of 'Free ion → Crystal Field → Crystal Field + Spin-Orbit' in Fig 6.2(a) is used to show how the different terms in the Hamiltonian lift the degeneracies of the 25 free ion levels. The fact that spin-orbit coupling is the last term does not imply its inclussion is perturbative, as it can be seen in (6.1) that both crystal field and spin-orbit terms have entered the Hamiltonian on the same footing.

Given that so far only the single ion picture has been discussed, the wavefunctions should be comparable with other single ion studies of Fe^{2+} (e.g. [11]) and indeed the same 0-field level scheme (i.e. singlet, triplet, doublet,...) is found for the 25 eigenstates here, and the irreducible representation notation of [11] is the motivation for the labelling of levels in the inset of Fig 6.2(a).

In anticipation of neutron scattering experiments on this system, the intensity of transitions between these levels accessible via inelastic neutron scattering (INS) were calculated by computing the matrix elements

$$|\langle f|\boldsymbol{L} + 2\boldsymbol{S}|i\rangle|, \tag{6.5}$$

where $|i\rangle$ and $|f\rangle$ denote the initial and final states, respectively of the Fe^{2+} ion.

Performing these calculations showed that the only transition excitable via INS from the groundstate to a level within the e multiplet is to the first excited state triplet, moreover these calculations suggest that the intensity spectrum is dominated by this transition, with the calculated intensity being at least a factor of 10 higher than other transitions within the e levels even at high (100K) temperatures. The

allowed transitions between states deriving from the e-doublet are shown in the inset of Fig 6.2(a) as white arrows between states (transitions between the e and t_2 states are also possible). Observation of such transitions via inelastic neutron scattering will then allow the single ion parameters λ and B_4 to be derived.

6.2.2 Hopping of Spin-Orbital Triplons

Single ion calculations have shown that the lowest energy excitation from the groundstate, the transition to the 1^{st} excited triplet, is in fact the dominant contribution to the spectrum from inelastic neutron scattering. In Section 2.4.3, repeated reference to the spin-orbital triplon was made; a triply degenerate excitation from the spin orbital singlet groundstate which acts as a spin-orbital analogue to the (spin-only) triplon, and indeed this lowest energy 'transition' can be interpreted in this context as *the creation of a spin-orbital triplon at a given lattice site*. This is shown schematically in Fig 6.2(b), where a spin half neutron comes into the sample and (by flipping its spin) transfers unit angular momentum to the Fe ion. This then breaks the SOS state, and a spin-orbital triplet is formed. Confined to a single site, these excitations are not very inspiring, and indeed if they were so happy living at the same point in the lattice for their lifetime, then the extension from the level scheme in Fig 6.2(a) to the bosonic excitation picture in Fig 6.2(b) is wholly unnecessary.

However, the dominant next-nearest exchange J_2 in $FeSc_2S_4$ allows these spin-orbital-triplons to hop over the lattice of Fe^{2+} sites, via an Heisenberg Hamiltonian,

$$\mathcal{H}_{\text{Heis}} = -\sum_{NNN} J_2 \boldsymbol{S_i} \cdot \boldsymbol{S_j}, \tag{6.6}$$

thus producing dispersive modes (i.e. modes whose energies will depend on their momentum $\boldsymbol{k}$) which should be measurable via neutron scattering. The model used to calculate this dispersion can be summarized as follows; in real space the spin-orbital triplons are created by bosonic operators $\alpha^\dagger(\boldsymbol{r})$, $\beta^\dagger(\boldsymbol{r})$, $\gamma^\dagger(\boldsymbol{r})$ (three operators for the three possible triplon orientations) with an energy cost Δ, i.e. the singlet to triplet gap in Fig 6.2(a) and (b). If an extra term is added to the Hamiltonian which lifts the degeneracy of the three-fold triplon state, then each excitation will have its own energy gap Δ_1, Δ_2, Δ_3. The exchange J_2 couples spins on the same FCC sublattice, or in the language of operators will lead to terms which are products of operators at different sites, hence leading to hopping.

This model then can be described as a '$\Delta - J_2$'-model, in the sense that only the gap Δ and exchange J_2 is considered. This is not to say that the single ion calculations introduced previously are not considered here, as Δ is itself a function of λ and B_4, and the wavefunctions used to form the basis of states are calculated from the numerical diagonalization above. Even with only two parameters, this '$\Delta - J_2$'-model is non-trivial to diagonalize, however using a method of R.M. White *et al* [12] this was solved, and dispersion relations for the spin-orbital triplon modes in $FeSc_2S_4$ were calculated, and the process is explained in detail in Appendix B. Neutron scattering is an ideal probe to measure such excitations in $FeSc_2S_4$, and in the next section such experiments are described.

6.3 Inelastic Neutron Scattering Experiments and Results

A high-quality, polycrystalline sample of $FeSc_2S_4$ were prepared through sintering stoichiometric mixtures of the pure elements by Dr. V. Tsurkan *et al* (see [4] for further information on synthesis). Powder neutron diffraction data on this sample was performed previously by Krimmel *et al* [3] and confirmed the $Fd\bar{3}m$ structure with lattice parameter $a = 10.51$Å. This sample, with total mass of 4 grams, was used for both zero field and in-field inelastic neutron scattering measurements, and these experiments will now be described in some detail.

It should be noted that, as these are powder scattering experiments, the dynamical structure factor $S(\boldsymbol{Q}, \omega)$ can only be measured as a function of the magnitude $|\boldsymbol{Q}|$, as the powder averaging essentially integrates over all possible directions of $\boldsymbol{Q}$.

6.3.1 Zero Field Neutron Scattering

The first attempt to measure the excitations of this SOS state took place on the MERLIN time of flight, Inelastic Neutron Spectrometer (INS) at ISIS. The above sample was placed, with annular geometry in an Aluminium 'can', into an Orange Cryostat, before being cooled to base temperature (2.2K). The white beam from the ISIS spallation source was filtered into monochromatic pulses using a Fermi Chopper, and these neutrons were focussed on the sample before being scattered into the array of He^3 detectors (see Section 3.1.5, for further information on experimentation).

Initially, a number of incident energies (E_i), up to 200meV were used, in an attempt to observe transitions from the ground state to one of the spin-orbit split crystal field levels (see Fig 6.2(a)). However, limited to the intrinsic error of the

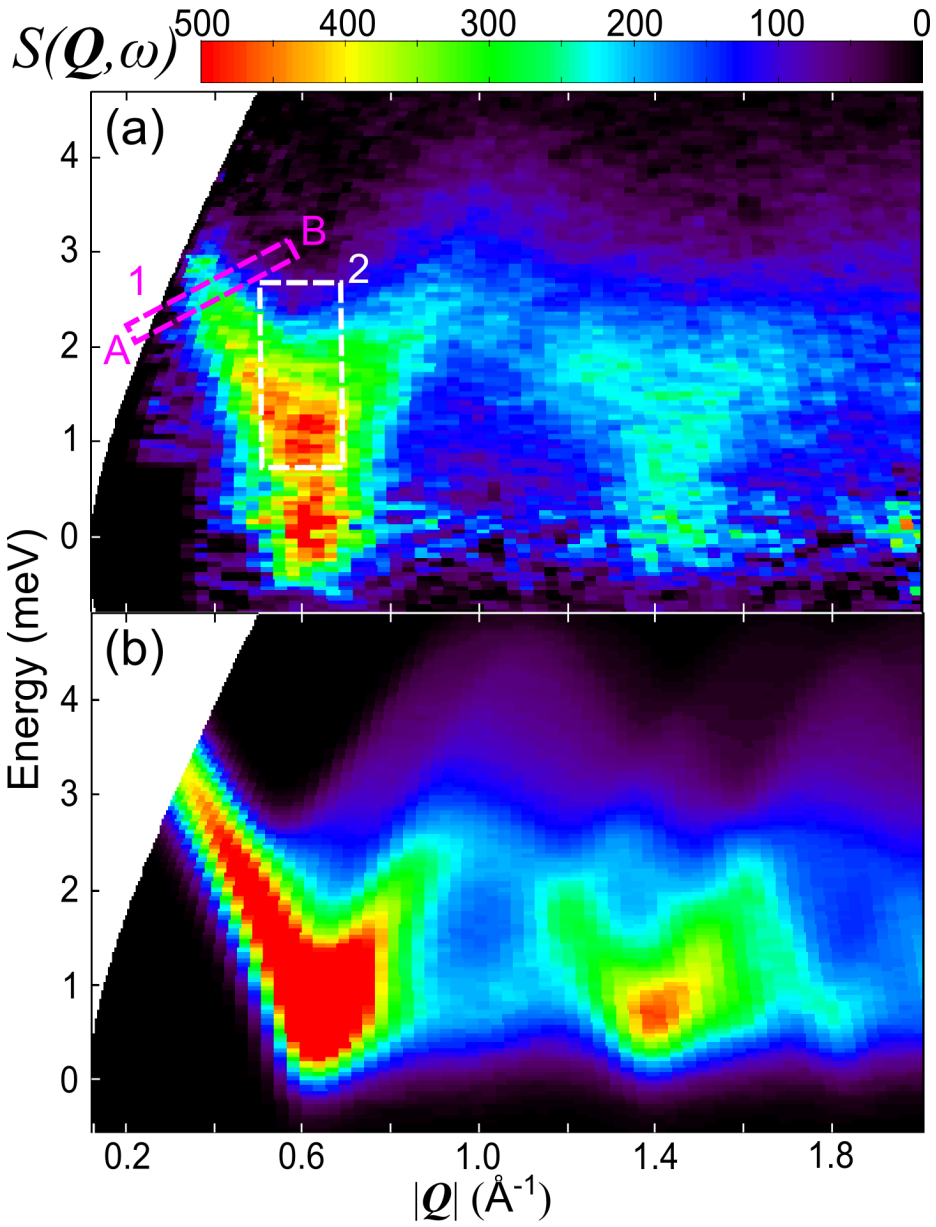


Figure 6.3: INS data and simulation from MERLIN experiment (a) Highly dispersive magnetic excitations as measured on MERLIN with E_i=15meV, low T (2.2K) data with high T (50K) data used for subtraction, cut regions for Fig 6.4(a) also shown (b) Simulation of data from calculations outlined here, data shown were spherically averaged by calculating the intensity for 20000 monte carlo iterations.

instrument, no such transitions were observed except for the singlet-triplet excitation with a band centred at around 2meV. This is consistent with the previous section's calculations' suggestion that the groundstate to 1^{st} excited triplet should dominate the spectrum.

Fig 6.3(a) shows the data recorded for an incident neutron energy of 15meV at base temperature, a high temperature data set has been used for subtraction of non-magnetic background, and this subtraction process shall be explained in detail shortly (Section 6.3.2). The data clearly show a dispersive (i.e. the energy of the excitation is not constant as a function of $\boldsymbol{Q}$) excitation, centred around 2meV, extending up to around 4 meV which is interpreted as the band of spin-orbital triplons. The mode is seen to soften at a wavector $Q \approx 0.6\text{Å}^{-1}$, which corresponds to the wavevector $2\pi/a(1,0,0)$ i.e. an ordering vector of Néel antiferromagnetic ordering on an FCC lattice. This was observed previously in neutron scattering measurements performed in a smaller region of $\boldsymbol{Q}$-ω space [3], and again confirms the case of a dominant J_2 interaction. The rather large energy resolution at this incident energy setting ($\Delta E \approx 0.8$meV) means that the gap to the excitation at this mode-softening point cannot be resolved, but the data suggest an upper bound to this gap of 0.4meV, as any bigger should have been resolveable. The small magnitude of this gap suggests that $FeSc_2S_4$ is in close proximity to a critical point between the SOS state and an ordered groundstate (the theoretical phase diagram of $FeSc_2S_4$ has been explored by Chen *et al* [13]).

Measurements were taken at a range of temperatures from base to 50K, and cuts along the energy axis at a mean value of $|\bar{\boldsymbol{Q}}| = 0.6\text{Å}^{-1}$, integrating over a region

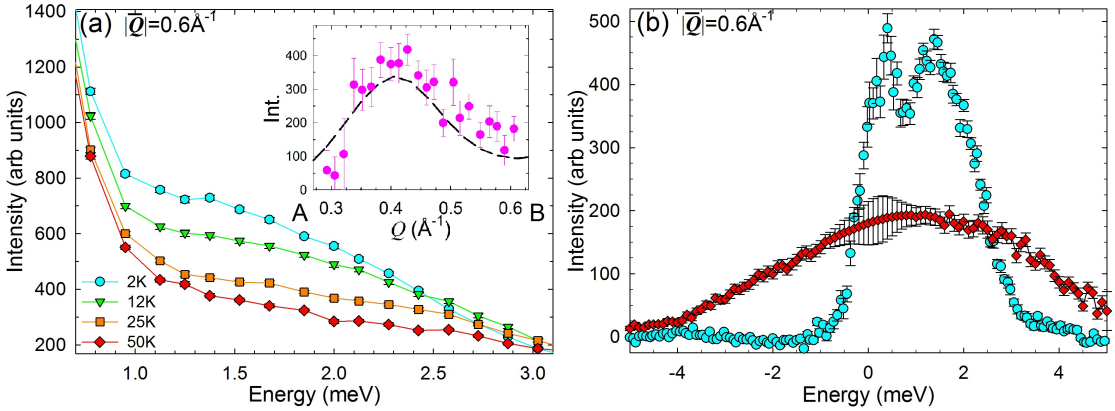


Figure 6.4: Cut along energy showing inelastic signal at $Q = 0.6\text{Å}^{-1}$ at several temperatures (region 2 in Fig 6.3(a)). Inset: Cut along the low-Q shoulder of the dispersion (region 1 in Fig 6.3(a)) magenta points are data and black line is from same region of the calculated $S(\boldsymbol{Q}, \omega)$ (Fig 6.3(b)) (b) An extended cut at the same wavevector for the background subtracted data at base temperature (cyan circles) and at 50 K (red diamonds).

$\pm 0.1\text{Å}^{-1}$ (the integration range is shown as region '1' in Fig 6.3(a)) are shown in Fig 6.4(a). The signal is seen to be heavily T-dependent, broadening as temperature is increased, and this is a clear sign of its magnetic origin. This is also apparent in the background subtracted data of Fig 6.4(b), where the signal is seen to smear out and conforms to the detailed balance described in (3.15). Note that the smooth data points in the 50K are a result of the background subtraction method outlined in the next section.

6.3.2 Background Subtraction

In discussing Fig 6.3(a), it was mentioned that a background subtraction had been performed, and indeed inspection of the data shows that this really must be the case, as no elastic line is evident, even though large parts of Section 3.1 were spent describing the unwanted contributions to signal in this region, as well as the inelastic parts of $\boldsymbol{Q}$-ω space.

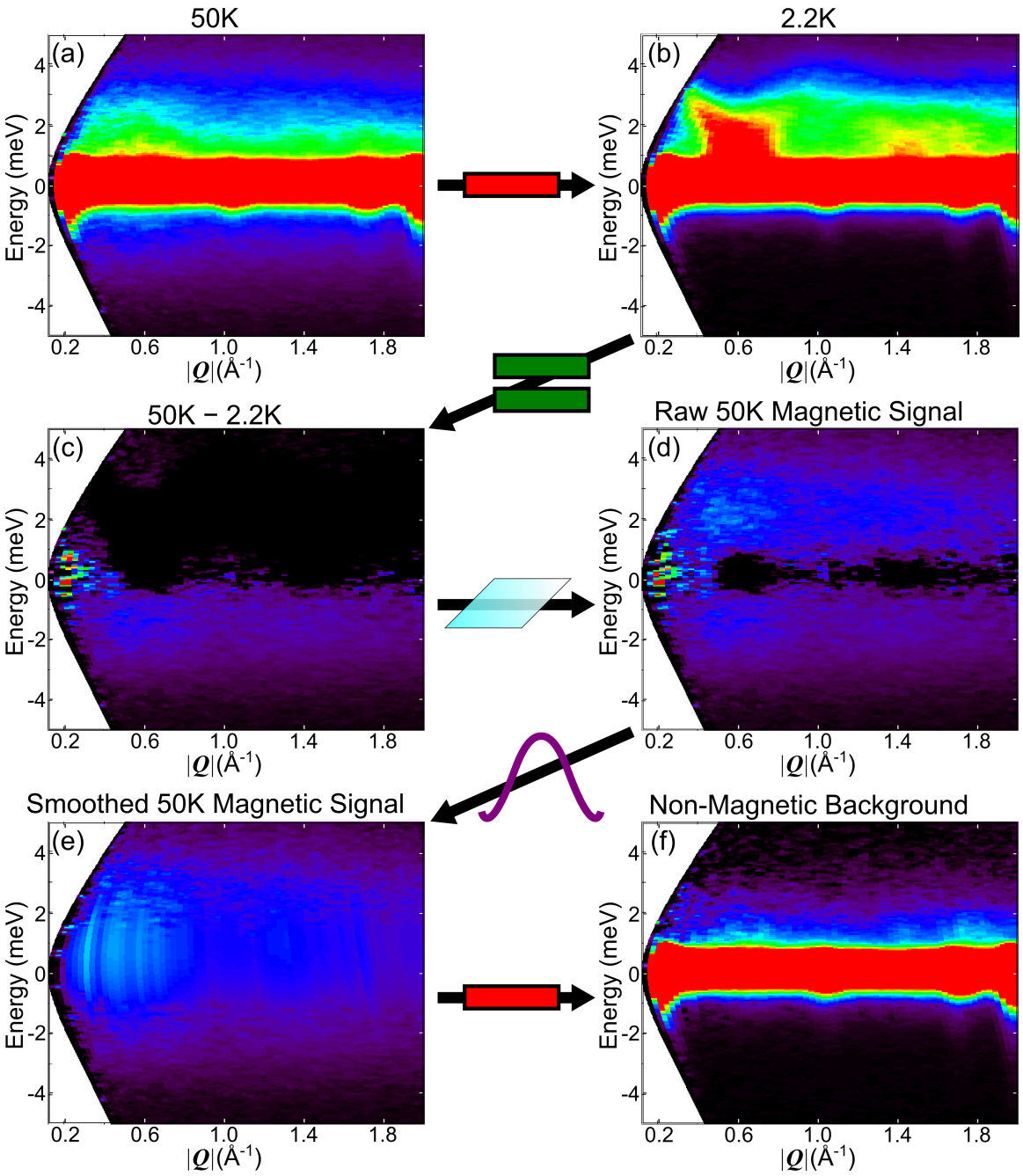


Figure 6.5: Background subtraction procedure for MERLIN data (a) A high temperature data set has the base temperature data shown in (b), subtracted from it, thus producing (c). The $E < 0$ portion is interpreted as the high-temperature magnetic signal, and is reflected about the elastic line to produce (d). This is then smoothed to produce (e), which is an estimate for the magnetic signal at 50K, subtracting this from (a) then leaves only the non-magnetic background, (f). Colour scale is same as in Fig 6.3.

Fig 6.5(b) shows the raw data at base temperature. One can see that, although it shows the same rough features as its 'clean' counterpart in Fig 6.3(a), a lot of the signal is obscured by the elastic line, and fitting a model Hamiltonian to such a data set would be rather inconclusive. Therefore, it would be advantageous to subtract away contributions to the dynamical structure factor of non-magnetic origin, such that only signal which could come from terms in the model Hamiltonian remain. In doing so the principle of detailed balance given in (3.15) and explained in the surrounding text is called upon, i.e. as the temperature is increased, the magnetic scattering does not 'disappear' but simply gets spread across energy and momentum space.

The process taken in going from Fig 6.5(b) to the data shown in Fig 6.3(a) is outlined in Fig 6.5. First the base temperature data (Fig 6.5(b)) is subtracted from a high temperature (50K) data set (Fig 6.5(a)) to produce the signal shown in Fig 6.5(c). In the colour scale chosen, most of the $E > 0$ side is 'blacked-out' in Fig 6.5(c), which simply shows that the sharp triplon scattering mode is not visible at 50K. The $E < 0$ side is however more interesting, it denotes processes in which energy is transferred *to* the neutron. At 2.2K such processes are unlikely, as the system does not have many modes thermally occupied which could transfer energy to the neutron, and is to a good approximation in the groundstate, at higher temperatures however, such processes are made possible by the Boltzmann term in (3.15). The intensity on the negative E part of Fig 6.5(c) is then interpretted as the high temperature magnetic scattering.

Taking into account the Boltzmann term in (3.15), this magnetic signal can be

'reflected' through the elastic line, with the result being the intensity spectrum in Fig 6.5(d). Again, dark regions can be seen, indicating regions of 'negative intensity', this is to be expected especially around the elastic line where incoherent scattering is spread across an energy window equal equal to the instrumental resolution. However, the present concern is not to model the dynamics in such close proximity to the elastic line, and so to move forward the rather reasonable assumption is made that the high temperature magnetic scattering will vary smoothly in $\boldsymbol{Q}$-ω space. In practice this was carried out by fitting each detector bank of signal – excluding the unphysical quasielastic part – in Fig 6.5(d) to a Gaussian function and the result is Fig 6.5(e). This represents an estimate of the high temperature magnetic scattering from the sample and subtracting this from the data shown in Fig 6.5(a), leaves Fig 6.5(f); the non-magnetic signal at 50K.

Cuts through the data at base and 50K with the same non-magnetic background (Fig 6.5(f)) subtracted are shown in Fig 6.4(b). With the non-magnetic background subtracted the magnetic signal is clear, and its signal spreads across the energy axis with increasing temperature, as governed by (3.15). The smoothing performed in going from Fig 6.4(d) to (e) results in the smooth/unrealistic variation in intensity over the quasielastic reigon for the 50K data, however one can see that the general trend of the signal is not altered by this subtraction process.

6.3.3 Neutron Scattering in Applied Magnetic Field

The dispersive mode shown in Fig 6.3(a) was argued to be a spin-orbital triplon mode which hops over the lattice due to a dominant next-nearest neighbour exchange J_2. The significance of such excitations is that they inherit their groundstate's spin

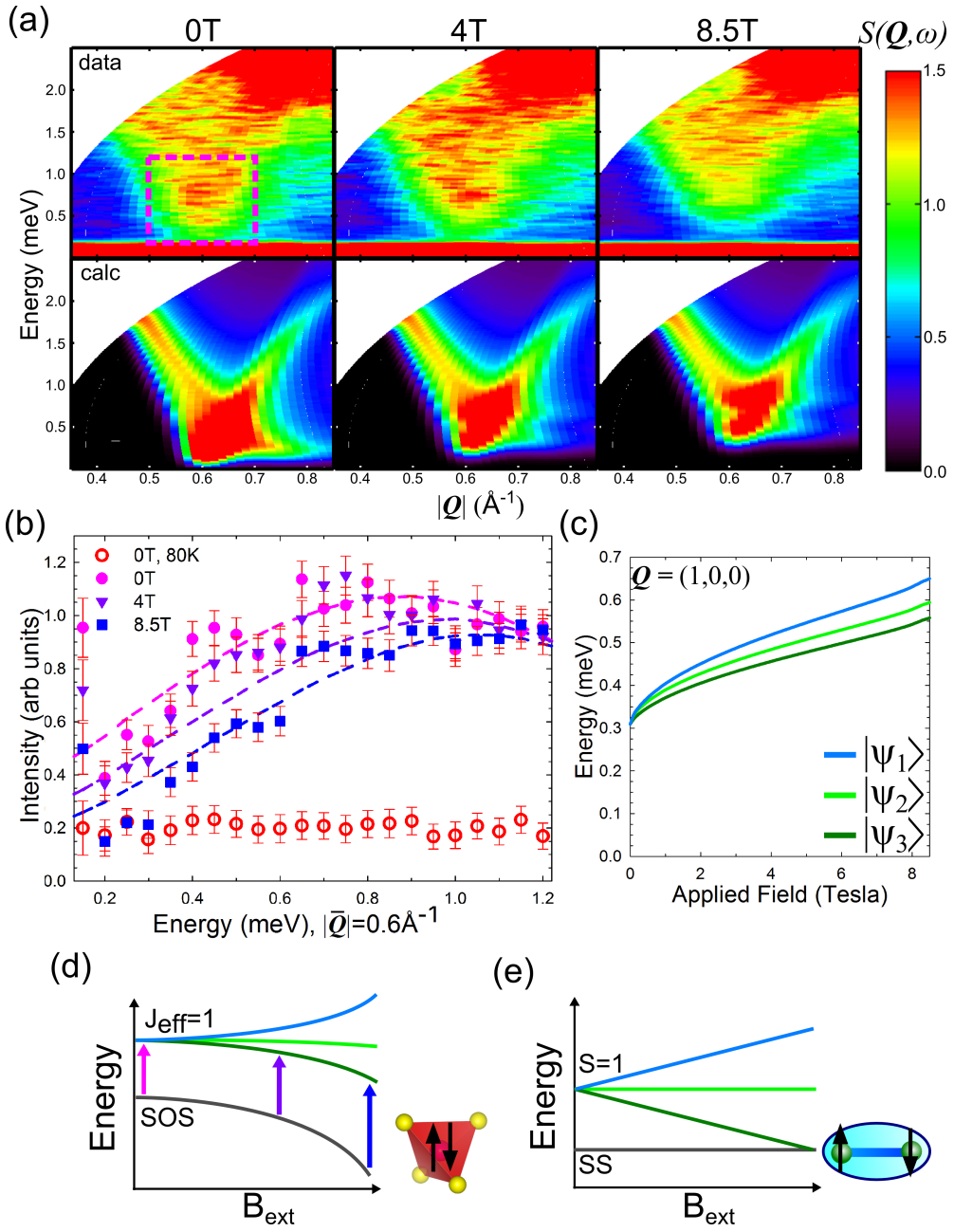


Figure 6.6: INS in magnetic field (a) Upper; FOCUS data at 0, 4 and 8.5 Tesla external fields. Lower; simulation of data for these values of field from caculations outlined here, data shown were spherically averaged by calculating the intensity for 20000 monte carlo iterations. (b) Cut through $S(\boldsymbol{Q},\omega)$ data as measured on FOCUS at $Q = 0.6\text{Å}^{-1}$ at several external fields. Dashed coloured lines are cuts through the calculated patterns of (a), and demonstrate the increasing gap in field. (c) Calculated gap to triplon mode at $\boldsymbol{Q} = 2\pi/a(1,0,0)$. (d) Schematic showing how the groundstate and first excited triplet vary in field, this is in stark contrast to what would be expected for a conventional spin singlet state, (e).

and orbital nature and so are qualitatively different from excitations in spin-only systems. Such a difference is not clear from the previous experiment; the resolved mode could just as easily perhaps be a spin excitation from $FeSc_2S_4$. However it will be seen in the following section how the behaviour of this mode in applied magnetic field clarifies the spin-orbital nature of these excitations.

Field dependent measurements were conducted on the same 4g sample on the FOCUS time of flight, Inelastic Neutron Spectrometer at PSI. An Oxford Instruments 9T Cryomagnet was used to apply a homogeneous field accross the sample, and again the powder was placed with annular geometry into an Aluminium can. Measurements were taken with incident neutron energies of 3.27meV ($\lambda = 5$Å) at a number of different fields, and the scattering intensity maps at 0, 4 and 8.5 Tesla are shown in the upper panel of Fig 6.6(a). The lower incident energy and subsequent higher resolution ($\Delta E \approx 0.16$ meV) compared with the MERLIN data of Fig 6.3(a) means that the full band can no longer be seen, however now a gap to the spin-orbital triplon mode can be clearly resolved in zero applied field. A cut along the energy axis through this data set centred near the mode softening wavevector $\boldsymbol{Q} = 0.6$Å^{-1} (magenta circles, Fig 6.6(b), cut region is also overplotted in Fig 6.6(a)) shows this gap to be somewhere between 0.3 and 0.4 meV.

By comparing the $S(\boldsymbol{Q}, \omega)$ plots in Fig 6.6(a) it is clear that upon increasing the applied magnetic field the gap to excitations increases. This is made more apparent when cuts over the same region (magenta box in Fig 6.6(a)) are compared, as shown in Fig 6.6(b). The magenta circle, purple triangle and blue square data points represent cuts at 0, 4 and 8.5 Tesla respectively and a high T (80K) data set (red circles with

red line) is shown as a background. The magenta, purple and blue lines are guides to the eye and a clear increase, by around 0.2meV is apparent.

This result is striking when one considers the behaviour of a spin singlet state in external field. This is shown schematically in Fig 6.6(e); as the magnetic field increase the three-fold degeneracy of the triplon is lifted, and the triplon corresponding to spins aligned with the external field has its energy reduced. One can imagine increasing the field until this level's energy crosses the groundstate, thus inducing order. The resulting state can also be considered as a condensate of spin-only triplons [14].

In the case of $FeSc_2S_4$, the excitations have been described as being of spin and orbital character, however these have an effective total angular moment $J_{\text{eff}} = 1$, and so each mode will have a different projection J_z onto the direction of the magnetic field, therefore naively one would expect one level to increase in energy, one to decrease and one to remain constant, just as in the spin only case of Fig 6.6(e). How then can the gap to these excitations increase? In Fig 6.6(d) the lowest four energy levels' behaviour in field is shown schematically, here then the reason for an increased gap is clear; the spin-orbital nature of the groundstate leads to the system preferring Zeeman type stabilization of the singlet. Such a situation is not possible for the spin only case of Fig 6.6(e), where the groundstate is a true $S = 0$ state and so is unaffected by the field.

6.4 Analysis of Inelastic Neutron Scattering Data

In the following section, the model of Section 6.2 will be applied to the results of Section 6.3, thus confirming the observed excitations as spin-orbital triplons and

allowing determination of all the relevant terms in Hamiltonians (6.1) and (6.6).

6.4.1 Fitting Zero Field Data

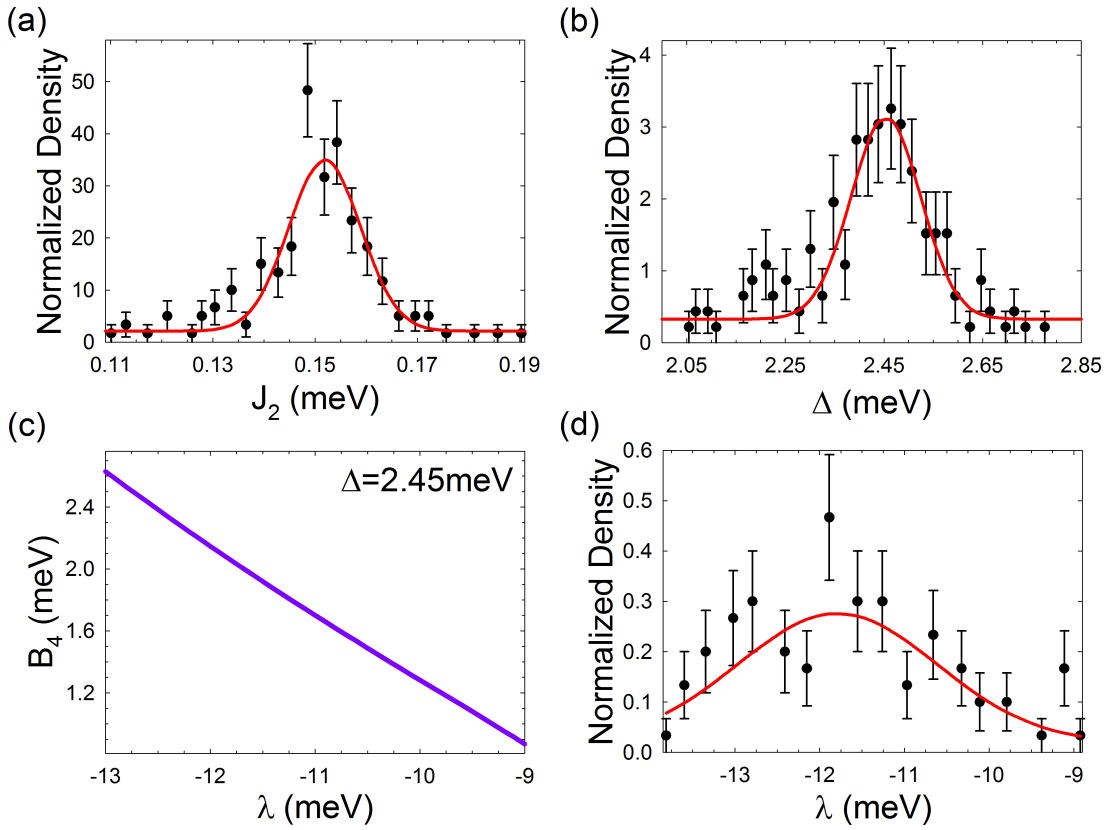


Figure 6.7: Fitting procedure for zero field INS data (a),(b) Histograms resulting from fits of the spin-orbital triplon model to the data (see text) (c) Numerical diagonalization of single ion Hamiltonian produces pairs of values (λ, B_4) constrained to give a constant groundstate-triplet zero field gap, Δ, which is used (d) to produce a fit to the spin-orbital coupling constant λ.

Powder samples can allow for very high purity compounds to be synthesised and relatively straight-forward scattering experiments, however analysing such data, or fitting model Hamiltonians can often be rather difficult. Instead of the sharp excitations which can be mapped throughout three-dimensional reciprocal space, allowing easy fitting and identification, all these modes are folded down onto one $|\boldsymbol{Q}|$ axis.

Fitting a model to a complete powder data set is then challenging and rather ambiguous, therefore instead one chooses certain characteristic features of the spectrum only.

The first of these features will be the gap at the mode softening wavevector $\boldsymbol{Q} = 2\pi/a(1,0,0)$, it represents the lowest energy of the triplon mode throughout reciprocal space and any model should reproduce the position and magnitude of this gap. Although not resolved on MERLIN, this gap can be seen in the zero-field FOCUS data of Fig 6.6(a), and a cut through this data is shown as magenta circles in Fig 6.6(a). The second feature is the low $|\boldsymbol{Q}|$ shoulder of the excitations seen in Fig 6.3(a); such a feature not only tells one about the terms in the Hamiltonian – e.g. a large exchange would push the dispersion to a higher energy at the Γ-point (i.e. the reciprocal space origin) and increase the gradient of the shoulder – but from a practical point of view it gives a region of intensity with a well defined edge to the background. Several cuts were made across this shoulder, and one example is cut '1' in Fig 6.3(a), shown as magenta circles in the inset of Fig 6.4(a).

The fitting procedure is then as follows; the dynamical structure factor is calculated for a given set of parameters, following the expressions shown in Section 6.2, this is then powder averaged using the *MSlice* software [15], which at each value of $|\boldsymbol{Q}|$ calculates $S(\boldsymbol{Q},\omega)$ for a (large) number of randomly oriented $\boldsymbol{Q}$ lying on a sphere of radius $|\boldsymbol{Q}|$. Then cuts through this calculated powder averaged dynamical structure factor are compared with cuts through the data, and through repeating this process of calculation and comparison, a subset of parameters are optimized.

Due to the inherent ambiguities associated with fitting powder data, a single

optimisation procedure was not sufficient to provide meaningful errors on the fitted parameters. Therefore, this optimisation process was performed several times, and before each fitting procedure the data points were shifted randomly, where the shift is governed by a Gaussian probability with FWHM corresponding to the experimental error. This procedure then simulates the result of fitting parameters to the same experiment conducted multiple times. Following each fitting process the optimum values are recorded, and initial values randomized before the next one begins. For each parameter then one can form a histogram of fitted values, which should hopefully follow some Gaussian distribution, and the centre is interpreted as the true value of the parameter and the full width half maximum as its error. Examples of such histograms are shown in Fig 6.7.

Some difficulties arise however; the calculations outlined in Section 6.2 followed the procedure of solving the single ion Hamiltonian, governed by spin orbit (λ) and crystal field B_4, then using the splitting between the groundstate and first excited triplet, Δ_1, Δ_2, Δ_3 and the calculated wavefunctions in the pseudo boson Hamiltonian to calculate dispersive modes, which in the approximation outlined here depend only on the next-nearest exchange, J_2. In other words, the first part of the calculation involved λ and B_4, and the second $\Delta_{1,2,3}$ (which are all functions of λ and B_4) and J_2. Therefore initial measurements at high E_i searching for crystal field levels had a clear motivaton; observation of two or more such levels would've allowed the single ion parameters λ and B_4 to be fitted, leaving only J_2 to be deduced from measuring the spin-orbital triplon dispersion spectrum. However, as explained no such crystal field levels were found, and so one is left with the awkward position of having to fit

all three parameters from a single, powder dispersion spectrum.

The following steps were taken then, first the pseudo boson parameters J_2 and Δ ($=\Delta_1=\Delta_2=\Delta_3$ in zero-field) are fitted using the procedure mentioned above, and the results of such fits are shown in Fig 6.7(a) and (b). Next using the numerical diagonalization of the single ion Hamiltonian described above, the pairs of values (λ, B_4) which result in the given value for Δ are calculated, which results in computing B_4 as a function of λ, as shown in Fig 6.7(c). Finally, the data is fitted by varying λ freely while constraining B_4 to lie on the line shown in Fig 6.7(c), the result being Fig 6.7(d). And through these steps estimates of values for J_2, λ and B_4 (where this is extrapolated by using the fitted value of λ in Fig 6.7(c)) were arrived at.

6.4.2 Zero Field Data Results

The resulting value for the next-nearest exchange J_2 was $-0.15(2)$ meV, where the fit is shown for 200 iterations in Fig 6.7(a). Assuming $J_1 = 0$ and fitting to the high temperature Curie-Weiss behaviour of susceptibility measurements [4] yields a value of $J_2 = -0.11$meV [13], moreover density functional calculations on this system have proposed a value $J_2 = -0.37$ meV [2] (both antiferromagnetic). The value here then is consistent, quite surprisingly so given that only a powder averaged dispersion could be fitted, however the affect of a small J_1 exchange can neither be tested nor ruled out.

The fitted value of Δ shown in Fig 6.7(b) is $\Delta = 2.45(16)$meV, which was used to produce the line of constant Δ in (λ, B_4)-space shown in Fig 6.7(c). Using this, as explained above, the spin-orbit coupling parameter λ was subsequently fitted to the data and the resulting histogram is shown in Fig 6.7(d). Note the very broad

Gaussian fitted here compared with those of Fig 6.7(a) and (b), this is to be expected. The fitting is made to a model whereby pseudobosons are excited across a gap Δ and allowed to disperse over a lattice through next-nearest exchange J_2, and so provided the assumptions that only transitions from the groundstate to this first excited triplet are strong and only next-nearest exchange is relevant one would expect a robust fit to the data. However, in deriving λ, B_4 from the data, essentially these single ion terms are being fitted given only one crystal field level (i.e. the position of the band in the absence of dispersion), an so obviously would expect to fall short.

These values were found to be $\lambda = -11.8 \pm 2.8$meV $B_4 = 2.05 \pm 1.1$meV. The spin orbit coupling parameter for Fe^{2+} in the sister compound $FeCr_2S_4$ has been previously experimentally deduced by Feiner [16] as $\lambda = -10.0(9)$meV and the crystal field term can be deduced from measurements in Fe^{2+} ions substituted into the spinel $CdIn_2S_4$ [17] as $B_4 = 2.85(21)$meV. The fits to the data here are consistent with this, though from the large error bars on such values this is not a surprise.

Given these parameters the wavefunctions for the groundstate and triplet states are calculated explicitly and shown in Table 6.1. As before, it can be seen that the groundstate is a complex admixture of spin and orbital states, and is more complex than the simplified $\lambda \to 0$ form expressed in (6.4), as the spin-orbit coupling has enabled mixing between the groundstate and t_2 levels. Specifically the spin-orbit term mixes only those levels in the same Γ_1 irreducible representation as the groundstate.

With the wavefunctions explicitly calculated, the spin-orbital triplon dispersion can be calculated for the fitted value of J_2, and the powder averaged dispersion is shown in Fig 6.3(b) and Fig 6.6(a) (lower), where experimental resolutions as

$\|M_L, M_S\rangle$	$\|$ G.S. $\rangle$	$\|\Psi_1\rangle$	$\|\Psi_2\rangle$	$\|\Psi_3\rangle$
$\|2,2\rangle$	0.405	-	-0.581	-
$\|2,1\rangle$	-	0.373	-	-
$\|2,-1\rangle$	-	-	-	0.322
$\|2,-2\rangle$	0.288	-	0.401	-
$\|1,2\rangle$	-	0.0383	-	-
$\|1,0\rangle$	-	-	-	0.156
$\|1,-1\rangle$	0.117	-	0.0357	-
$\|1,-2\rangle$	-	0.0888	-	-
$\|0,1\rangle$	-	-	-	0.851
$\|0,0\rangle$	0.692	-	-	-
$\|0,-1\rangle$	-	0.851	-	-
$\|$-1, 2$\rangle$	-	-	-	0.0888
$\|-1,1\rangle$	0.117	-	-0.0358	-
$\|-1,0\rangle$	-	0.156	-	-
$\|-1,-2\rangle$	-	-	-	0.0383
$\|-2,2\rangle$	0.288	-	-0.401	-
$\|-2,1\rangle$	-	0.322	-	-
$\|-2,-1\rangle$	-	-	-	0.373
$\|-2,-2\rangle$	0.405	-	0.581	-

Table 6.1: The 4 lowest energy wavefunctions for $\lambda = -11.7$meV and $B_4 = 2.0$meV (0-field) expressed in the 25-element basis of $|M_L, M_S\rangle$ states.

derived from elastic line widths have been applied. One can see that the qualitative features of the spectrum in Fig 6.3(b) are reproduced; the mode softens at $|\boldsymbol{Q}| = 2\pi/a$, with a linear branch extending upwards from there to the Γ point, moreover a second softening at around $|\boldsymbol{Q}| = 5\pi/a$ is also reproduced. The zone boundary of the calculation stretches to around 5meV, as does the observed triplon mode. The cut region labelled '1' in Fig 6.3(a) is shown both for the data and calculation in the inset of Fig 6.4(a) and the cut through the gap (magenta box, Fig 6.6(a)) measured on FOCUS is plotted for data and calculation in Fig 6.6(b) (magenta circles and black line respectively on both occassions). In both plots, one can see that the calculated intensity profile follows the measured profile reasonably well (FOCUS and MERLIN data were fitted with seperate amplitudes), though there appears to be some 'filling in' of intensity at higher energies in the measured dispersion.

6.4.3 Field Dependent Analysis

With the application of an external magnetic field, another term must be added to the single ion Hamiltonian of (6.1), namely a Zeeman term, $\mathcal{H}_{\mathrm{Z}}$ where

$$\mathcal{H}_{\mathrm{Z}} = \mu_B \boldsymbol{B} \cdot (\boldsymbol{L} + 2\boldsymbol{S}), \tag{6.7}$$

where μ_B is the Bohr magneton and $\boldsymbol{L}$ and $\boldsymbol{S}$ are the orbital and spin angular momentum operators respectively, such that there are three contributions to the single ion physics;

$$\mathcal{H}_{\mathrm{Fe}} = \mathcal{H}_{cf} + \mathcal{H}_{SO} + \mathcal{H}_{\mathrm{Z}}. \tag{6.8}$$

The result of such a term is to further split the levels depicted in Fig 6.2(a) and lift the three fold degeneracy of the triplet, such that the gap to the triplet level Δ is re-expressed as Δ_1, Δ_2 and Δ_3. This has been previously discussed, and indeed such a splitting was built into the pseudo-boson calculations of Section 6.2. However, in confining the consideration of the magnetic field only to the single ion physics, the fact that as the spin-orbital singlet state gains Zeeman energy – it must have some moment aligned with the field – and these aligned moments can interact via next-nearest neighbour exchange is neglected. Therefore the full Hamiltonian that should be considered is:

$$\mathcal{H} = \mathcal{H}_{cf} + \mathcal{H}_{SO} + \mu_B \boldsymbol{B} \cdot (\boldsymbol{L} + 2\boldsymbol{S}) - \sum_{NNN} J_2 \boldsymbol{S}_i \cdot \boldsymbol{S}_j. \tag{6.9}$$

But, rather than solve (6.9) explicitly, a mean field approach was taken, such that the ion at site i is assumed to be surrounded by 12 NNN with identical spin configurations (assumed to lie parallel to the applied field), i.e. the model Hamiltonian,

$$\mathcal{H} = \mathcal{H}_{cf} + \mathcal{H}_{SO} + \mu_B \boldsymbol{B} \cdot (\boldsymbol{L} + 2\boldsymbol{S}) - 12 J_2 \boldsymbol{S} \cdot \langle \boldsymbol{S} \rangle. \tag{6.10}$$

The ansatz considered is

$$\langle \boldsymbol{S} \rangle = m \hat{\boldsymbol{B}}, \tag{6.11}$$

i.e. that the resulting spin state will be parallel to the applied field, with some effective magnetization m. With this substitution it is then possible to diagnalize (6.10) numerically and extract the state wavefunction $|0\rangle$, and thus the value of the magnetization

$$m' = \langle 0 | \boldsymbol{S} \cdot \hat{\boldsymbol{B}} | 0 \rangle, \tag{6.12}$$

can be calculated. This forms the workings of an iterative process, where the m of (6.11) is varied, (6.10) diagonalized and m' of (6.12) calculated until a consistent solution ($m' = m$) is found. From this value of m, an effective external field B_{eff} is derived which can be substituted inplace of B in (6.8). In this way, the 'single ion (B_4, λ, B) $\rightarrow$ pseudo boson ($\Delta_{1,2,3}$, J_2)' approach can remain, the only difference is that B is replaced by B_{eff}.

Such mean-field calculations were performed for the 4 Tesla and 8.5 Tesla fields corresponding to data sets shown in Fig 6.6(a), and simulations were performed as in the zero-field case to produce the dynamical structure factors plotted in Fig 6.6(b). Again, the calculations show the qualitative features present in the data, namely a shift upwards in the dispersion band (or equivalently an increase in the gap) and a decrease in intensity. The latter effect is a combination of this shift as well as the splitting of the bands, this splitting is pronounced in the calculations where a single, low energy tail is seen to split as the field increases, though such fine structure is not present in the data from FOCUS. The gap at $\boldsymbol{Q} = 2\pi/a(1, 0, 0)$ is calculated explicitly for the fitted parameters and plotted in Fig 6.6(c), where it can be seen that the gap gradually increases for all three modes due to the stabilization of the SOS in field, as shown schematically in Fig 6.6(d).

6.5 Conclusions

To conclude, the system $FeSc_2S_4$, a candidate for a spin-orbital singlet ground-state where both spin and orbital moments remain disordered down to the lowest measurabole temperatures, has been probed via inelastic neutron scattering and the

results of these experiments compared to a model of spin-orbital triplons hopping on a lattice of next-nearest neighbours. The results of INS measurements on MERLIN (0-field) showed the full bandwidth of a dispersive excitation which was interpreted as the excitation of spin-orbital triplons, and allowed the parameters of the microscopic Hamiltonian to be fitted. Further experiments in field revealed the true spin-orbital nature of these excitations by confirming a predicted increase in the gap between them and the ground state as field is increased. Such an effect is in contrast to the expected behaviour for spin-only excitations of spin-singlet systems.

References

[1] W. Roth, Journal de Physique **25**, 507 (1964).

[2] S. Sarkar, T. Maitra, R. Valentí, and T. Saha-Dasgupta, Physical Review B **82**, 041105 (2010).

[3] A. Krimmel, M. Mücksch, V. Tsurkan, M. Koza, H. Mutka, and A. Loidl, Physical Review Letters **94**, 237402 (2005).

[4] V. Fritsch, J. Hemberger, N. Büttgen, E.-W. Scheidt, H. Krug von Nidda, A. Loidl, and V. Tsurkan, Physical Review Letters **92**, 116401 (2004).

[5] A. Ramirez, Chapter 4: Geometrical frustration, in *Handbook of Magnetic Materials*, edited by K. Buschow Vol. 13, pp. 423 – 520, Elsevier, 2001.

[6] H. A. Jahn and E. Teller, Proceedings of the Royal Society A: Mathematical, Physical and Engineering Sciences **161**, 220 (1937).

[7] R. White, *Quantum Theory of Magnetism*, 2^{nd} ed. (Springer, 1982).

[8] M. Hutchings, *Point-Charge Calculations of Energy Levels of Magnetic Ions in Crystalline Electric Fields*, 1^{st} ed. (OUP, 1963).

[9] R. Shankar, *Principles of Quantum Mechanics*, 2^{nd} ed. (Kluwer, 1994).

[10] G. Slack, S. Roberts, and J. T. Vallin, Physical Review **187**, 511 (1969).

[11] C. Testelin, C. Rigaux, A. Mauger, A. Mycielski, and C. Julien, Physical Review B **46**, 2183 (1992).

[12] R. White, M. Sparks, and I. Ortenburger, Physical Review **139**, 450 (1965).

[13] G. Chen, A. P. Schnyder, and L. Balents, Physical Review B **80**, 224409 (2009).

[14] T. Giamarchi, C. Rüegg, and O. Tchernyshyov, Nature Physics **4**, 2 (2008).

[15] R. Coldea, *mslice* software.

[16] L. Feiner, Journal of Physics C: Solid State Physics **1515** (1982).

[17] S. Wittekoek, R. V. Stapele, and A. Wijma, Physical Review B **308** (1973).

Chapter 7

Crystal Field levels and Dynamics of $Ba_3CoSb_2O_9$

In this chapter, inelastic neutron scattering (INS) experiments on the triangular antiferromagnet (TAF) $Ba_3CoSb_2O_9$ are described. Firstly, high energy INS measurements will allow the crystal field levels of Co^{2+} ions to be resolved, and subsequently the terms relevant to its single ion Hamiltonian will be derived. Following this, low energy, high-resolution INS experiments will reveal the spin wave excitations emanating from the 120° ordered phase below $T_N = 3.8K$. However, as will be seen, such linear spin wave calculations are not sufficient to describe all the features of the data, and these anomalies hint at quantum dynamics beyond linear spin wave theory within this realisation of the canonical S=1/2 TAF system.

7.1 Crystal Structure and single-ion energy levels of TAF $Ba_3CoSb_2O_9$

In the following section the crystal structure and crystal field levels are introduced. It will be seen that the crystal structure contains planes of magnetic Co^{2+} ions with perfect three-fold symmetry, while the spin-orbit coupling present means that these ions act with effective $J_{\text{eff}} = 1/2$.

7.1.1 Crystal Structure of $Ba_3CoSb_2O_9$

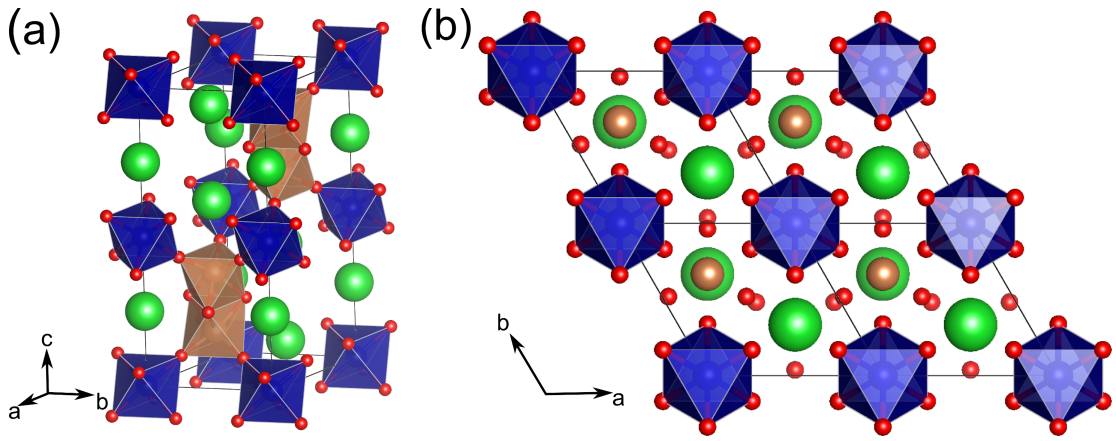


Figure 7.1: Crystal structure of $Ba_3CoSb_2O_9$ (a) Single unit cell showing Co (blue), Ba (green), Sb (gold) and O (red) ions. Cobalt and Antimony are located in the centre of weakly distorted Oxygen octahedra, and these are shown as polyhedra. (b) *ab*-plane showing the triangular lattice of magnetic Co^{2+} ions.

A single unit cell of $Ba_3CoSb_2O_9$ is shown in Fig 7.1(a), it can be seen that layers of CoO_6 octahedra (blue polyhedra) are seperated by a layer of Barium and Antimony ions (green and gold respectively) [1]. Note that the Sb ions form 'dumbbells' from pairs of face-sharing octahedra, such features are also present in $Ba_3CuSb_2O_9$ [2], but there the dumbbells are formed from a pair of Cu and Sb ions. Such structures are then intrinsically prone to site-disorder, as the energy cost for Cu/Sb ions to sit in one octahedron or another is very similar. Here however, only Sb ions sit in the dumbbells, meaning that they are in completely distinct sites from the magnetic ion in the system, resulting in the absence of such site disorder [1].

The structre is highly symmetric, and described by the hexagonal space group $P6_3/mmc$ (no. 194) with lattice constants a=5.8562 Å and c=14.4561 Å (at room temperature) [3]. In the *ab*-plane magnetic Co^{2+} ions form a perfect triangular lattice, as shown in Fig 7.1(b). The nonmagnetic layer of Ba^{2+} ions and pairs of SbO_6

octahedra means that the exchange within these triangular Co layers dominates, meaning that $Ba_3CoSb_2O_9$ is a prime candidate to study a two-dimensional triangular antiferromagnet.

Magnetic susceptibility and specific heat measurements have been performed previously by Doi *et al* [3]. The former show, at high temperature (300K - 400K), Curie-Weiss behaviour with $\theta_{\mathrm{CW}} = -51(4)$K, as well as a broad peak at around 6K typical for frustrated magnetic systems [4]. A sharp cusp is seen at 3.8K, which signals magnetic order stabilized by the weak inter-layer coupling. The specific heat measurements confirm the presence of ordering, showing a λ-type anomaly at 3.8K.

7.1.2 Crystal Field Levels in $Ba_3CoSb_2O_9$

The magnetic Co^{2+} ions are in a $3d^7$ configuration with $L = 3$, $S = 3/2$. The effect of a cubic ligand field on such an ion is to split the degenerate $L = 3$ levels into the irreducible representations Γ_2, Γ_5, Γ_4 (an orbital singlet and two orbital triplets, in this order, respectively) [5], and this is shown schematically in Fig 7.2(a).

The crystal field levels of Co^{2+} in such a configuration have been extensively studied in a variety of systems, and from diagonalising the crystal field Hamiltonian, the following wavefunctions are found for the lower triplet [6],

$$\Gamma_4 \begin{cases} (\sqrt{5}/\sqrt{6})\phi_2 + (1/\sqrt{6})\phi_{-1} &= |-1\rangle \\ (2/3)\phi_0 - (\sqrt{5}/3\sqrt{2})(\phi_3 - \phi_{-3}) &= |0\rangle \\ (\sqrt{5}/\sqrt{6})\phi_{-2} - (1/\sqrt{6})\phi_1 &= |1\rangle \end{cases}, \tag{7.1}$$

ϕ_m represents the orbital wavefunction for $L_z = m$. By considering the description of these levels as $|-1\rangle$, $|0\rangle$ and $|1\rangle$ it can easily be verified that

$$\langle \pm 1|L_z|\pm 1\rangle = \mp\frac{3}{2}, \quad \langle 0|L_z|0\rangle = 0. \tag{7.2}$$

That is, within the states Γ_4, the matrix elements of $\boldsymbol{L}$ are excatly the same as the matrix elements of $-3\boldsymbol{l}/2$ between the associated $l = 1$ p-wavefunctions. This vastly simplifies matters when considering the ground state of the Co^{2+} ion, the Γ_4 representation is seperated from its neighbours by an order of 1eV ($\approx 10^4$K), so in typical experiments, only these states will contribute to the physics. Therefore as far as the orbital angular momentum goes, the state can be treated as an effective $l = 1$ triplet.

The dominant contributions still to consider for these states are the spin orbit interaction – as explained above, the orbital moment is not quenched – (2.9) and a uniaxial, trigonal distortion of the octahedra along the cubic [1,1,1] axis [7]. The latter of these contributions is shown schematically in Fig 7.2(a) as orange arrows compressing an octahedron of CoO_6 and is defined by its eigenvalues, which are given as [6]

$$\begin{aligned} \langle 0|V_{\text{trig}}|0\rangle &= 2\delta/3, \\ \langle \pm 1|V_{\text{trig}}|\pm 1\rangle &= -\delta/3, \end{aligned} \tag{7.3}$$

where V_{trig} is the distorting potential. The Hamiltonian can then be written as:

$$\mathcal{H} = -\frac{3}{2}\lambda(\boldsymbol{l}\cdot\boldsymbol{S}) - \delta\left[(l_z)^2 - \frac{2}{3}\right], \tag{7.4}$$

where $\boldsymbol{l}$ ($l = 1$) is the effective orbital moment, $\boldsymbol{S}$ is the spin ($S = 3/2$), λ is the spin-orbit coupling parameter and δ is as defined in (7.3). The Hamiltonian of (7.4) can be diagonalized numerically in the basis of the 12 $|m_l, m_S\rangle$ states, and using typical

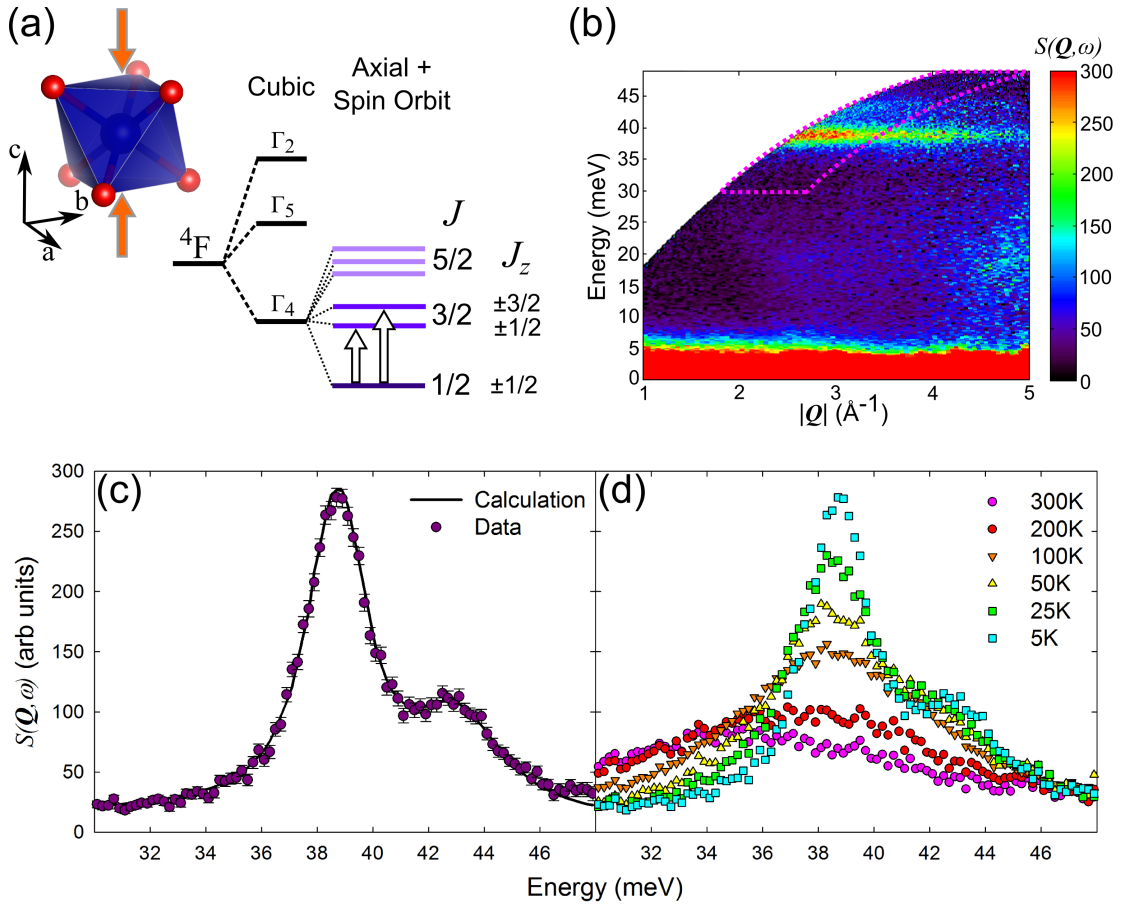


Figure 7.2: Single ion energy levels in $Ba_3CoSb_2O_9$ (a) Schematic showing single ion energy levels as succesive terms are considered in the Hamiltonian, white arrows denote transitions observed via neutron scattering, inset sketches the effect of a trigonal distortion on a Co^{2+} ion (b) Neutron Scattering data from MERLIN (c) Cut through region shown as magenta box in (b) (magenta circles) and a fit to the data (solid black line) (d) the same cut at various temperatures.

values (e.g. those for Co^{2+} in $CsCoCl_3$ [8]), one arrives at the level scheme shown schematically in Fig 7.2(a). N.B. the ordering of the $J_{\text{eff}} = 3/2$ levels is depicted the opposite way from how they appear in $CsCoCl_3$, for reasons which will be explained later.

It can be seen that each level is doubly degenerate (they are Kramer's doublets), and that the lowest level is a $J_{\text{eff}} = 1/2$ doublet, therefore in its groundstate, Co^{2+} ions in $Ba_3CoSb_2O_9$ *are effective spin half ions on a triangular lattice.* Studying the level scheme sketched in Fig 7.2(a), it is clear that a strong neutron scattering amplitude is to be expected for transitions from the $J_{\text{eff}} = 1/2$ groundstate to the $J_{\text{eff}} = 3/2$ states, as these transitions involve a unit change in angular momentum, which is facilitated in a neutron scattering experiment by the flipping of the $S = 1/2$ spin of a neutron. These suspected strong transitions are denoted as white arrows in Fig 7.2(a), and the experiments used to search for such levels are described in Section 7.2.1.

Magnetization measurements on $Ba_3CoSb_2O_9$ [1] confirm this single ion picture, where an effective saturation moment $\mu_{\text{eff}} \approx 2\mu_{\text{B}}$ was measured and derived g-factors close to 4 are found. Moreover the g-factor is found to be almost completely isotropic, which is a very unusual result for a material containing cobalt, as usually these Co^{2+} ions have a strongly Ising character due to strong distortions in the local ligand environment, e.g. in $CoNb_2O_6$ $J_{zz}/J_{\perp} \approx 4$ [9] and in $CsCoCl_3$ $J_{zz}/J_{\perp} \approx 10$ [10].

It is interesting to note, given that a number of candidate systems for triangular antiferromagnets contain Cu^{2+} as the magnetic ion (e.g. Cs_2CuCl_4 [11], Cs_2CuBr_4 [12], $\kappa-(\text{BEDT-TTF})_2Cu_2(CN)_3$ [13]), that it is not thought possible to realize a

regular triangular lattice with Cu^{2+} ions in an octahedral environment [14]. Cu^{2+} is in a $3d^9$ configuration, giving $L = 2$, therefore in an octahedral environment, the orbital levels split to the usual e_g and t_{2g} states (2.11), with a lower, completely filled t_{2g} and doubly degenerate e_g. A trigonal distortion is not able to lift the degeneracy of these e_g levels [5], and so a large Jahn-Teller energy of order 3000K cannot be released [14], therefore such trigonal Copper compounds are not in general stable at low temperatures.

7.2 Inelastic Neutron Scattering Experiments on $Ba_3CoSb_2O_9$

In the next section the inelastic neutron scattering (INS) experiments performed on a high quality powder sample of $Ba_3CoSb_2O_9$ synthasised by Prof. M.A. Hayward *et al* (see [1] for further information on synthesis) are described and interpretted.

7.2.1 Searching for Single Ion Levels

A 16.5g powder sample was placed, with annular geometry into an aluminium can (extra aluminium spacers were included to avoid scattering into the base of the sample can) before being placed in a CCR and lowered to base temperature ($\approx$ 5K) wthin the MERLIN spectrometer. Starting with incident beam energy, E_i, of 500meV it was possible to search for transitions from the groundstate to other single-ion levels. The first signal of such a transition was observed with E_i=300meV, which displayed a broad band of intensity centred at around 40meV. With lower E_i the feature could be clearly seen, and Fig 7.2(b) shows an example of a MERLIN data set with E_i=50meV, where in fact two features can be seen, a high intensity band just below 40meV and a

weaker broader one slightly above this energy. Cuts through this region demonstrate the signal clearer, and these are shown in Fig 7.2(c) and (d).

The sharp drop-off in intensity with increasing Q which can be seen in Fig 7.2(b) is a clear sign of its magnetic origins, as well as the broadening of the signal with increasing temperature (Fig 7.2(d)). As the experiments were conducted at low enough temperatures (5K $\approx$ 0.4meV) such that the system may be considered as being in its groundstate, and the fact that these were the only transtions observed, the signal is interpreted as the transitions from the $J_{\text{eff}} = 1/2$ groundstate to the two (both doubly degenerate) $J_{\text{eff}} = 3/2$ states (shown as white arrows in Fig 7.2(b)).

These levels were then fit by numerically diagonalising (7.4), and values of $\lambda =$ 18.2meV and $\delta = 8.64$meV were obtained, with the calculated intensity profile being shown as the black line in Fig 7.2(c). The value for the spin-orbit coupling should not vary greatly from other systems of Co^{2+} ions, and indeed the value is extremely similar to that found in $CsCoCl_3$ [8], $\lambda = -18.4$meV, whereas the axial distortion will be very dependent on the specific system (type of ligand, etc) and so the deviaton ($\delta = -51.3$meV in $CsCoCl_3$ [8]). From these values for the single ion Hamiltonian, a value of $g = 4.66$ is calculated, which although larger than the expected value, is of the same order as that derived from high field experiments [15].

The much smaller distortion parameter here is also consistent with the measured g-factors being nearly isotropic [1], as such a result implies a rather symmetric local environment for the Co^{2+} ions. The change in sign between the two values is the reason for the aforementioned switch of the order of $J_{\text{eff}} = 3/2$ levels between $Ba_3CoSb_2O_9$ and $CsCoCl_3$.

From Fig 7.2(c) it is seen that there is a reduced intensity for transitions to the upper $J_z = \pm 3/2$ level. This is understandable; spin correlations between x and y components are possible between it and the $J_{\text{eff}} = 1/2$ groundstate, however there can be no correlations between z components. This is not the case between the groundstate and the $J_z = \pm 1/2$ level, where all components contribute to the intensity, so one would naively assume that the intensities would be in the ratio 3:2, i.e. $I_{\pm 1/2}/I_{\pm 3/2} = 1.5$. For the parameters found here it is calculated that $I_{\pm 1/2}/I_{\pm 3/2} = 1.46$. This difference in intensity allows unambiguous determination for the ordering of these states in energy.

During the fitting procedure the fullwidths of the Lorentzian lineshapes used to model the transitions were fit seperately, to give some measure of the consistency of the model. The ratio for these full widths is given by, $\text{FWHM}_{\pm 1/2}/\text{FWHM}_{\pm 3/2} = 0.49$, implying that the higher of the two levels in Fig 7.2(b) is twice as broad. Such an effect could have a physical origin; exchanges between Co^{2+} sites cause a dispersion of the band, which in a powder averaging appears as a broadening of the band (note that the full width of ≈ 5 meV is far greater than the instrumental resolution 1.7meV). Indeed, in the following section it will be seen that such exchange is indeed present in the system, and so it is not an unphysical assumption. The resulting bandwidth for exchange will be related to the projection of the exchange Hamiltonian onto the crystal field level states, therefore one would not expect it to be the same for all levels.

7.2.2 Excitations From the Ordered Phase

Due to a weak interlayer coupling – $J/J' \approx 37$ [15] where J' and J denote the inter and intra layer exchange, respectively – $Ba_3CoSb_2O_9$ orders in a 120° helical

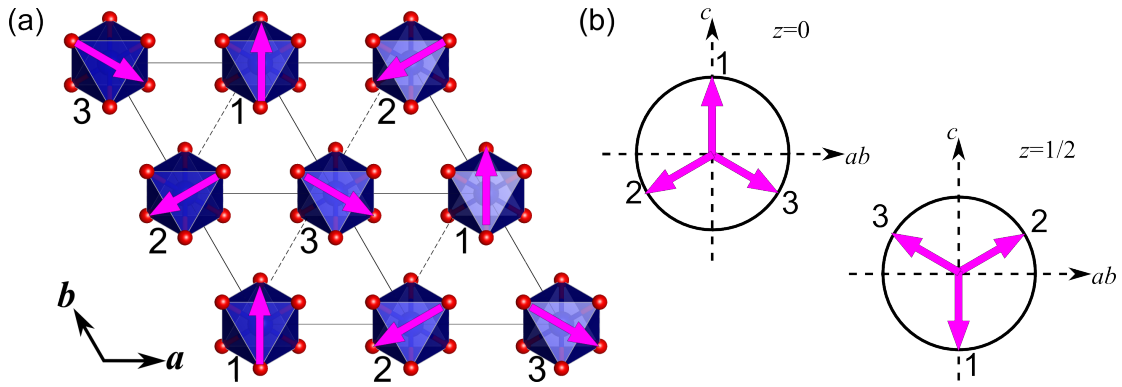


Figure 7.3: Low temperature 120° order in $Ba_3CoSb_2O_9$ (b) *ab*-plane showing the triangular lattice of magnetic Co^{2+} ions, magenta arrows represent the $J_{\text{eff}} = 1/2$ moments in projection. Three magnetically distinct sites are labelled 1-3. (b) These moments lie out of the *ab* plane and there is a phase of π difference between triangular planes upon moving up the *c*-axis. Labels 1-3 correspond to the positions shown in (a).

structure with ordering vector $\boldsymbol{q} = (\frac{1}{3}\frac{1}{3}1)$ [3]. This structure is shown schematically in Fig 7.3(a), where again, the triangular arrangement of Co^{2+} ions is evident. The ordering introduces a six-sublattice structure, with the $J_{\text{eff}} = 1/2$ moments ordered out of the triangular plane, and their six possible orientations are shown in Fig 7.3(b), where the numberings 1-3 correspond to those in Fig 7.3(a), but on different planes within the unit cell. There are two such planes within each unit cell, at $z = 0, 1/2$ (as seen in Fig 7.1(a)), and from Fig 7.3(b) it is clear that they are equivalent but for a phase difference of π.

As explained in Section 3.1.4, the exciations from such an ordered state are the Goldstone modes resulting from broken symmetry, more commonly known as spin waves. The derivation of the dynamical structure factor for two dimensional systems with helical ordering is explained in detail in Appendix C, however here it is beneficial to note some outcomes from this result.

In the case of an isotropic $S = 1/2$ triangular antiferromagnet, the ordering vector

is calculated as $\boldsymbol{q}_{2D} = (\frac{1}{3}, \frac{1}{3}, 0)$, meaning that, as one moves between neighbouring lattice sites there is a $2\pi/3$ rotation of the spins. These spins lie in the same plane, plotting out helical order within the system. The plane in which spins rotate need not be parallel to the triangular plane, in fact, as has already been noted, in $Ba_3CoSb_2O_9$ it is the case that the spins are out of the triangular, *ab*-plane (Fig 7.3(b)). One would then expect spin wave excitations to emanate from the magnetic Bragg peaks governed by $\boldsymbol{q}$. These spin waves have the physical interpretation of deviations from the ordered moment direction, and such deviations are possible both in and out of the ordering plane, resulting in sharp modes in the dynamical structure factor. This is shown in Fig 7.4, where the dynamical structure factor for an isotropic, $S = 1/2$ TAF is plotted along the $(0, k, 0)$ direction, where the orthorhombic lattice appropriate to the anisotropic TAF – described in Appendix C and [11] – has been used. In generating Fig 7.4 the value of the exchange was set to that derived from high magnetic field measurements on $Ba_3CoSb_2O_9$ [1] ($J \approx 1.59$meV). The red solid and green dashed lines represent out of and in plane excitations, respectively, and it can be seen that they are sinusoidal in character, extending up to J and $\sqrt{5/2}J \approx 1.6J$ and indeed emanate from magnetic Bragg peaks (at $(0, \frac{2}{3}, 0)$ and $(0, \frac{4}{3}, 0)$ in the orthorhombic notation).

Deviations along the ordered spin direction are also possible due to zero-point quantum fluctuations in the ground state. When expanded in terms of magnon operators, the spin operator along the ordered moment direction is bilinear (see (C.3)), hence such excitations result in two magnon processes. This results in a continuum of excitations, extending from the lowest magnon mode at a given $\boldsymbol{k}$ to $2\times$ the zone

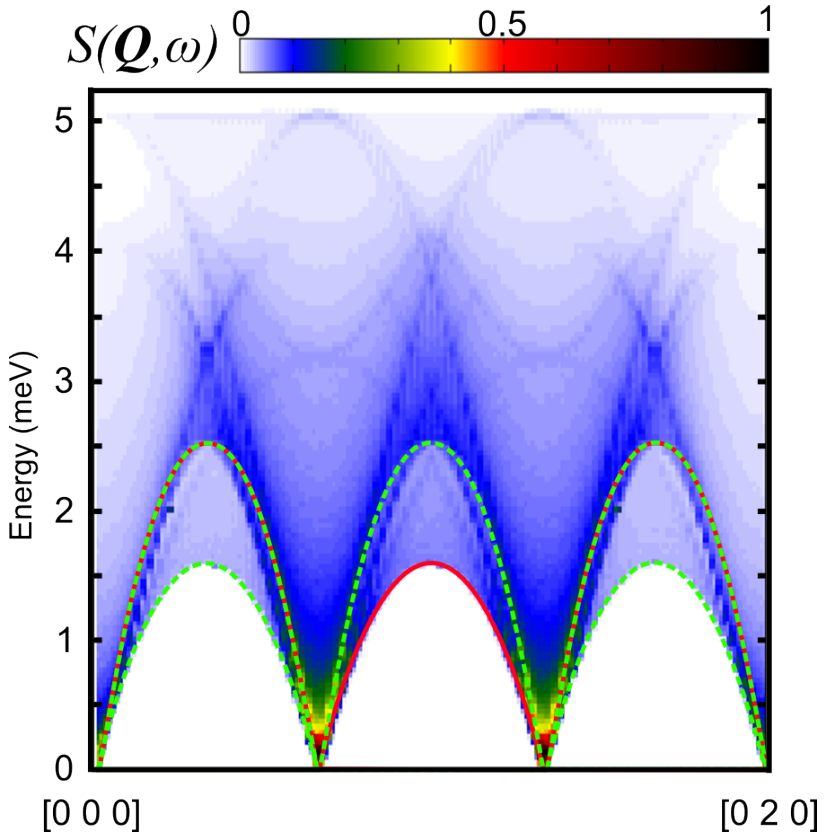


Figure 7.4: Dynamical structure factor for two-magnon processes in the $S = 1/2$ isotropic TAF, as calculated from linear spin wave theory. Red (solid) and green (dashed) lines denote single magnon modes out of and in the plane respectively, and the in-plane two-magnon scattering is normalised such as to satisfy the sum rules. This procedure is explained further in Appendix C.

boundary energy. This extended scattering is seen in Fig 7.4, and was calculated by randomly generating 10^{10} pairs of magnons in the first Brillouin using a weighted Monte Carlo method, using the same code as in [11].

In a powder neutron scattering experiment, the dynamical structure factor is averaged over all directions in k-space, therefore the sharp magnon modes and fine structure of the continuum scattering shown in Fig 7.4 will not be measureable. However, certain characteristics will remain in the powder-averaged pattern; the sharp modes at J and $\approx 1.6J$ will map out bands of scattering intensity at these energies, and two-magnon processes will contribute to a continuum above this energy.

7.2.3 Inelastic Neutron Scattering from Spin Waves

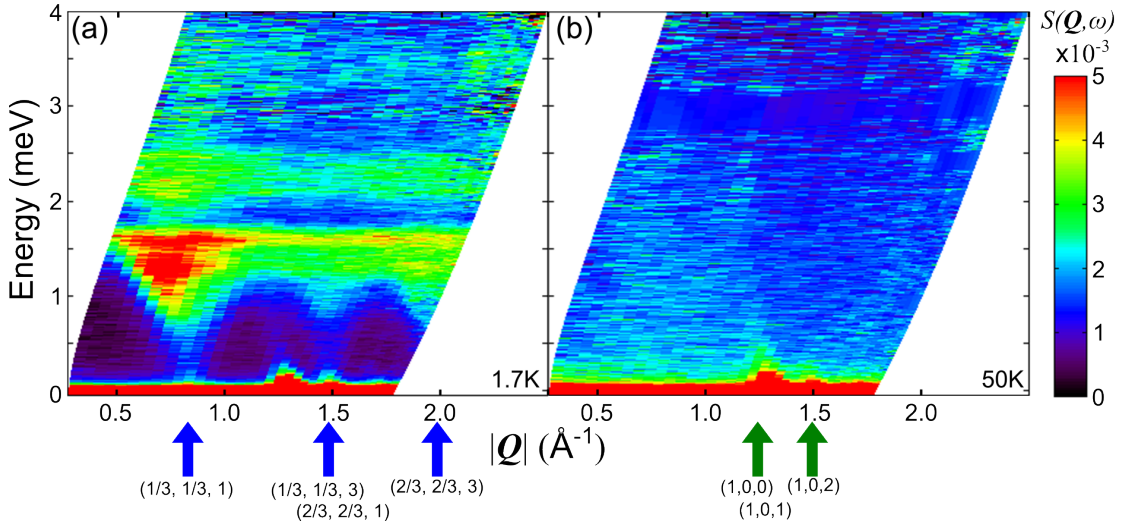


Figure 7.5: Dynamical structure factor measured on OSIRIS at two temperatures (a) 1.7K and (b) 50K. (a) Below the ordering temperature, spin waves emanating from magnetic Bragg peaks are apparent and labelled by blue arrows, whereas in (b) broad paramagnetic scattering is observed, and the structural Bragg peaks remain (green arrows). A spurious feature at around 3meV has been removed from both data sets (see text).

The same 16.5g of powder sample as for the MERLIN experiments of Section

7.2.1 (again an Aluminium can with annular geometry was used) was placed in the OSIRIS instrument and lowered to base temperature (1.7K). After trialing several configurations, the PG002 (i.e. Pyrolytic Graphite's (0,0,2) reflection, see Section 3.1.5 for further information on OSIRIS) setup was used, with the chopper set at 25Hz, and resulting plots of $S(\boldsymbol{Q}, \omega)$ are shown in Fig 7.5.

In Fig 7.5(a), the low temperature data is shown, and spin waves are clearly visible, emanating from magnetic Bragg peaks with ordering vector $\boldsymbol{q} = (\frac{1}{3}, \frac{1}{3}, 1)$. The Bragg peaks visible in this setting are labelled in Fig 7.5(a) and shown as blue arrows. Also the peak at $(\frac{2}{3}, \frac{2}{3}, 3)$ is labelled, though not visible, the excitation emerging from it can be seen. A lower and upper zone boundary, as in Fig 7.4, can be seen at around 1.5meV (J) and 2.4meV ($\approx 1.6J$), as well as a very intense region of scattering at around 0.7 Å^{-1}. This wavevector corresponds to a saddle point in the magnon dispersion, and the increased intensity is a result of a Van Hove singularity [16] (occuring at the M-point in the TAF model described above). Above the zone boundary, a continuum of scattering can be seen, extending up to at least 4meV.

At high temperature, the system is in the paramagnetic phase, and the sharp intensity of spin wave modes is spread over $(\boldsymbol{k}, \omega)$-space, this can be seen in the data shown in Fig 7.5(b). The magnetic Bragg peaks are no longer apparent, however the structural Bragg peaks, labelled by green arrows remain.

The indirect geometry used on OSIRIS allows high resolution, however the method is intrinsically prone to spurious features, particularly repetitions of the elastic line in the data. Such a spurious feature, or 'spurion' was present in the data sets of Fig 7.5. To remove it, an arbitrary, smooth function was assumed for the high temperature

data in the vicinity of the feature, and this smooth estimated signal was subtracted from the raw 50K data to leave only spurious intensity in each detector. This spurious signal was then subtracted from both high and low temperature raw data sets to yield the data shown in Fig 7.5. Evidence of this process can be seen in Fig 7.5(b), where subtraction has left the smoothed stripe at 3meV.

7.2.4 Background Subtraction

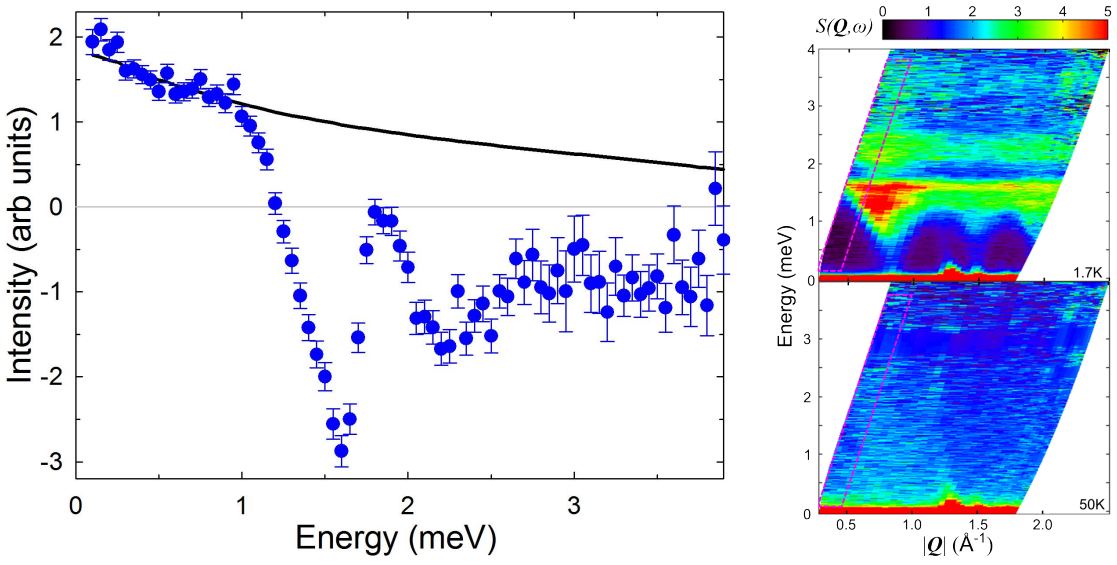


Figure 7.6: Background subtraction procedure. Low temperature data is subtracted from equivalent high temperatre data set, at low $|\boldsymbol{Q}|$, this leaves only the paramagnetic signal (blue circles), which can be fitted with the known form of the second moment, $\langle\omega^2_{\boldsymbol{Q}}\rangle$, assuming a Gaussian line shape (black line). Right: Region of cut shown for high (lower) and low (upper) as magenta box.

In Section 6.3.2 it was explained how knowledge of the negative energy transfer in neutron scattering experiments allowed one to arrive at an estimation for the high temperature magnetic signal through the principle of detailed balance. Here though, OSIRIS only allows windows of $(\boldsymbol{k},\omega)$-space to be measured, therefore the negative energy transfer part was not recorded, and so this method cannot be used to estimate

the high temperature signal.

The sum rule requires that the integral of $S(\boldsymbol{Q},\omega)$ over all $(\boldsymbol{k},\omega)$-space be independent of temperature, such that even though sharp spin wave modes are no longer present at temperatures $\gg T_{\mathrm{N}}$, the scattering signal remains, but is spread out over $(\boldsymbol{k},\omega)$-space. The second moment of $S(\boldsymbol{Q},\omega)$, denoted by $\langle\omega^2_{\boldsymbol{Q}}\rangle$, and defined as [17]:

$$\langle\omega^2_{\boldsymbol{Q}}\rangle = \frac{\int d\omega\, \omega^2 S(\boldsymbol{Q},\omega)}{\int d\omega\, S(\boldsymbol{Q},\omega)}, \tag{7.5}$$

also satisfies a sum rule, and for the TAF it is found that [11], in the limit $T \to \infty$

$$\langle\omega^2_{\boldsymbol{Q}}\rangle = \frac{2}{3}S(S+1)\sum_{\boldsymbol{\delta}} J^2_{\boldsymbol{\delta}}\left[1-\cos(\boldsymbol{Q}\cdot\boldsymbol{\delta})\right], \tag{7.6}$$

where the sum is taken over all exchange couplings $J_{\boldsymbol{\delta}}$, and $\boldsymbol{\delta}$ is a vector connecting sites. Using this, the high temperature data in Fig 7.5(b) was fitted using the $T \to \infty$ limit of (7.6), assuming a Gaussian line shape and assuming that $S(Q)$ is constant. I.e. at each value of $\boldsymbol{Q}$ the high temperature signal is approximated as a Gaussian function, centred on the elastic line with a full width half maximum given by $\approx 2.35\sqrt{\langle\omega^2_{\boldsymbol{Q}}\rangle}$. Using the isotropic exchange J from [1], and $S = 1/2$ in (7.6) leaves only an overall amplitude as an adjustable parameter to fit.

Inspection of the low temperature data of Fig 7.5(a) reveals a kinematically disallowed region at low $|\boldsymbol{Q}|$ below 1meV. Therefore, in creating a data set by subtracting the low temperature data form the high temperature set of Fig 7.5, one can attribute any signal in this region as resulting from paramagnetic scattering. A cut through precisely this data set, in the low $|\boldsymbol{Q}|$ region is shown in Fig 7.6 (blue circles). Using the model described above, the amplitude of the paramagnetic signal was fitted for

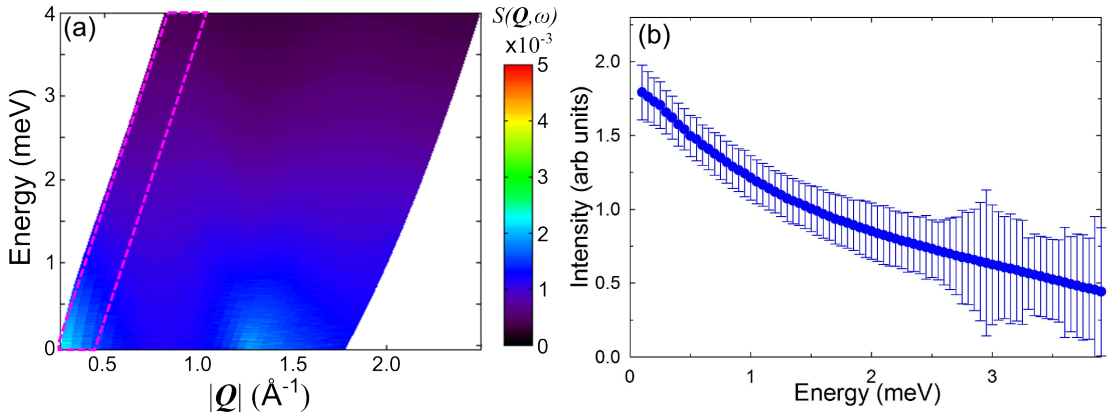


Figure 7.7: Paramagnetic signal (a) Calculated paramagnetic signal using the second moment sum rule (see text). (b) Cut through this data over the same region as in Fig 7.6

the region E $<$ 1 meV, and this fit is shown as the black line in Fig 7.6. From this, the high T paramagnetic signal is generated for the entire $(\boldsymbol{k}, \omega)$-range probed, and subtracting this from the high T data set leads to an estimate of the non-magnetic background, shown in Fig 7.7.

7.2.5 2D TAF Spin Wave Model

This background was subtracted from the low temperature data in Fig 7.5(a) to produce the data shown in Fig 7.8(a). Cuts through this data were then fit to the linear spin wave theory model on the 2D TAF introduced in Section 7.2.3; only the exchange J and an overall amplitude was fitted. The value of the exchange fitted was found to be $J = 1.55(5)$meV, which agrees with the value of $J = 1.59$meV previously derived from magnetization measurements [1]. Following this fitting, the spin wave spectrum for the entire $(\boldsymbol{k}, \omega)$-range was generated, and this is shown in Fig 7.8(b).

Several features are reproduced by this model. Firstly, the pattern of spin wave modes emanating linearly from magnetic Bragg peaks is present in both Fig 7.8 (a)

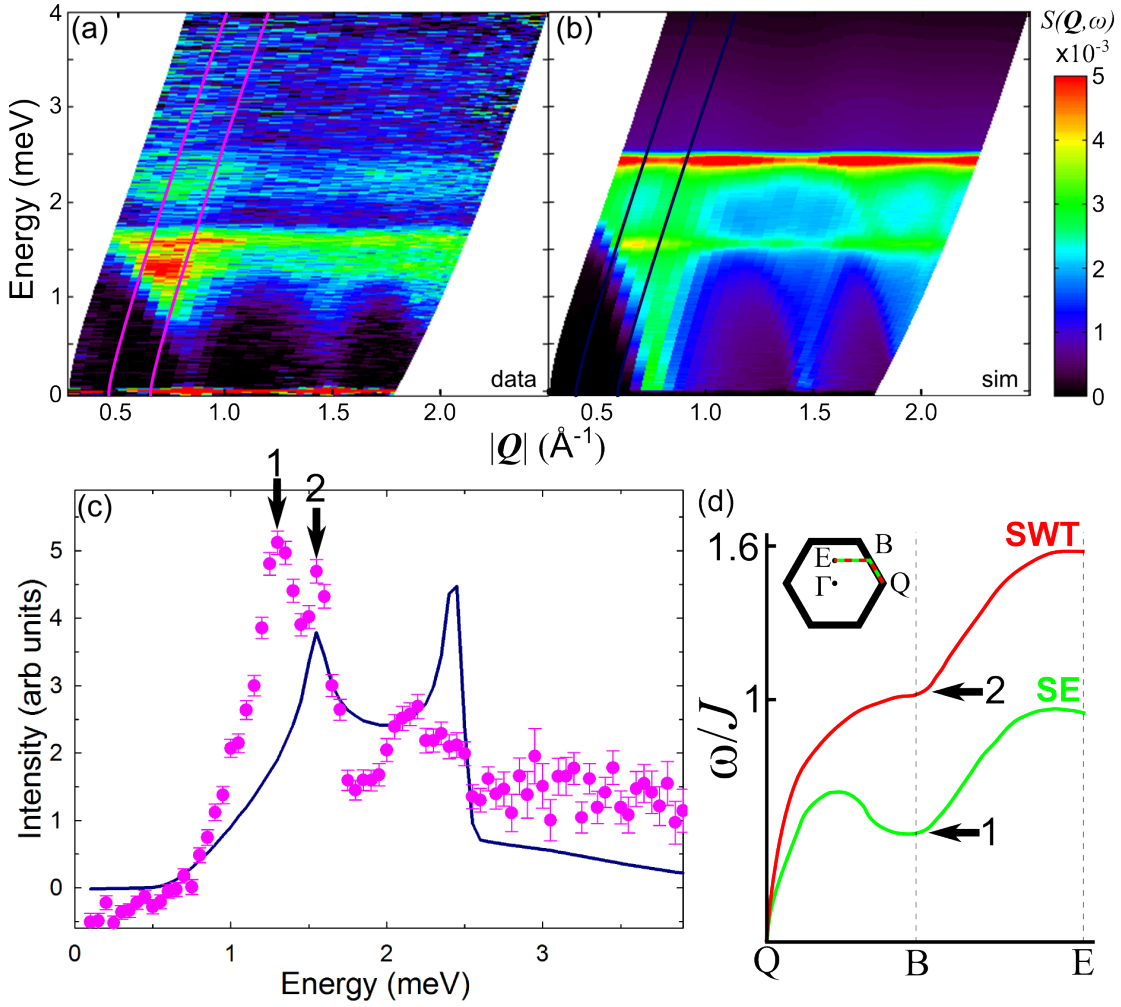


Figure 7.8: Comparisson with the 2D TAF spin wave model (a) Low temperature data with non-magnetic signal subtracted (see text). (b) Spherically-averaged simulation using the classical spinwave model on a 2D TAF with the exchange $J = 1.55$meV. (c) Cuts through data (magenta circles) and simulation (navy line), these cut regions are also overplotted onto the respective data sets in (a) and (b). (d) Schematic dispersion relation along a path in reciprocal space for a spin wave calculation and series expansion for an $S = 1/2$ lattice, showing the qualitative difference between the two (after [18]). Inset: first Brillouin zone with the path through reciprocal space plotted.

and (b). However, being produced by a 2D model, the simulation does not describe the three-dimensional magnetic ordering; e.g. the first magnetic Bragg peak occurs at $(\frac{1}{3}, \frac{1}{3}, 1)$ (≈ 0.84 Å^{-1}) in the data but at $(\frac{1}{3}, \frac{1}{3}, 0)$ (≈ 0.72 Å^{-1}) in the calculation. As shown for a single reciprocal lattice direction in Fig 7.4, the single magnon modes have maxima at J and $\approx 1.6J$, and this is mapped onto two sharp bands at these energies in the powder averaged data of Fig 7.8(b), these two modes are also present in the data of Fig 7.8(b), though certainly the higher of these seems a lot broader. Moreover, continuum scattering produced by two-magnon terms extends up to around 4 meV in the calculation shown in Fig 7.8(b), and having removed the majority of non-magnetic contributions to the signal, it is clear that there are contributions to the measured dynamical structure factor of Fig 7.8(a), extending up to and perhaps beyond 4meV.

There are however qualitative differences between the classical spinwave simulation and the data. The magnon mode softening at magnetic Bragg peaks is sharp in the classical spin wave model, with near constant intensity along the linear part of the dispersion. Experimentally however, these modes seem much softer. Moreover the strong scattering feature at a value of Q corresponding to the M-point – which earlier was attributed to an enhancement in the density of states – looks more like two features seperated slightly in energy. This is more apparent in Fig 7.8(c), where a cut through this feature is shown by magenta data points, and peaks at lower and higher energies are marked by black arrows. This is clearly not captured in the classical spin wave calculation (navy line in Fig 7.8(c)), and is likely due to the dispersion relation displaying quantum effects not captured by linear spin wave theory. One

such modification is the presence of a roton like minimum theoretically predicted through series expansion methods in [18]. These dispersions are shown schematically in Fig 7.8(d), and would seem to provide a qualitative explanation for this 'double peak' structure; the higher energy feature occurs at J and is described by the classical calculation ('1' in Fig 7.8(d)), however the theoretically calculated dispersion taking into account quantum effects introduces a stationary point at M in the dispersion at a lower energy ('2' in Fig 7.8(d)). Clearly further work on single crystals must be performed to justify this identification.

A further discrepancy between the data and the 2D TAF spin wave model is in the intensity of continuum scattering above the zone boundary. In the calculation, Fig 7.8(d) navy line, this appears as a decaying signal at energies above the sharp zone boundary at ≈ 2.5meV, and as explained, is the result of two-magnon processes. In the data however, the zone boundary is far less sharp, and the intensity seems instead to be contributing to significant continuum scattering instead.

The observed pronounced anomalous broadening effects and enhanced intensity of continuum scattering compared to the linear spin wave theory model indicate important quantum dynamics effects at intermediate and high energies not captured in the $1/S$ (non-interacting) spin wave level. Some of the effects observed may be due to magnon decay effects predicted to be present if one takes into account magnon-magnon interactions as in [19]. Other more exotic explanations could be that those anomalous dynamic effects at high energy may indicate a more dramatic failure of the spin wave description at high energies, which one might expect if the system was close in parameter space to a nearby quantum phase with very different excitations, such

as a quantum spin liquid phase often discussed in the context of the triangular lattice. There, the characteristic excitations are predicted to be deconfined spin-1/2 spinons, manifested in a strong continuum scattering in the neutron cross-section. One can imagine varying some parameter in the Hamiltonian continuously going from the ordered phase to the spin liquid phase, in doing so the sharp magnon excitations will be replaced by a continuum of deconfined spinons, and so the latter must grow continuously out of a feature of the former [11]. The multi-magnon processes provide such a feature, and so one might attribute the increase in continuum scattering seen by comparing the $S(\boldsymbol{Q}, \omega)$ plots of Fig 7.8(a) and (b) and the cuts in Fig 7.8(c) as a sign that $Ba_3CoSb_2O_9$ may lie in close proximity to a spin liquid phase.

Further analysis is clearly necessary here, however comparisson to the linear spin wave calculations hints at the presence of quantum dynamics, with qualitatively different dispersions that cannot be captured in this $1/S$, linear spin wave calculation.

7.3 Conclusions

To conclude, the TAF $Ba_3CoSb_2O_9$ has been studied using inelastic neutron scattering on powder samples. High energy neutrons allowed probing of Co^{2+}'s crystal field levels, and the relevant parameters in a single ion Hamiltonian were derived. Those results showed that axial distortions of the ligand environment of cobalt are relatively small here, which is rather unusual given that Co^{2+} tends to be Ising-like in magnetic systems, and this is consistent with previous magnetization measurements of $Ba_3CoSb_2O_9$ were a highly isotropic g-factor was found. The resulting ground state has $J_{\text{eff}} = 1/2$, and the excitations of these ordered moments was also probed

by neutron scattering. Though a model of lineal spin waves propagating on a two-dimensional triangular lattice can describe some features of the data, and yield a value of exchange $J = 1.55$meV comparable to that previously derived from magnetization measurements, there are some features qualitatively different from those produced by this model. These anomalous features were discussed in the context of roton like minima and quantum dynamics beyond linear spin wave theory.

References

[1] Y. Shirata, H. Tanaka, A. Matsuo, and K. Kindo, Physical Review Letters **108**, 057205 (2012).

[2] S. Nakatsuji, K. Kuga, K. Kimura, R. Satake, N. Katayama, E. Nishibori, H. Sawa, R. Ishii, M. Hagiwara, F. Bridges, T. U. Ito, W. Higemoto, Y. Karaki, M. Halim, a. a. Nugroho, J. a. Rodriguez-Rivera, M. a. Green, and C. Broholm, Science (New York, N.Y.) **336**, 559 (2012).

[3] Y. Doi, Y. Hinatsu, and K. Ohoyama, Journal of Physics: Condensed Matter **16**, 8923 (2004).

[4] A. Ramirez, Chapter 4: Geometrical frustration, in *Handbook of Magnetic Materials*, edited by K. Buschow Vol. 13, pp. 423 – 520, Elsevier, 2001.

[5] A. Abragam and B. Bleaney, *Electron Paramagnetic Resonance of Transition Ions*, 1^{st} ed. (Dover, 1970).

[6] M. E. Lines, Physical Review **131** (1963).

[7] S. Nagler, W. Buyers, R. Armstrong, and B. Briat, Physical Review B **27**, 1784 (1983).

[8] T. Nguyen, S. Nagler, R. A. Cowley, T. Perring, and R. Osborn, Journal of Physics: Condensed Matter **7**, 2917 (1995).

[9] D. Prabhakaran, F. Wondre, and A. Boothroyd, Journal of Crystal Growth **250**, 72 (2003).

[10] J. Goff, D. Tennant, and S. Nagler, Physical Review B **52** (1995).

[11] R. Coldea, D. Tennant, M. Tsvelik, and Z. Tylczynski, Physical Review Letters **86**, 1335 (2001).

[12] T. Ono, H. Tanaka, H. Aruga Katori, F. Ishikawa, H. Mitamura, and T. Goto, Physical Review B **67**, 104431 (2003).

[13] Y. Shimizu, K. Miyagawa, K. Kanoda, M. Maesato, and G. Saito, Physical Review Letters **91**, 107001 (2003).

[14] H. Tanaka, H. Dachs, K. Iio, and K. Nagata, Journal of Physics C: Solid State Physics **19**, 4861 (1986).

[15] T. Susuki, N. Kurita, T. Tanaka, H. Nojiri, A. Matsuo, K. Kindo, and H. Tanaka, Physical Review Letters **110**, 267201 (2013).

[16] C. Kittel, *Quantum Theory of Solids*, 2^{nd} ed. (Wiley, 1987).

[17] W. Marshall and S. W. Lovesey, *Theory of Thermal Neutron Scattering*, 1^{st} ed. (OUP, 1971).

[18] W. Zheng, J. Fjæ restad, R. Singh, R. McKenzie, and R. Coldea, Physical Review B **74**, 224420 (2006).

[19] A. Chernyshev and M. Zhitomirsky, Physical Review B **79**, 144416 (2009).

Chapter 8

Concluding Remarks

The first part of this thesis dealt with three-dimensional polytypes of lithium iridate, namely γ-Li_2IrO_3 (Chapter 4) and β-Li_2IrO_3 (Chapter 5), in which the three-fold connectivity of magnetic Ir^{4+} ions and anisotropic spin interactions lead to the proposal that these systems could be physical realizations of Kitaev physics. The former of these is a new structural polytype within the lithium iridates, and the discovery and refinement of this non-trivial, stripyhoneycomb structure was described. Through performing resonant magnetic x-ray diffraction (RMXD) experiments, the low temperature magnetic structure of γ-Li_2IrO_3 and β-Li_2IrO_3 was unambiguously deduced. Such a result was possible even though the former experiments were performed with no prior knowledge of the magnitude of the ordering wavevector, and latter experiments were performed on a sample with maximum dimension 17 μm. The structure in both cases was found to be incommensurate and non-coplanar with a pattern of counter-rotating moments which cannot be stabilized by Heisenberg interactions alone, however both can be described by a model of Heisenberg and Kitaev exchange.

Not only are these systems physical realisations of magnetic structures stabilized

by anisotropic Kitaev exchange, but in fact the same Hamiltonian can be used to describe both γ-Li_2IrO_3 and β-Li_2IrO_3 (the mapping between these two structures is explained in some detail in Section 5.7). This outcome was tentatively suggested when bulk measurements showed the very similar ordering temperatures of these polytypes ($T_N \approx 38$ K [1], $T_N \approx 39.5$ K [2]), but here is found explicitly. The similarities of behavior between these two structural polytypes, which have different global lattice topologies but the same local connectivity, is strongly suggestive that the same magnetic interactions and the same underlying mechanism governs the stability of the magnetic order in both materials, indicating that both β- and γ-Li_2IrO_3 are strong candidates to realize dominant Kitaev interactions in a solid state material. Moreover, the apparent universality of the physics in β-Li_2IrO_3 and γ-Li_2IrO_3 naturally brings about the question as to whether the same physics can be applied to α-Li_2IrO_3.

Polytype	T_N (K)	θ_{CW} (K)	μ_{eff} (μ_B)	μ_{ord} (μ_B)	ϕ (°)
α	15 [3]	-33 [3]	1.83 [3]	-	-
β	38 [4]	40 [4]	1.61 [4]	0.47	55
γ	39.5	-	1.6 [1]	-	42

Table 8.1: Various magnetic properties of the polytypes α-, β-, and γ-Li_2IrO_3

A tentative model for an equivalent helical ordering in α-Li_2IrO_3 has been proposed [5], and this is one among many theoretical works on the honeycomb iridates, suggesting that experiments to determine the magnetic structure of α-Li_2IrO_3 are a priority for this field. Again, RMXD would appear to be the ideal tool here, however as yet no single crystals of the honeycomb iridate α-Li_2IrO_3 have been synthesised, and it seems that only powder RMXD experiments will be possible. Though such experiments are simple in some respects, as it is not necessary to align the sample for

example, they carrry with them their own difficulties as instruments (e.g. I16) are optimised for single crystal environments. Also, even if such experiments are successful, they do not provide an unambiguous solution to the magnetic structure, but rather peaks in k-space which can restrict possible values of the ordering vector, much like the neutron diffraction data mentioned in Section 5.2. Table 8.1 lists some magnetic properties of the polytypes α-, β-, and γ-Li_2IrO_3, and is the current 'state-of-play' as far as the Lithium Iridates are concerned.

Another avenue for further research in γ-Li_2IrO_3 and β-Li_2IrO_3 is to probe the excitations of the magnetic state. These low lying excitations would be the Goldstone modes resulting from the magnetic ordering, but may exhibit anomalous features due to the anisotropic interaction which stabilize the groundstate. An avenue for theoretical work would then be the calculation of such excitations given the model Hamiltonian in [6]. Due to high neutron absorption and small sample size, single crystal inelastic neutron scattering (INS) seems to be out of the question, and again resonant x-ray scattering would be the best probe here. Though currently its resolution is around an order of magnitude greater than INS, resonant inelastic x-ray scattering (RIXS) experiments have proved extremely fruitful in probing iridate systems, e.g. Na_2IrO_3 [7], Sr_2IrO_4 [8], and it seems reasonable that this technique could be used to measure excitations in γ-Li_2IrO_3 and β-Li_2IrO_3.

In Chapter 6, the spin-orbital singlet state of $FeSc_2S_4$ was introduced to describe the atypical properties of the groundstate, namely its refusal to order in the spin or orbital degrees of freedom. Excitations from this spin-orbital singlet groundstate inherit its spin and orbital nature and are termed 'spin-orbital triplons' in analogy with

the spin-only triplons of the equivalent spin only system, and these were measured through INS experiments. A model involving crystal field and spin-orbit coupling contributions to the spin Hamiltonian and next-nearest neighbour exchange between the Fe^{2+} ions was sufficient to reproduce the key features in the dispersion, and fitting to cuts through the powder pattern yielded reasonable values for the spin-orbit coupling and next nearest exchange. INS experiments in magnetic field revealed the true spin-orbital nature of excitations when the gap to the triplons was seen to increase with increasing field. Again, this was reproduced by a model of spin-orbit entangled moments interacting through Heisenberg exchange, and simulations made using the parameters fitted from the zero field data and a mean-field estimation of the effective magnetic field at each Fe^{2+} site agreed well with the data.

As discussed in Section 6.4, fitting parameters to powder averaged data is not ideal, and leads to large uncertainties in the values of such quantities. Therefore, inelastic experiments on single crystal samples of $FeSc_2S_4$ would be ideal for this purpose, and would allow one to map the dispersion of spin-orbital triplons throughout reciprocal space. Such samples were indeed synthesised by Dr V. Tsurkan, and an array of 5 such samples was co-alligned, with total mass 200 mg, and (hhl) in the scattering plane. However, experiments on the time-of-flight spectrometer SNS at Oak Ridge and triple-axis spectrometers TASP and EIGER at PSI, on this array did not yield the expected spin-orbital triplon dispersion, but rather a broad signal, perhaps centred around 2 meV. This central value of the dispersion at least is consistent with the powder data. It is likely that site disorder – a common occurence in spinel structures where the A site ions (Fe^{2+}) and B site ions (Sc^{3+}) switch places randomly throughout the lattice

– is far more prevalent in the single crystal synthesis than for the powder. Such disordering would be expected to have a detrimental effect on coherent excitations, and so the broad signal is perhaps a sign of this.

Awaiting the synthesis of clean single crystal samples, future work on $FeSc_2S_4$ could involve driving the ground state to order through the application of pressure. Such experiments would be similar to measurments on the spin-singlet system $TlCuCl_3$ [9], where the the dynamics near the quantum critical point were probed with the application of pressure and magnetic field. Here it would be hoped that with increasing pressure, the next nearest exchange J_2 would increase sufficiently to drive $FeSc_2S_4$ through a quantum critical point and into the ordered regime, where the triplon modes would condense at the critical point to be replaced by the Goldstone modes of the associated order. Theoretical models of $FeSc_2S_4$ suggest a rich phase diagram on the ordered side of the critical point [10], where orbital and spin moments order at different values of exchange couplings and it would be interesting to confirm such predictions experimentally.

Finally, in Chapter 7 $Ba_3CoSb_2O_9$, a physical realization of a $S = 1/2$ triangular antiferromagnet (TAF) was introduced, which is known to order in a 120° spin structure at low temperatures. INS experiments were performed to probe the single ion levels of $Ba_3CoSb_2O_9$, and revealed two such levels, interpretted as the spin-orbit split $J = 3/2$ levels. This allowed determination of the spin-orbit coupling and trigonal/axial distortion parameters, and it was found that this distortion was rather weak, resulting in Heisenberg like Co^{2+} moments. In itself this was a rather significant result, as cobalt is usually highly Ising-like, but here can be described by

$J = 1/2$ moments with $g = 4$. Further, high-resolution INS experiments were then performed to explore the spin excitations from this ordered state. Fits of this data to the modes of a $S = 1/2$ TAF linear spin wave theory could explain some of the features observed, but qualitative differences were also found, which could possibly be explained by considering magnon-magnon interactions, and may be evidence for proximity to an exotic groundstate, e.g. quantum spin liquid. Further work will first involve modelling the three-dimensional magnetic ordering to arrive at the correct position of magneic Bragg peaks. Also a quantitative comparison to series expansions should be made, as these produce features not present in the $1/S$ linear spin wave spectra, but which might help explain some anomalous features of the data (e.g. roton minima). Single crystals would be required to unambiguously decipher these features.

From a synthesis point of view, $Ba_3CoSb_2O_9$ is but one member of a large family of such triangular compounds, e.g. $Ba_3NiTa_2O_9$ has also been synthesised by collaborators, which promise to be interesting systems to study the canonical triangular antiferromagnet model.

References

[1] K. A. Modic, T. E. Smidt, I. Kimchi, N. P. Breznay, A. Biffin, S. Choi, R. D. Johnson, R. Coldea, P. Watkins-Curry, G. T. McCandless, J. Y. Chan, F. Gandara, Z. Islam, A. Vishwanath, A. Shekhter, R. D. McDonald, and J. G. Analytis, Nature communications **5**, 4203 (2014).

[2] A. Biffin, R. D. Johnson, I. Kimchi, R. Morris, A. Bombardi, J. G. Analytis, A. Vishwanath, and R. Coldea, arXiv:1407.3954v1 (2014).

[3] Y. Singh, S. Manni, J. Reuther, T. Berlijn, R. Thomale, W. Ku, S. Trebst, and P. Gegenwart, Physical Review Letters **108**, 127203 (2012).

[4] T. Takayama, A. Kato, R. Dinnebier, J. Nuss, and H. Takagi, arXiv:1403.3296 (2014).

[5] I. Kimchi, R. Coldea, and A. Vishwanath, arXiv:1408.3640v1 (2014).

[6] I. Kimchi, J. Analytis, and A. Vishwanath, arXiv:1309.1171v2 (2013).

[7] H. Gretarsson, J. P. Clancy, Y. Singh, P. Gegenwart, J. P. Hill, J. Kim, M. H. Upton, H. Said, D. Casa, T. Gog, and Y.-J. Kim, Physical Review B **87**, 220407 (2013).

[8] J. Kim, M. Daghofer, a. H. Said, T. Gog, J. van den Brink, G. Khaliullin, and B. J. Kim, Nature communications **5**, 4453 (2014).

[9] P. Merchant, B. Normand, K. W. Krämer, M. Boehm, D. F. McMorrow, and C. Rüegg, Nature Physics **10**, 373 (2014).

[10] G. Chen, A. P. Schnyder, and L. Balents, Physical Review B **80**, 224409 (2009).

Appendix A

Azimuth Dependence of the Magnetic Resonant X-ray Diffraction Intensity

Here the azimuth dependence of the magnetic x-ray diffraction intensity is obtained and it is shown how it can be used to determine the relative phase between magnetic basis vectors.

A.1 Calculation for a General Azimuth

As discussed in Sec. 4.4 the magnetic diffraction intensity is proportional to $|\mathcal{F}_{\parallel}|^2$ where $\mathcal{F}_{\parallel} = \boldsymbol{\mathcal{F}} \cdot \hat{\boldsymbol{k}}'$ is the projection of the structure factor vector onto the scattered beam direction. To calculate this dot product it is convenient to express both vectors in terms of their components in the laboratory reference frame (this convenient coordinate system was first introduced by Blume and Gibbs [1]) illustrated in Fig A.1 and defined by the orthonormal set of vectors:

$$\hat{\boldsymbol{U}}_{\mathbf{2}} = \hat{\boldsymbol{k}} \times \hat{\boldsymbol{k}}', \quad \hat{\boldsymbol{U}}_{\mathbf{3}} = -\hat{\boldsymbol{Q}}, \quad \hat{\boldsymbol{U}}_{\mathbf{1}} = \hat{\boldsymbol{U}}_{\mathbf{2}} \times \hat{\boldsymbol{U}}_{\mathbf{3}}. \tag{A.1}$$

I.e. $\hat{\boldsymbol{U}}_{\mathbf{2}}$ is normal to the scattering plane and $\hat{\boldsymbol{U}}_{\mathbf{1}}$ is in the scattering plane making

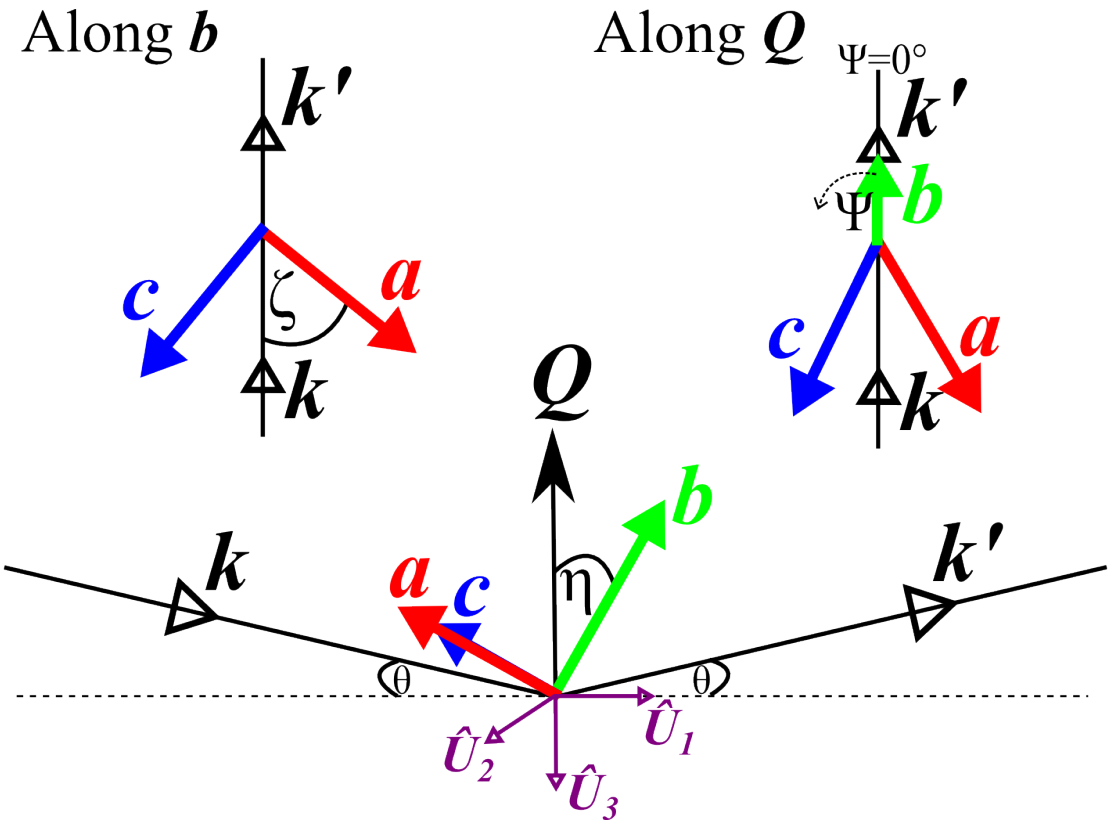


Figure A.1: Schematic diagram of the x-ray diffraction experiment at zero azimuth ($\Psi = 0$). $\boldsymbol{k}$ and $\boldsymbol{k'}$ are the incident and scattered x-ray beam wavevectors, and $\boldsymbol{Q} = \boldsymbol{k'} - \boldsymbol{k}$ is the scattering wavevector. Main (bottom) panel shows the orientation of the laboratory frame unit vectors $\hat{\boldsymbol{U}}_{\mathbf{1,2,3}}$ and the orthorhombic crystal axes ($\boldsymbol{a}$,$\boldsymbol{b}$,$\boldsymbol{c}$). Top left inset: view along $\boldsymbol{b}$ showing the angle ζ subtended from the scattering plane by the $\boldsymbol{a}$ vector. Right inset: view along $\boldsymbol{Q}$. During an azimuth scan the crystal axes are rotated around $\boldsymbol{Q}$ by an angle Ψ (in the sense shown in the figure), the reference position $\Psi = 0$ is defined as the azimuth angle for which $\boldsymbol{b}$ lies in the scattering plane making the smallest angle with the incident beam direction $\hat{\boldsymbol{k}}$.

an angle θ with both $\boldsymbol{k}$ and $\boldsymbol{k'}$, where 2θ is the total scattering angle. The scattered beam direction then can be written as $\hat{\boldsymbol{k'}} = (\cos\theta, 0, -\sin\theta)_L$, where the L subscript indicates that the components are with respect to the laboratory basis of $\hat{\boldsymbol{U}}_{\mathbf{1,2,3}}$ vectors, as opposed to the crystal basis, defined by the orthonormal set of vectors $\hat{\boldsymbol{x}}$, $\hat{\boldsymbol{y}}$, $\hat{\boldsymbol{z}}$ (along the orthorhombic axes $\boldsymbol{a}$, $\boldsymbol{b}$, $\boldsymbol{c}$).

The magnetic structure factor vector $\boldsymbol{\mathcal{F}}$ defined in (4.2) is most naturally expressed in terms of the crystal basis as $(\mathcal{F}_x, \mathcal{F}_y, \mathcal{F}_z)_C$. The components in the laboratory basis $(\mathcal{F}_1, \mathcal{F}_2, \mathcal{F}_3)_L$ are obtained through a linear transformation encoded in a matrix $T(\Psi)$ via

$$\begin{bmatrix} \mathcal{F}_1 \\ \mathcal{F}_2 \\ \mathcal{F}_3 \end{bmatrix} = T(\Psi) \begin{bmatrix} \mathcal{F}_x \\ \mathcal{F}_y \\ \mathcal{F}_z \end{bmatrix}, \tag{A.2}$$

where the dependence of the transformation matrix on the azimuth angle Ψ, which defines the rotation angle of the crystal axes around the scattering wavevector $\boldsymbol{Q}$, has been introduced. To find the transformation matrix, first the reference position of zero azimuth, $\Psi = 0$, depicted in Fig. A.1 is considered. In this case the orientation of the crystal axes with respect to the laboratory axes is specified by two angles η and ζ. Where η is the angle between the $\boldsymbol{b}$-axis and the scattering wavevector $\boldsymbol{Q}$, and given by

$$\eta = \cos^{-1} \hat{\boldsymbol{Q}} \cdot \hat{\boldsymbol{b}}, \tag{A.3}$$

and ζ is the angle between the $\boldsymbol{a}$-axis and the scattering plane, given by

$$\zeta = \tan^{-1} \frac{\boldsymbol{Q} \cdot \hat{\boldsymbol{c}}}{\boldsymbol{Q} \cdot \hat{\boldsymbol{a}}} \,. \tag{A.4}$$

Using the diagram in Fig. A.1 the transformation matrix is obtained as

$$T(0) = \begin{bmatrix} -\cos\zeta\cos\eta & \sin\eta & -\sin\zeta\cos\eta \\ \sin\zeta & 0 & -\cos\zeta \\ -\cos\zeta\sin\eta & -\cos\eta & -\sin\zeta\sin\eta \end{bmatrix}. \tag{A.5}$$

When moving away from the reference position to a finite azimuth angle Ψ the coordinates in the laboratory frame need to be multiplied by the rotation matrix

$$R(\Psi) = \begin{bmatrix} \cos\Psi & \sin\Psi & 0 \\ -\sin\Psi & \cos\Psi & 0 \\ 0 & 0 & 1 \end{bmatrix}, \tag{A.6}$$

such that the resulting transformation matrix from the crystal to the laboratory bases in (A.2) becomes

$$T(\Psi) = R(\Psi)\ T(0). \tag{A.7}$$

Explicitly, substituting (A.5) and (A.6) into (A.7) yields

$$T(\Psi) = \begin{bmatrix} \sin\Psi\sin\zeta - \cos\Psi\cos\zeta\cos\eta & \cos\Psi\sin\eta & -\cos\Psi\sin\zeta\cos\eta - \sin\Psi\cos\zeta \\ \sin\Psi\cos\zeta\cos\eta + \cos\Psi\sin\zeta & -\sin\Psi\sin\eta & \sin\Psi\sin\zeta\cos\eta - \cos\Psi\cos\zeta \\ -\cos\zeta\sin\eta & -\cos\eta & -\sin\zeta\sin\eta \end{bmatrix}. \tag{A.8}$$

Once the structure factor components are obtained in the laboratory basis, then the projection of the structure factor vector along the scattered beam direction is readily obtained as

$$\mathcal{F}_{\parallel} = \cos\theta\ \mathcal{F}_1 - \sin\theta\ \mathcal{F}_3. \tag{A.9}$$

A.2 Calculation for a Specific Bragg Peak - $Fddd$

To illustrate the usefulness of measuring the azimuth dependence of the magnetic x-ray diffraction intensity for determining the relative phase between magnetic basis vectors, the magnetic peak at $(-6, 6, 8) + \boldsymbol{q}$ in β-Li_2IrO_3 is considred. This peak is a good example because it has multiple basis vectors contributing to its intensity. Its azimuth dependence is shown in Fig. 5.5(a). Specifically, in this peak the A_x and F_z basis vectors contribute, therefore $\boldsymbol{\mathcal{F}} = (\mathcal{F}_x, 0, \mathcal{F}_z)_C$ where the structure factor components $\mathcal{F}_x$ and $\mathcal{F}_z$ are of the type $\mathcal{F}_A$ and $\mathcal{F}_F$ in (5.5), (5.3), respectively. Using (A.9) combined with (A.2) and (A.8) one obtains

$$\mathcal{F}_{\parallel}(\Psi) = g_x(\Psi)\ \mathcal{F}_x + g_z(\Psi)\ \mathcal{F}_z, \tag{A.10}$$

where the geometric factors are

$$\begin{aligned} g_x(\Psi) &= (\sin\Psi\sin\zeta - \cos\Psi\cos\zeta\cos\eta)\cos\theta + \cos\zeta\sin\eta\sin\theta, \\ g_z(\Psi) &= \sin\zeta\sin\eta\sin\theta - (\cos\Psi\sin\zeta\cos\eta + \sin\Psi\cos\zeta)\cos\theta. \end{aligned} \tag{A.11}$$

The magnetic scattering intensity is then proportional to

$$|\mathcal{F}_{\parallel}(\Psi)|^2 = |g_x(\Psi)\ \mathcal{F}_x|^2 + |g_z(\Psi)\ \mathcal{F}_z|^2 + 2\mathrm{Re}(\mathcal{F}_z\mathcal{F}_x^*)\ g_x(\Psi)g_z(\Psi), \tag{A.12}$$

where Re() means the real part. The first two terms give the sum of the separate contributions from the two basis vectors, whereas the last (cross-term) is sensitive to the relative phases between the two basis vectors. Using eqs. (5.3), (5.5) the cross-term is proportional to

$$\mathcal{F}_z\mathcal{F}_x^* \propto \begin{cases} \mp i\sin\frac{\pi l}{6}\cos\frac{\pi l}{6} & , \quad F_z \pm A_x \\ \pm\sin\frac{\pi l}{6}\cos\frac{\pi l}{6} & , \quad F_z \pm iA_x \end{cases}. \tag{A.13}$$

The cross-term is therefore directly sensitive to the phase difference between the two contributing basis vectors. If F_z and A_x are in-phase or π out-of-phase (denoted as $F_z \pm A_x$) the product $\mathcal{F}_z\mathcal{F}_x^*$ is purely imaginary, so the cross-term cancels and the intensity is given by the sum of the contributions from the two basis vectors taken separately. This is clearly inconsistent with the data (purple curve in Fig. 5.5(a)). A phase difference of $\pm\pi/2$ between the two basis vectors (denoted as $F_z \pm iA_x$) gives a finite cross-term, which changes sign between those two cases, and the data in Fig. 5.5(a) identifies the basis vector combination as $F_z + iA_x$ (red solid line).

A.3 Calculation for a Specific Bragg Peak - *Cccm*

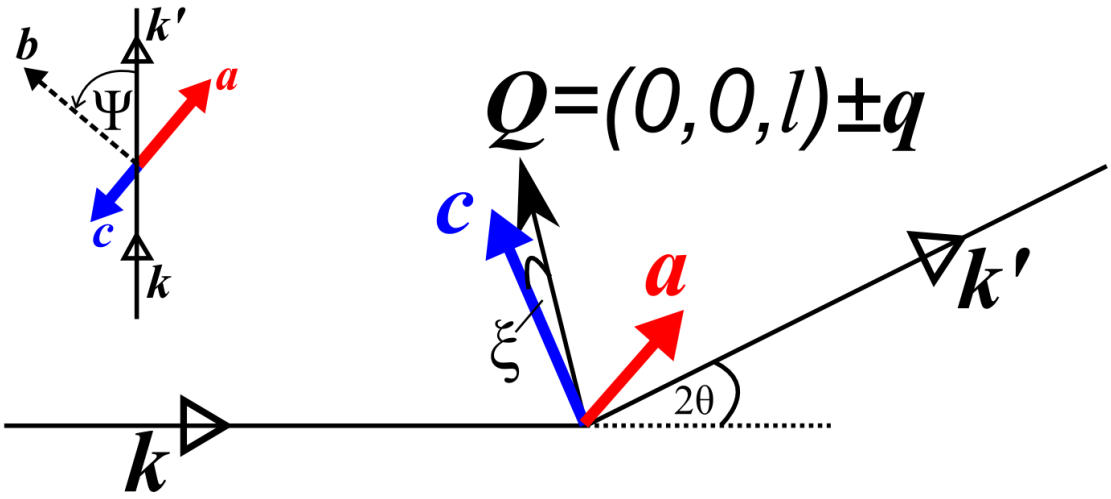


Figure A.2: Schematic of the x-ray scattering experiment probing the magnetic scattering at $\boldsymbol{Q} = (0, 0, l) \pm \boldsymbol{q}$ showing the orientation of the orthorhombic crystal axes at a general azimuth angle Ψ (inset shows projection in the plane normal to $\boldsymbol{Q}$ indicating the azimuth angle origin). In the main diagram ξ is the angle between $\boldsymbol{Q}$ and the c-axis, i.e. $\xi = \cos^{-1}(\hat{\boldsymbol{Q}} \cdot \hat{\boldsymbol{c}})$.

The same procedure can of course be carried out for magnetic Bragg peaks of the γ-Li_2IrO_3 phase, where in fact the expressions are somewhat simplified, due to the more convenient morphology of the γ-Li_2IrO_3 sample (i.e. c-axis very nearly surface

normal). Specifically, considering the peak $(q, 0, 16)$ whose azimuth dependence is shown in Fig 4.5, the experimental setup can be sketched as shown in Fig A.2. The situation described in Fig A.2 is simply a special case of Fig A.1, where $\eta = 90°$ and $\zeta = 90° - \xi$. In this case (A.8) becomes:

$$T(\Psi) = \begin{bmatrix} \sin\Psi\cos\xi & \cos\Psi & -\sin\Psi\sin\xi \\ \cos\Psi\cos\xi & -\sin\Psi & -\cos\Psi\sin\xi \\ -\sin\xi & 0 & -\cos\xi \end{bmatrix}. \tag{A.14}$$

At this position in reciprocal space, only x and y components of the magnetic moment are found to contribute, therefore $\boldsymbol{\mathcal{F}} = [\mathcal{F}_x \ 0 \ \mathcal{F}_z]^{\mathrm{T}}$, and using (A.2) and (A.9) one arrives at the result

$$\mathcal{F}_{\parallel}(\Psi) = \mathcal{F}_x(\sin\xi\sin\theta + \cos\xi\cos\theta\sin\Psi) + \mathcal{F}_z(\cos\xi\sin\theta - \sin\xi\cos\theta\sin\Psi), \tag{A.15}$$

where $\mathcal{F}_{x,z}$ are the separate structure factors for the magnetic moment components along the x, z-axes and the angles 2θ and ξ are defined in the scattering diagram in Fig. A.2. From this the azimuth dependence of the magnetic scattering intensity is obtained as

$$\begin{aligned} |\mathcal{F}_{\parallel}(\Psi)|^2 \ &= \ |\mathcal{F}_z|^2(\cos\xi\sin\theta - \sin\xi\cos\theta\sin\Psi)^2 + |\mathcal{F}_x|^2(\sin\xi\sin\theta + \cos\xi\cos\theta\sin\Psi)^2 \\ &\quad + \mathrm{Re}(\mathcal{F}_z\mathcal{F}_x^*)\left[\sin 2\xi\left(\sin^2\theta - \cos^2\theta\sin^2\Psi\right) + \sin 2\theta\cos 2\xi\sin\Psi\right]. \end{aligned} \tag{A.16}$$

The first two terms give the sum of the scattering intensities separately from moments along the two directions, whereas the last term is the cross term. For the specific case of $\boldsymbol{Q} = (0, 0, l{=}16) + \boldsymbol{q}$, the cross term pre-factor is

$$\mathrm{Re}(\mathcal{F}_z\mathcal{F}_x^*) \propto \begin{cases} \mp\cos\frac{\pi l}{6}\sin\frac{\pi l}{6}, & \pm i(A,-A)_x,(F,F)_z \\ 0, & \pm(A,-A)_x,(F,F)_z \end{cases}, \tag{A.17}$$

where $\mathcal{F}_x$ and $\mathcal{F}_z$ are of the form $\mathcal{F}_{(A,-A)}$ and $\mathcal{F}_{(F,F)}$, respectively, from equations (4.3), (4.5). There is no cross-term if moments are in-phase or π out-of-phase and a finite cross-term if moments are $\pm\pi/2$ out-of-phase. The azimuth data in Fig. 4.5(c) clearly shows a large asymmetry around $\Psi = 0$, which is quantitatively explained (red line) by the basis vector combination $i(A,-A)_x,(F,F)_z$ with moments rotating in the xz plane, and rules out in-phase or π out-of-phase moments along the x and z axes (blue line).

References

[1] M. Blume and D. Gibbs, Physical Review B **37**, 1779 (1988).

Appendix B

Diagonalization of Pseudo Boson Hamiltonian

In this appendix, the pseudo Boson technique, used to describe the spin orbital excitations in $FeSc_2S_4$ of Chapter 6, is introduced and the corresponding Hamiltonian for these spin-orbital triplons is diagonalised.

B.1 Pseudo Boson Technique

As discussed in Section 6.2.2, excitations from the ground state to the triplet state are interpreted as the creation of a pseudo-boson, which is termed a 'spin-orbital triplon'. One can define bosonic creation operators for such excitations, by:

$$\alpha^\dagger(\boldsymbol{r})|0\rangle = |\psi_1(\boldsymbol{r})\rangle, \tag{B.1}$$

$$\beta^\dagger(\boldsymbol{r})|0\rangle = |\psi_2(\boldsymbol{r})\rangle, \tag{B.2}$$

$$\gamma^\dagger(\boldsymbol{r})|0\rangle = |\psi_3(\boldsymbol{r})\rangle, \tag{B.3}$$

where $|0\rangle$ is the groundstate (vacuum) and the triplet state $|\psi_1(\boldsymbol{r})\rangle$ is regarded as the state with an α particle at site $\boldsymbol{r}$ in the crystal, and the triplet state $|\psi_2(\boldsymbol{r})\rangle$ is regarded as the state with a β particle at site $\boldsymbol{r}$, and so on. The Hermitian conjugates

of (B.1), (B.2), (B.3) are the respective annihilation operators, and these are given by:

$$\alpha(\boldsymbol{r})|\psi_1(\boldsymbol{r})\rangle = |0\rangle, \tag{B.4}$$

$$\beta(\boldsymbol{r})|\psi_2(\boldsymbol{r})\rangle = |0\rangle, \tag{B.5}$$

$$\gamma(\boldsymbol{r})|\psi_3(\boldsymbol{r})\rangle = |0\rangle. \tag{B.6}$$

Note that products of such operators are taken in the conventional way, operating first with the right most element.

Calculations were made in the approximation that the Fock space defined by the basis of states $|0\rangle$, $|\psi_1\rangle$, $|\psi_2\rangle$, $|\psi_3\rangle$ is complete, which is reasonable given that the neutron transition spectrum is found to be dominated by the groundstate to triplet transition and that the neutron scattering experiments described in Section 6.3 were carried out at low temperatures, where it can be assumed that each Fe^{2+} ion is in its ground state.

Therefore, all operators of interest can be expanded in terms of products of these creation operators (B.1), (B.2) and (B.3), their Hermitian conjugates (corresponding annihilation operators) and the identity. They have representations as 4×4 matrices, e.g. a general operator $\hat{O}$ acting on these states has a representation:

$$\hat{O} \rightsquigarrow \begin{bmatrix} \langle 0|\hat{O}|0\rangle & \langle 0|\hat{O}|\psi_1\rangle & \dots \\ \langle \psi_1|\hat{O}|0\rangle & \langle \psi_1|\hat{O}|\psi_1\rangle & \dots \\ \vdots & \vdots & \ddots \end{bmatrix}. \tag{B.7}$$

The pseudo-bosonic operators, as defined in (B.1)-(B.6), are trivial matrices in

such a representation, e.g. for the creation of an α excitation, the matrix is

$$\alpha \rightsquigarrow \begin{bmatrix} 0 & 1 & 0 & 0 \\ 0 & 0 & 0 & 0 \\ 0 & 0 & 0 & 0 \\ 0 & 0 & 0 & 0 \end{bmatrix}. \tag{B.8}$$

It can be shown (and by comparing (B.7) and (B.8), it is clear) that each operator's 4×4 matrix representation may be decomposed to a sum of linear and bilinear terms in the operators and the identity. Subsequently, once the states $|0\rangle$, $|\psi_1\rangle$, $|\psi_2\rangle$, $|\psi_3\rangle$ have been explicitly calculated using the numerical diagonalization mentioned in Section 6.2.1, then the representations of $\boldsymbol{S}$ and $\boldsymbol{L}$ can be found by computing (B.7) for all components $S_x, L_x,$ *etc* in the basis of states $|M_L, M_S\rangle$ introduced in Section 6.2.1.

B.2 Dispersion of Triplons

In Section 6.1 the exchange interactions in $FeSc_2S_4$ were discussed in the context of frustration opposing a spin ordered ground state, so one would expect that these interactions will have to be built into this model for comparison to be made with experiment. The feature of interest here is the hopping of the spin-orbital triplons described above which is facilitated by exchange on the diamond lattice of Fe^{2+} sites. The case of $J \ll \Delta$ (where Δ is the energy gap between the singlet and triplet levels in the absence of exchange) is considered, in this limit the exchange is assumed not to alter the nature of the groundstate, such that it can still be described as a product of singlets, but only make possible the hopping of excitations between sites. That is, the calculations are to first order in J/Δ. As explained in Section 6.1, the J_2 exchange is dominant here, so only NNN exchange is considered where excitations propagate on FCC sublattices, and the model is described by a Heisenberg Hamiltonian:

$$\mathcal{H}_{\text{Heis}} = -\sum_{NNN} J_2 \boldsymbol{S_i} \cdot \boldsymbol{S_j}. \tag{B.9}$$

This can be expanded as,

$$\mathcal{H}_{\text{Heis}} = -\sum J_2 (S_z(\boldsymbol{r}_i) S_z(\boldsymbol{r}_j) + \frac{1}{2}[S_+(\boldsymbol{r}_i) S_-(\boldsymbol{r}_j) + S_-(\boldsymbol{r}_i) S_+(\boldsymbol{r}_j)]), \tag{B.10}$$

where $S_z(\boldsymbol{r}_i)$ is the z-component of the spin operator acting at site $\boldsymbol{r}_i$ on the lattice, and so on.

As discussed, the goal is to convert this Hamiltonian from one in terms of spin operators to one in terms of triplon creation/annihilation operators. It is found that the forms of $S_+(\boldsymbol{r})$, $S_-(\boldsymbol{r})$ and $S_z(\boldsymbol{r})$ are given – to linear order in the operators – by:

$$S_+(\boldsymbol{r}) = F_1 \alpha(\boldsymbol{r}) + F_2 \gamma(\boldsymbol{r})^\dagger, \tag{B.11}$$

$$S_-(\boldsymbol{r}) = F_1 \alpha(\boldsymbol{r})^\dagger + F_2 \gamma(\boldsymbol{r}), \tag{B.12}$$

$$S_z(\boldsymbol{r}) = S_1 (\beta(\boldsymbol{r}) + \beta(\boldsymbol{r})^\dagger), \tag{B.13}$$

where F_1, F_2, S_1 are calculated for a given set of values λ and B_4.

Substituting (B.11), (B.12), (B.13) into (B.10) gives the desired spin Hamiltonian which is bilinear in terms of triplon operators. To allow this Hamiltonian to be diagonalized, and thus the normal modes of the system to be deduced, Fourier transformed operators $a_{\boldsymbol{k}}$, $b_{\boldsymbol{k}}$, $c_{\boldsymbol{k}}$ are introduced, defined by,

$$\alpha(\boldsymbol{r}) = \frac{1}{\sqrt{N}} \sum_{\boldsymbol{k}} a_{\boldsymbol{k}}^\dagger e^{-i\boldsymbol{k}\cdot\boldsymbol{r}}, \tag{B.14}$$

$$\beta(\boldsymbol{r}) = \frac{1}{\sqrt{N}} \sum_{\boldsymbol{k}} b_{\boldsymbol{k}}^\dagger e^{-i\boldsymbol{k}\cdot\boldsymbol{r}}, \tag{B.15}$$

$$\gamma(\boldsymbol{r}) = \frac{1}{\sqrt{N}} \sum_{\boldsymbol{k}} c_{\boldsymbol{k}}^{\dagger} e^{-i\boldsymbol{k}\cdot\boldsymbol{r}}, \tag{B.16}$$

where N is the number of exchange-active atoms on the lattice. The Hamiltonian (B.10) now becomes a sum of terms bilinear in the above operators.

Following the method of R.M. White et al [1] the Hamiltonian is written as

$$\mathcal{H} = \sum_{\boldsymbol{k}} \boldsymbol{X}_{\boldsymbol{k}}^{\dagger} \boldsymbol{H}_{\boldsymbol{k}} \boldsymbol{X}_{\boldsymbol{k}}, \tag{B.17}$$

where $\boldsymbol{X}_{\boldsymbol{k}}$ is a column matrix consisting of the independent operators appropriate to the system, the row matrix $\boldsymbol{X}_{\boldsymbol{k}}^{\dagger}$ is its transposed Hermitian adjoint, and $\boldsymbol{H}_{\boldsymbol{k}}$ is a (Hermitian) matrix with c-number elements that produces the original quadratic form. For ease of notation, the $\boldsymbol{k}$ subscript will be dropped and the wavevector dependence be implicit for these objects. For NNN interations, to cast the Hamiltonian in the form of (B.17) requires

$$\boldsymbol{X}^{\dagger} = [a_{\boldsymbol{k}}^{\dagger}\ c_{\boldsymbol{k}}^{\dagger}\ b_{\boldsymbol{k}}^{\dagger}\ a_{-\boldsymbol{k}}\ c_{-\boldsymbol{k}}\ b_{-\boldsymbol{k}}], \tag{B.18}$$

and

$$\boldsymbol{X} = [a_{\boldsymbol{k}}\ c_{\boldsymbol{k}}\ b_{\boldsymbol{k}}\ a_{-\boldsymbol{k}}^{\dagger}\ c_{-\boldsymbol{k}}^{\dagger}\ b_{-\boldsymbol{k}}^{\dagger}]. \tag{B.19}$$

The resulting Hamiltonian's representation is a 6×6 matrix,

$$\boldsymbol{H} = \begin{bmatrix} \boldsymbol{A}_{\boldsymbol{k}} & \boldsymbol{B}_{\boldsymbol{k}} \\ \boldsymbol{B}_{\boldsymbol{k}} & \boldsymbol{A}_{\boldsymbol{k}} \end{bmatrix}, \tag{B.20}$$

with

$$\boldsymbol{A}_{\boldsymbol{k}} = \begin{bmatrix} \frac{\Delta_1}{2} + \frac{J_2 F_1^2}{2}\gamma_{\boldsymbol{k}} & 0 & 0 \\ 0 & \frac{\Delta_2}{2} + \frac{J_2 F_2^2}{2}\gamma_{\boldsymbol{k}} & 0 \\ 0 & 0 & \frac{\Delta_3}{2} + J_2 S_1^2 \gamma_{\boldsymbol{k}} \end{bmatrix}, \tag{B.21}$$

$$\boldsymbol{B_k} = J_2\gamma_{\boldsymbol{k}} \begin{bmatrix} 0 & \frac{F_1F_2}{2} & 0 \\ \frac{F_1F_2}{2} & 0 & 0 \\ 0 & 0 & S_1^2 \end{bmatrix}, \tag{B.22}$$

and

$$\gamma_{\boldsymbol{k}} = \sum_{NNN} \frac{1}{2}\exp(-i\boldsymbol{k}\cdot\boldsymbol{v}_{NNN}), \tag{B.23}$$

where $\boldsymbol{v}_{NNN}$ is a vector linking a Fe^{2+} ion to a nearest neighbour, and the sum is taken over all such vectors and divided by 2 to avoid double counting. Δ_1, Δ_2 and Δ_3 are the zero dispersion (i.e. $J_2 = 0$) splittings between the singlet and triplet states. So far these modes have been considered as degenerate, but the effect of an external magnetic field is to lift this degeneracy, and so the modes are treated as non-degenerate, such that comparisons to experiments with and without a field applied (Sections 6.3.1 and 6.3.3, respectively) can be made with the same model. N.B. $\Delta_1 = \Delta_2 = \Delta_3$ in 0-field.

Diagonalizing (B.20) after the method of [1] leads to the disperssion, $\omega(\boldsymbol{k})$, for the three triplet levels given by:

$$\omega_1(\boldsymbol{k}) = \frac{F_1^2 J_2\gamma_{\boldsymbol{k}} + \Delta_1}{2}\left(1 - \phi_1 + \sqrt{(1+\phi_1)^2 - \xi_1^2}\right), \tag{B.24}$$

$$\omega_2(\boldsymbol{k}) = \frac{F_2^2 J_2\gamma_{\boldsymbol{k}} + \Delta_2}{2}\left(1 - \phi_2 + \sqrt{(1+\phi_2)^2 - \xi_2^2}\right), \tag{B.25}$$

$$\omega_3(\boldsymbol{k}) = \Delta_3\sqrt{1+2\theta}, \tag{B.26}$$

where,

$$\begin{aligned}
\phi_1 &= \tfrac{F_2^2 J_2\gamma_{\boldsymbol{k}}+\Delta_2}{F_1^2 J_2\gamma_{\boldsymbol{k}}+\Delta_1},\\
\phi_2 &= \tfrac{F_1^2 J_2\gamma_{\boldsymbol{k}}+\Delta_1}{F_2^2 J_2\gamma_{\boldsymbol{k}}+\Delta_2},\\
\xi_1 &= \tfrac{2F_1F_2 J_2\gamma_{\boldsymbol{k}}}{F_1^2 J_2\gamma_{\boldsymbol{k}}+\Delta_1},\\
\xi_2 &= \tfrac{2F_1F_2 J_2\gamma_{\boldsymbol{k}}}{F_2^2 J_2\gamma_{\boldsymbol{k}}+\Delta_2},\\
\theta &= \tfrac{2S_1^2 J_2\gamma_{\boldsymbol{k}}}{\Delta_3}.
\end{aligned} \tag{B.27}$$

In order to find the proper diagonalizing transformation, $\boldsymbol{Q}$, of $\boldsymbol{H}$ at each $\boldsymbol{k}$ vector in the first Brillouin zone, three conditions must be met [2]:

$$\boldsymbol{QgAQ^{-1}} = \boldsymbol{gH}, \tag{B.28}$$

$$\boldsymbol{QgQ}^\dagger = \boldsymbol{g}, \tag{B.29}$$

$$\boldsymbol{Q}^\dagger\boldsymbol{HQ} = \boldsymbol{\Lambda}, \tag{B.30}$$

where $\boldsymbol{\Lambda}$ is the diagonalized form of $\boldsymbol{H}$ and $\boldsymbol{g}$ is the boson commutator matrix

$$\boldsymbol{g} = [\boldsymbol{X}^\dagger, \boldsymbol{X}]. \tag{B.31}$$

This transformation introduces a new set of boson operators,

$$\boldsymbol{Y} = [a'_{\boldsymbol{k}}\ c'_{\boldsymbol{k}}\ b'_{\boldsymbol{k}}\ a'^\dagger_{-\boldsymbol{k}}\ c'^\dagger_{-\boldsymbol{k}}\ b'^\dagger_{-\boldsymbol{k}}], \tag{B.32}$$

which are related to the original ones (B.18, B.18) via

$$\boldsymbol{X} = \boldsymbol{QY}. \tag{B.33}$$

The goal is to calculate $\boldsymbol{Q}$ such that matrix elements (6.5) may be calculated. As mentioned earlier, the operators $\boldsymbol{L}$ and $\boldsymbol{S}$ can be expanded in terms of a linear combination of the triplon operators (given that experiments will be conducted at low enough temperatures that the ground state can be treated as fully occupied, therefore

all bilinear terms in $\boldsymbol{L}$ and $\boldsymbol{S}$ would have zero contribution, thereby justifying this linear expansion), and a general expansion for a component ν ($= x, y$ or z) of angular momentum contribution $\boldsymbol{J}$ ($= \boldsymbol{S}$ or $\boldsymbol{L}$) in the case of non-interacting moments can be written as

$$J_\nu = \boldsymbol{J_\nu} \cdot \boldsymbol{X}, \tag{B.34}$$

where $\boldsymbol{J_\nu}$ is a 6 element vector of c-numbers, e.g. for S_z, $\boldsymbol{S_z} = [0\ 0\ S_1\ 0\ 0\ S_1]$.

Substituting (B.33) into (B.34) one can calculate the k-dependent angular momentum operators, $J_\nu(\boldsymbol{k})$ as

$$J_\nu(\boldsymbol{k}) = \boldsymbol{J_\nu} \cdot \boldsymbol{QY}. \tag{B.35}$$

By comparison of (B.35) with (6.5), and noting that in experiments the initial state will be such that $|i\rangle = |0\rangle$, only the first three columns of $\boldsymbol{Q}$ need be considered. This truncated matrix is denoted by '$\boldsymbol{Q_3}$' and is found to be, following the method of [2],

$$\boldsymbol{Q_3} = \begin{bmatrix} 0 & \frac{-\xi_1}{\sqrt{2A_1(1+\phi_1-A_1)}} & 0 \\ \frac{-\xi_2}{\sqrt{2A_2(1+\phi_2-A_2)}} & 0 & 0 \\ 0 & 0 & \frac{-\theta}{\sqrt{2A_3(1+\theta-A_3)}} \\ \sqrt{\frac{1+\phi_2}{2(A_2-1)}} & 0 & 0 \\ 0 & \sqrt{\frac{1+\phi_1}{2(A_1-1)}} & 0 \\ 0 & 0 & \sqrt{\frac{1+\theta}{2(A_3-1)}} \end{bmatrix}, \tag{B.36}$$

where,

$$\begin{aligned} A_1 &= \sqrt{(1+\phi_1)^2 - \xi_1^2}, \\ A_2 &= \sqrt{(1+\phi_2)^2 - \xi_2^2}, \\ A_3 &= \sqrt{1+2\theta}. \end{aligned}$$

From (B.36) and the expressions (B.24), (B.25) and (B.26) it is then possible to calculate the dynamical structure factor of (3.14), $S(\boldsymbol{Q}, \omega)$, for the outlined triplon model.

References

[1] R. White, M. Sparks, and I. Ortenburger, Physical Review **139**, 450 (1965).

[2] A. G. D. Maestro and M. J. P. Gingras, Journal of Physics: Condensed Matter **16**, 3339 (2004).

Appendix C

Linear Spin Wave Theory in a Helical Ordered Magnet

In the following appendix, spin waves from helically ordered moments on a triangular lattice are considered. Initially the case of anisotropic exchanges will be considered and the dispersion relations and dynamical structure factors calculated. These general calculations will then be applied to the isotropic triangular antiferromagnet (TAF), appropriate to the $Ba_3CoSb_2O_9$ system of Chapter 7. This derivation is taken from [1] and is reproduced here for clarity.

C.1 Spin Waves in the Anisotropic TAF

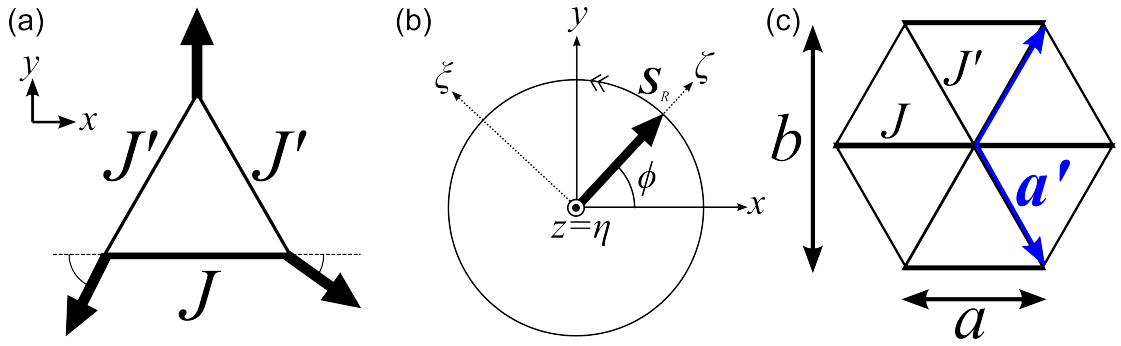


Figure C.1: (a) Mean field groundstate in a TAF showing anisotropic exchanges J, J'. (b) Co-ordinate transformation from x, y, z to ζ, ξ, η (see text). (c) Orthorhombic/triangular lattice for the an/isotropic TAF shown by black/blue arrows.

Consider the ordered moments on a triangular lattice shown in Fig C.1(a), which represent the mean field groundstate of these moments for the given distribution of exchanges J and J'. Note that $J \neq J'$ here, a case referred to as the 'anisotropic triangular antiferromagnet'. The Hamiltonian appropriate to this system is that of Heisenberg, and here the general form in equation (2.4) is simplified to,

$$\mathcal{H} = \sum_{i,i'} J\boldsymbol{S}_i \cdot \boldsymbol{S}_{i'} + \sum_{i,j} J'\boldsymbol{S}_i \cdot \boldsymbol{S}_j. \tag{C.1}$$

As discussed in Section 3.1.4, this magnetic ordering – or equivalently symmetry breaking in spin space – leads to Goldstone modes; magnetic excitations (quantized as magnons) which correspond to a spin flip shared among spins.

The helical order is defined by an ordering vector $\boldsymbol{q}$, such that the rotation angle at a site $\boldsymbol{R}$ is $\phi = \boldsymbol{q}\cdot\boldsymbol{R}+\phi_0$ where ϕ_0 is some constant phase determined by the choice of origin. Such ordering means that the usual cartesian coordinates of the spin x, y, z are not convenient to describe the spin ordering, therefore a transformation is made to coordinates ζ, ξ, η which rotate with the spins throughout the lattice. Specifically, ζ is defined to be along the spin direction at a given site, ξ is perpendicular to the moment and in the helical plane, and η is perpendicular to this plane. This transformation is illustrated in Fig C.1(b), and from here the relation to the cartesian components is clear, namely

$$S^x = S^\zeta \cos\phi - S^\xi \sin\phi, \quad S^y = S^\zeta \sin\phi + S^\xi \cos\phi, \quad S^z = S^\eta. \tag{C.2}$$

Deviations of the spins from their ordered orientations can be expressed in terms of magnon (boson) operators using the Holstein-Primakoff formalism [2]

$$\begin{aligned} S^{+}_{\boldsymbol{R}} &= S^{\xi}_{\boldsymbol{R}} + iS^{\eta}_{\boldsymbol{R}} = \sqrt{2S}a_{\boldsymbol{R}} + \cdots , \\ S^{-}_{\boldsymbol{R}} &= S^{\xi}_{\boldsymbol{R}} - iS^{\eta}_{\boldsymbol{R}} = \sqrt{2S}a^{\dagger}_{\boldsymbol{R}} + \cdots , \\ S^{\zeta}_{\boldsymbol{R}} &= S - a^{\dagger}_{\boldsymbol{R}}a_{\boldsymbol{R}}, \end{aligned} \tag{C.3}$$

where the ellipses denote higher order terms involving three or more operators.

The operator $a^{\dagger}_{\boldsymbol{R}}$ creates a spin deviation at site $\boldsymbol{R}$, whereas $a_{\boldsymbol{R}}$ annihilates a spin deviation at this site. $a^{\dagger}_{\boldsymbol{R}}a_{\boldsymbol{R}}$ is the number operator, and the S^{ζ} component (defined as along the spin, Fig C.1(b)) is equal to the total spin S minus the number of deviations at this site. As expected, the expressions in (C.3) are no different from the ones for the co-linear case [3].

As with the pseudo-boson technique described in Appendix B, the key to diagonalizing the Heisenberg Hamiltonian (C.1) between spins is through transforming the magnon operators to their Fourier equivalents:

$$a^{\dagger}_{\boldsymbol{k}} = \frac{1}{\sqrt{N}} \sum_{\boldsymbol{R}} a^{\dagger}_{\boldsymbol{R}} e^{-i\boldsymbol{k}\cdot\boldsymbol{R}}, \tag{C.4}$$

where N is the total number of spins.

Dismissing the terms with greater than two operators in (C.3) results in the Hamiltonian (C.1) being quadratic in these operators. This can be diagonalized, and the resulting dispersion is found to be [4]:

$$\omega_{\boldsymbol{k}} = 2S\sqrt{(J_{\boldsymbol{k}} - J_{\boldsymbol{q}})[(J_{\boldsymbol{k}-\boldsymbol{q}} + J_{\boldsymbol{k}+\boldsymbol{q}})/2 - J_{\boldsymbol{q}}]}, \tag{C.5}$$

where

$$J_{\boldsymbol{k}} = J\cos(2\pi h) + 2J'\cos(\pi h)\cos(\pi k), \tag{C.6}$$

is the Fourier transform of the exchange couplings as defined in Fig C.1(a), and h, k are reciprocal lattice co-ordinates appropriate for the orthorhombic unit cell shown in Fig C.1(c).

The spin wave spectrum described by (C.5) has a sinusoidal shape with gapless modes at the zone center $\boldsymbol{k} = \mathbf{0}$ and at incommensurate points $\boldsymbol{k} = \pm\boldsymbol{q}$. The $\omega_{\mathbf{0}}$ mode corresponds to rotations of the spins within the ordering plane, whereas $\omega_{\pm\boldsymbol{q}}$ denotes spin waves where the spins cant out of the ordering plane.

The dynamical correlations $S^{\alpha\beta}(\boldsymbol{k},\omega)$ (3.27) can now be calculated, and in fact $S^{\alpha\beta}(\boldsymbol{k},\omega) = 0$ for $\alpha \neq \beta$ as the Hamiltonian (C.1) conserves the total spin component S^z. One magnon ($1M$) excitations occur for excitations transverse to the ordered spin direction ζ, and the corresponding correlations are given by [4]

$$\begin{aligned} S^{\xi\xi}_{1M}(\boldsymbol{k},\omega) &= \frac{Z^{\xi}_{1M}\tilde{S}}{2}\left|u_{\boldsymbol{k}} + v_{\boldsymbol{k}}\right|^2 \delta(\omega - \omega_{\boldsymbol{k}}), \\ S^{\eta\eta}_{1M}(\boldsymbol{k},\omega) &= \frac{Z^{\eta}_{1M}\tilde{S}}{2}\left|u_{\boldsymbol{k}} - v_{\boldsymbol{k}}\right|^2 \delta(\omega - \omega_{\boldsymbol{k}}). \end{aligned} \tag{C.7}$$

Here, Z^{ξ}_{1M} and Z^{η}_{1M} are renormalization factors which take account of the sum rules, and are explained in detail in Section C.3, $\tilde{S}$ is the reduced spin (which will be explained in detail later), $u_{\boldsymbol{k}} = \cosh\theta_{\boldsymbol{k}}$ and $v_{\boldsymbol{k}} = \sinh\theta_{\boldsymbol{k}}$ where $\tanh 2\theta_{\boldsymbol{k}} = B_{\boldsymbol{k}}/A_{\boldsymbol{k}}$ and

$$\begin{aligned} A_{\boldsymbol{k}} &= 2S\left\{\frac{J_{\boldsymbol{k}}}{2} + \frac{1}{4}\left[J_{\boldsymbol{k}-\boldsymbol{q}} + J_{\boldsymbol{k}+\boldsymbol{q}}\right] - J_{\boldsymbol{q}}\right\}, \\ B_{\boldsymbol{k}} &= 2S\left\{\frac{J_{\boldsymbol{k}}}{2} - \frac{1}{4}\left[J_{\boldsymbol{k}-\boldsymbol{q}} + J_{\boldsymbol{k}+\boldsymbol{q}}\right]\right\}. \end{aligned} \tag{C.8}$$

The result of these transverse modes is sharp excitations, governed by the dispersion relation in (C.5).

From (C.3) it is seen that fluctuations polarized along the spin directon, ζ, involve two operators, therefore dynamic correlations along this direction lead to two magnon processes ($2M$), given explicitly by:

$$S^{\zeta\zeta}_{2M}(\boldsymbol{k},\omega) = \frac{Z_{2M}}{2N}\sum_{\boldsymbol{k}_1,\boldsymbol{k}_2} f(\boldsymbol{k}_1,\boldsymbol{k}_2)\delta(\omega-\omega_{\boldsymbol{k}_1}-\omega_{\boldsymbol{k}_2})\delta(\boldsymbol{k}+\boldsymbol{k}_1-\boldsymbol{k}_2+\boldsymbol{\tau}), \tag{C.9}$$

where $f(\boldsymbol{k}_1,\boldsymbol{k}_2) = |u_{-\boldsymbol{k}_1}v_{\boldsymbol{k}_2}+u_{\boldsymbol{k}_2}v_{-\boldsymbol{k}_1}|^2$ is the scattering weight, and Z_{2M} is a renormalization factor to satisfy the sum rules, and will be discussed in Section C.3. As with (C.7), this formula is valid when only terms up to quadratic order are considered in the Hamiltonian (C.1), e.g. no magnon-magnon interactions are considered. In (C.9) $\boldsymbol{k}_1$ and $\boldsymbol{k}_2$ are the wavevectors of two magnons, which can be created anywhere in the first Brillouin zone and $\boldsymbol{\tau}$ is a vector of the reciprocal lattice. For a given $\boldsymbol{k}$ two-magnon processes contribute an extended scattering continuum at energies above a lower threshold. This threshold corresponds to creating one magnon in the lowest energy state (in this case $\omega_{\boldsymbol{k}_1}$=0 at a wave vector $\boldsymbol{k}_1 = \boldsymbol{0}, -\boldsymbol{q}$ or $+\boldsymbol{q}$) and the other magnon at another place in the zone.

Such correlations parallel to the direction of the moment are possible because in the groundstate zero-point quantum fluctuations introduce disorder into the system, and in the linear spin wave approximation this spin reduction is calculated as

$$\Delta S = \sum_{\boldsymbol{k}} |v_{\boldsymbol{k}}|^2/N, \tag{C.10}$$

where $\boldsymbol{k}$ spans the Brillouin zone. This reduction in moment leads to a reduction in the transverse spin wave intensity,

$$\tilde{S} = S - \Delta S - \frac{\langle uv \rangle^2}{(1 + 2\Delta S)}, \tag{C.11}$$

where $\langle uv \rangle = \sum_{\boldsymbol{k}} u_{\boldsymbol{k}} v_{\boldsymbol{k}} / N$.

Though the co-ordinate transformation shown in Fig C.2 provides a convenient way to diagonalize the Hamiltonian (C.1), experiments will take place in the laboratory frame (i.e. not rotating co-ordinate axes at every spin site), therefore dynamical correlations of the cartesian components of the spin will be the ones measured. The transformations in (C.2) must then be used, and it is found that sharp magnon modes appear both in the out of plane,

$$S^{zz}_{1M}(\boldsymbol{k}, \omega) = S^{\eta\eta}_{1M}(\boldsymbol{k}, \omega) = \frac{\tilde{S}}{2} \frac{A_{\boldsymbol{k}} - B_{\boldsymbol{k}}}{\omega} \delta(\omega - \omega_{\boldsymbol{k}}), \tag{C.12}$$

and in-plane dynamic correlations,

$$\begin{aligned} S^{xx}_{1M}(\boldsymbol{k}, \omega) &= S^{yy}_{1M}(\boldsymbol{k}, \omega) = \frac{1}{4} \left[S^{\xi\xi}_{1M}(\boldsymbol{k} - \boldsymbol{q}, \omega) + S^{\xi\xi}_{1M}(\boldsymbol{k} + \boldsymbol{q}, \omega) \right] \\ &= \frac{\tilde{S}}{8} \frac{A_{\boldsymbol{k}-\boldsymbol{q}} + B_{\boldsymbol{k}-\boldsymbol{q}}}{\omega} \delta(\omega - \omega_{\boldsymbol{k}-\boldsymbol{q}}) + \\ &\quad \frac{\tilde{S}}{8} \frac{A_{\boldsymbol{k}+\boldsymbol{q}} + B_{\boldsymbol{k}+\boldsymbol{q}}}{\omega} \delta(\omega - \omega_{\boldsymbol{k}+\boldsymbol{q}}). \end{aligned} \tag{C.13}$$

Inspection of (C.12) and (C.13) reveals that three single magnon modes will be present in a neutron scattering experiment; $\omega_{\boldsymbol{k}}$ polarized out of plane, which is gapless at the zone center and two out of plane modes $\omega_{\boldsymbol{k}-\boldsymbol{q}}$ and $\omega_{\boldsymbol{k}+\boldsymbol{q}}$, i.e. the same disperssion pattern as for that out of plane, but shifted by $\pm\boldsymbol{q}$.

The two magnon contribution given in (C.9) transforms to

$$S^{xx}_{2M}(\boldsymbol{k},\omega) = S^{yy}_{2M}(\boldsymbol{k},\omega) = \frac{1}{4}\left[S^{\zeta\zeta}_{2M}(\boldsymbol{k}-\boldsymbol{q},\omega) + S^{\zeta\zeta}_{2M}(\boldsymbol{k}+\boldsymbol{q},\omega)\right], \tag{C.14}$$

which results in a continuum of scattering emanating from the magnetic Bragg peaks at $\pm\boldsymbol{q}$ (see for example [1]).

C.2 Isotropic TAF

The ordering wavevector $\boldsymbol{q}$ for the anisotropic system shown in Fig C.1(a) is found by minimizing the exchange energy (C.6), and it is found that $\boldsymbol{q} = (0.5 + \epsilon_c, 0, 0)$ where $\epsilon_c = \sin^{-1}[J'/(2J)]/\pi$ is the incommensuration relative to Néel order. This wavevector is expressed in terms of the reciprocal lattice of the orthorhombic unit cell appropriate for the isosceles triangle of Fig C.1(a).

In the case of $J = J'$, the resulting ground state is that of a three sublattice, 120° ordering, and from above it is seen that $\epsilon_c = 1/6$ and $\boldsymbol{q} = (2/3, 0, 0)$. However, this ordering wavevector is still expressed in the orthorhombic reciprocal lattice, when for an isotropic triangular lattice, clearly the hexagonal cell is most appropriate, and the projection of this cell is shown in Fig C.1(c), where the axes are labelled as $\boldsymbol{a'}$ and drawn as blue arrows. In terms of this lattice, the 120° ordering vector is $\boldsymbol{q}' = (1/3, 1/3, 0)$, and it is this basis which shall be used in Chapter 7.

C.3 Sum Rules

In order to quantify the weight of the different contributions to the dynamical structure factor it is insightful to consider general sum rules that apply to the total

integrated intensity. For a given spin quantum number S the dynamical structure factor integrated for wavevectors spanning a full Brillouin zone and all energies, i.e. the total scattering,

$$\frac{1}{N}\sum_{\boldsymbol{k},\alpha}\int_{-\infty}^{\infty} d(\hbar\omega) S^{\alpha\alpha}(\boldsymbol{k},\omega) = S(S+1). \tag{C.15}$$

For spin half systems, a more stringent sum rule applies, whereby each individual Cartesian component of the dynamical structure factor integrates to a third of the total [5], i.e.:

$$\frac{1}{N}\sum_{\boldsymbol{k}}\int_{-\infty}^{\infty} d(\hbar\omega) S^{\alpha\alpha}(\boldsymbol{k},\omega) = \frac{1}{4}, \tag{C.16}$$

for each $\alpha = x, y$ and z. This is independent of temperature, magnetic field, the nature of the Hamiltonian and in fact if spins are interacting or not. Linear spin wave theory is an approximate theory which does not satisfy the above general sum rules and in order to make the theory consistent as a first approximation one can consider the dynamical structure factor calculated within spin wave theory to capture correctly the wave-vector and energy dependence of the intensity and apply an intensity renormalization factor to enforce the sum rules separately for each of the components of the dynamical structure factor. It is most transparent to consider the sum rules in the rotated frame where in the ground state the spins are ferromagnetically-aligned along the ζ axis. The dynamical correlations along the longitudinal (along ζ) axis contain the elastic Bragg peak contribution, of magnitude $(S - \Delta S)^2$, and the two-magnon contribution in (C.9), where the Z_{2M} pre-factor was chosen such as to have the total sum Bragg peak and 2-magon intensity add up to 1/4 (the spin reduction ΔS is obtained as 0.1924 from (C.10)). The dynamical structure factors along the transverse

ξ and η directions both contain one-magnon cross-sections, and the pre-factors Z_{1M}^{ξ} and Z_{1M}^{η} were chosen such that,

$$\frac{1}{N}\sum_{\boldsymbol{k}}\int_{-\infty}^{\infty} d(\hbar\omega) S^{\alpha\alpha}(\boldsymbol{k},\omega) = \frac{1}{4}, \qquad \alpha = \eta, \xi \tag{C.17}$$

separately for each of the two transverse components.

References

[1] R. Coldea, D. Tennant, M. Tsvelik, and Z. Tylczynski, Physical Review Letters **86**, 1335 (2001).

[2] T. Holstein and H. Primakoff, Physical Review **58**, 1098 (1940).

[3] C. Kittel, *Quantum Theory of Solids*, 2^{nd} ed. (Wiley, 1987).

[4] R. Kubo and T. Nagamiya, *Solid State Physics. Edited by Ryogo Kubo and Takeo Nagamiya. Contributors: Ryukiti R. Hasiguti (And Others) Translator: Scripta-Technica; Editor of English Ed.: Robert S. Knox* (Mcgraw-Hill Book Company, 1969).

[5] J. Lorenzana, G. Seibold, and R. Coldea, Physical Review B **72**, 224511 (2005).